Spectroscopic Properties of Photosystems Revealed by Single-molecule Spectroscopy at Low Temperature

Dissertation

der Mathematisch-Naturwissenschaftlichen Fakultät
der Eberhard Karls Universität Tübingen
zur Erlangung des Grades eines
Doktors der Naturwissenschaften
(Dr. rer. nat.)

vorgelegt von
Frau Sepideh Skandary
aus dem Iran, Rasht

Tübingen
2016

Gedruckt mit Genehmigung der Mathematisch-Naturwissenschaftlichen Fakultät der Eberhard Karls Universität Tübingen.

Tag der mündlichen Qualifikation:	02.12.2016
Dekan:	Prof. Dr. Wolfgang Rosenstiel
1. Berichterstatter:	Prof. Dr. Marc Brecht
2. Berichterstatter:	Prof. Dr. Alfred J. Meixner

Abstract

In this thesis, single-molecule spectroscopy (SMS) at low temperature is utilized to comprehensively investigate the spectroscopic properties of the light-harvesting antenna complexes such as photosystem I (PSI) and II (PSII).

The fluorescence of single PSII core complexes (PSIIcc) shows that the spectra are dominated by sharp lines, which come from multiple emitters and not only from one lowest trap. These datasets show the existence of the three well-known fluorescence bands denoted F685, F689, and F695. Further analysis of dimeric PSIIcc (dPSIIcc) presents that these sharp lines are the result of weak to intermediate exciton-vibrational coupling and slow spectral diffusion. The Huang-Rhys factors, which are a measure of the strength of exciton-vibrational coupling, vary between 0.03 and 0.8 in single dPSII. Based on these values, there is no obvious correlation between coupling strength and wavelength position. These results show that electrostatic, rather than exchange or dispersive interactions, are the main contributors to the exciton-vibrational coupling in dPSII systems.

The SMS of single monomeric PSII core complexes (mPSIIcc) at 1.6 K, also shows the same three fluorescence bands detected in dPSIIcc, however, the intensity of F695 in mPSIIcc SMS datasets is reduced as compared to the single dPSIIcc. The mPSIIcc contains one β-Carotene less than dPSIIcc at the monomer-monomer interface of dPSIIcc, which leads to an increased lifetime of the triplet state by Chl17. This explains the reduced singlet emission of F695 in mPSIIcc.

The results from fluorescence measurements of single PSIIcc and PSI complexes demonstrate different spectroscopic properties. The fluorescence of single PSI complexes show besides the sharp lines also broad emission bands at 1.6 K. Polarization dependent SMS provides detailed insight into the fluorescence dynamics of the red Chls, demonstrating that Chls absorb light at longer wavelengths than reaction center, and their interactions with other chromophores are mainly happened by excitation energy transfer (EET). The spectral dynamics between the single PSI trimer (PSI-T) and monomer (PSI-M) complexes in both S- and P-polarization dependent datasets indicate that the single PSI-M complexes feature less spectral diversity of their fluorescence than single PSI-Ts. The analysis of polarization dependent datasets from single PSI-M complexes

demonstrates two spectrally separate emissions corresponding to two fluorescence pools in PSI-M. Representatively, an almost perpendicular orientation is estimated between them, where they are not connected with each other via energy transfer pathways. Finally, several candidates for red-coupled Chl dimers based on the X-ray structure of PSI-M are discussed .

The fluorescence enhancements of PSI-T in proximity to bimetallic plasmonic nanostructures are reported using SMS at cryogenic temperature (1.6 K). Moreover, controlled modification of fluorescence and energy transfer properties of PSI complexes are shown by using a Fabry-Perot resonator with silver mirrors. Finally, resolution enhancement of a confocal scanning microscope using immersion liquid under cryogenic conditions for imaging the biological specimens is discussed.

Contents

Zusammenfassung

In dieser Arbeit wird Einzelmolekülspektroskopie (SMS) bei tiefer Temperatur verwendet, um die spektroskopischen Eigenschaften der zwei Lichtsammelkomplexen in der Photosynthese, wie beispielsweise Photosystem I und II (PSI und PSII) ausführlich zu untersuchen.
Die Fluoreszenz der einzelnen PSII-Komplex zeigt, dass die Spektren durch scharfe Linien dominiert sind, die von unterschiedlichen Emittern und nicht von nur einem energisch tiefesten zustand herrühren. Die weitere Analyse zeigt, dass diese scharfen Linien aufgrund einer schwachen bis mittleren Exzitonen-Schwingungskopplung und einen langsamen spektralen Diffusion entstehen. Diese Ergebnisse zeigen, dass die elektrostatische, und nicht Austausch- oder Dispersionswechselwirkungen die wichtigsten Beiträge zu der Exzitonen-Schwingungskopplung in PSII-System liefern.
Die Fluoreszenz von einzelnen monomeren PSIIcc (mPSII) zeigt die Existenz der drei bekannten Banden F685, F689 und F695. Außerdem ist in mPSIIcc SMS Datensätzen die Intensität von F695 im Vergleich zu einzelnen dPSIIcc verringert. Das mPSII enthält eine β-Carotene weniger als dPSII an seiner Monomer-Monomer-Interface, was zu einer längeren Triplett-Lebensdauer des Chl 17 führt. Dies könnte die geringere Singulett-Emission von F695 in einzelnen mPSII erklären. Die Ergebnisse aus der Fluoreszenz einzelner PSI zeigen unterschiedliche optische Eigenschaften im Vergleich zu PSII. Die Fluoreszenz von einzelnen PSI weist neben den scharfen Linien auch die zusätliche breite Emission auf. Die polarisationsabhängige Einzelmolekülspektroskopie liefert detaillierte Einblicke in die Fluoreszenzdynamik der roten Chls. Diese Chls absorbieren Licht bei längeren Wellenlängen als Reaktionszentrum P700 in PSI. Die Wechselwirkungen mit anderen Chromophoren werden hauptsächlich durch Anregungsenergietransfer (EET) passiert. Beim Vergleich der spektralen Dynamik zwischen den einzelnen PSI Trimere (PSI-T) und monomeren (PSI-M) Komplexe in beiden S- und P-polarisationsabhängigen Datensätzen zeigen die einzelnen PSI-M-Komplexe weniger spektrale Vielfalt in ihrer Fluoreszenz als einzelne PSI-T-Komplexe. Die Analyse der polarisationsabhängigen Daten von einzelnen PSI-M-Komplexe zeigt zwei spektral getrennte Emitteren entsprechend zweier Fluoreszenz-Pools in PSI-M. Aus den Daten lässt sich eine nahezu senkrechte Ausrichtung dieser beiden Emitter abschätzen. Da sie beiden den Spektralen

beobachten werden können, kann man darauf schließen, dass sie nicht miteinander über Energieübertragungswege verbunden sind. Schließlich kann man geeignete Kandidatin für rot gekoppelter Chl Dimere basierend auf der X-Ray strukturen des PSI-M herausfinden.
Fluoreszenzverstärkungen wird durch Kopplung von PSI an verschiedene plasmonischer Nanostrukturen beobachtet. Darüber hinaus ist die kontrollierte, modifizierte Fluoreszenz und Energieübertragungseigenschaften des PSI durch Verwendung eines Fabry-Perot-Resonators aus Silberen Spiegel. Schliesslich wird Auflösungsverbesserung unter Verwendung von Immersionsflüssigkeit bei kryogenen Temperaturen zur Abbildung biologischer Proben mittels SMS diskutiert.

Abbreviation

Photosystem I: PSI,

Photosystem II core complex: PSIIcc,

Photosystem I trimer: PSI-T,

Photosystem I monomer: PSI-M,

Photosystem II: PSII,

Photosystem II dimer: dPSII,

Photosystem II monomer: mPSII,

Thermosynechococcus elongatus: *T. elongatus*,

Intrinsic antenna protein subunits of PSII: CP43, CP47,

Adenosine triphosphate: ATP,

Nicotinamide adenine dinucleotide phosphate: NADP,

Zero-phonon line: ZPL,

Phonon wing: PW,

Highest occupied molecular orbital: HOMO,

Lowest unoccupied molecular orbital: LOMO,

Reaction center: RC,

Chlorophyll *a*: Chl*a*,

Long wavelength chlorophyll: LWC,

Carotene: Car,

β carotene: BCR,

Single-molecule spectroscopy: SMS,

Excitation electron transfer: EET,

Two level-system: TLS,

Transition dipole moment: TDM,

Franck-condon: FC,

Avalanche photodiode: APD,

Acousto-optical tunable filter: AOTF,

Continuous wave: CW,

Charge-coupled device: CCD,

Lens: L,

Mirror: M,

Long-pass filter: LPF,

Liquid nitrogen: LN,

Helium: He,

Liquid helium: LHe,

Electron microscope: EM,

Discrete Fourier transformation: DFT,

Spectral hole burning: SHB,

Nonphotochemical hole burning: NPHB,

Fluorescent line narrowing: FLN,

Full width at half maximum: fwhm,

Numerical aperture: NA,

Microscope objective: MO,

Quantum dots: QDs,

Point spread function: PSF,

List of Publications and Conferences

1- M. Brecht, **S. Skandary**, J. Hellmich, C. Glöckner, A. Konrad, M. Hussels, A. J. Meixner, A. Zouni, E. Schlodder: "Spectroscopic Properties of Photosystem II Core Complexes from *Thermosynechococcus elongatus* Revealed by Single-Molecule Experiments", *Biochim. Biophys. Acta*, 1837, 773–781, **(2014)**.

2- A. Konrad, A.L. Trost, **S. Skandary**, M. Hussels, A. J. Meixner, N. V. Karapetyan, M. Brecht: "Manipulating the Excitation Transfer in Photosystem I by a Fabry- Perot Metal Resonator with Optical Sub-wavelength Dimensions", *PCCP* 16, 13, 6175–6181, **(2014)**.

3- **S. Skandary**, M. Hussels, A. Konrad, T. Renger, F. Müh, M. Bommer, A. Zouni, A. J. Meixner, M. Brecht: "Variation of Exciton-Vibrational Coupling in Photosystem II Core Complexes from *Thermosynechococcus elongatus* as Revealed by Single-Molecule Spectroscopy". *J. Phys. Chem. B*, 119 (11), 4203–4210, **(2015)**.

4- I. Ashraf, **S. Skandary**, M. Y. Khaywah, M. Metzger, A. J. Meixner, P. M. Adam, M. Brecht. "Effects of Irregular Bimetallic Nanostructures on Optical Properties of Photosystem I from *Thermosynechococcus elongatus*", *Photonics*, 2(3), 838-854, **(2015)**.

5- **S. Skandary**, A. Konrad, M. Hussels, A. J. Meixner, M. Brecht, "Orientations Between Red Antenna States of Photosystem I Monomers from *Thermosynechococcus elongatus* Revealed by Single-Molecule Spectroscopy " *J. Phys. Chem. B*, 119, 13888-13896, (2015) **(2015)**.

6- **S. Skandary**, A. Konrad, M. Hussels, A. J. Meixner, M. Brecht, "Polarization Dependent Single-Molecule Spectroscopy of Photosystem I", *Proc. SPIE 9554*, **(2015)**.

7- **S. Skandary**, F. Müh, I. Ashraf, M. Ibrahim, M. Metzger, A. Zouni, A. J. Meixner, M. Brecht , " Role of Missing Caroteniod in Reducing the Fluorescence of Single Monomeric photosystem II", submitted in PCCP.

8- M. Metzger, A. Konrad, **S. Skandary**, I. Ashraf, A. J. Meixner, M. Brecht , "Resolution Enhancement for Low-Temperature Scanning Microscopy by Cryostat Immersion Imaging", *Opt. Express*, 24(12), 13023–13032 **(2016)**.

9- I. Ashraf, A. Konrad, H. Lokstein, **S. Skandary**, M. Metzger, J. M. Djouda, P. M. Adam, A. J. Meixner, M. Brecht, " Temperature Dependence of Metal-Enhanced Fluorescence of Photosystem I Thermosynechococcus elongatus ", submitted.

Conferences

1- "Single-Molecule Spectroscopy on Photosystem II of *Thermosynechococcus elongatus* at Light-Harvesting Processes LHP 2013, March 2013, Banz Monastery, Germany.

2- " *Thermosynechococcus elongatus* by Single-Molecule Spectroscopy" at 13th Conference on Methods and Applications of Fluorescence: Spectroscopy, Imaging and Probes, September 2013, Genoa, Italy.

3- "Site Specific Immobilization of Photosynthetic Proteins on Gold Nanostructures" at COST Action MP1302 Nanospectroscopy, March 2014, Tübingen Germany.

4- "Single-Molecule Spectroscopy of Photosystem II from *Thermosynechococcus*" in the Meeting Photosynthesis Research for Sustainability in honor of Vladimir A. Shuvalov, Jun 2014, Pushchino, Russia. (Best poster award).

5- "Variation of Exciton-Vibrational Coupling in Photosystem II Core Complexes from *Thermosynechococcus elongatus* as Revealed by Single-molecule Spectroscopy", Processes LHP 2015, March 2015, Banz Monastery, Germany.

6- "Polarization Dependent Single-Molecule Spectroscopy of Photosystem I", SPIE Optics and Photonics 2015, August 2015, San Diego, CA, United States.

Motivation

The Earth is warming; clearly rising global temperatures are accompanied by changes in weather and climate. The oceans become more acidic, ice caps are melting, and sea levels are rising. As these and other changes become more pronounced in the coming decades, they will likely present challenges to our society and environment.

Over the last century, human activities have released large amounts of carbon dioxide (CO_2), and other greenhouse gases into the atmosphere. The majority of greenhouse gases come from burning fossil fuels to produce energy. Greenhouse gases act like a blanket around the Earth, trapping heat in the atmosphere and causing to warm. CO_2 can stay in the atmosphere for nearly a century, so the Earth will continue to warm in upcoming decades [1], and the risk of severe climate changes increases. Moreover, energy is the most pressing demand in the contemporary world. The limited amount of nonrenewable energy sources, which are available for less than 200 years, and steadily increasing costs of fossil energy force researchers to explore for fuels do not depend on oil, coal, etc. Our decisions today will shape the world for the next generations.

Future prospects for clean, green and renewable energy may depend on our ability to mimic and improve upon photosynthesis- the chemical process by which plants, algae and some bacteria store energy from the sun in the form of carbohydrates. The idea seeks to emulate the systems that already exist in nature and more than that, to exploit the basic chemical pathways of photosynthesis in order to create hydrogen, methanol, and other clean fuels [2]. An artificial version of photosynthesis uses sunlight and produce liquid fuels from nothing more than CO_2 and water. This will be an ideal solution for recycling CO_2, which is the global concern with regard of pollution nowadays.

The processes occurring during photosynthesis, such as dynamic self-repair and light harvesting can be integrated into artificial photovoltaic devices [3, 4]. Similarly, proteins that enable the natural photosynthesis process are integrated into existing solar-energy technologies [5, 6]. One of the most frequently used photoactive building block for that purpose is the protein complex called photosystem I (PSI). PSI contains a large antenna system in which light is harvested by molecules called chlorophylls (Chls), absorb at distinct wavelengths and funnel

the excitation energy to a special pair of Chls (P700), where charge separation takes place. Based on these findings, biophotovoltaic devices similar to dye-sensitized solar cells were fabricated by self-assembly of PSI on 3D nanostructured semiconductor electrodes using a liquid electrolyte as redox mediator [7].

The protein complex known as photosystem II, (PSII), splits water molecules to release oxygen using sunlight and relatively simple biological building blocks. The oxidation of water molecules, which takes place during the photosynthetic reactions, is one of the essential processes of photosynthesis. It provides the necessary electrons to convert CO_2 into glucose, and also creates O_2 gas as a byproduct. Although water can also be split artificially using an electrical voltage and a precious metal catalyst, researchers continue to strive to mimic the efficient natural process [8].

Due to progress in experimental and theoretical techniques, it has become possible to develop a microscopic picture of the primary photosynthetic processes. Biophysical measurements are utilizing various spectroscopic techniques to find details of the spectral dynamics, structure and function of photosynthetic systems. Understanding details of these systems requires the knowledge of the microscopic structure of the antenna complexes. The goal of this thesis is to show more details of spectroscopic properties of PSI and PSII using single-molecule spectroscopy (SMS) [9, 10], a fascinating tool that can be used to observe optical signals of individual molecules. The optical signals of protein-embedded pigments can be used to study the specific pigment-protein interactions. It serves as a powerful method to study the spectroscopic details of individual systems, where obscured by ensemble averaging. Using the advantages of SMS together with the benefit of working at low temperature e.g. decreasing spectral diffusion and photo-bleaching, one is able to detect dominant details of fluorescence from single PSI and PSII complexes such as extremely narrow linewidths of fluorescence emission, different fluorescence bands, the respective orientations between fluorescence pools, enhanced, controlled, modified fluorescence and excitation energy transfer pathways. These findings provide potential information regarding the whole process of photosynthesis for more practical use of photosystems in future.

Introduction

Photosynthesis captures energy for life on the Earth. In oxygenic photosynthesis of cyanobacteria, green algae and higher plants, the harvested energy is used to oxidize water and reduced plastoquinone in a membrane-embedded pigment-protein complex (PPC) called PSII [11, 12]. Another trans-membrane PPC essential for oxygenic photosynthesis is PSI, which is located in the thylakoid membranes of cyanobacteria, algae and plants. It mediates light-induced electron transfer from plastocyanin or cytochrome C_6 on the lumenal side to Ferredoxin on the stromal side [13].

The first step of the photosynthetic reaction is the absorption of a photon by the antenna system of PSII and PSI followed by subsequent energy transfer to the reaction center (RC). The PSI was named "I" since it was discovered before PSII, but this does not represent the order of the electron flow. The efficient excitation energy transfer (EET) to RC in photosynthetic light-harvesting complexes (also termed antenna proteins), is done by an intricate interplay between different pigment molecules [14, 15]. The captured excitation energy is used to induce a trans-membrane charge separation starting at the Chl pairs, P680 in PSII and P700 in PSI, which their main absorptions are around 680 and 700 nm in PSII and PSI, respectively [13, 16].

A fascinating feature of the antennas in PSII and PSI complexes are the presence of several Chl *a* molecules absorbing at longer wavelengths (lower energies) than e.g. P700 in PSI, with respect to the usual Q_y absorption at 664 nm for Chl *a* in 80% Acetone [17, 18]. However, the Q_y absorption in PSI is around 680 nm, this red shift is due to the interaction between the bulk Chls in the protein scaffold. These red-shifted Chl *a* molecules are often referred to red Chl *a* or long-wavelength Chl (LWC) [19, 20]. LWCs of PSI from different cyanobacteria show remarkable differences concerning the number and the spectral positions. The spectral heterogeneity of the antenna Chls can be explained by site-energy differences arising from pigment–protein interactions and strong pigment–pigment interactions of excitonically coupled Chls. These coupled Chls, form as dimers or trimers with strongly red-shifted absorption

(see above). LWCs have a pronounced effect on the energy transfer within the whole antenna system. EET processes from the bulk to LWCs occur within a few picoseconds [21].

At room temperature, the quantum efficiency of photochemistry is virtually not affected by the LWCs. Thermal energy of the surroundings enables efficient uphill energy transfer via bulk Chls to the primary donor in the RC. At cryogenic temperatures, however, the fluorescence of the LWCs increases considerably, suggesting that a significant part of the excitation energy is no longer able to reach primary donor in the RC [22]. Thus, at lower temperatures, the red Chls act as traps for the excitation energy, which means that the quantum efficiency of the charge separation decreases, while the fluorescence intensity increases [22, 23].

The PSI from cyanobacteria can be isolated in monomeric and trimeric forms [24, 25]. The trimer is proposed to be the native form, at least under certain physiological conditions [26]. Both, the trimeric and monomeric species, absorb light at room temperature and show more than 95 % probability of inducing charge separation [27]. This indicates that energy exchange between monomers is negligible, and a single monomer can be used to describe the optical properties of PSI [28]. The PSI core complex coordinates all of the redox cofactors and the core antenna of 96 Chl *a* and 20 β–carotene (BCR) molecules. After absorption of light by an antenna pigment, the excitation energy is efficiently trapped within 30 ps via charge separation in the RC leading to $P700^{+}A_{0}^{-}$ [17]. Detailed analysis of the absorption spectra of PSI from *Thermosynechococcus elongatus* (*T. elongatus*) allows to distinguish the red emitting Chl *a* into two main pools denoted C708 and C719 [29, 30, 31, 32] (see Figure 1 a,b) .

The PSII core complex (PSIIcc) is a light-driven water-plastoquinone-oxidoreductase, which is the heart of oxygenic photosynthesis due to its ability to subtract electrons from water [11, 12, 35, 36]. PSIIcc from *T. elongatus* exists in dimeric (dPSIIcc) and monomeric (mPSI Icc) forms. The mPSIIcc contains the same protein subunits as dPSIIcc and is of sufficient purity for protein crystallization [37]. At 3.6 Å resolution, large cofactors such as Chl *a* and pheophytin molecules are well-defined by the arrangement of all chlorins in the RC and all 29 Chl *a* molecules bound to the core antenna proteins CP43 (13 Chl *a*) and CP47 (16 Chl

a) [37]. The crystal structure of a highly active mPSIIcc [37] revealed that 1.3 ± 0.2 BCR pigments per monomer are missing in mPSIIcc as compared to dPSIIcc. Five of the 12 Cars in the dPSIIcc are located at the monomer-monomer interface; remarkably, only one of these five molecules is missing in the monomer. This Car is found in a bridging position across the monomer-monomer interface. The best defined Car in the mPSIIcc is Car_{D2} close to cytochrome b_{559} [37]. The absorbance difference spectra of Car-pigments of redissolved crystals of monomeric and dimeric PSIIcc in 80% (v/v) aqueous acetone confirmed the lack of one Car between monomeric and dimeric PSIIcc [37]. It has been proposed that Car is

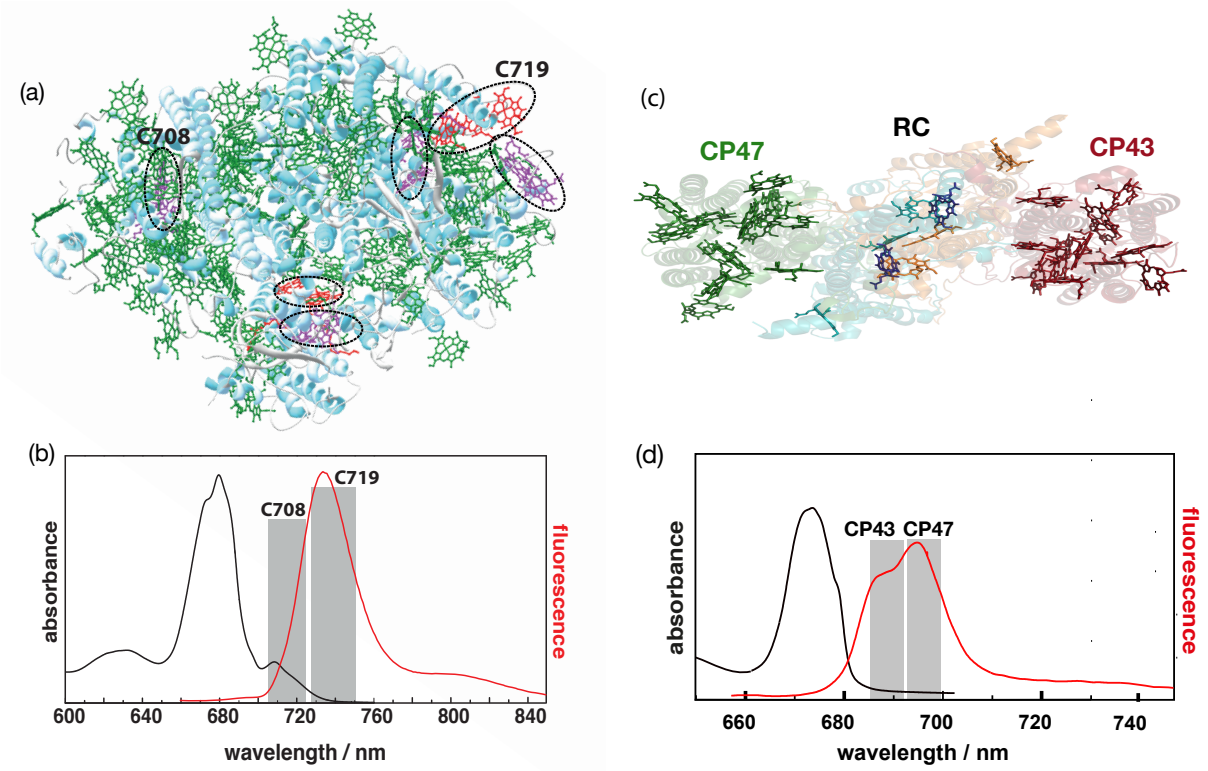

Figure 1: (a): Arrangement of Chls in one monomer of PSI from *T. elongatus*. The figure is produced by PDB file 1JB0 [33] using the program Swiss–PdbViewer. LWCs are colored red (contributions of red pools C719) and dark pink (contributions of red pools C719). (b): Absorption and fluorescence spectra of PSI at cryogenic temperatures. Dark areas show the emission wavelength ranges of red pools C708 and C719. (c): Arrangement of Chls in subunits of PSIIcc from *T. elongatus*. The Chls coordinated by CP47, CP43, RC are colored in green, orange, cyan and red. The two Pheos are colored in blue. The figure was drawn using the program PyMol based on the coordinates of the PSII structure of (*S. vulcanus)* [34]. (d): Absorption and fluorescence spectra of PSIIcc at cryogenic temperatures. Dark areas show the emission wavelength ranges of the contributions CP43 and CP47.

the initial donor of the secondary electron-transfer pathway to $P680^+$ [38]. Given the close proximity of the Chls within the inner antenna proteins CP43 and CP47 (4-6 Å), a cation radical in the antenna could rapidly move to other Chl and Car, because the rates of electron transfer among these densely packed pigment molecules are expected to be very fast [39].

The fluorescence spectrum of dPSIIcc exhibits a complicated temperature dependence in both plants [40, 41] and cyanobacteria [42, 43]. They are characterized by a fluorescence maximum at 685 nm at temperatures above 140 K and the emergence of a second fluorescence peak at 695 nm upon cooling down to 77 K. Further cooling reduces the intensity of fluorescence at 695 nm, so that mainly one peak at 685 nm is left at around 4 K. This complex behavior was explained in terms of two distinct pools of Chls, F685 and F695, emitting at different wavelengths and both absorb at lower wavelengths than the primary electron donor state in the RC [43]. Besides F685 and F695, the third emitter termed F689 can be detected at temperatures below 77 K [44]. F685 was assigned to Chls in CP43 [45], whereas F695 was assigned to Chls in CP47 [45, 46, 47]. Indeed, some models allocated F689 to either CP43 or CP47, and left open the possibility that Chls of CP47 contribute to F685 [44] (see Figure 1 c,d) .

Some spectroscopic techniques such as spectral hole burning (SHB) and fluorescence light narrowing (FLN) detecting fluorescence by ensemble spectra, cannot reveal spectroscopic details clearly due to overlapping signals in inhomogeneous broadened spectra in single-molecule levels, the trivial optical details of single-complexes can be distinguished. SMS is an excellent technique to cope with inhomogeneous spectral broadenings and represents subtle spectral details often obscured by averaging over heterogeneous ensembles [9, 48]. At room temperature, spectral diffusion and photo-bleaching hamper the collection of detailed spectroscopic information for the most single molecules [49, 50, 51, 52]. Lowering the temperature reduces the impact of spectral diffusion [52, 53, 54], and the emission profile of a single emitter is composed of a sharp zero-phonon line (ZPL), it belongs to pure electronic transition, and a vibrational side so-called phonon wing (PW), becomes observable [55, 56, 57, 58]. The PW on the low energy side of the ZPL belongs to electronic transitions with excitations of vibrational quanta. This coupling is due to the interaction of the

chromophore with its surrounding. The ZPL and PW can only be distinguished at low temperatures, because the temperature dependence of the exciton-vibrational coupling causes the PW to mask the zero-phonon contributions completely at temperatures above 100 K. The ratio between the intensity of the ZPL and PW depends on the strength of exciton-vibrational coupling expressed by the Huang-Rhys factor (S) [59, 60, 61]. The dimensionless factor S is a measure for the linear exciton-vibrational coupling strength and characterizes the average number of vibrational quanta excited during a particular electronic transition [62].

In this thesis, the results of SMS measurements from PSI and PSII samples at 1.6 K are presented. The experimental datasets are analyzed using MATLAB algorithms. The methods of the experiment, together with the algorithms used for analyzing the datasets, are explained in Materials and Methods section.

In Chapter 1, a combination of absorption, fluorescence and low temperature SMS are used to investigate on the spectral properties, heterogeneities and dynamics of the Chl$a$ molecules responsible for the fluorescence emission of dPSIIcc. At the ensemble level, the absorption and fluorescence spectra show a temperature dependence similar to plant PSII. The fluorescence of single dPSIIcc is reported for the first time. The time dependent datasets of single PSIIcc present several information of spectroscopic properties of one single–complex. The spectra are dominated by ZPLs in the range between 680 – 705 nm. Single-molecule experiments unambiguously show that different emitters, and not only the lowest energy trap, contribute to the low temperature emission spectrum. The average spectrum obtained from more than a hundred single complexes shows three main contributions that are in good agreement with the reported fluorescence bands F685, F689 and F695. Additionally, it is shown that the red-most emitter does not contribute to the fluorescence spectrum as long as it is in the triplet state. In addition, quenching of fluorescence by the triplet state may lead to a decrease of long wavelength emission.

In Chapter 2, the spectral properties, dynamics and relative occurrence of ZPLs in single dPSIIcc datasets are analyzed. The sharp ZPLs are the result of weak to intermediate exciton-vibrational coupling and slow spectral diffusion. For several datasets, it is possible

to surpass the effect of spectral diffusion by applying a shifting algorithm. The increased signal-to-noise ratio enables one to determine the exciton-vibrational coupling strength (Huang-Rhys factor) with high precision. The values of the Huang-Rhys factors show no obvious correlation between coupling strength and wavelength position. Therefore, it is concluded that electrostatic, rather than exchange or dispersive interactions is the main contributors to the exciton-vibrational coupling in this system.

In Chapter 3, the results from fluorescence of single mPSII sample at 1.6 K are shown in details. The accumulation of Chl triplet states (^{3}Chl) in PSIIcc subunits, CP47 and CP43, can be expected by those Chls, which have the lowest singlet transition energies and contribute mostly to the fluorescence. In particular, F695 has the lowest transition energy, will be subject to intersystem crossing and triplet accumulation. The lack of one Car in mPSIIcc leads to the stronger fluorescence quenching at the longest wavelength range, because when one Car is absent, the energy is trapped in the adjacent Chl. This SMS datasets show that the intensity of F695 is reduced in single mPSIIcc compared to single dPSIIcc and Chl17 in the CP47 subunit is discussed as a potential candidate for F695.

In Chapter 4, the fluorescence of single PSI-M and PSI-T are compared. Moreover, polarization dependent measurements demonstrate the spectrally separate emissions corresponding to C708 and C719 in single PSI-M and PSI-T. Polarization dependent single-molecule spectroscopy provides detailed insight into the fluorescence dynamics of the red Chls and their interactions with other chromophores mainly happened by EET. The spectral dynamics between trimeric and monomeric single PSI complexes reveal that the fluorescence of single PSI-M complexes show less spectral diversity than single PSI-T.

In Chapter 5, more detailed information about the LWCs of PSI-M responsible for the fluorescence of these contributions revealed by polarization dependent experiments on single PSI-M. Polarization dependent measurements representatively show two spectrally separated fluorescence bands at low temperature with distinguishable polarization. The analysis of experimental datasets indicates that the orientation between the emitters in PSI-M depends on the mutual orientation of the TDMs of the respective emitters. Moreover, the experimental

results are compared with simulations based on the projected polarization of randomly–oriented pairs of emitting dipoles with fixed angles. This comparison enables one to estimate the real angle between the TDMs of the respective emitters of C708 and C719 in PSI-M. Finally, several candidates for red coupled Chl dimers based on the X-ray structure of PSI are discussed.

In Chapter 6, the fluorescence of PSI-T in proximity to bimetallic plasmonic nanostructures is explored by SMS at 1.6 K. Different enhancement factors are observed for individual PSI complexes coupled to Au/Au and Ag/Au samples. Additionally, a wavelength dependence of fluorescence enhancement is observed, which is explained by the multichromophoric composition of PSI.

In Chapter 7, it is discussed how excitation transfer within PSI is affected by the microcavity using experimental datasets and simulation methods. Comparing the experimental data with simulations assuming uncoupled emitters provides the intensity changes caused by altered energy transfer pathways. It is shown that the control of energy transfer within such efficient energy converters as photosynthetic proteins can establish the opportunity for enhancing the efficiencies in bio-solar applications.

In Chapter 8, a simple method for resolution enhancement using the confocal microscope under cryogenic conditions is shown. Using a microscope objective (MO) together with the immersion fluid with low freezing temperature, one is able to create a high–resolution image of biological samples at 160 K. The MO and the sample are both placed inside the inner chamber of the cryostat to reduce induced distortions by temperature gradients. The resolution of images from Quantum Dots (QDs) with and without immersion liquid at both room and cryogenic temperatures are compared.

Optical Transitions in Pigments

A molecule absorbs light only in resonance condition, i.e. when the energy of the incident photon $h\nu$ matches the energy difference between an initial occupied state and a final unoccupied state of the molecular system. The first approximation for the electronic transition energy of an organic pigment molecule with alternating single and double bonds can be estimated from the length of its delocalized π-electron system. The optical properties of Chls are determined by extended conjugated π-electron systems [63, 64]. The strong optical transitions in the blue (Soret band) and in the red (Chl) are due to $\pi \rightarrow \pi^*$ transitions. These transitions arise from linear combinations of one electron between the two highest occupied (HOMO and HOMO-1) and the two lowest unoccupied (LUMO and LUMO+1) π-type molecular orbitals [63, 65].

After an electron is excited, the energy may be transferred in different ways. One will be through vibrational relaxation, a non-radiative process (see Figure 2). This process is very fast, between 10^{-14} and 10^{-11} s, therefore, it is likely to occur immediately following absorbtion. Another process is internal conversion, which is a radiationless transition from a higher to a lower electronic state, see the Jablonski diagram in Figure 2. Internal conversion occurs, because of the overlap of vibrational levels of different electronic energy states. Internal conversion occurs in the same time frame as vibrational relaxation, therefore, it is a very likely way for molecules to dissipate energy from light perturbation. Another pathway for molecules to deal with energy received from photons is to emit a photon. This is termed fluorescence. Fluorescence is a process on the order of nanoseconds; therefore, it is not a very likely path for an electron to dissipate energy especially at electronic energy states higher than the first excited state. Fluorescence is mostly often observed between the first excited electron state and the ground state for any particular molecule because at higher energies it is more likely that energy will be dissipated through internal conversion. Another possible path is through quenching, energy transfer between molecules through overlapping their absorption and fluorescence spectra. It is a non-emitting process that will compete with fluorescence as the molecule relaxes back down to the ground electronic state (see Figure 2). Another competing process to fluorescence emission is intersystem crossing, the transition

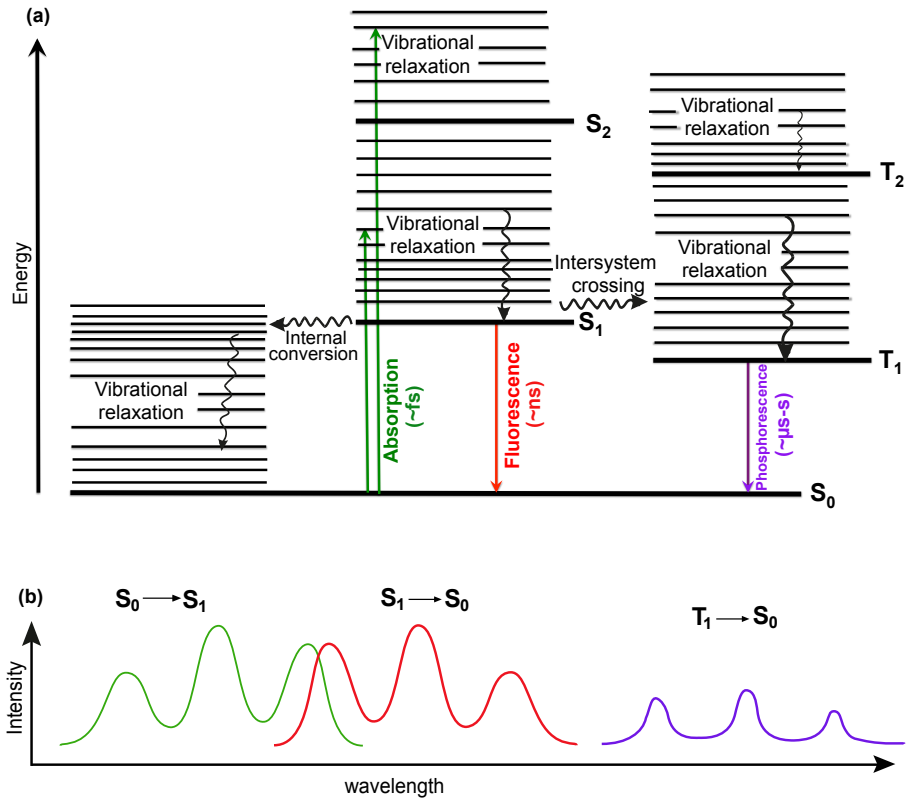

Figure 2: (a): Jablonski diagram describing the electronic levels of common organic molecules and possible transitions between different singlet and triplet states. (b): Relative wavelength positions of absorption, fluorescence, and phosphorescence. The approximate mirror symmetry between absorption and fluorescence including the Stoke shift leading to a shift of the fluorescence emission as well as differences in spectroscopic line widths for fluorescence and phosphorescence are schematically taken into account.

from a singlet to a triplet state of the molecular system. Due to the optical selection rules the transition between triplet and singlet states are forbidden. This restriction is partially lifted by spin-orbit couplings in the molecular system. The forbidden nature of the T_1 to S_0 transition results in reduced transition probabilities and therefore, in relatively long triplet state lifetimes. In comparison to the typical fluorescence lifetimes in the range of nanoseconds, triplet lifetimes vary between microseconds to seconds for different pigments.

Before the absorption (at low temperature), the molecule is in the lowest vibrational state of its lowest electronic state (Figure 3). According to the Born-Oppenheimer approximation, electronic transitions occur much faster than any nuclear rearrangements, because the nuclei

are much more massive than the electrons, so that an electronic transition takes place very much faster than the nuclei can respond. This is referred to the Franck-Condon (FC) principle [66]. According to the FC principle, the most intense vibronic transition is from the ground

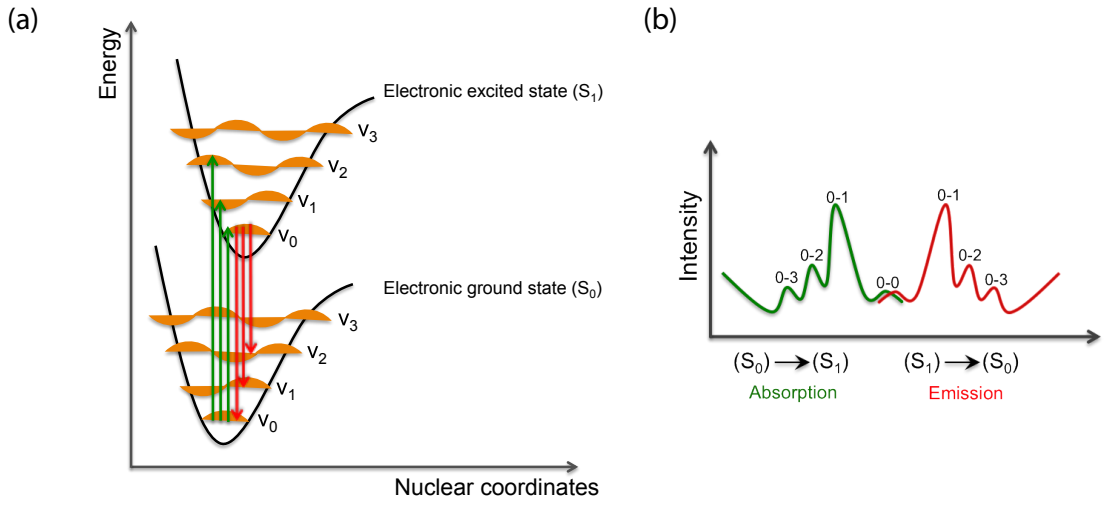

Figure 3: (a): According to the FC principle, the most intense vibronic transition is from the ground vibrational state to the vibrational state lying vertically above it. Transitions to other vibrational levels with lower intensity also will occur. Green arrows show the absorption and red arrows show the fluorescence transitions. In the quantum mechanical version of the FC principle, the molecule undergoes a transition to the upper vibrational state that most closely resembles the vibrational wavefunction of the vibrational ground state of the lower electronic state [66]. (b): The representation of the absorption (green) and fluorescence (red) spectra corresponding to the energy diagram in (a). Since energy spacings between the vibrational levels in S_0 and S_1 are (almost) equal, the fluorescence and absorption have the same shape. Electronic transitions between the lowest vibrational levels of the electronic states (the 0–0 transition) have the same energy in both absorption and fluorescence.

vibrational state to the vibrational state lying vertically above it [66] (Figure 3). Transitions to other vibrational levels also occur, but with lower intensity. The separation of the vibrational lines of an electronic absorption spectrum depends on the vibrational energies of the upper electronic state. The probability for fluorescence towards the different vibrational levels of the S_0 electronic ground state manifold scales with the respective FC factors connected to the (S_1, v_0) to (S_0, v_i) transitions. Prerequisite for an optical transition is the interaction of the pigment with the electromagnetic field. This is possible if the molecule at least temporally has a dipole, which can oscillate with the frequency of the incident light. A measure for the

strength of the coupling of electromagnetic field and electronic transition of a molecule is the transition dipole moment (TDM), which is determined by molecular structure and symmetry. The quantum mechanical expression of the TDM of a molecule is [66]:

$$\overrightarrow{\mu} = \int \psi_i^* \hat{\mu} \psi_f d\tau \tag{1}$$

ψ_i the initial ground state associated wavefunction and ψ_f the final excited state wavefunction of the molecule. The dipole moment operator is a sum over all electrons in the molecule:

$$\hat{\mu} = -e \sum_i \overrightarrow{r_i} \tag{2}$$

Here $\overrightarrow{r_i}$ is the electronic coordinate. The overall state of the molecule consists of an electronic part, $|\varepsilon>$, and a vibrational part, $|\nu>$. Therefore, within the Born–Oppenheimer approximation, the TDM factorizes as follows:

$$\overrightarrow{\mu}_{fi} = < \varepsilon_f \nu_f | - e \sum_i \overrightarrow{r_i} | \varepsilon_i \nu_i > \tag{3}$$

For two different electronic states which are orthogonal $< \varepsilon_f | \varepsilon_i >$ is zero, therefore,

$$\overrightarrow{\mu}_{fi} = -e \sum_i < \varepsilon_f | \overrightarrow{r_i} | \varepsilon_i >< \nu_f | \nu_i >= \mu_{\varepsilon_f, \varepsilon_i} S(\nu_f, \nu_i) \tag{4}$$

where,

$$\overrightarrow{\mu}_{\varepsilon_f, \varepsilon_i} = -e \sum_i < \varepsilon_f | \overrightarrow{r_i} | \varepsilon_i >, \quad S(\nu_f, \nu_i) = < \nu_f | \nu_i > \tag{5}$$

The matrix element $\mu_{\varepsilon_f, \varepsilon_i}$ is the electric-TDM arising from the redistribution of electrons. The factor $S(\nu_f, \nu_i)$, is the overlap integral between the vibrational state $|\nu_i>$ in the initial electronic state of the molecule, and the vibrational state $|\nu_f>$ in the final electronic state of the molecule.

Because the transition intensity is proportional to the square of the TDM magnitude, $|\mu_{fi}|^2$, the intensity of an absorption is proportional to $|S(\nu_f, \nu_i)|^2$, which is known as the FC factor for the transition. It follows that, the greater the overlap of the vibrational state wavefunction

in the upper electronic state with the vibrational wavefunction in the lower electronic state is, the greater the absorption intensity of that particular simultaneous electronic and vibrational transition. This conclusion is the basis of the illustration in Figure 3b, where we see that the vibrational wavefunction of the ground state has the greatest overlap with the vibrational states that have peaks at similar bond lengths in the upper electronic state.

Pigment–Pigment Interactions

All pigments in a protein are part of a well-organized network of energy transfer pathways. This arrangement suggests that excitation energy is distributed extremely fast over the whole complex due to the efficient transfer rates between neighboring pigments. When pigments are excited by photons, they interact with each other via different coupling conditions. These interactions can change the energy transfer pathways in a protein unit.

Weak Coupling

A weak coupling has no influence on the energy level of the molecules, and the quantum states remain localized on the molecules. Under these conditions, two different nonradiative energy transfer paths from an excited donor molecule (D^*) to an acceptor molecule (A) are possible. The coupling is sufficiently weak that the spectra of D and A are not affected [67]. The efficiency of radiationless transfer of electronic excitation energy depends on the distance, the orientation and the energy ratios of D and A from each other. In pigment-protein complexes of photosynthetic organisms occur two energy transfer processes, which mechanisms differ fundamentally: via Förster resonance energy transfer (FRET) [68], which is mediated by dipole–dipole coupling, or Dexter transfer [69], takes place at the exchange of electrons (Figure 4a).

The Förster process involves the simultaneous excitation of A and deexcitation of D due to the mutual perturbation of the electrons in the two molecules, but without electron exchange between the molecules. The efficiency of energy transfer strongly depends on the

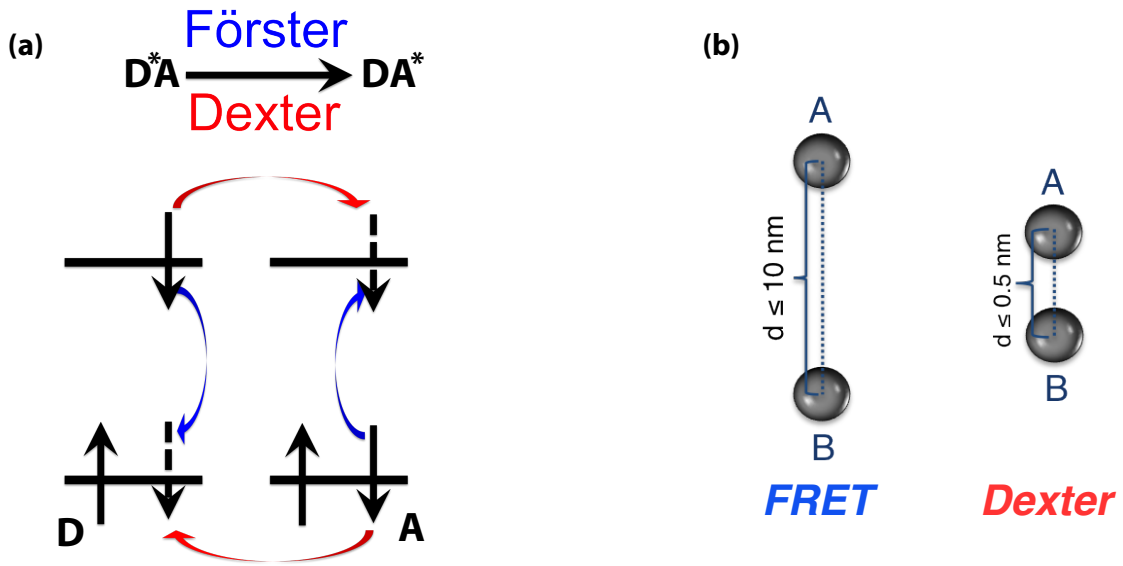

Figure 4: (a): Schematic representation of the Förster transfer (blue) and the exchange (Dexter) transfer (red) in EET. In the Förster energy transfer, the excitation energy is transferred without exchanging electrons between the molecules, while in the Dexter transfer there is a simultaneous exchange of two electrons. (b) Both EET in week couplings are distance dependent; distance limit for Dexter is small as 0.5 nm and for Förster is around 10 nm.

actual center-to-center distance (r) and the Förster radius (R_0) according to the Förster equation, $E = {R_0}^6/({R_0}^6 + r^6)$. The Förster radius ($R_0$) in turn depends on the quantum yield of the donor, the spectral overlap between donor emission and acceptor absorption, the refractive index of the medium and an orientation factor κ [70], which is related to the relative orientation of the donor emission and acceptor absorption dipole moments (see Figure 7a). Due to the distance dependence of FRET, typical critical FRET distances R_0 for spectrally overlapping pigments are around 10 nm [71] (Figure 4b).

The Dexter-transfer involves electron exchange between the pigment molecules. This only occurs when the orbitals of the participating pigments overlap [69], the Coulomb term is small, e.g., if forbidden transitions are involved, and at short distances as small as 0.5 nm [71] (Figure 4b). While Förster type energy transfer can only occur between singlet states of D and A, Dexter transfer can also happen between the triplet states of the molecules such as the transfer of the Chl triplet (Chl^T) state toward a closely located carotenoid molecule [71]:

$$Chl^T + Car \rightarrow Chl + Car^T \tag{6}$$

The Chl^T state in the absence of carotenoid molecules have a long lifetime. In the photosynthesis, the Dexter transfer in eq. (6) is an important process in which the triplet states of Chl molecules transferred through Car in order to prevent the building of extremely reactive singlet oxygen [72].

Strong Coupling

When two pigments are close enough in space, their electron clouds will interact and, as a consequence, the spectral and dynamic properties of this pair of molecules will be changed [67]. In strong coupling conditions the energetic levels split and the delocalized electronic states are formed after light excitation. The excitation energy relaxes between those delocalized states [73]. As an illustration of this coupling, see Figure 5a, the energy levels of the individual pigments E_1 and E_2 split into new states with energies E_+ and E_- (see energy level splitting scheme in Figure 5a), then the pigment–pigment interaction is in strong coupling condition. For a dimer, the relevant Hamiltonian that must be diagonalized is given by:

$$\begin{pmatrix} E_1 & V_{12} \\ V_{12} & E_2 \end{pmatrix} \tag{7}$$

in which E_1 and E_2 represent the excited state energies of the original molecules and V_{12} is coupling, which for dipole-dipole interactions is given by:

$$V_{12} = \frac{\overrightarrow{\mu_1}.\overrightarrow{\mu_2}}{r^3} - 3\frac{(\overrightarrow{\mu_1}.\overrightarrow{r})(\overrightarrow{\mu_2}.\overrightarrow{r})}{r^5}. \tag{8}$$

Where, $\overrightarrow{\mu_1}$ and $\overrightarrow{\mu_2}$ represent the TDMs, $\overrightarrow{r}$ is the vector connecting the centers of the dipoles. Depending on the relative orientations of the TDMs of the pigments, the occupation of the

energy levels E_+ and E_- varies, leading to the energy levels of a coupled pigment dimer to [74]:

$$E_{\pm} = \frac{1}{2}(E_1 + E_2) \pm \frac{1}{2}\sqrt{(E_1 - E_2)^2 + 4V_{12}^2}. \tag{9}$$

In the strong coupling, the excitation is delocalized between D and A and it does not stay instantaneously localized on either molecule [71].

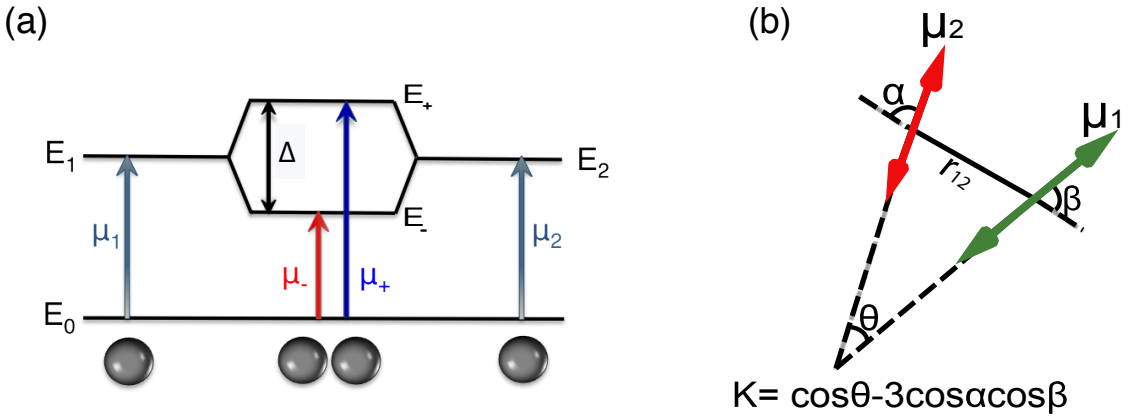

Figure 5: (a): Energy level splitting of pigments in strong coupling conditions. Δ is the energy difference between the excitonic states. The occupancy of the E_+ and E_- states depends on the mutual orientation of the TDMs. (b): Illustration of the orientation between TDMs. The orientation factor κ depends on the angles α, β and θ describing the relative orientations of the interacting dipoles μ_1 and μ_2 with the intermolecular distance r_{12}.

The Excitation-energy Transfer in Photosynthetic Systems

Chls are part of a well-organized network of energy transfer pathways. This arrangement suggests that excitation energy is distributed extremely fast over the whole complex due to the efficient transfer rates between neighboring Chls. This may explain the observed short lifetimes of excitation energy equilibration processes in the bulk antenna. The lowest excited state of the 1st Chl molecule is the Q_y state (Figure 6), V_{12} denotes the coupling between the 1st and 2nd Chls. The electronic coupling, V_{12}, between excited states of two Chls has two contributions,

$$V_{12} = V_{12}^c + V_{12}^{ex} \tag{10}$$

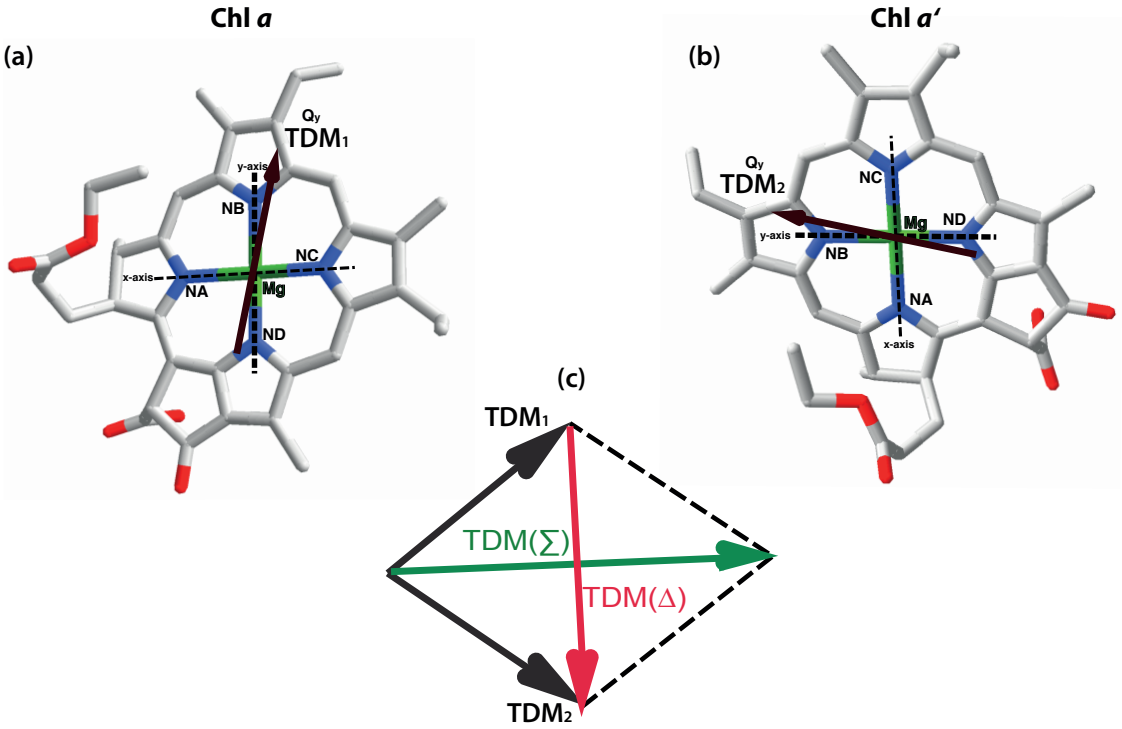

Figure 6: (a): Molecular model of Chl *a* molecule shows the structure of the porphirinic ring (green: Magnesium, blue: Nitrogen and red: Oxygen), the carbon atoms (grey) within it and the direction of the TDM vector (the vector); from 1JB0. PDB; Jordan et al. [33]. (b): Chl *a'* molecule with different direction of TDM. The EET between these two Chls is via strong coupling. (c): The strong coupling vectors; green arrow shows the sum band ($\sum$), and the red one shows the difference band (Δ).

where V_{12}^{c} corresponds to a direct Coulomb term and V_{12}^{ex} corresponds to an electron exchange term. In PSI, almost all of the Chls are at a Mg-Mg distance of greater than 7 Å, a range in which Coulomb interaction dominates [75, 76]; therefore, we use only the contribution of the direct Coulomb term, V_{12}^{c}. The electronic couplings due to the direct Coulomb interaction are calculated base on the dipole–dipole interaction between transition dipole moments of the Chl Q_y states. In this approximation, the couplings are given by eq. (8) where $\overrightarrow{\mu_1}$ and $\overrightarrow{\mu_2}$ represent the TDMs of the Chls and r is the vector connecting the Mg atoms of the 1st Chl (e.g. Chl *a* in Figure 6a) and the 2nd Chl (e.g. Chl *a'* in Figure 6b) in Q_y state; the TDMs for the Q_y state are taken to be along the vector connecting the N_B and N_D atoms (Figure 6a,b) [30, 77]. For excitonically coupled dimers, the new TDMs are given by the vector sum ($\sum$) and difference (Δ) of TDMs of the uncoupled Chls and are oriented perpendicular to

each other, accordingly [30, 77] (Figure 6c). The distribution of the oscillator strength over these two exciton bands depends on the angle between the TDMs of the Chls, whereas the sign of the interaction energy (i.e., whether the excitonic band related to the vector sum is higher or lower in energy) depends also on the angles between the TDMs of the Chls and the vector connecting them. The Chl pairs, which have the strongest couplings, as well as the higher oscillator strength in the lower lying state, are suggested as red Chl candidates [75].

Several red Chls in e.g. PSI from *T. elongatus*. are denoted according to their absorption peak and those are coupled via strong coupling are contributed to the red pools (Figures 7a and 1a,b). Following this, matching the red shift with the strongest coupling, it has been suggested that that coupled Chls denoted e.g. B31B32 is responsible for the C719, A24-A35 for the C715, and B18-B19 for the C708 [19, 33, 75, 78, 79]. This insight allows us to discuss the possible energy transfer pathways between these red pools, e.g. C708 and C719 in PSI from complex from *T. elongatus*. However, there are some conditions that allow these red coupled Chls in the red pools participate in the EET pathways in PSI; (a) strong coupling between the Chls of the aggregate, and (b) orientation of the transition dipole of the low-energy exciton state parallel to the membrane plane [79]. If all of these conditions fulfilled, they are part of EET pathways in PSI [77, 79].

The EET between these red pools depends on several factors; when the intermolecular distance is large compared to molecular sizes, we can further invoke the dipole-dipole approximation for intermolecular interactions. Förster-type excitation energy transfer between two pools depends on their spectral overlap, their inter-pigment distance and their relative orientation. The orientational factor κ [70], $\kappa = \hat{u} \cdot \hat{v} - 3\,(\hat{u} \cdot \hat{R})\,(\hat{v} \cdot \hat{R})$ $\hat{u}$ and $\hat{v}$ are unit vectors of TDMs of the red pools (calculated by sum or difference relation between TDM of each Chl), and $\hat{R}$ is the unit vector connecting the centers of TDMs of the red pools. If the orientation is fixed, κ can be 0 and 1 for perpendicular and parallel orientations, respectively. Therefore, changes in relative orientation can have significant effects on the energy transfer efficiency. According to this, if the TDMs of two dipoles are oriented almost perpendicular to each other, their κ tend toward zero ($V_{12} \simeq 0$), if their connection vector also has a perpendicular orientation to the center of TDMs (Figure 7b). For such a weak coupling, they are not connected each other via EET pathways and each pool can be considered as a separate emitter with different

spectral emitting wavelength. For parallel orientation, the coupling potential is maximized and there is a linear downhill EET from antenna states according to the energy states of red pools (Figure 7c).

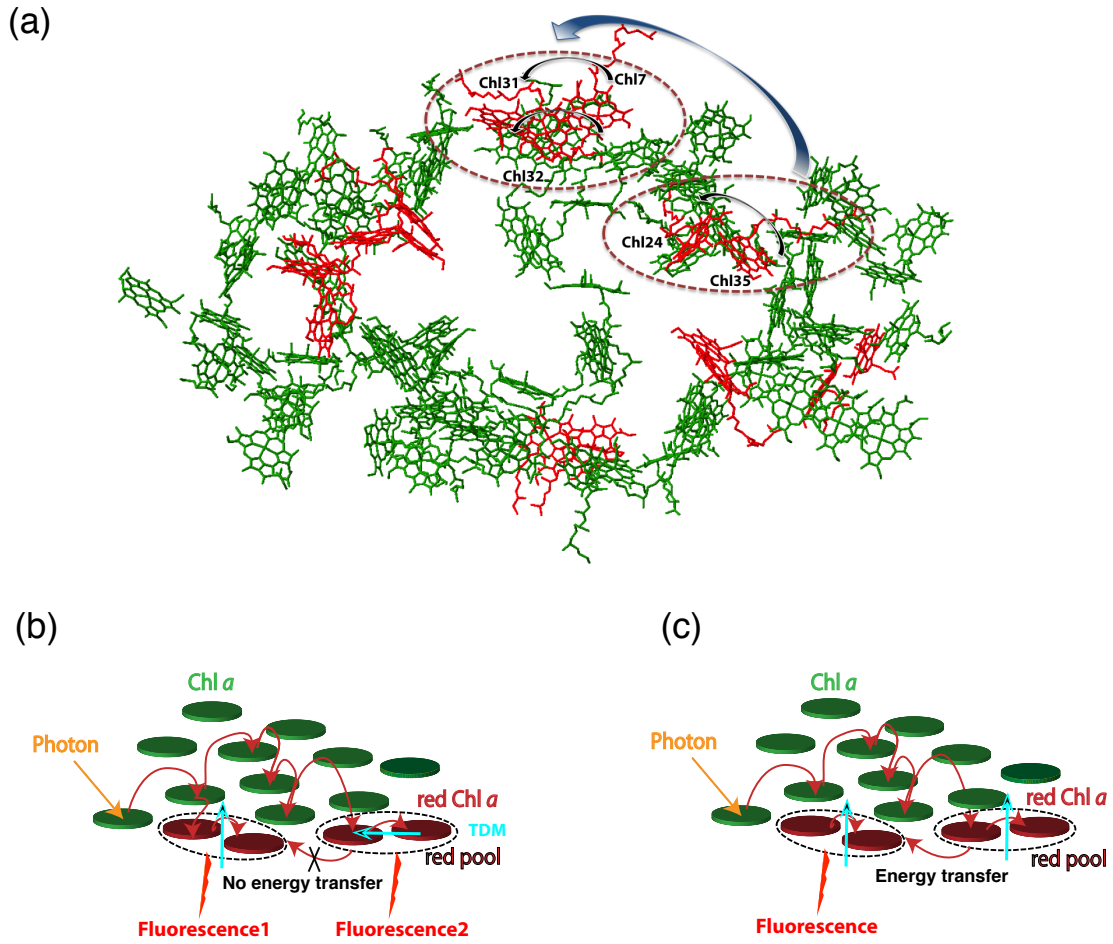

Figure 7: (a): Arrangement of the Chls in PSI-M from *T. elongatus*. The figure is produced from Protein Data Bank file 1JB0 [33]. Red colors are red Chls. Black arrows show the EET between red Chls. Dotted lines shows the red pools and blue arrow shows the EET between the red pools. The direction of arrows are arbitrary. (b): Schematic arrangement of the Chl *a* molecules in a photosystem. Green colors are Chl *a* molecules, red colors are red Chls. The red arrows show the EET between red Chls and the red pools (dotted circles). When the TDMs of two red pools are perpendicular, there is no EET between the red pools and they are feeding directly from higher lying Chls, therefore, each of them, emits separately. (c): When the TDMs of two red pools are parallel, there is a downhill EET between the red pools and therefore, one emitting state is expected.

Single-molecule Spectroscopy at Low Temperature

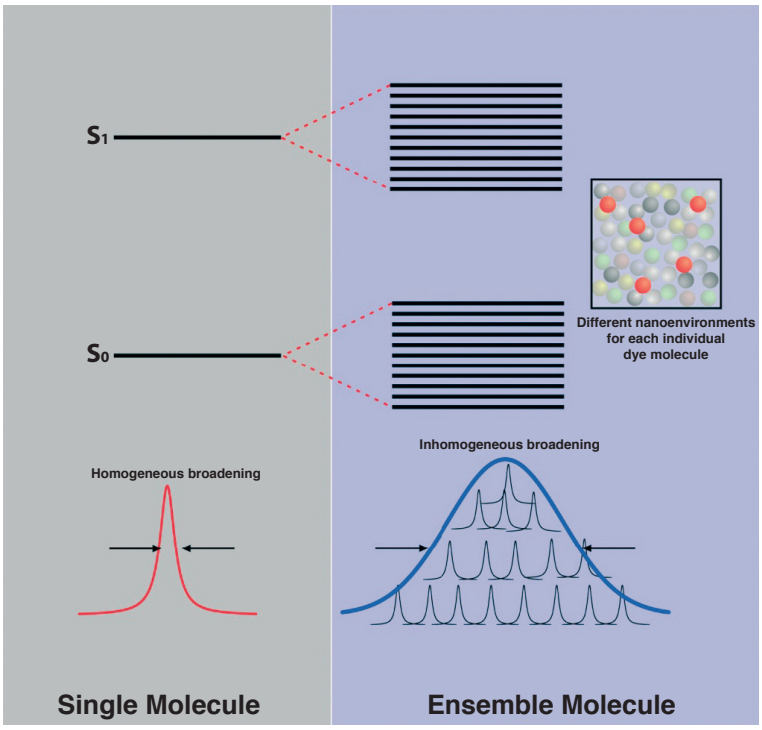

Figure 8: Comparing between single-molecule and ensemble spectra distribution together with homogeneous and inhomogeneous broadening at low temperatures are shown [80].

The transition energy of an emitter basically represents its electronic properties . However, the local chemical environment holds the ability to tune the transition energy remarkably. Accordingly, each emitter in this host matrix experiences slight differences in its local chemical environment, leading to slight shifts in the frequency of the transition for both, the excitation ($S_0 \rightarrow S_1$) and the emission ($S_1 \rightarrow S_0$) [80], see Figure 2b. For ensemble emitters, all molecules in the focal volume contribute to the measured signal, which results in an averaged spectrum that is broadened, see Figure 8. While the inhomogeneous broadening might bring us general information about the matrix system, but more we can achieve by investigating single-molecules. At very low temperatures, detail information becomes visible in the excitation and emission spectrum of an individual molecule [81, 82]. This, in turn, can be used to selectively address individual emitters among many others, as it is shown in Figure 8.

We can monitor the emission of an individual emitter at low temperatures by exactly tuning the excitation wavelength of a small bandwidth laser source or diluted sample solutions.

Thus, for a given excitation wavelength, the number of molecules in the detection volume, which are in resonance with the excitation, can be reduced to an extent, where exactly one molecule is excited.

SMS is an excellent technique to cope with inhomogeneous spectral widths and it reveals subtle spectral details often obscured by averaging over heterogeneous ensembles [9, 48]. The fluorescence spectra at room temperature are very broad and unstructured because spectral diffusion and photobleaching hamper the collection of detailed spectroscopic information of the most single molecules [49, 50, 51, 52]. Mainly, these mechanisms can be suppressed by lowering the temperature. At low-temperature, the homogeneous line width (Γ) of the sharp line is determined by the total dephasing time T_2 of the optical transition [83, 84]

$$\frac{1}{T_2} = \frac{1}{2T_1} + \frac{1}{T_2^*} \tag{11}$$

where T_1 is the decay time of the excited state and T_2^* is the pure dephasing time determined by fast residual thermal motion. The temperature dependence of Γ arises from T_2^* [83]. The T_2^* is due to the modulation of the single site transition frequency, which results from the interaction of the excited state with the phonon's baths [84]. The resulting homogeneous broadened spectral linewidth is as small as 10–100 MHz for typical fluorescent molecules with nanosecond excited-state lifetimes [80].

Photo-bleaching and Photo-blinking of a Single-molecule

The most fascinating and intensively studied features of single-molecules are fluorescence intermittency or blinking, i.e., the reversible transitions of a molecule from a bright state to a dark state, and fluorescence bleaching, i.e., the irreversible conversion into non-fluorescent products [85]. They depend on several factors such as: the experimental conditions, host matrix whether is solid or a fluid environment, temperature, excitation wavelength and intensity, etc. One of the major factors in blinking and bleaching is the presence and the diffusion of molecular oxygen in the neighborhood of the molecule [85]. The average duration

of the dark periods during blinking is determined by the triplet lifetime.

Photo-blinking and photo-bleaching mechanisms are complex and usually involve several pathways. They occur when the molecule is pumped into its long-lived triplet state. Even in the absence of oxygen, the triplet state may relax towards other dark states [85]. The triplet state is a long waiting time during which no fluorescence can be emitted, before the molecule relaxes back to the singlet ground state (Figure 9). The severe requirements on the photophysical (intersystem crossing) parameters of the triplet state strongly reduce the number of compounds accessible to SMS.

Triplet formation will also occur under native working conditions on Chls in the antenna

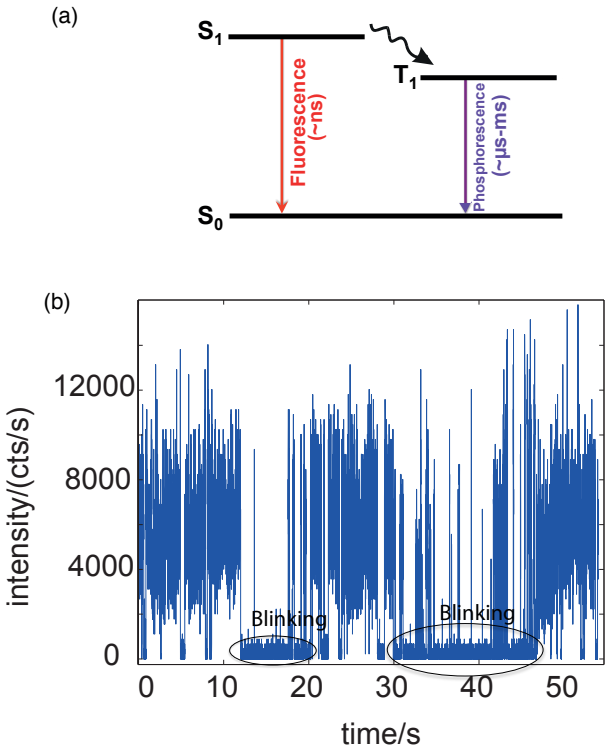

Figure 9: (a): Typical diagram of the electronic energy levels of a molecule with singlet and triplet systems. (b): The time trace of fluorescence intensity. The typical single-molecule blinking behavior from single PSI [86].

system. Avoiding the formation of harmful singlet oxygen, nature employs carotenoids to quench ^{3}Chl by triplet-triplet energy transfer. This transfer requires a wavefunction overlap between Chl and carotenoid and thus a close vicinity of the two pigments. At low temperatures, a significant part of the excitation is trapped on energetically low-lying antenna

Chls, because uphill energy transfer to the RC is impossible. Due to the longer lifetime of the excited Chl, the yield of fluorescence and triplet formation increases. Car triplets are formed subsequently by triplet-triplet transfer. The lifetime of Chl triplets decaying by triplet energy transfer to Car is most likely in the sub-microsecond domain [87].

Line Shape of a Single-emitter

The emission profile of a single emitter at low temperature limit is schematically given in Figure 10a. The profile consists of a sharp zero-phonon line (ZPL) with the line width γ accompanied by a phonon wing (PW) on its low energy side. The PW is due to the interaction with phonons. The frequency dependent line shape, L(ω), for the low temperature condition is [88]:

$$L(\omega) = \underbrace{e^{-S} l_0(\omega - \Omega)}_{\text{ZPL}} + \underbrace{\sum_{R=1}^{\infty} S^R \frac{e^{-S}}{R!} l_R(\omega - \Omega + R\omega_m)}_{\text{PW}} \tag{12}$$

with Ω the energy of the zero-phonon transition (0–0 transition), ω_m the phonon energy, S the Huang-Rhys factor, l_0 a Lorentzian line shape and l_R a line profile with asymmetric Lorentzian and Gaussian line shape contribution. The relative intensity of the ZPL and the whole intensity, $\alpha = I_{ZPL}/(I_{ZPL} + I_{PW})$, gives the strength of the electron-phonon coupling. The coupling of the pure electronic transition to the phonons/lattice vibration is due to the different shape of the charge distribution in ground and excited states of the chromophore. By absorption of a photon the charge distribution changes accordingly. Thereby the created electric field is changed. Molecules in the close surrounding of the chromophore are influenced by this change of the electric field. Those molecules which react, e.g. by reorientation, on the change of the field reduce the side energy as well as transition energy of the chromophore.
At low temperatures the ZPL begins to dominate the spectra, because its line width γ becomes much smaller than the width of the PW as shown by simulation for the temperature range from 0 – 250 K [56] in Figure 10b. The context between properties of the ground/excited state of a chromophore and the electron-phonon coupling can be rationalized as follows: The

changes in geometry along specific normal coordinates accompanying electronic excitation from the ground state G to the excited state X is named Δ. If the ground and excited-state surfaces are considered harmonic, the intensity of each vibronic band in a chromophore can be expressed as the appropriate product of the individual FC factors for all of the modes in the chromohore. The 0-0-FC factor (Figure 3b) for each mode i is given by $\exp(-S_i)$, where $S_i = 1/2\Delta_i^2$ is the Huang-Rhys factor and Δ is defined above. The intensity of the pure 0-0-transitions, in which no vibrational or phonon excitation in any mode accompanying electronic excitation occurs, is thus $\exp(-S_{total})$ where $S_{total} = \sum_i S_i$. At zero temperature α is given by $\alpha = \exp(-S_{total})$. Thereby the value of the electron-phonon coupling becomes directly accessible at low temperatures.

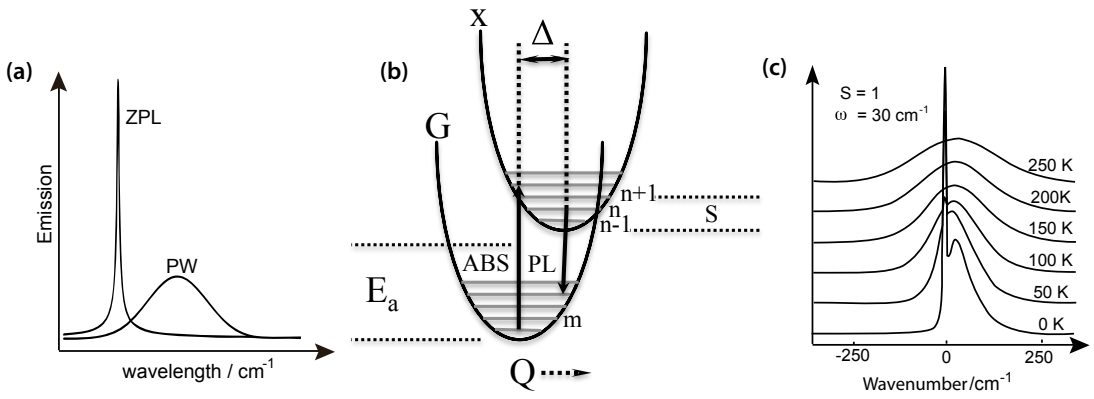

Figure 10: (a): Schematic representation of the line shape of a single emitter at low temperature consisting of a ZPL and a PW. (b): representation of the ground (G) and excited (X) state of a chromophore by parabolas. (c): Temperature dependence of electron-vibrational band according to Ref. [56]. Parameters used for calculations: S = 1, energetic shift of the PW relative to the position of the ZPL is $\omega = 30$ cm^{-1}. ZPL of the 0 K spectrum is cut off at a certain value.

Conformational Dynamics

A detailed information of the molecular mechanism that leads through the energy landscape, introduced by Frauenfelder et. al. [89], is a prerequisite for understanding of protein function. Further on, modifications of the protein environment induce additional changes, e.g. changes

of electronic energy levels of a protein-embedded pigment, referred to as spectral diffusion [90, 91]. These variations might be of considerable impact, if they are able to induce different routes in the energy landscape. In that case, they can delicately influence the function of the protein. This may lead to a disfunction of the protein itself. If proteins are embedded in large interacting networks the disfunction can result in disruption of a whole functional sequence [92].

Site-selective techniques like SHB [84] and their descendants the single-molecules techniques [9] delivered the possibility to look at small sub-ensembles or even single molecules. It became possible to observe the conformational motion of proteins directly by monitoring the spectral response of protein embedded chromophores [93]. Utilizing these techniques at room temperature yields in most cases broad spectra showing similarities to spectra taken at ensembles rather than the characteristics of single emitters [94]. This is due to the fast fluctuations of the protein at ambient temperatures and thereby, a slaved fluctuation of the site energy of the embedded chromophores. Time dependent site energy changes of chromophores are often called spectral diffusion.

At room temperature, proteins vary between conformational sub-states on a picosecond timescale. This dynamics can be slowed down remarkably by lowering the temperature. At cryogenic temperatures the residual motion relies basically on tunneling processes between minima in the ground state of the energy landscape [95]. Due to the small mass residual, tunneling dynamics are dominated by dislocation of protons.

For chromophores with different conformational sub-states line jumps can be induced by illumination. This process is schematically shown in Fig. 11. The process relies basically on additional possibilities to cross barriers in the excited state. Therefore, molecules have to be excited from ground state to excited state. This approach is often explained in a simple "two level"-system (TLS) consisting of two conformational sub-states [84]. The superscripts α and β label the TLS for the ground and excited electronic states of the chromophore. In the presented figure, excitation occurs on the left side. The relaxation through the barrier into the right potential takes place in the excited electronic state (β). The transition frequency of the chromophore in the configuration after barrier crossing is higher than for the initial configuration. The distribution of the energies would lead to a blue-shifted emission. If

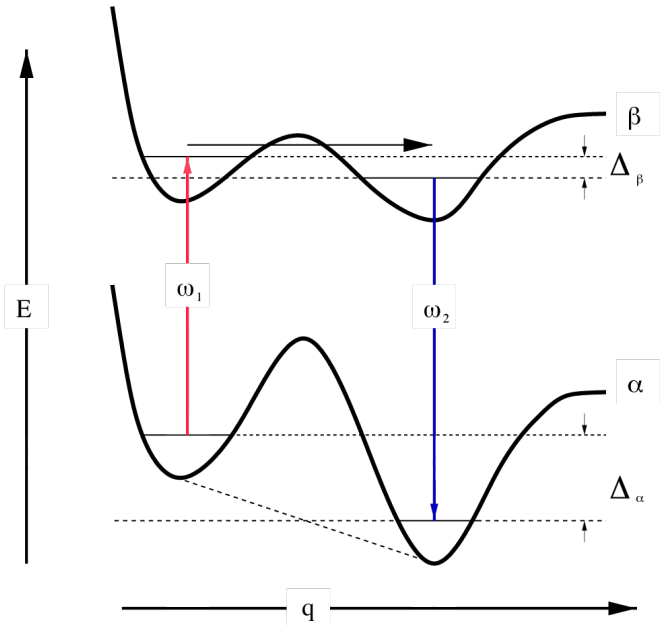

Figure 11: Illustration of a two-level system (TLS) [84]. Potential energy diagrams for a TLS in its ground state (α) and excited electronic state (β). Δ is the asymmetry parameter; and q, the intermolecular coordinate. ω_1 is the laser frequency, and ω_2 is the emission wavelength.

instead, excitation energy corresponds to the blue-shifted state (ω_2), and barrier crossing is in opposite direction and red-shifted emission (ω_1) would occur, accordingly. In cases where the chromophore can be excited with both frequencies ω_1 and ω_2 successively, a perpetual cycling of the chromophore between these two states can be induced. Expanding the simple TLS model to schemes with larger number of conformational states. For simplification of the picture, it is shown that the conformational dynamics occur only in the ground state (as denoted α in Figure 11). In this case the observed emission depends strongly on the probability of barrier crossing as well as on the time needed for acquisition.

High energetic barriers between the different conformational substates characterize the highest tier in the energy landscape. Under the given low-temperature conditions, the barriers cannot be crossed and the system rests in one given conformational substate in the first tier. Two different situations are illustrated in Figure 12. The energetic barriers between the different substates within the second tier are lower, as a consequence, these barriers can be crossed under the experimental conditions. The crossing of these barriers induces the observed line broadenings and spectral jumps. The jumps are induced by small conformational changes

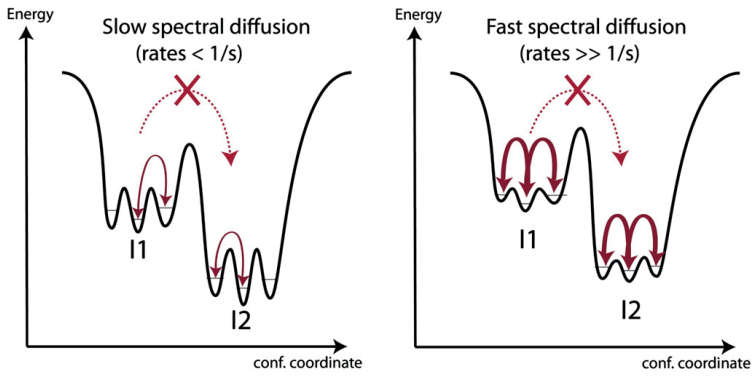

Figure 12: Schematic illustration of the protein energy landscape. $I1$ and $I2$ represent different intermediate states in the first tier. The energetic barrier between $I1$ and $I2$ cannot be crossed on the given low temperature conditions, but the barriers within $I1$ and $I2$ can be crossed (red arrows), yielding the observed jumps of the ZPLs in the emission spectra. The barrier heights within $I1$ and $I2$ determine the rates of the conformational changes. (a): The barriers within $I1/I2$ are high. Jumps occur with low rates. If the rates are in the range of the acquisition time, stable ZPLs and discrete jumps can be observed in the resulting emission spectra (slow spectral diffusion). (b): Reduced barrier height yields increased rates, if the barriers are crossed with rates much higher than the acquisition time only broadened lines can be observed (fast spectral diffusion). This figure is from ref. [42]

.

that are possible in the second tier. Nevertheless, these changes are able to induce jumps covering a major fraction of the whole inhomogeneous line width [96]. The observation of stable ZPLs or broadened lines depends on the rates of these jumps [97].

Observing spectral diffusion on single proteins gives insights into pathways taken by proteins in their highly individual energy landscape. The energy landscape is shaped dominantly by the close environment of the chromophore [91]. Changes therein have larger effects on the actual shape. Such changes can be monitored by SMS at cryogenic temperatures [98].

Photosynthesis

Photosynthesis is a crucial biochemical process which utilizes energy of sunlight and converts it into series of chemical reactions. It can be defined as a photochemical process by which photosynthetic organisms (plant, algae, and some types of bacteria) use light energy to drive

organic compounds synthesis. The photosynthesis that uses water as a substrate and produces oxygen is called oxygenic photosynthesis. The overall chemical reaction can be summarized in the following equation:

$$6CO_2 + 12H_2O \longrightarrow C_6H_{12}O_6 + 6H_2O + 6O_2 \tag{13}$$

Nonoxygenic photosynthetic organisms can use another donor of protons instead of water,

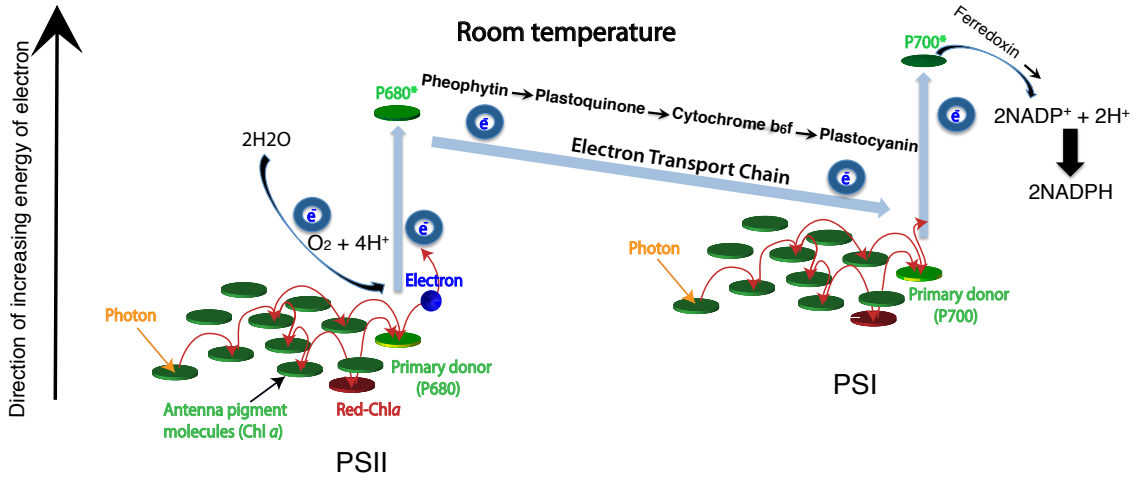

Figure 13: Z-scheme of oxygenic photosynthesis and excitation-energy transfer pathways at room temperatures. The photosynthesic process in chloroplasts begins when an electron of primary donor (P680) of PSII attains an higher-energy level. This energy is used to reduce a chain of electron acceptors, which have subsequently lower redox-potentials. The final product of PSII is plastoquinol, a mobile electron carrier in the membrane, and the ultimate electron donor of PSII is water. Plastoquinol transfers the electron from PSII to the proton pump, cytochrome b_6f. Cytochrome b_6f proceeds the electron chain to PSI through plastocyanin molecules. When this chain reaches PSI, an electron is again excited, creating a high redox-potential. PSI is able to continue the electron transfer in two different ways. It can transfer the electrons either to plastoquinonol again, creating a cyclic electron flow, or to an enzyme called FNR creating an non-cyclic electron flow. PSI releases FNR into the stroma, where it reduces $NADP^+$ to NADPH.

e.g. H_2S, succinate, or malate.

Oxygenic photosynthesis shows two different types of reactions, depending on light conditions. They are called correspondingly, dark- and light-reactions. The dark reactions of photosynthesis are enzymatic reactions that do not require light. Carbon dioxide is fixed and reduced during this phase. In the light reaction, water is split into electrons, protons and

oxygen. During the reaction an electric field gradient over the photosynthetic membrane is built up. This gradient is used for synthesis of ATP and reduction of $NADP^+$. ATP and NADPH are the prerequisite of reduction of CO_2 in the subsequent process called Calvin-cycle. Assimilation of CO_2 can proceed in presence of NADH and ATP. For the initial steps four trans-membrane protein complexes are needed within the thylakoid-membrane. PSI and PSII, the cytochrome b_6f and the ATP-synthase. To focus directly on the energetic shuttling of electrons through this chain of proteins usually the so called Z-scheme is depicted. The naming is due to the redox diagram from P680 to P700 resembling the letter Z. This representation is given in Figure 13. In the following the structural composition and the optical properties of Chl *a*, PSI and PSII complexes are described in more detail.

Chlorophyll *a*

Chl *a* serves a dual role in oxygenic photosynthesis: in light harvesting as well as in converting energy of absorbed photons to release chemical energy. The molecular structure of Chl *a* is shown in Figure 14a. The molecular structure of Chl *a* consists of a chlorin ring, whose four nitrogen atoms surround a central magnesium atom, and has several other attached side chains and a hydrocarbon tail. Chl *a* absorbs light within the violet, blue and red wavelengths, while mainly reflects green. Since the Chl *a* molecules only capture certain wavelengths, organisms may use accessory pigments to capture a wider range of light energy. They then transfer captured light through Chls until reaching the special Chl *a* molecules called P680 in PSII and P700 in PSI, in the RC (see Figure 13).

The spectrum of Chl *a* molecules exhibits essentially two characteristic absorption bands: one of them called the Soret band, which can be found in the blue wavelength region of visible spectrum and is a complex band composed of a large series of electronic transitions. The other band called Q, is in the visible region of the spectrum and is the most important for the photophysics involved in the photosynthetic process. This band can usually be decomposed in two distinct bands called Q_x and Q_y according to their predominant polarization [99]. Figure 14 shows the room temperature absorption spectra of Chl *a* molecules in 80% acetone (black)

and trimeric PS I complexes from *Thermosynechococcus elongatus* (*T. elongatus*) (green). The absorption maximum of the Q_y band is shifted from 664 nm for Chl *a* to 680 nm in PSI, whereas the width is enlarged by a factor of 1.5 [17]. The red shift is caused by the interaction of Chls with the protein scaffold and varies at different species. At physiological temperatures the presence of the red Chls does not significantly decrease the quantum efficiency of charge separation. Even if these Chls are excited directly, thermal energy of the surrounding enables efficient uphill transfer to P700. At lower temperatures, however, the red Chls act as traps for excitations. Therefore, the quantum efficiency of the charge separation decreases and the fluorescence increases. Figure 15 shows the schematic energy transfer between the antennas in the photosystem at low temperature.

Photosystem I

PSI is one of two trans-membrane pigment-protein complexes essential for oxygenic photosynthesis. It is located in the thylakoid membranes of cyanobacteria, algae and plants and

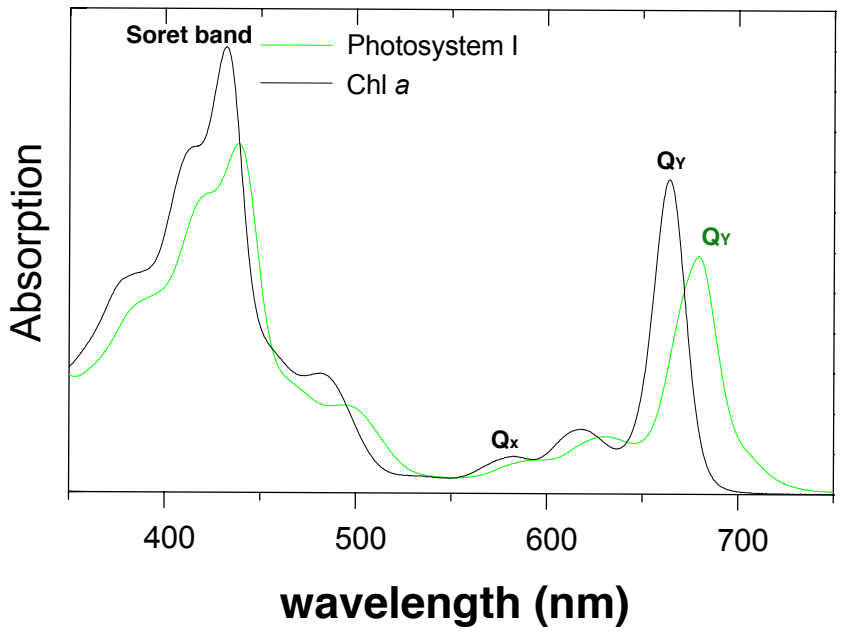

Figure 14: Absorption spectra of the Chl *a* (black) and PSI (green) are shown.

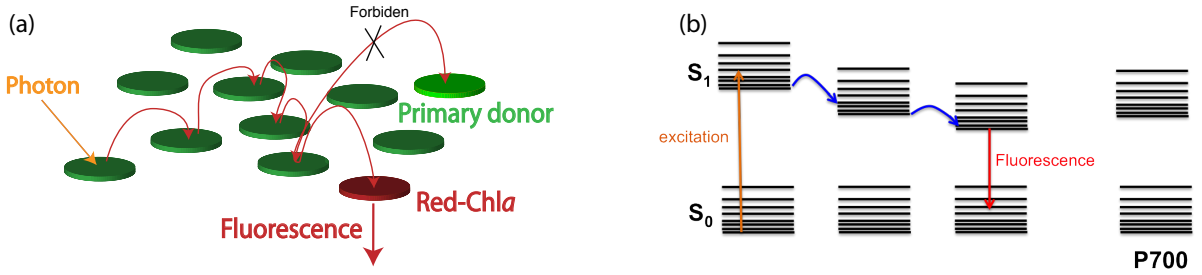

Figure 15: (a): The EET towards the primary donor in the photosystem at low temperatures is partially blocked and the excited energy trapped in the red Chls becomes strongly fluorescent. (b): At low temperature, the transfer towards P700 in PSI from higher laying Chls is partially blocked and the energy is trapped by LWCs and is emitted fluorescence.

mediates light-induced electron transfer from plastocyanin or cytochrome C_6 on the lumenal side to Ferredoxin on the stromal side [13]. The first step of the photosynthetic reaction is the absorption of a photon by the antenna system of PSI followed by subsequent energy transfer to the RC. The captured excitation energy is used to induce a trans-membrane charge separation starting at the Chl pair P700, with the main absorption at 700 nm [13, 16]. The PSI complex from cyanobacteria differs from higher plants and algae in organization and content of polypeptides. The PSI from cyanobacteria can be isolated in a monomeric and a trimeric form [24, 25]. The well-resolved structural model for the cyanobacterium *T. elongatus* from X-ray crystallography [33, 100, 101] exhibits the structure of 12 protein subunits and 127 cofactors performing light harvesting and electron transfer. These cofactors include 96 Chls, 22 carotenoids (Car), two phylloquinones, three ironsulfur (4Fe-4S) clusters, and four lipids for each PSI monomer [33, 100, 102]. The trimer is proposed to be the native form, at least under certain physiological conditions [26]. Both, the trimeric and monomeric species, absorb light at room temperature and show a probability of >95 % of inducing charge separation [27]. This indicates that energy exchange between monomers is negligible and a single monomer can be used to describe the optical properties of PSI [28]. Each monomer in PSI-T contains the same subunit as individual PSI-M except 3 red Chls noted A31-A32-B7 from C719 contribution. These excitonically coupled Chls are located on the luminal side close to the trimerization domain, that are lost during monomerization process in PSI [33]. The Chl arrangements are shown in Figure 16 for monomers and trimers.

Absorption and Fluorescence of Photosystem I

The absorption spectra of PSI from green plants, algae and cyanobacteria show the existence of Chl *a* molecules absorbing at lower energy with respect to the usual Q_y absorption at 664 nm for Chl *a* in 80% Acetone [17, 18], and in particular at wavelengths larger than the primary donor P700 [22, 103]. These red-shifted Chl *a* molecules are often called the long-wavelength (also red or low-energy) Chls (LWC) [20]. Among possible causes for this red shift in the absorption peak of these chls are the effect of the local protein environment on the site energies and the effect of excitonic splitting due to a strong coupling between pairs of Chls [75]. If the excitation energy is localized at these LWCs, a direct excitation of P700 to $P700^+$ is not possible any more and the energy is trapped (Figures 13 and 15). Additional activation energy, e.g., thermal energy provided by the phonon bath, is necessary to oxidize P700 and starts the charge separation process [75, 104, 105, 106] (For a detailed discussion of the properties of the red-Chl *a*, it is referred to Ref.[107]).

A detailed analysis of the absorption spectra of *T. elongatus* allows one to distinguish the red emitting Chl *a* into two pools [29, 30, 31, 32]. Their main absorption bands are at 708 and 719 nm denoted commonly as C708 and C719, respectively. The distinction of these two pools remains tentative due to a large spectral overlap of the respective bands [29]. Additionally, a red subpool (C715) was found by analysis of nonphotochemical hole burning (NPHB) spectra [108].

Estimations for the number of Chl *a* molecules involved in the red pool in *T. elongatus* are based on the integrated absorbance at wavelengths longer than 700 nm. Zazubovich et al. determined seven Chl *a*'s belonging to the red pool (under the assumption that 96 Chl *a* 'molecules are in one PSI monomer) [108], while Palsson et al. estimated between nine to eleven Chl *a* molecules (assuming 110 Chl *a* molecules) [29, 109]. Normalized to the same number of Chl *a*, both estimations are in reasonable agreement [110]. Numerous studies, revealed that these Chls have a crucial impact on the kinetics of energy transfer and trapping [20, 22, 30].

At room temperatures, the quantum efficiency of photochemistry is virtually not affected by the LWCs. However, recent studies using far-red excitation provided a deeper insight into the

efficiency of the charge separation by LWCs in PSI [107]. Thermal energy of the surrounding enables efficient uphill energy transfer via bulk Chls to P700. At cryogenic temperatures, however, the fluorescence of the LWCs increases considerably, suggesting that a significant part of excitation energy is no longer able to reach P700 [22] and red Chls act as traps for the excitation energy, therefore, the quantum efficiency of the charge separation decreases while the fluorescence intensity increases [22, 23], see Figure 13b.

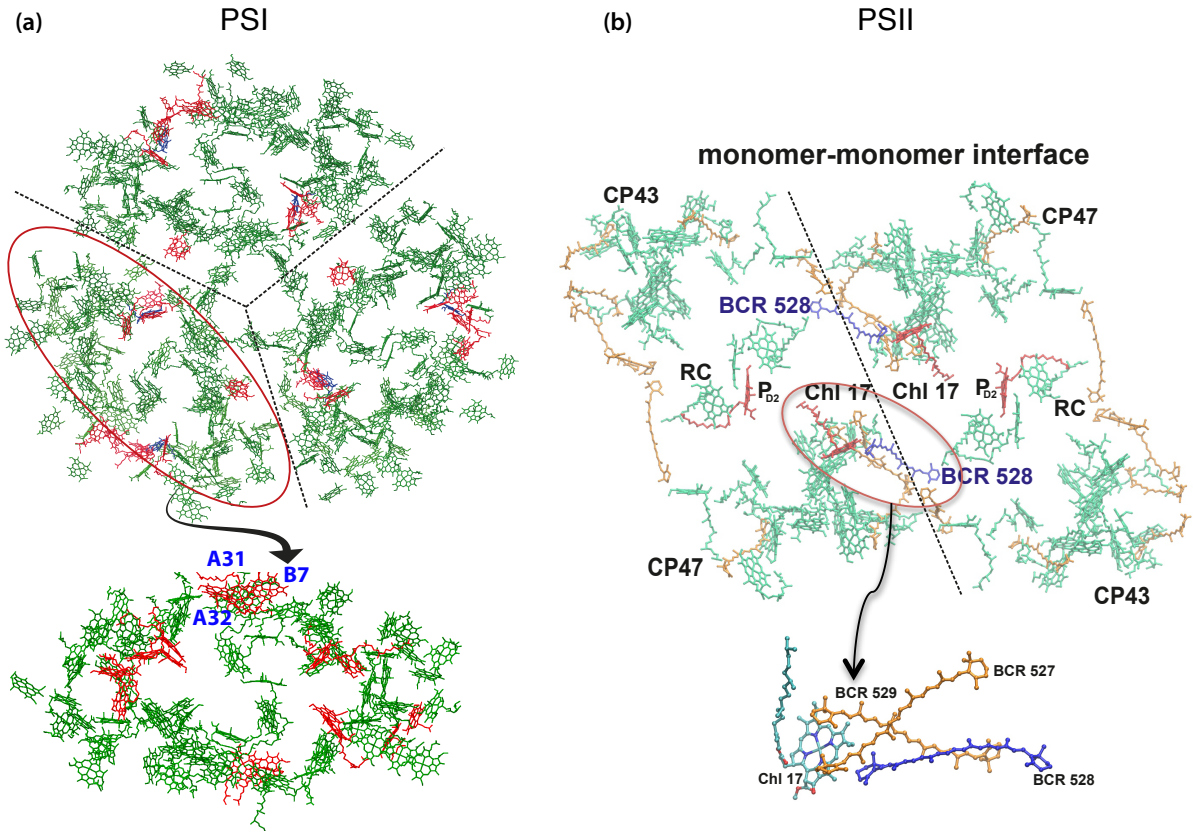

Figure 16: (a): Arrangement of Chls (green) and red Chls (red) within one timer and monomer of PSI. A31A32B7 are the red Chls which are absent in PSI-M and present in PSI-T. (b): Arrangement of Chls (green) and β-Car (BCR, orange) pigments in dPSIIcc (from PDB 3BZ1 and 3BZ2); the monomer-monomer interface (dashed line), Chl17 of CP47 and Chl PD2 of the RC (red). A closer look at the interaction of Chl 17 in CP47 with the β-Car BCR 528 (blue) as well as BCR 527 and 529 (orange) are located at the monomer-monomer interface. BCR 528 (blue) is missing in mPSIIcc.

Photosystem II

In oxygenic photosynthesis of cyanobacteria, green algae and higher plants, the harvested energy is used to oxidize water and reduce plastoquinone in a membrane-embedded PPC called PSII [11, 12]. The functional unit of PSII is a core complex (PSIIcc) that exists as monomeric (mPSII) and dimeric (dPSII) forms in cyanobacteria [111, 112] or is part of a supercomplex with peripheral antennas in higher plants [113, 114]. PSIIcc contains, besides the RC, two core antenna subunits referred to as CP43 and CP47 which are responsible for ultimately transferring the excitation energy to the RC, where the charge separation is initiated [43, 115, 116, 117]. Figure 16 shows the X-ray structures of mPSII and dPSII from *T. elongatus*.

There is no major structural difference of PSIIcc in monomeric and dimeric forms, and both are fully active in water oxidation [37, 38]. As regards the pigment composition, mPSIIcc has the same Chl inventory as dPSIIcc, but 1.3±0.2 β-Car are missing per monomer in mPSIIcc samples based on a spectroscopic analysis of pigment extracts in 80 % (v/v) aqueous acetone [37]. This result is confirmed by X-ray crystallography. The arrangement of Chls and β-Cars in dPSIIcc according to PDB 3BZ1/2 is shown in Figure 16b. Based on this, the arrangement of these pigments is the same in mPSIIcc, but one particular β-Car is missing, i.e., BCR 528 highlighted in blue in Figure 16b. This β-Car is found in a bridging position across the monomer-monomer interface. Therefore, it may detach due to its exposed location in the monomer. However, there are five β-Cars at the monomer-monomer interface in dPSIIcc, so that four further β-Cars are to a certain extent surface-exposed (i.e., exposed to the detergent phase) in mPSIIcc. In the X-ray analysis of mPSIIcc at 3.6 Å resolution [37], the electron density for most Cars is not continuous, and their localization is mainly based on the electron density of the ionone rings and by analogy to the β-Car positions in the dPSIIcc-structure at 2.9 Å resolution. Thus, it cannot be excluded that there is an inhomogeneity in the crystal as regards the occupancy of the β-Car binding sites. This together with the exposed positions of the carotenoids at the monomer-monomer interface implies that actually more than one β-Car could be missing in a single mPSIIcc.

Absorption and Fluorescence of Photosystem II

The absorption as well as the fluorescence show a complex temperature dependence in PSIIcc [40, 41, 44, 118]. Important information is obtained from the spectral properties of the fluorescence emitters of the antenna system [40, 119, 120]. The fluorescence spectrum of dPSIIcc exhibits a complicated temperature dependence both in plants [40, 41] and cyanobacteria [42, 43]. Both cases are characterized by a fluorescence maximum at 685 nm at higher temperatures (above 140 K) and the emergence of a second 695 nm fluorescence peak upon cooling down to 77 K. Further cooling reduces the intensity at 695 nm, so that mainly one peak at 685 nm is left at around 4 K. This complex behavior was explained [43] in terms of two distinct pools of Chls, F685 and F695, emitting at different wavelengths and both absorbing at lower wavelengths than the primary electron donor state in the RC. F695 carries the oscillator strength of one Chl, F685 has a larger oscillator strength due to a delocalized exciton state. At 4 K the fluorescence maximum is determined by the state with the higher oscillator strength, i.e., F685. Upon increasing the temperature, EET from F685 to the RC and subsequent quenching by electron transfer sets in and thereby diminishes the fluorescence intensity of this state. Since energy transfer from F695 is frozen out below 77 K, this state is still fully fluorescent and the fluorescence maximum shifts to the red between 4 and 77 K [43]. The isolated CP47 complexes do not show such a behavior, since no EET to the RC and subsequent quenching by electron transfer is possible. Instead, in isolated intact [121] CP47 complexes, the position of the fluorescence maximum was shown [122] to remain constant at 695 nm for T $\leq$75 K and to move to shorter wavelengths at higher temperatures due to thermal population of higher exciton states.

Besides F685 and F695, a third emitter noted F689 was identified in plant material, that can be detected only in time-resolved fluorescence experiments below 77 K [44]. F685 was assigned to Chls in CP43 [45], whereas F695 was assigned to Chls in CP47 [45, 46, 47]. Two tentative models assigned F689 to either CP43 or CP47 and left open the possibility that Chls of CP47 contribute to F685 [44]. Similar assignments were made on the basis of theoretical studies aimed at the description of a variety of spectroscopic properties of dPSIIcc [43, 115].

Materials and Methods

Confocal Principle

The key feature of confocal microscopy is the ability to produce in-focus images of thick specimen, a process known as optical sectioning. Images are acquired point-by-point and imaged with a computer, allowing three-dimensional reconstructions of topologically-complex objects. The principle of confocal microscopy was originally patented by Marvin Minsky in 1957 [123]. In a confocal laser microscope, a point light source (often coupled through the single mode fiber) is reflected by a dichroic beamsplitter and then focused by an objective lens to a small (diffraction limited) focal volume (see Figure 17). If a fluorescent species is found in the focal volume, a mixture of emitted fluorescence as well as reflected laser light from the illuminated spot is recollected by the objective lens. The collected light is separated by a dichroic beam splitter reflecting with the wavelength of the excitation source and allowing only red-shifted light relative to the initial excitation wavelength to pass through the detection section. Light emitted from areas out of focus is spatially removed by a pinhole. The resulting images are sharper than those from conventional fluorescence microscopy techniques. Imaging of various z axis planes (also known as z stacks) of the sample is possible. After passing the pinhole, the remaining light is detected by a photodetection device e.g. an avalanche photodiode (APD), transforming the light into an electrical signal that is counted by a computer. The detected light originating from an illuminated volume element within the specimen represents one pixel in the resulting image. As the sample is scanned in x–y direction, the whole image is obtained pixel-by-pixel and line-by-line, whereas the brightness of a resulting image pixel corresponds to the relative intensity of the detected fluorescence.

The advantage of confocal microscopey is the resolution achieved in z-direction, which is given by $\Delta z = \frac{\lambda n}{4NA}$. The resolution increase in x–y direction, is given by $\Delta x = 0.32\frac{\lambda}{NA}$ compared to the resolution of a conventional microscope ($\Delta x = 0.47\frac{\lambda}{NA}$) is low in this dimension. It also depends on the size of pinhole [124]. The advance in the resolution yields 3D pictures of

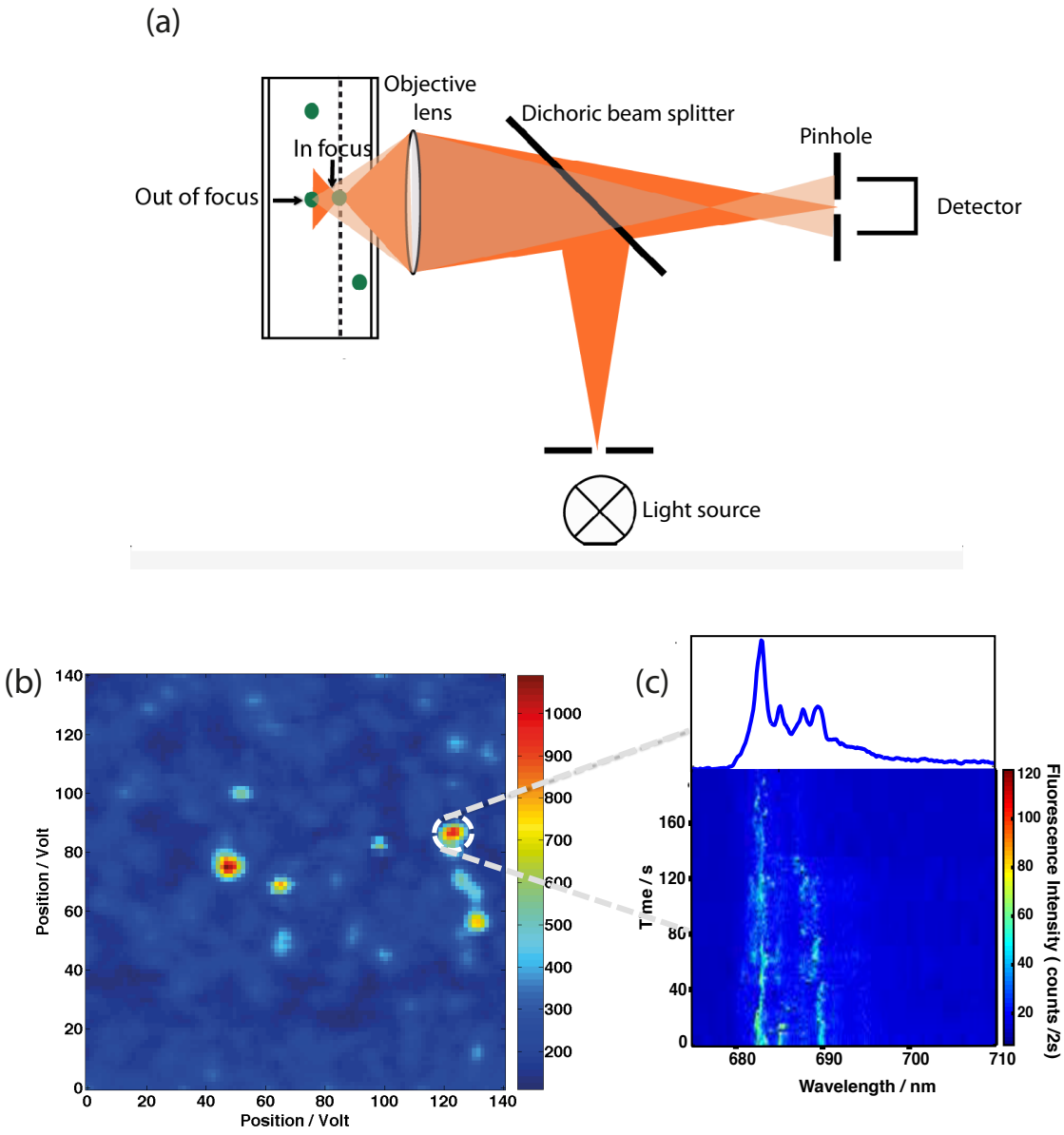

Figure 17: (a): Schematic representation of the confocal principle. Fluorescence that originates from the focal volume passes through a pinhole (orange) and light from outside the focal volume will be rejected by the pinhole (light orange, see also text). (b): A single-complex scan image at 1.6 K. (c): The time dependent spectra of a single-complex marked by white circle in the scan image. The average spectrum is shown on top.

whole cells.

For single-molecule spectroscopy, the experiments were carried out using a home-built confocal microscope operating at 1.6–300 K as described in ref. [125] (see Figure 18 for details of

confocal setup and cryostat used in experiments). A 665 nm CW diode laser and a broadband white light pulsed laser with 40 MHz repetition rate (SuperK Extreme 40 MHz VIS, NKT photonics) combined with an acousto-optical tunable filter (AOTF) set to 675 nm were used for excitation in different single-molecule experiments [77, 125, 126]. For polarization measurements a combination of a $\lambda/2$-waveplate on a motorized rotator and a polarizing beamdisplacer can be moved into the optical path in front of the spectrograph (Figure 18a). The polarizing beam-displacer splits the light into two beams with perpendicular polarizations, which can be acquired individually by the CCD-camera. In combination with the rotating $\lambda/2$-waveplate it is possible to measure the spectrally resolved fluorescence intensity with S- and P-polarized component simultaneously as a function of the rotator angle [77, 125, 127].

Sample Preparation

Preparation and crystallization of dPSIIcc from *T. elongatus* were done in the group of Prof. Dr. Athina Zouni at the Humboldt University of Berlin. Extensive biochemical characterization of dPSIIcc are summarized in Ref. [128]. For SMS redissolved crystals in a buffer solution containing 100 mM PIPES (pH 7.0), 5 mM $CaCl_2$, 0.5 M betaine, and 0.03% β-DM show high oxygen evolution activity [129]. The final dPSIIcc concentration was $\sim$3 pM.

PSI-M from *T. elongatus* have been isolated as described in Ref [79, 102]. The purified PSI-M were diluted in a buffer solution (pH 7.5) containing 20 mM Tricine, 25 mM $MgCl_2$, and 0.4 mM % β-DM detergent to reach Chl *a* concentration of 20 μM. This amount of detergent is adequate for the critical solubilization of PSI-M concentration of 0.5 μM to avoid PSI aggregation [130]. In further steps, the PSI-containing (buffer) solution was diluted (with the same buffer conditions) to a PSI-M concentration of $\sim$3 pM.

For single-molecule experiments less than 1 μL of the samples, PSI or PSII, were sandwiched between two coverslips and inserted into the pre-cooled cryostat.

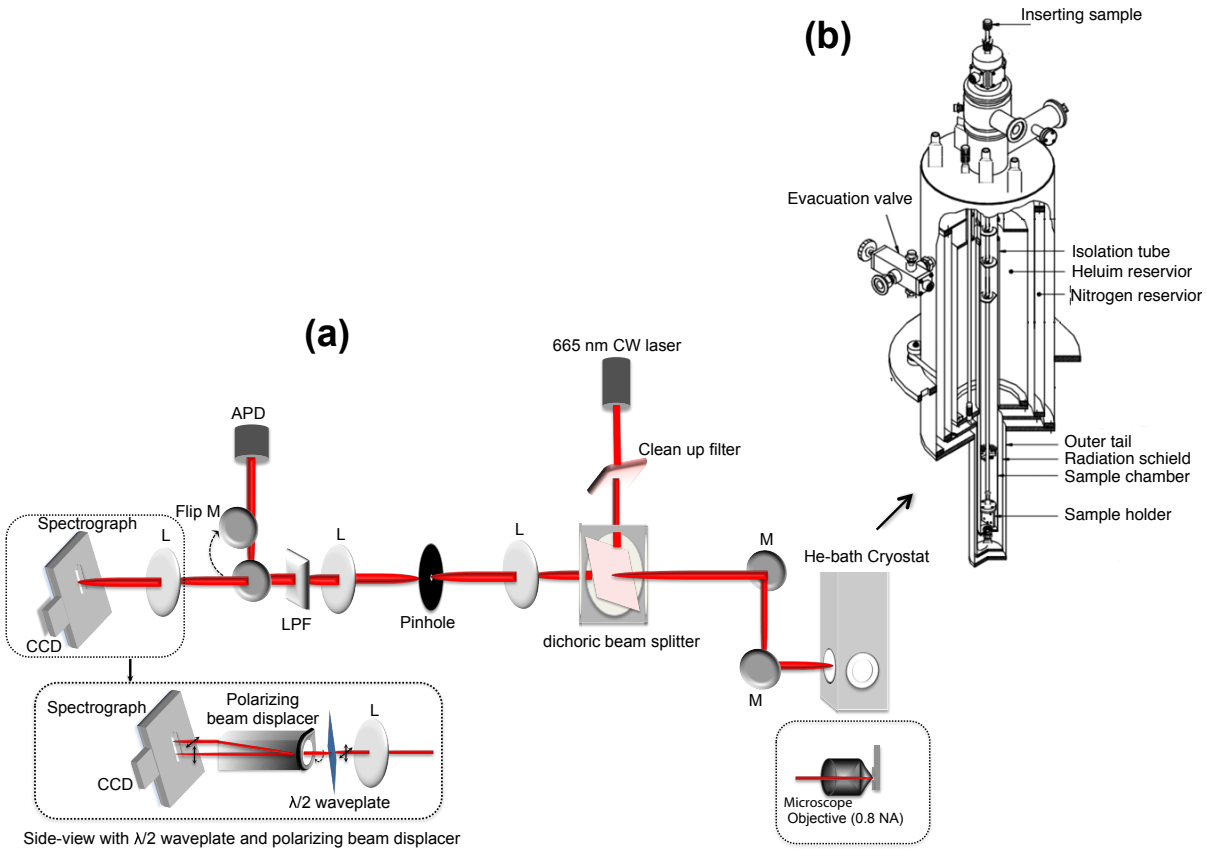

Figure 18: (a): Scheme of the home-built confocal microscope designed for SMS measurement at temperature 1.6 K. The laser beam passes through a laser clean-up filter before it enters the excitation pathway. The laser is guided using a dichoric beam splitter and two mirrors into the cryostat. The microscope objective (MO) is located together with the sample inside the cryostat. The fluorescence signal passes through the dichroic beam splitter and is focussed onto a pinhole followed by a re-collimating lens. A fluorescence cut-off filter (LPF) is positioned behind the lens and only allows the red-shifted fluorescence to be detected either by an APD or by a CCD camera mounted on the exit slit of a grating spectrograph. The signal is conducted for detecting by APD and CCD using a flipping mirror (Flip M). For polarization measurements a combination of a $\lambda/2$-waveplate on a motorized rotator and a polarizing beamdisplacer can be moved into the optical path in front of the spectrograph. For more information see refs. [77, 125, 127]. (b): Scheme of the liquid Helium (LHe) bath cryostat (SVT-200, Janis). Inside of the sample area contains a sample holder, Attocube sample stage and scanner. Liquid Nitrogen (LN) shielded LHe reservoir in order to reduce the radiational heat load into He reservoir. Therefore, at first the cryostat is pre-cooled by LN and then by filling with LHe it cools down up to 4.2 K. Temperatures below 4.2 K are generated by pumping the LHe down to superfluid He, the temperature is controlled and tuned around 1.6 K.

Data Evaluation process

Shifting Algorithm

The algorithm using the MATLAB software package has been used to evaluate the single PSIIcc datasets. This algorithm is useful to overcome the broadening of spectra of single emitters, which are affected by spectral diffusion, for long accumulation time. It works on time dependent spectra series, where the position of the maximum intensity of an emitter is detected in a user-selected wavelength range. Then the single spectra are shifted in a circular manner, whereas the intensity maxima are at the same position. Circular shifting means data points shifted out of the matrix boundaries are moved to the opposite end of the matrix. In the next step the shifted spectra are summed up giving a spectrum of the single emitter with better signal-to-noise ratio. To achieve highly resolved single emitter profiles, the shifting wavelength range is selected around the ZPL and the PW and single spectra showing low intensity or multiple positions of the single emitter are excluded. It should be noted that due to shifting along wavelength, the original wavelength scale changed and the time scale converts to number of spectrum.
To determine the Huang-Rhys factor the intensities of the ZPL, I_{ZPL}, and the PW, I_{PW}, are calculated by numerical integration and the Huang-Rhys factor, S, is calculated by:

$$\mathrm{e}^{-S} = \frac{I_{\mathrm{ZPL}}}{I_{\mathrm{ZPL}} + I_{\mathrm{PW}}}. \tag{14}$$

To suppress overlapping emission a linear baseline correction is applied. For more details of this algorithm, see Appendix A.

Determination of the phase difference between two emitters in experimental datasets

For determining the phase between different contributions in fluorescence emission, an analysis based on discrete Fourier transformation (DFT) was applied on two dimensional fluorescence

spectra, which are recorded as a function of waveplate rotation angle. Using our setup described in Figure 18, the s- and the p-polarized components of the emission are acquired simultaneously. Rotating the $\lambda/2$ waveplate two fluorescence spectra series can be recorded depending on the rotation angle of the waveplate with respect to the initially orientation. Both spectra series contain same information and differ only in phase. The $\lambda/2$ waveplate rotates the polarization of the incident light by the double of the angle between the polarization plane and towards the crystal axis. Together with the symmetry of polarization this leads to a modulation period of 90° rotation angle of the waveplate. In addition, with the known frequency of the rotator this gives the expected modulation frequency of the spectra along the angle axis.

Figure 19 shows the workflow to determine the angle between two components clearly differing in polarization. Figure 19a shows the 2D dataset of fluorescence spectra in dependence of the angle of the $\lambda/2$-waveplate. For analysis, DFT is applied on this dataset along the angular (also time) axis.

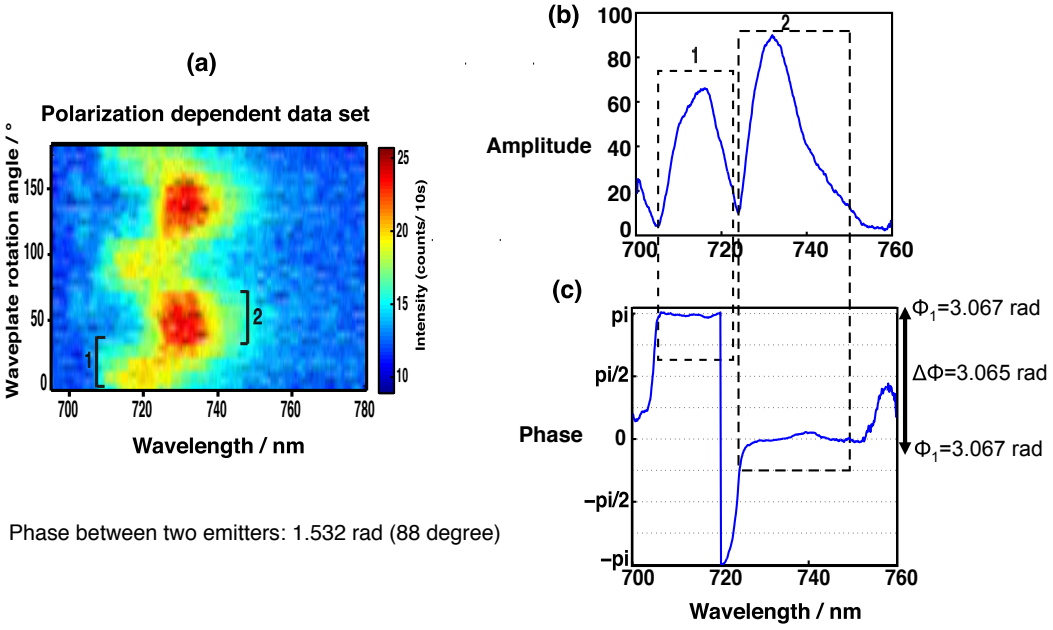

Figure 19: (a): Polarization dependent datasets with the angle nearly 90 degree between two emitters (1) and (2). (b): The amplitude modulation calculated by DFT. (c) The phase modulation calculated by DFT.

In the second step, those Fourier components are selected corresponding to the expected modulation frequency caused by rotation of the $\lambda/2$-waveplate. Figure 19b and c show the amplitude and the phase of these components. In Figure 19b, two ranges of high amplitude can be identified and correlated to ranges of stable phase which is indicated by two dashed squares in Figure 19c. Then, using the phase plot (Figure 19c) their phase difference is calculated to 3.065 rad (nearly π). Due to the two-fold rotational symmetry of the polarization this gives two times the angular difference. Therefore, the angular difference of the polarization is then divided by two, which gives 1.532 rad (88 degree) for this example.

Determination of the phase difference between two arbitrary distributed vectors-simulation

For a pair of emitting dipoles, representing the contributions of the polarization dependent fluorescence datasets, their TDMs are denoted as $\overrightarrow{\mu_1}$ and $\overrightarrow{\mu_2}$ enclosing the angle α. In our case, $\overrightarrow{\mu_1}$ corresponds to the TDM of the emitter C708 and $\overrightarrow{\mu_2}$ corresponds to the TDM of the emitter C719, whereby the angle α is assumed to be constant for all single PSI-M complexes. However, the orientation of each observed single PSI-M complex and also the pair of vectors corresponding to the respective emitters are arbitrarily distributed in space. By our measurement technique, we are not able to observe the three-dimensional polarization vectors but only their two-dimensional projections onto the plane of the camera, denoted as $\overrightarrow{v_1}$ and $\overrightarrow{v_2}$, which enclose the angle β.

However, determining a large distributions of angles β from different polarization dependent datasets of the single PSI-M complexes, enables us to draw conclusions on the value of α. Therefore, a simple simulation is used to illustrate the distribution of the projected angles for the randomly oriented vector-pair depending only on the angle α. Therefore, two vectors $\overrightarrow{\mu_1}$ and $\overrightarrow{\mu_2}$ with angle α are randomly rotated using Euler rotation theorem and then projected into the detection plane in order to get the projected angle β. For more details, see Appendix C-S2. Repeating this procedure for a large number of random rotations, yields a broad distribution for a given α, exhibiting its maximum occurrence around the value of α. In

Figure 20 the distribution of the observable angles β are shown exemplarily for α=10°, 60° and 90°. It can be seen that each histogram exhibits its maximum around the given angle α. Respecting the experimental restriction, we are not able to detect fluorescence of emitters, $\overrightarrow{\mu_1^*}$ or $\overrightarrow{\mu_2^*}$, oriented perpendicular to the detection plane. We excluded the respective angles β from the distribution of one of the randomly oriented vectors has 10 or less degree to the optical axis because they can not be detected due to the limitation of objective numerical aperture. Thus, by experimentally determining a statistically significant number of angles β, each representing the evaluated phase of a polarization dependent datasets, we are able to determine α.

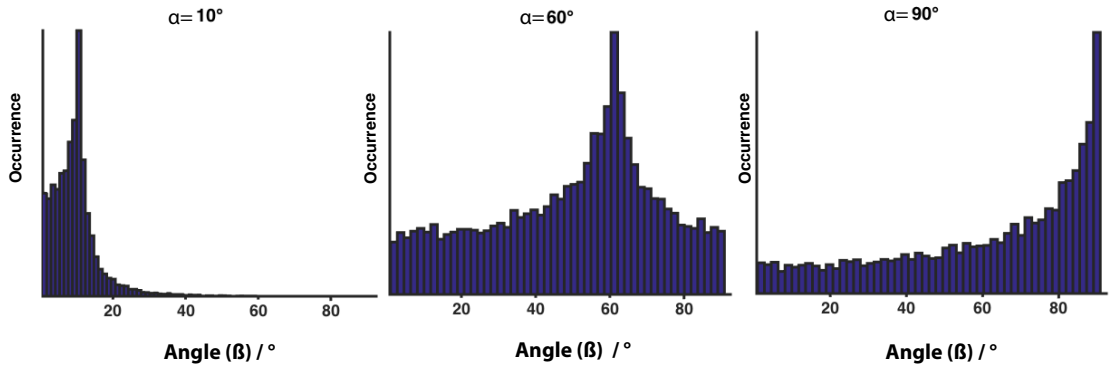

Figure 20: Angular distribution for the projection of a randomly rotated pair of vectors with fixed angles α= 10°, 60° and 90 °. The maximum of the phase difference distributions stays with the fixed angle.

For a pair of emitting dipoles with arbitary distributions, $\overrightarrow{\mu_1}$ and $\overrightarrow{\mu_2}$ are representing their TDMs responsible for fluorescence in polarization dependent datasets. The vectors $\overrightarrow{\mu_1}$ and $\overrightarrow{\mu_2}$ with angle α are shown in Figure 21 by green arrows. With respect to the arbitrary orientation of each observed single monomer, this pair of vectors is rotated by a random angle around a random axis (calculated by the Euler rotation theorem). The new vectors, $\overrightarrow{\mu_1^*}$ and $\overrightarrow{\mu_2^*}$, shown in Figure 21 by blue arrows, represent now the emitters C708-C719 for a certain single PSI-M complex. The experimentally determined vectors $\overrightarrow{v_1}$ and $\overrightarrow{v_2}$, shown in Figure 21 by red arrows, enclosing the angle β can now be easily given by the projection onto the xy-plane, which is defined as the plane of the camera (detection plane).

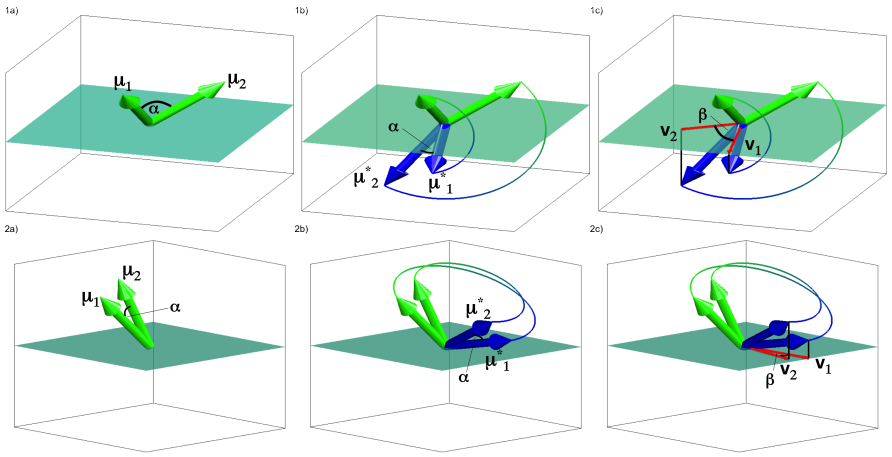

Figure 21: The TDMs of two emitters (green), the rotated vector pair (blue) and the projected vectors (red) which we detect during our polarization dependent measurements; (a): α= 60°, (b): α= 20°.

Chapter 1: Spectroscopic Properties of Photosystem II Core Complexes from *Thermosynechococcus elongatus* Revealed by Single-Molecule Experiments

The optical properties of intact, oxygen-evolving dPSIIcc from *T. elongatus* at the single-molecule level have been investigated for the first time. We utilized the combination of absorption, fluorescence and low temperature SMS to elucidate the spectral properties, heterogeneities and dynamics of the Chl*a* molecules responsible for the fluorescence of dPSIIcc.

The fluorescence spectra of single PSIIcc are dominated by ZPLs in the range between 680 – 705 nm. The single-molecule experiments show unambiguously that different emitters and not only the lowest energy trap contribute to the low temperature emission spectrum. Each spectrum exhibits unique features. In the wavelength range 680 – 690 nm all spectra show several ZPLs. The dynamics of the ZPLs are characterized by discrete spectral jumps with different widths and not by continuous changes in their positions. A satisfactory Gaussian decomposition of the average emission spectrum shows at least three contributions that are in good agreement with the reported fluorescence bands F685, F689 and F695. This indicates that the excitation energy is trapped at different low energy states in the PSII core antenna. However, the intensity of F695 in the single dPSIIcc datasets is lower than in conventional ensemble spectroscopy. The reason for the deviation might be due to the accumulation of triplet states on the red most Chls (e.g. Chl29 in CP47) or on Cars close to these long-wavelength traps by the high excitation power used in the single-molecule experiments. The red most emitter will not contribute to the fluorescence spectrum as long as it is in the triplet state. In addition, quenching of fluorescence by the triplet state may lead to a decrease of long-wavelength emission. Nevertheless, emission lines are observed in the respective spectral region; as a consequence photodamage of these chromophores can be ruled out by our single-molecule data. This chapter is adapted from ref. [42].

Biochimica et Biophysica Acta 1837 (2014) 773–781

Contents lists available at ScienceDirect

Biochimica et Biophysica Acta

journal homepage: www.elsevier.com/locate/bbabio

Spectroscopic properties of photosystem II core complexes from *Thermosynechococcus elongatus* revealed by single-molecule experiments

Marc Brecht [a,b,*], Sepideh Skandary [a], Julia Hellmich [c], Carina Glöckner [c], Alexander Konrad [a], Martin Hussels [a], Alfred J. Meixner [a], Athina Zouni [c,d], Eberhard Schlodder [c]

[a] Universität Tübingen, IPTC and Lisa + Center, Auf der Morgenstelle 18, Tübingen, Germany
[b] Zurich University of Applied Sciences, Technikumstrasse 13, 8401 Winterthur, Switzerland
[c] Technische Universität Berlin, Max-Volmer-Institut, Straße des 17. Juni 135, Berlin, Germany
[d] Humboldt Universität zu Berlin, Institut für Biologie, Philippstr. 13, 10099 Berlin, Germany

ARTICLE INFO

Article history:
Received 30 October 2013
Received in revised form 28 January 2014
Accepted 31 January 2014
Available online 6 February 2014

Keywords:
Photosystem II core complex
CP43
CP47
Single-molecule spectroscopy
Low temperature spectroscopy
Fluorescence quenching

ABSTRACT

In this study we use a combination of absorption, fluorescence and low temperature single-molecule spectroscopy to elucidate the spectral properties, heterogeneities and dynamics of the chlorophyll *a* (Chl*a*) molecules responsible for the fluorescence emission of photosystem II core complexes (PS II cc) from the cyanobacterium *Thermosynechococcus elongatus*. At the ensemble level, the absorption and fluorescence spectra show a temperature dependence similar to plant PS II. We report emission spectra of single PS II cc for the first time; the spectra are dominated by zero-phonon lines (ZPLs) in the range between 680 and 705 nm. The single-molecule experiments show unambiguously that different emitters and not only the lowest energy trap contribute to the low temperature emission spectrum. The average emission spectrum obtained from more than hundred single complexes shows three main contributions that are in good agreement with the reported bands F685, F689 and F695. The intensity of F695 is found to be lower than in conventional ensemble spectroscopy. The reason for the deviation might be due to the accumulation of triplet states on the red-most chlorophylls (e.g. Chl29 in CP47) or on carotenoids close to these long-wavelength traps by the high excitation power used in the single-molecule experiments. The red-most emitter will not contribute to the fluorescence spectrum as long as it is in the triplet state. In addition, quenching of fluorescence by the triplet state may lead to a decrease of long-wavelength emission.

1. Introduction

Photosystem II (PS II) is the membrane protein complex of higher plants, green algae and cyanobacteria that uses solar energy to catalyze the electron transfer from water to plastoquinone [1,2]. The photo-oxidized electron donor of PS II ($P680^+$) is one of the most powerful oxidizing species capable of driving the oxidation of water to oxygen. The structure of dimeric PS II core complexes (PS II cc) from cyanobacteria has been determined by X-ray crystallography to a resolution of up to 1.9 Å [3,4]. Fig. 1 shows the chlorophyll containing subunits of PS II cc according to the structural model at 2.9 Å resolution [4]. Subunits CP43 and CP47 contain 13 and 16 chlorophyll *a* (Chl*a*) molecules, respectively. The PS II reaction center (RC), which is formed by the subunits D1, D2 and Cyt *b559*, binds six Chl*a* and two pheophytin *a* molecules. The RC is surrounded by the subunits CP47 and CP43. The primary function of CP47 and CP43 is to harvest light and transfer the absorbed energy to the RC, where the photochemical charge separation takes place.

The optical properties of PS II cc, its individual subunits (CP43, CP47) and the RC have been studied in detail [5–15]. The shape of the fluorescence emission spectrum depends remarkably on temperature [6,7,10–13]. Two spectral components at 685 nm and 695 nm, called F685 and F695, were used to explain the temperature dependence. Andrizhiyevskaya et al. [11] concluded that F695 originates from excitations that are irreversibly transferred to the red-absorbing 690 nm chlorophylls of CP47 and that F685 originates from excitations that are slowly transferred to the RC, where they are irreversibly trapped by charge separation. At 4 K almost all excitations that reach the 690 nm chlorophylls of CP47 will remain on this chlorophyll, whereas some excitations will become trapped on the red-most chlorophylls of CP43. Information about the optical properties of CP43 and CP47 core antennae was obtained from high-resolution spectroscopy in the frequency domain [6,16]. Excitation dependent fluorescence line narrowing spectra of PS II from spinach gave first evidence that CP43 holds two emitting states with different inhomogeneous distributions at low temperatures

Abbreviations: PS I, photosystem I; PS II, photosystem II; PS II cc, photosystem II core complex; CP43 CP47, chlorophyll binding subunits of PS II; ZPL, zero-phonon line; RC, reaction center; Chl*a*, chlorophyll *a*; Car, carotenoid

* Corresponding author.
E-mail address: marc.brecht@uni-tuebingen.de (M. Brecht).

0005-2728/$ – see front matter © 2014 Elsevier B.V. All rights reserved.
http://dx.doi.org/10.1016/j.bbabio.2014.01.025

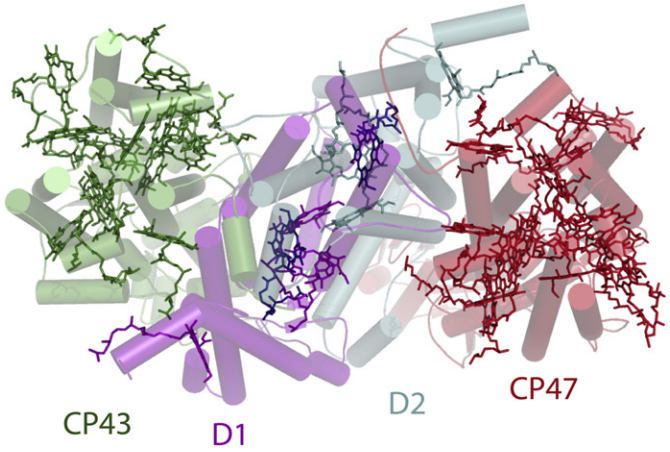

Fig. 1. Chlorophyll containing subunits of PS II cc. The Chl*a* molecules coordinated by the subunits CP43, D1, D2 and CP47 (cartoon mode) are shown in green, purple, cyan and red, respectively. The two Pheophytin (Pheo) a molecules are colored in dark blue. The figure was made with PyMol using the coordinates of the structural model of PS II cc from *Thermosynechococcus elongatus* at 2.9 Å resolution (Ref. [4], (PDB code 3BZ1)).

[6]. Komura et al. [12] performed picosecond time-resolved fluorescence spectroscopy on spinach PS II at 4, 40, and 77 K and identified an additional fluorescence band at 689 nm (F689). The fast decay of F689 suggests an energy transfer directly from F689 to P680 [12]. The complex interrelation between the different subunits and the strong influence of the inhomogeneous widths of the different red-states makes a set of optical techniques necessary to solve their function in the excitation energy transfer.

In this study we investigate the optical properties of intact, oxygen-evolving PS II cc dimers of *Thermosynechococcus elongatus* at the single-molecule level. Single-molecule techniques overcome the inhomogeneous broadening. This is especially useful if the influence of inhomogeneity is covered by ensemble averaging [17]. At ambient temperatures, the susceptibility of the chromophores to fluctuations of the protein moiety and its surrounding media leads to line broadening (spectral diffusion) [18–20]. Lowering the temperature is one possibility to reduce the impact of fluctuations on the chromophores' site energies. Low temperature experiments have the additional advantage to minimize photobleaching and limitations in the observation time [21]. Assuming that all fluctuations are suppressed, the emission profile of a single emitter composed out of a sharp zero-phonon-line (ZPL) and a phonon-wing becomes observable. The ZPL belongs to an electronic transition between the vibronic ground state of the first electronic excited state and the vibronic ground state of the electronic ground state. This kind of emission is not accompanied by the creation or annihilation of phonons. The phonon wing on the low-energy side of the ZPL is due to the reorganization of the surrounding induced by the excitation of the chromophores from the ground to the excited state. The reorganization leads to the excitation of phonons (lattice vibrational modes). Due to the small line width of the ZPLs, it is possible to observe the process of spectral diffusion in slow-motion as nicely shown by experiments on LH2 and PS I at 1.4 K [22,23]. The widths of those spectral jumps reach into the range of several nanometers indicating remarkable changes in the site energy of the emitting chlorophyll molecules. In a recent study on PS I, we were able to show that a large portion of the spectral dynamics in the lower hierarchical levels is connected to fluctuations of protons located close to the chromophores [24]. Such protons can be found e.g. in hydrogen bonds between the chromophore and nearby amino acid residues, or structural water molecules [24,25]. The consideration of site-energy changes induced by all of these fluctuations is necessary to understand the optical properties of these proteins, especially if the chromophores take part in energy transfer. Coupled chromophores are found in almost all pigment proteins that are involved in light harvesting. Then, spectral jumps of only one chromophore are able to redirect the actual pathways of a traveling exciton and as a consequence it takes influence on the function of the whole protein complex [26,27].

2. Material and methods

2.1. Single-molecule fluorescence spectroscopy

Dimeric PS II cc from *T. elongatus* have been isolated and purified as described in Ref. [28]. The purified PS II cc dimers were diluted in buffer solution containing 100 mM PIPES (pH7.0), 5 mM $CaCl_2$, 0.5 M betaine, and 0.03% β-DM. For single molecule experiments, PS II complexes were diluted in buffer to a final PS II concentration of about 3 pM. About 1 μl of this suspension was placed between cover slips made of glass. Finally the sample was transferred directly into the cryostat and rapidly plunged into liquid helium. Experiments were carried out using a home-built confocal microscope operating at 1.6 K as described recently in Ref. [29].

The excitation intensity of the laser, measured before entering the cryostat, was 100 μW resulting in a flux of approximately $6.6 \cdot 10^{20}$ photons/(cm^2 s). The excitation wavelength was 665 nm for all experiments. The highest resolution of the spectrometer (Shamrock 500 spectrograph with 200 lines/mm and 400 lines/mm gratings in combination with Andor Newton back illuminated deep depleted CCD) is ~0.05 nm. In a sequence of spectra, the usual exposure time for each spectrum is 2 s resulting in a typical S/N ratio of >6 for single PS II cc dimers at the given excitation power referred to as time resolution in the following context.

2.2. Measurement of steady state absorption and fluorescence spectra

Absorption spectra were recorded with a spectral resolution of 1 nm on a Cary-1E-UV/VIS spectrophotometer (Varian, Inc.). Fluorescence spectra were recorded in a FluorMax 2 (Jobin Yvon) photon counting spectrofluorometer. The spectra were corrected for the spectral sensitivity based on the measurement of a calibrated light source. For the measurements, PS II complexes were diluted to a final Chl concentration of about 5 μM with buffer containing 20 mM MES-NaOH (pH 6.5), 10 mM $MgCl_2$, 10 mM $CaCl_2$, 0.02% (w/w) β-DM and glycerol (final concentration about 65% (v/v)), to obtain a transparent glass at low temperatures. For experiments at cryogenic temperatures, the cuvette was placed in a variable temperature liquid nitrogen bath cryostat (Oxford DN1704) or an Oxford liquid helium flow cryostat (Oxford CF1204). A home-built cryostat holder was used in the spectrophotometer and spectrofluorometer.

3. Results and discussion

3.1. Ensemble absorption and emission spectra of PS II cc

Fig. 2 presents temperature-dependent absorption and fluorescence emission spectra of PS II cc dimers from *T. elongatus*. At 5 K the Q_Y absorption exhibits peaks at 674 nm and 684 nm and shoulders near 669 nm, 677 nm, 680 nm and 694 nm. The second derivative of the 5 K spectrum shows minima at the specified wavelengths indicating various pigment pools (not shown).

The emission band at 290 K is centered at around 683 nm. At 50 K, two bands located at 685 nm and 694 nm are resolved. These bands are generally named F685 and F695. The 20 K fluorescence spectrum exhibits the maximum at 691 nm. The overall behavior is in good agreement with measurements on PS II samples from spinach [5,11]. The band at 695 nm (F695) has been assigned to the lowest lying energy state of the chlorophylls in CP47 [5,11] that is associated with Chl29 by several groups (using the nomenclature used in Loll et al. [30]) [2,7,31,32]. Low energy chlorophylls become traps for the excitation energy, if the thermal

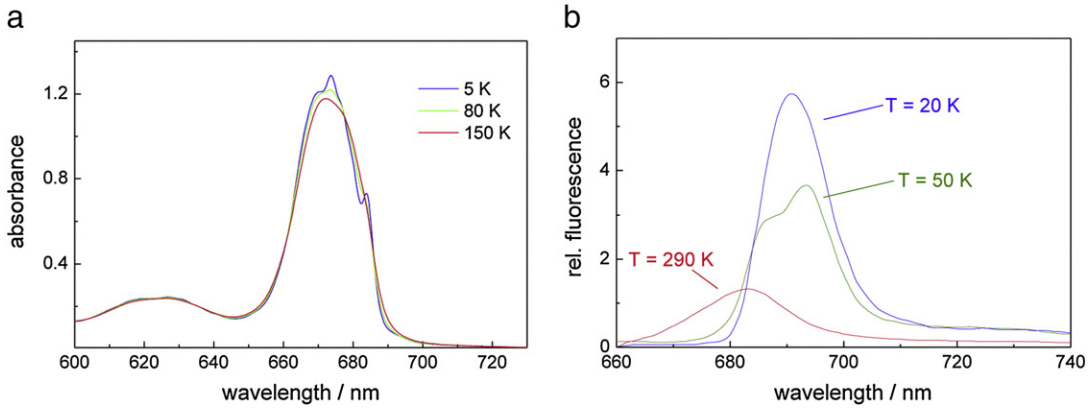

Fig. 2. (a) The panel on the left shows absorption spectra of dimeric PS II cc from *T. elongatus* at 5 K, 80 K and 150 K. The Q_y absorption band is centered at about 673 nm. (b) The panel on the right shows fluorescence spectra of dimeric PS II cc from *T. elongatus* at 20 K, 50 K and 290 K.

energy (kT) is not sufficient to enable uphill energy transfer to the RC. Lowering the temperature from 50 K to 5 K causes the fluorescence to increase and its maximum to shift to the blue to 691 nm at 20 K and 687 nm at 5 K (see Fig. 2b and Refs. [5,10–12]). This blue shift and fluorescence increase may be interpreted by the assumption that chlorophylls, absorbing at slightly shorter wavelengths than the lowest energy chlorophyll start to successively trap the excitation energy if the temperature is lowered. There are two possibilities for this case: (a) These chlorophylls are all part of the inhomogeneous distribution of transition energies of the lowest lying energy state of the chlorophylls in CP47 or (b) structurally different chlorophylls in the PS II antenna become a trap, which are not connected by fast energy transfer with the lowest state in CP47.

3.2. Emission spectra of individual PS II cc dimers

Fig. 3 shows a selection of six fluorescence emission spectra (denoted I–VI) of different single PS II cc dimers. The acquisition time for the spectra was 40 s. Single PS II cc dimers can be detected at low temperature using the fluorescence emission of several Chl*a* molecules acting as traps for the excitation energy at cryogenic temperatures with a significant fluorescence quantum yield.

The emission spectra of single PS II cc are characterized by ZPLs covering the whole range of fluorescence from 680 to 750 nm. Each spectrum exhibits unique features. In the wavelength range 680 to 690 nm all spectra show several ZPLs. Their number varies between two (spectrum VI) and six to seven (spectrum I). At wavelengths larger than 690 nm clearly visible lines are only observed in spectra I–III. Their intensities are reduced compared to the lines in the range 680–690 nm.

Fig. 4 shows a series of fluorescence emission spectra recorded on one single PS II cc within 2, 10, 50, 100 and, 200 s. The spectra show one pronounced line at ~684 nm and a line with smaller intensity at ~682 nm. The line width (fitted by a Gaussian) increases in the spectra taken at 2 and 200 s from ~0.35 nm (for both lines) to 1.15 nm (line at 682 nm) and 1.20 nm (line at 684 nm). The time dependent broadening of the lines indicates that spectral diffusion is the main underlying broadening process. Further details about the number and spectral positions of emitters responsible for the fluorescence emission of single PS II cc dimers are obtained from the analysis of their polarization. Fig. 5 shows the fluorescence emission of a single PS II cc dimer in dependence of the polarizer angle in front of the spectrograph. This angle is defined with respect to an arbitrary laboratory axis and is uncorrelated to the polarization of the excitation light [33]. In Fig. 5, the dependence of the whole emission spectra as a function of the polarizer orientation is shown. Three pronounced contributions at 684.7 nm, 686.2 nm and, 689.7 nm can be distinguished. The intensity of these contributions vanishes at specific angles almost completely; therefore a strong linear polarization can be assumed. Similar intensity variations were observed for all PS II cc investigated in this way. A strong polarization of the fluorescence emission from the different Chls requires either a single emitter as the origin of the emission or a number of emitters with parallel transition dipole moments. Since the PS II cc are randomly oriented in our samples, it is unlikely that the transition moments of several emitters would appear parallel in all cases. Therefore, the number of emitters responsible for the fluorescence emission of a single PS II cc can be determined by this method. A detailed study on this topic is in preparation.

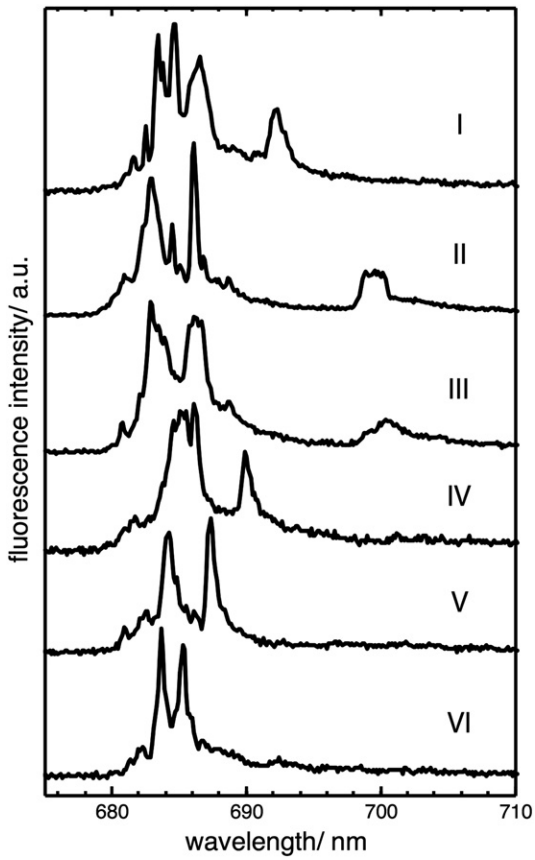

Fig. 3. Single-molecule fluorescence emission spectra from PS II cc dimers of *Thermosynechococcus elongatus*. Spectra were recorded on different individual complexes. The accumulation time was 40 s for each complex. For better comparability, the spectra that exhibited intensity differences were scaled to a similar magnitude. Excitation wavelength 665 nm; temperature 1.6 K.

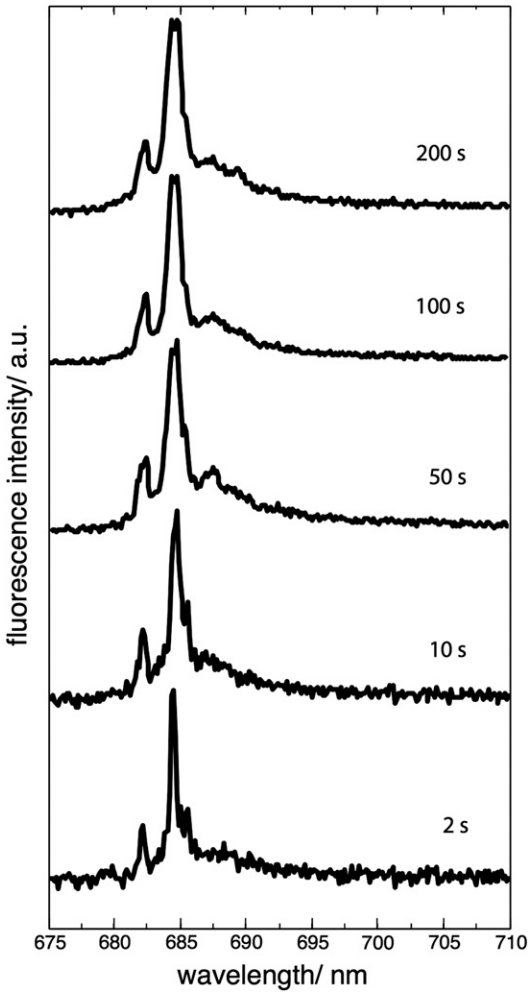

Fig. 4. Dependence of fluorescence emission spectra of one single PS II cc dimer on acquisition time. Excitation wavelength 665 nm; temperature 1.6 K.

3.3. Spectral dynamics and intensity variations of ZPLs

The basis of the dynamical process leading to the spectral broadening can be analyzed in our setup with sufficient S/N ratio using an acquisition time of 2 s. In order to analyze the spectral dynamics in the emission of PS II cc sequences of fluorescence spectra of 140 complexes were recorded. In Fig. 6 two representative examples of the time-dependent behavior of ZPLs are shown. The sequences consist of 100 spectra consecutively recorded with 2 s acquisition time. The average spectra are shown on top. The average spectrum (Fig. 6a) is dominated by two intense emitters at 682.9 nm (fwhm = 1.34 nm) and 686.2 nm (fwhm = 0.35 nm) and one broad line at 699.8 nm (fwhm = 1.66 nm). In the sequence it becomes obvious that these emitters show quite different spectral diffusion behavior. The intense line around 682.9 nm remains in the first 80 s within a limited spectral range. In the interval 100–160 s, its spectral width is expanded. Starting at 160 s up to the end of the sequence, the bandwidth is reduced again. The line around 686.2 nm remains for the most of the time at one spectral position. Only in time intervals e.g. 60–65 s, 140–148 s the line undergoes discrete jumps in frequency. In all cases the jump width is ~0.8 nm. The third line at 699.8 nm shows also pronounced spectral diffusion, but even more striking are the intensity variations of this line. In the first 80 s, the line has a low intensity. During the interval 80–150 s, the intensity is increased and the line shows several jumps in frequency until the intensity drops down completely. The sequence (Fig. 6b) shows an example for ZPLs without changes in the wavelength position during time. The average spectrum shows two intense ZPLs at 682.6 nm (fwhm = 1.0) and 684.4 nm (fwhm = 0.6) as well as a ZPL with lower intensity at 690.1 nm (fwhm = 0.6). All three lines are visible during the whole time of data acquisition. The lines at 682.6 nm and at 690.1 nm show almost no change in wavelength during time, whereas for the line at 684.4 nm slight changes are observed. Both lines show intensity variations of almost 100%, whereas the line at 690.1 nm emits with almost constant intensity.

Different lines in single-molecule spectra (e.g. see Fig. 3) may be the result of spectral diffusion (i), static disorder (ii), or different emitters (iii): (i) As can be seen in Fig. 6 spectral jumps are typically less than 1.5 nm. Lines, which are close together, may be assigned to a single emitter whose site-energy changes due to protein dynamics during the accumulation period. In general, spectral diffusion leads to a time dependent broadening of the lines (see Fig. 4) and not to separated lines. (ii) Chlorophylls bound at the same site in both monomers of the PS II dimer might have different transition energies. A Gaussian distribution is often used to describe the extent of static disorder within an ensemble with a full width at half maximum of about 200 cm^{-1} corresponding to about 10 nm [13]. (iii) Different low energy traps bound at CP43 and CP47 give rise to separated lines if the low energy states are not connected to each other by efficient energy transfer leading rapidly to thermal equilibrium. Taking the above-mentioned processes together it is reasonable that at least 2–3 emitters contribute to the emission spectra shown in Fig. 3; nevertheless an uncertainty in the determination of their correct number remains. To remove this remaining uncertainty, polarization dependent measurements (shown above) are a perfect tool to unravel overlapping signals and to account for the correct number of emitters.

The movement of the ZPLs is characterized by discrete spectral jumps with different widths and not by continuous changes in their positions (Fig. 6). A plausible explanation of the spectral dynamics observed in LH2 based on the hierarchy of tiers in the energy landscape of a protein is given in Ref. [22]. We adopt this explanation for the observed spectral dynamics in PS II. High energetic barriers between the different conformational substates characterize the highest tier in the energy landscape. Under the given low-temperature conditions, the barriers cannot be crossed and the system rests in one given conformational substate in the first tier. Two different situations are illustrated

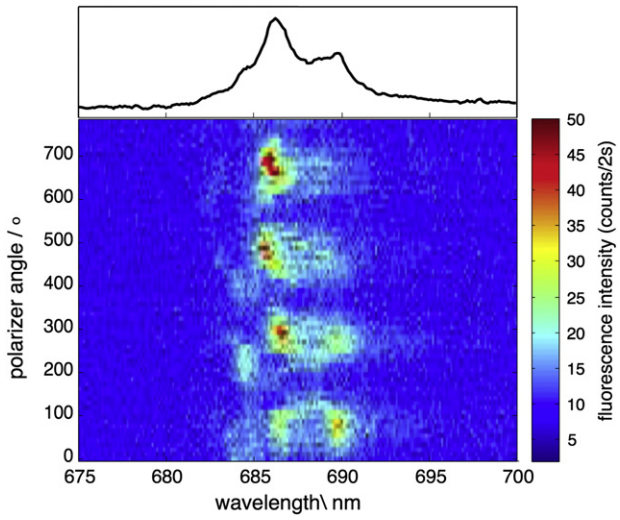

Fig. 5. Sequence of fluorescence emission spectra of a single PS II cc dimer as a function of the orientation of the polarizer in front of the spectrograph. The acquisition time was 2 s for each spectrum. Excitation wavelength 665 nm; temperature 1.6 K. The individual spectra were recorded in steps of 10°. The angle of the polarizer is shown on the left side.

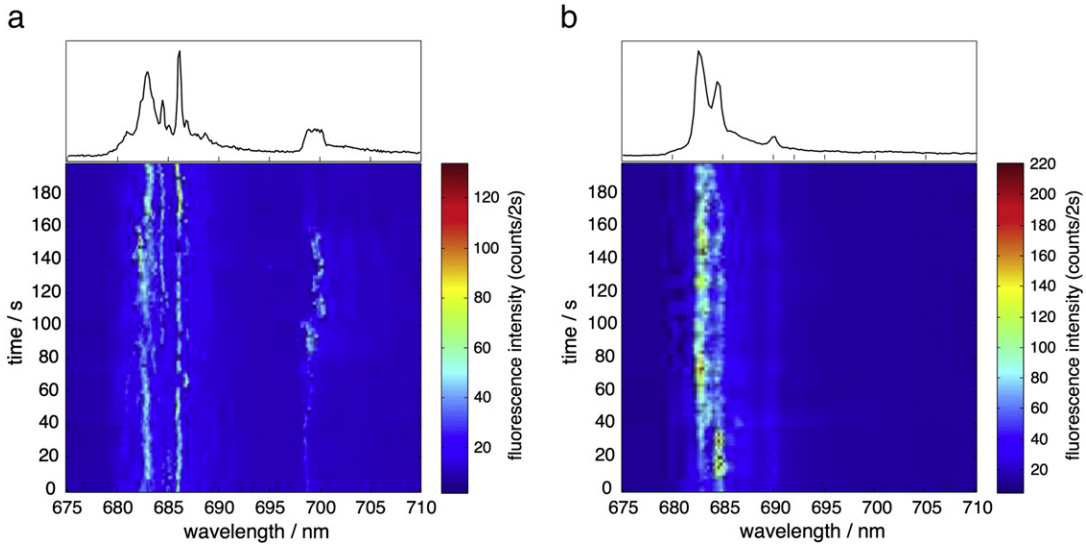

Fig. 6. Plots of time-dependent fluorescence emission spectra of single PS II cc dimers. The time sequences of 100 spectra with an accumulation time of 2 s for each spectrum are displayed for both complexes. Excitation wavelength 665 nm; temperature 1.6 K.

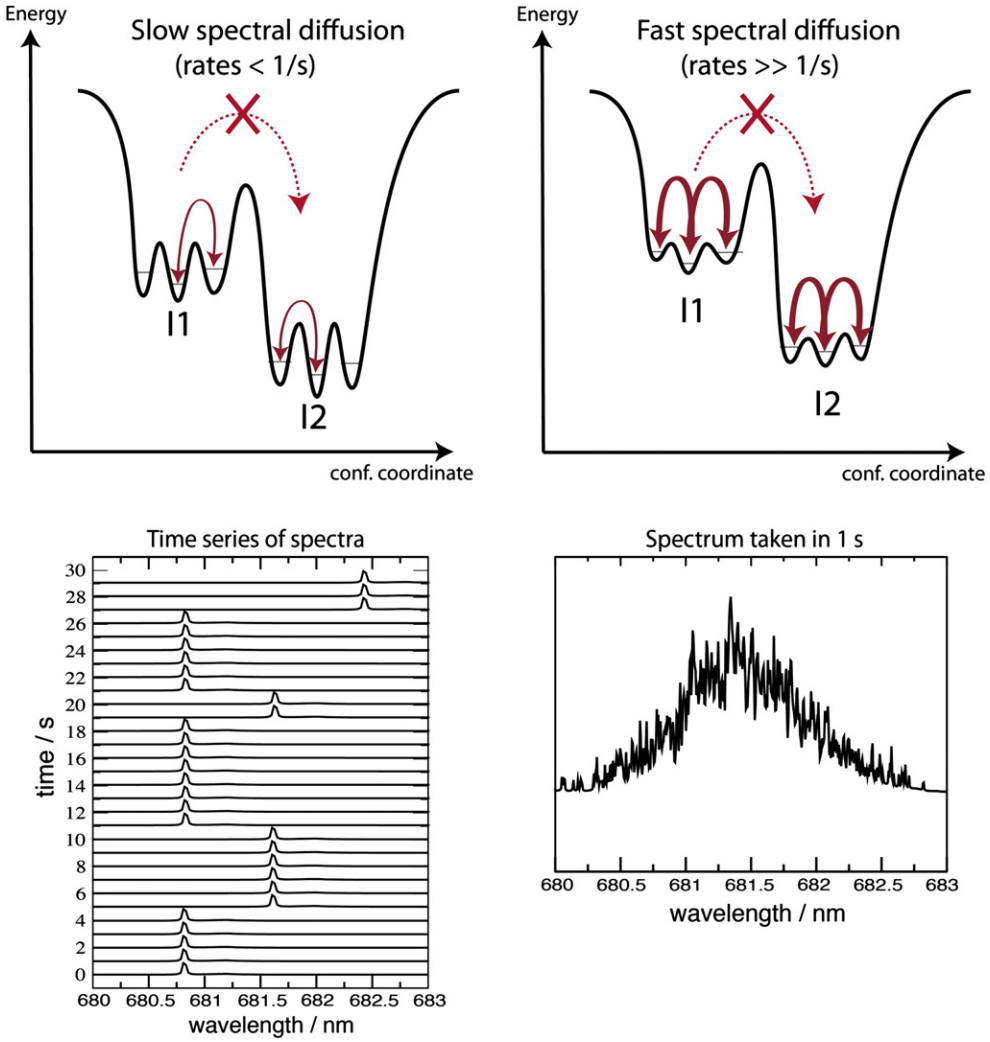

Fig. 7. Schematic illustration of the protein energy landscape. I1, I2 represent different intermediate states in the first tier. The energetic barrier between I1 and I2 cannot be crossed at low temperatures, but the barriers within I1 and I2 can be crossed (red arrows), yielding the observed jumps of the ZPLs in the emission spectra (see also Fig. 6). The barrier heights within I1 and I2 determine the rates of the conformational changes. (Left) The barriers within I1/I2 are high. Jumps occur with low rates. If the rates are in the range of the acquisition time (here ~2 s) stable ZPLs and discrete jumps can be observed in the resulting emission spectra (slow spectral diffusion). (Right) Reduced barrier heights yields increased rates, if the barriers are crossed with rates much higher than the acquisition time only broadened lines can be observed (fast spectral diffusion).

in Fig. 7. The energetic barriers between the different substates within the second tier are lower. As a consequence, these barriers can be crossed under the experimental conditions. The crossing of these barriers induces the observed line broadenings (Fig. 4) and spectral jumps (Fig. 6). The jumps are induced by small conformational changes that are possible in the second tier. Nevertheless, these changes are able to induce jumps covering a major fraction of the whole inhomogeneous line width [24]. The observation of stable ZPLs or broadened lines depends on the rates of these jumps [34].

The contributions of CP43 and CP47 are both inhomogenously broadened and their emission bands show certain overlap. The complex temperature dependence of PS II fluorescence is interpretable by noting that excitation transfer from CP43 and CP47 to the RC is slow, and strongly dependent on the precise energy at which a slow-transfer pigment in CP43 or CP47 is located within its inhomogeneous distribution [2,11,32,35]. The observed intensity variations of the emitters in Fig. 6 are most probably induced by slight changes in the site energies of the Chl*a* involved in the excitation energy transfer [26]. Especially, site-energy fluctuations of the low energy states of CP43 and CP47 will have a remarkable effect on the excitation energy transfer between the subunits and the RC.

3.4. Single-molecule average emission spectrum

As shown e.g. for PSI, the average spectrum can be reconstructed by the summation of ≥100 spectra of individual pigment protein complexes [36]. Fig. 8 shows the average emission spectrum obtained by summation of all spectra of single PS II cc dimer. The maximum fluorescence intensity is located around 685 nm. A pronounced shoulder is observed on the long-wavelength side between 690 and 695 nm. The fwhm of the peak is about 8 nm.

A satisfactory Gaussian decomposition of the average emission spectrum can be achieved by using at least three contributions (see Fig. 8). The maxima of the Gaussian bands are around 684.7, 689.3, and 691.4 nm. Vibrational contributions are taken into account by the fourth component at 701.8 nm. The overall agreement between the spectrum and the fitting function is quite good; a minor deviation is visible only at around 691 nm. The three Gaussian bands cover the wavelength regions, in which ZPLs are predominantly observed in the emission spectra of single PS II cc dimer (see Figs. 3, 5 and 6).

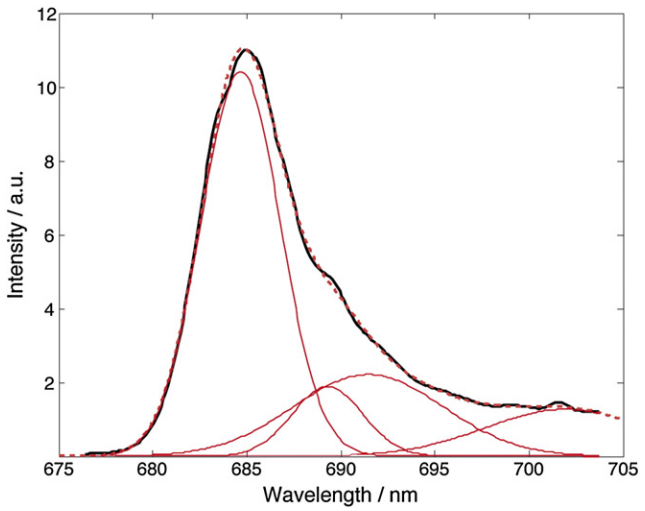

Fig. 8. The summation (average) of all fluorescence spectra taken on individual single PS II cc dimers (black) fitted by four Gaussian functions. The individual Gaussians are given in red, the summation of all Gaussians is given by the red-dotted curve. The wavelength positions and the widths of the Gaussians are: 684.7 nm/6.0 nm, 689.3 nm/5.3 nm, 691.4 nm/11.2 nm, and 701.9 nm/12.0 nm.

The contribution around 684.7 nm is in good agreement with the position of F685 assigned to a contribution from CP43 [2,11,32]. The shape of the emission spectrum shows a certain dependence on the wavelength of the excitation light. The highest intensity of the CP43 contribution was reported for excitation in the wavelength range between 665 and 673 nm [11]. In our experiment, we used 665 nm for excitation; therefore, the contributions of CP43 should also be enhanced. The second contribution is found at around 689.3 nm. The wavelength position and the width of this contribution are in good agreement with the F689 contribution reported by Komura et al. [12]. The third band is centered at around 691.4 nm. It has been proposed that the band F695 shifts from ~695 nm at 70 K to ~692 nm at 5 K [10]. This assignment can be used for the interpretation of the contributions in the single-molecule spectra e.g. Fig. 5. The weak contribution at 684.7 nm and the intense line at 686.2 nm fall into the wavelength range assigned to CP43, whereas the component with the lowest energy belongs most likely to CP47. Therefore, it can be concluded that the fluorescence of PS II results from different sites between which the energy transfer is frozen out (see Introduction section).

The complex temperature dependence of PS II fluorescence can be interpreted by noting that excitation transfer from CP43 and CP47 to the RC is slow, and strongly dependent on the precise energy at which a low-energy pigment in CP43 or CP47 is located within its inhomogeneous distribution [2]. Therefore, future single-molecule experiments will be helpful to get further insights into the influence of the inhomogeneity of the different spectral bands on the energy transfer in PS II.

The single-molecule average emission spectrum shown in Fig. 8 is significantly different from ensemble emission spectra measured by conventional fluorescence spectrometer. In ensemble experiments, the maximum emission for PS II cc was found between 687.5 nm and 690 nm below 20 K (see Fig. 2 and Refs. [10–12,37]); i.e. a few nm shifted to the red. The fwhm of the ensemble spectra is about 14 nm, i.e. nearly a factor two larger than that of the single-molecule average emission spectrum shown in Fig. 8. A notable exception is the recently reported fluorescence spectrum of PS II cc from *T. vulcanus* that was obtained by time integrals of time-wavelength 2-D images obtained with a Streak camera set-up [32]. This spectrum is virtually identical to our single-molecule average emission spectrum shown in Fig. 8. It should also be noted that emission spectra reported for the RC and CP43 from spinach PS II exhibit the maxima at 683.7 nm and 682.8 nm [6,11]. The line width of the RC is larger, whereas the line width of CP43 is close to the low value found by the single-molecule experiments.

The emission spectra of single PS II cc dimers (see Fig. 3) and the single-molecule average emission spectrum (see Fig. 8) clearly demonstrate that three or more emitters contribute to the fluorescence spectrum of PS II core complexes at low temperature. This indicates that the excitation energy is trapped at different low energy states in the PS II core antenna. Due to their low Q_Y transition energy, uphill excitation energy transfer to the RC becomes impossible at cryogenic temperatures. These states are not connected to each other by efficient energy transfer leading to thermal equilibration, because otherwise the excitation energy would be localized at 5 K on the lowest energy state being the only emitting state.

The sum of all contributions determines the shape of the fluorescence spectrum. The reason for the observed difference between the single-molecule average spectrum and the ensemble spectrum is most likely that the intensities of the contributions are different, as different quenching mechanisms might be effective under the respective conditions of the experiments.

Upon illumination at cryogenic temperatures, the light-induced formation of $P680^+Q_A^-$ in PS II is followed by charge recombination, as the electron transfer from Q_A^- to Q_B and from Y_Z to $P680^+$ is inhibited. The extent of $P680^+Q_A^-$ formation decreases progressively with

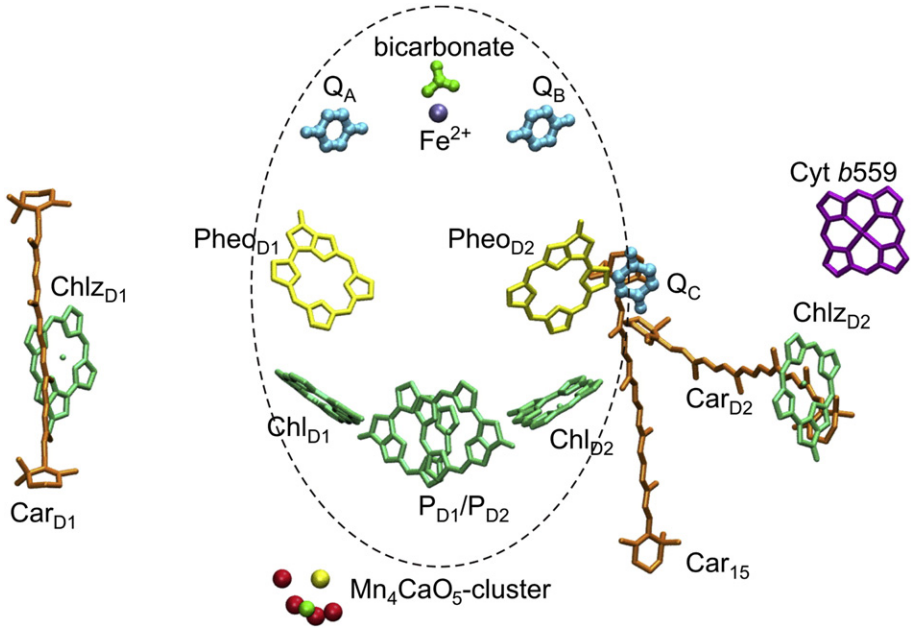

Fig. 9. Arrangement of the cofactors of the RC of PS II cc including the presumably involved co-factors of the secondary electron transfer (view perpendicular to the pseudo-C2 axis) based on the structural model of PS II cc from *T. elongatus* at 2.9 Å resolution (Ref. [4], (PDB code 3BZ1)). Shown are the two Chl*a*s constituting P680, P_{D1}/P_{D2} (green), the two peripheral Chls, Chl_{ZD1} and Chl_{ZD2} (green), the β-carotene (Car) molecules identified so far in the RC, Car (orange), and cytochrome (Cyt) b559 (violet).

successive turnovers. The reason is the oxidation of secondary electron donors (Car, Chl_Z, Cyt *b*559, Y_Z) by $P680^+$, which occurs with low quantum yield in competition to the charge recombination of $P680^+Q_A^-$. Thereby, long-living states as e.g. $Q_A^-P680Car^+$, $Q_A^-P680Cyt\ b559^+$, or $Q_A^-P680Chl_Z^+$ are accumulated after several turnovers [38]. Fig. 9 shows the arrangement of the mentioned cofactors in the X-ray structure. In the presence of Q_A^- (closed PS II), the primary radical pair $P680^+Pheo^-$ can still be formed, but stabilization of the charge separation is not possible. Fluorescence induction experiments have shown that the fluorescence yield increases upon reduction of Q_A [39,40]. The increase is stronger for PS II frozen with Cyt *b*559 in the reduced state than for PS II frozen with Cyt *b*559 oxidized. In the first case, it is $Q_A^-P680Cyt\ b559^+$, whereas in the second case, it is $Q_A^-P680Car^+$ and $Q_A^-P680Chl_Z^+$, that is predominantly accumulated upon illumination at low temperature. This difference might be due to trapped Chl^+ and Car^+, which are known to be efficient quencher of the excitation energy [41,42].

There is no need for high excitation intensities, to accumulate the discussed long-living states. Therefore, reduced Q_A and oxidized secondary donors are most likely present while measuring fluorescence spectra by conventional ensemble spectroscopy as well as single-molecule spectroscopy. Thus, the described light-induced reactions in the RC cannot explain the differences in the shape of the emission spectra (single-molecule vs. ensemble).

However, in single-molecule experiments the photon flux has to be much higher than in conventional fluorescence spectroscopy in order to achieve a satisfactory signal-to-noise ratio. In our experiments, the flux was approximately $6.6 \cdot 10^{20}$ photons/(cm^2 s). With an absorption cross section σ for PS II of about $7 \cdot 10^{-15}$ cm^2 at 665 nm, the excitation rate $\sigma \cdot I$ is of the order of 10^6 s^{-1}. A relatively high excitation power was also used for the time-resolved fluorescence measurements with the streak camera set-up by Shibata et al. [32]. With an excitation power of 0.5 W/cm^2 at 430 nm, the excitation rate is about $1.4 \cdot 10^4$ s^{-1}.

Under such conditions, the accumulation of triplet states, ^3Chl and ^3Car, in CP47 and CP43 can be expected. The structural data of PS II show that about one third of the chlorophylls in CP47 (Chl17, Chl22, Chl26, Chl27 and Chl29) as well as in CP43 (Ch33, Chl43, Chl47, and Chl49) are in close contact ($\leq$5 Å) to a β-carotene [43]. This structural information is in line with triplet-minus-singlet absorbance difference spectra of isolated CP43 and CP47 [6,16]. Carotenoid triplets formed by triplet transfer from chlorophylls as well as chlorophyll triplets decaying with half-lives in the ms range have been characterized by their absorbance difference spectra [6,16]. Chlorophyll triplets in CP47 and CP43 are certainly accumulated at an excitation rate above 10^4 s^{-1}. In single-molecule experiments even the decay rate of ^3Car at cryogenic temperatures is almost a factor of 10 lower than the excitation rate of 10^6 s^{-1} [16]. When the low energy chlorophylls in CP47 and CP43 itself are kept in the triplet state due to the high photon flux directed to the traps, the emission of these lowest lying states (e.g. F695) will be drastically reduced in the single-molecule experiment. Alternatively, it is quite possible that chlorophylls in the vicinity of the low energy states are predominantly in the triplet state. ^3Chl is also known to be an efficient quencher of the excitation energy [44], i.e. the emission of the low energy states might be quenched and their contribution to the fluorescence spectrum might be significantly reduced. Nevertheless, emission lines are observed in the respective spectral region; as a consequence photodamage of these chromophores can be ruled out by our single-molecule data.

As a consequence, the accumulation of triplet states in CP47 and CP43 holds the potential to change the shape of the emission spectra remarkably. In future experiments, the difference between the shape of the single-molecule average spectrum and the ensemble spectra will be used to determine the spectral characteristics of the emitters that undergo triplet formation.

The strongest reduction of the emission intensity is found for the contribution assigned to CP47 (Fig. 3). The most likely candidate for the low energy trap in CP47 is Chl29. Chl29 is located at the outside of PS II far away from the RC. At ambient conditions, the excitation transferred to Chl29 can easily be transferred back to the RC. It is interesting, why the lowest energy trap in PS II is located at the edge of PS II. One reason might be that Chl29 is a member of an additional quenching site formed by the whole photosynthetic unit including the peripheral light-harvesting complexes CP26, CP29 and LHC II. In the architecture of PS II supercomplexes of higher plants a small distance

between CP29 and CP47 was found [45]. A small distance between CP29 and CP47 could allow for efficient energy transfer between them [32].

4. Conclusion

A combination of absorption, fluorescence and low temperature single-molecule spectroscopy was used to investigate the spectral properties, heterogeneities and dynamics of the fluorescence emission of intact PS II cc from *T. elongatus*. At the ensemble level, the absorption and fluorescence spectra show a temperature dependence similar to plant PS II.

With single-molecule techniques, we are able to observe individual PS II cc. The emission spectra of these individual complexes are dominated by ZPLs showing dynamic site-energy changes. The ZPLs can be assigned to F685, F689 and F695. It is not sufficient to explain the observed spectra by assuming only one lowest trap. Single-molecule spectroscopy is especially helpful in assigning the components in the emission of PS II, because the inhomogeneous broadenings of CP43 and CP47 are responsible for the complex temperature dependence of the absorption and emission spectra of PS II. The observed spectral dynamics of ZPLs (site-energy changes) have remarkable effects on the excitation energy transfer and trapping between CP43, CP47 and the RC.

The average emission spectrum based on single PS II cc dimers shows a reduced intensity of F695 compared to reported ensemble data. The deviation can be explained by quenching of fluorescence by triplet states accumulated on Car or the red-most Chl*a* molecules like on Chl29 in CP47 induced by the excitation laser light.

Acknowledgement

This work was supported by the Heisenberg-Programm of the Deutsche Forschungsgemeinschaft DFG (BR 4102/1-1 and BR 4102/2-1) and by the DFG within the framework of the cluster of excellence on unifying Concepts in catalysis (UniCat) project B1, coordinated by the TU Berlin and Sfb 1078, project A5 (A.Z.).

References

[1] F. Rappaport, B.A. Diner, Primary photochemistry and energetics leading to the oxidation of the $(Mn)_4Ca$ cluster and to the evolution of molecular oxygen in photosystem II, Coord. Chem. Rev. 252 (3–4) (2008) 259–272.
[2] T. Renger, E. Schlodder, Optical properties, excitation energy and primary charge transfer in photosystem II: theory meets experiment, J. Photochem. Photobiol. B 104 (1–2) (2011) 126–141.
[3] Y. Umena, K. Kawakami, J.R. Shen, N. Kamiya, Crystal structure of oxygen-evolving photosystem II at a resolution of 1.9 Å, Nature 473 (7345) (2011) 55–60.
[4] A. Guskov, J. Kern, A. Gabdulkhakov, M. Broser, A. Zouni, W. Saenger, Cyanobacterial photosystem II at 2.9-angstrom resolution and the role of quinones, lipids, channels and chloride, Nat. Struct. Mol. Biol. 16 (3) (2009) 334–342.
[5] E.J.G. Peterman, H. van Amerongen, R. van Grondelle, J.P. Dekker, The nature of the excited state of the reaction center of photosystem II of green plants: A high-resolution fluorescence spectroscopy study, Proc. Natl. Acad. Sci. U.S.A. 95 (11) (1998) 6128–6133.
[6] M.L. Groot, R.N. Frese, F.L. de Weerd, K. Bromek, A. Pettersson, E.J.G. Peterman, I.H.M. van Stokkum, R. van Grondelle, J.P. Dekker, Spectroscopic properties of the CP43 core antenna protein of photosystem II, Biophys. J. 77 (6) (1999) 3328–3340.
[7] F.L. de Weerd, M.A. Palacios, E.G. Andrizhiyevskaya, J.P. Dekker, R. van Grondelle, Identifying the lowest electronic states of the chlorophylls in the CP47 core antenna protein of photosystem II, Biochemistry 41 (51) (2002) 15224–15233.
[8] J.L. Hughes, B.J. Prince, S.P. Arskold, E. Krausz, R.J. Pace, R. Picorel, M. Seibert, Photo-conversion of chlorophylls in higher-plant CP43 characterized by persistent spectral hole burning at 1.7 K, J. Lumin. 108 (1–4) (2004) 131–136.
[9] J.L. Hughes, B.J. Prince, E. Krausz, P.J. Smith, R.J. Pace, H. Riesen, Highly efficient spectral hole-burning in oxygen-evolving photosystem II preparations, J. Phys. Chem. B 108 (29) (2004) 10428–10439.
[10] E. Krausz, J.L. Hughes, P.J. Smith, R.J. Pace, S.P. Arskold, Assignment of the low-temperature fluorescence in oxygen-evolving photosystem II, Photosynth. Res. 84 (1–3) (2005) 193–199.
[11] E.G. Andrizhiyevskaya, A. Chojnicka, J.A. Bautista, B.A. Diner, R. van Grondelle, J.P. Dekker, Origin of the F685 and F695 fluorescence in photosystem II, Photosynth. Res. 84 (1–3) (2005) 173–180.
[12] M. Komura, Y. Shibata, S. Itoh, A new fluorescence band F689 in photosystem II revealed by picosecond analysis at 4–77 K: function of two terminal energy sinks F689 and F695 in PSII, Biochim. Biophys. Acta Bioenerg. 1757 (12) (2006) 1657–1668.
[13] G. Raszewski, B.A. Diner, E. Schlodder, T. Renger, Spectroscopic properties of reaction center pigments in photosystem II core complexes: revision of the multimer model, Biophys. J. 95 (1) (2008) 105–119.
[14] N.C. Dang, V. Zazubovich, M. Reppert, B. Neupane, R. Picorel, M. Seibert, R. Jankowiak, The CP43 proximal antenna complex of higher plant photosystem II revisited: modeling and hole burning study. I, J. Phys. Chem. B 112 (32) (2008) 9921–9933.
[15] B. Neupane, N.C. Dang, K. Acharya, M. Reppert, V. Zazubovich, R. Picorel, M. Seibert, R. Jankowiak, Insight into the electronic structure of the CP47 antenna protein complex of photosystem II: hole burning and fluorescence study, J. Am. Chem. Soc. 132 (12) (2010) 4214–4229.
[16] M.L. Groot, E.J.G. Peterman, I.H.M. van Stokkum, J.P. Dekker, R. van Grondelle, Triplet and fluorescing states of the CP47 antenna complex of photosystem-II studied as a function of temperature, Biophys. J. 68 (1) (1995) 281–290.
[17] P. Tamarat, A. Maali, B. Lounis, M. Orrit, Ten years of single-molecule spectroscopy, J. Phys. Chem. A 104 (1) (2000) 1–16.
[18] H.P. Lu, X.S. Xie, Single-molecule spectral fluctuations at room temperature, Nature 385 (6612) (1997) 143–146.
[19] D. Rutkauskas, V. Novoderezhkin, R.J. Cogdell, R. van Grondelle, Fluorescence spectroscopy of conformational changes of single LH2 complexes, Biophys. J. 88 (1) (2005) 422–435.
[20] F. Schleifenbaum, C. Blum, V. Subramaniam, A.J. Meixner, Single-molecule spectral dynamics at room temperature, Mol. Phys. 107 (18) (2009) 1923–1942.
[21] Y. Berlin, A. Burin, J. Friedrich, J. Köhler, Low temperature spectroscopy of proteins. part II: experiments with single protein complexes, Phys. Life Rev. 4 (1) (2007) 64–89.
[22] C. Hofmann, T.J. Aartsma, H. Michel, J. Köhler, Direct observation of tiers in the energy landscape of a chromoprotein: a single-molecule study, Proc. Natl. Acad. Sci. U.S.A. 100 (26) (2003) 15534–15538.
[23] M. Brecht, H. Studier, A.F. Elli, F. Jelezko, R. Bittl, Assignment of red antenna states in photosystem I from *Thermosynechoccocus elongatus* by single-molecule spectroscopy, Biochemistry 46 (3) (2007) 799–806.
[24] M. Brecht, H. Studier, V. Radics, J.B. Nieder, R. Bittl, Spectral diffusion induced by proton dynamics in pigment–protein complexes, J. Am. Chem. Soc. 130 (2008) 17487–17493.
[25] A.R. Faro, V. Adam, P. Carpentier, C. Darnault, D. Bourgeois, E. de Rosny, Low-temperature switching by photoinduced protonation in photochromic fluorescent proteins, Photochem. Photobiol. Sci. 9 (2) (2010) 254–262.
[26] M. Brecht, V. Radics, J.B. Nieder, R. Bittl, Protein dynamics-induced variation of excitation energy transfer pathways, Proc. Natl. Acad. Sci. U.S.A. 106 (29) (2009) 11857–11861.
[27] T.P.J. Kruger, C. Ilioaia, L. Valkunas, R. van Grondelle, Fluorescence intermittency from the main plant light-harvesting complex: sensitivity to the local environment, J. Phys. Chem. B 115 (18) (2011) 5083–5095.
[28] J. Kern, B. Loll, C. Luneberg, D. DiFiore, J. Biesiadka, K.D. Irrgang, A. Zouni, Purification, characterisation and crystallisation of photosystem II from *Thermosynechococcus elongatus* cultivated in a new type of photobioreactor, Biochim. Biophys. Acta Bioenerg. 1706 (1-2) (2005) 147–157.
[29] M. Hussels, A. Konrad, M. Brecht, Confocal sample-scanning microscope for single-molecule spectroscopy and microscopy with fast sample exchange at cryogenic temperatures, Rev. Sci. Instrum. 83 (2012) 123706.
[30] B. Loll, J. Kern, W. Saenger, A. Zouni, J. Biesiadka, Towards complete cofactor arrangement in the 3.0 Angstrom resolution structure of photosystem II, Nature 438 (7070) (2005) 1040–1044.
[31] G. Raszewski, T. Renger, Light harvesting in photosystem II core complexes is limited by the transfer to the trap: can the core complex turn into a photoprotective mode? J. Am. Chem. Soc. 130 (13) (2008) 4431–4446.
[32] Y. Shibata, S. Nishi, K. Kawakami, J.R. Shen, T. Renger, Photosystem II does not possess a simple excitation energy funnel: time-resolved fluorescence spectroscopy meets theory, J. Am. Chem. Soc. 135 (2013) 6903–6914.
[33] M. Brecht, V. Radics, J.B. Nieder, H. Studier, R. Bittl, Red antenna states of photosystem I from Synechocystis PCC 6803, Biochemistry 47 (20) (2008) 5536–5543.
[34] M. Brecht, Spectroscopic characterization of photosystem I at the single-molecule level, Mol. Phys. 107 (2009) 1955–1974.
[35] E. Krausz, J.L. Hughes, P. Smith, R. Pace, S.P. Arskold, Oxygen-evolving photosystem II core complexes: a new paradigm based on the spectral identification of the charge-separating state, the primary acceptor and assignment of low-temperature fluorescence, Photochem. Photobiol. Sci. 4 (9) (2005) 744–753.
[36] M. Hussels, M. Brecht, Effect of glycerol and PVA on the conformation of photosystem I, Biochemistry 50 (18) (2011) 3628–3637.
[37] J.P. Dekker, A. Hassoldt, A. Pettersson, H. van Roon, M.L. Groot, R. van Grondelle, On the nature of the F695 and F685 emission of photosystem II, photosynthesis: from light to biosphere, 1 (1995) 53–56.
[38] B. Hillmann, E. Schlodder, Electron-transfer reactions in photosystem-II core complexes from Synechococcus at low-temperature—difference spectrum of P680(+) Q(a)(−)/P680 Q(a) at 77 K, Biochim. Biophys. Acta Bioenerg. 1231 (1) (1995) 76–88.

[39] S. Okayama, W.L. Butler, The influence of cytochrome b 559 on the fluorescence yield of chloroplasts at low temperature, Biochim. Biophys. Acta Bioenerg. 267 (3) (1972) 523–529.
[40] F. Müh, M. Cetin, E. Schlodder, Temperature dependence of fluorescence induction in photosystem II core complexes from *Thermosynechococcus elongatus*, in: A. van der Est, D. Bruce (Eds.), Proceedings of the 13th International Congress of Photosynthesis in Montreal, Canada, International Society of Photosynthesis, 2005, pp. 309–311, (Vol.).
[41] R.H. Schweitzer, G.W. Brudvig, Fluorescence quenching by chlorophyll cations in photosystem II, Biochemistry 36 (38) (1997) 11351–11359.
[42] R. Steffen, H.J. Eckert, A.A. Kelly, P. Dormann, G. Renger, Investigations on the reaction pattern of photosystem II in leaves from *Arabidopsis thaliana* by time-resolved fluorometric analysis, Biochemistry 44 (9) (2005) 3123–3133.
[43] F. Müh, T. Renger, A. Zouni, Crystal structure of cyanobacterial photosystem II at 3.0 Å resolution: a closer look at the antenna system and the small membrane-intrinsic subunits, Plant Physiol. Biochem. 46 (3) (2008) 238–264.
[44] E. Schlodder, M. Cetin, M. Byrdin, I.V. Terekhova, N.V. Karapetyan, P700(+)- and (3) P700-induced quenching of the fluorescence at 760 nm in trimeric photosystem I complexes from the cyanobactenium *Arthrospira platensis*, Biochim. Biophys. Acta Bioenerg. 1706 (1-2) (2005) 53–67.
[45] S. Caffarri, R. Kouril, S. Kereiche, E.J. Boekema, R. Croce, Functional architecture of higher plant photosystem II supercomplexes, EMBO J. 28 (19) (2009) 3052–3063.

Chapter 2: Variation of Exciton-Vibrational Coupling in Photosystem II Core Complexes from *Thermosynechococcus elongatus* as Revealed by Single-Molecule Spectroscopy

In this chapter, using the results from single-molecule experiments of PSIIcc at low temperature, we show that the sharp ZPLs present in the emission spectra of single dPSII are the result of weak to intermediate exciton-vibrational coupling and slow spectral diffusion. To overcome the effect of spectral diffusion for a selected number of the lines, shifting algorithm has been used [131, 132]. As a result, the resolved emission profiles of single emitters become visible and the Huang-Rhys factor S can be determined with high accuracy. The dimensionless factor S is a measure for the linear exciton-vibrational coupling strength and characterizes the average number of vibrational quanta excited during a particular electronic transition [62]. The S values vary between 0.03 and 0.8. Most of the ZPLs occurred at 685±1 nm and their mean S value is 0.3, in agreement with hole-burning spectra on isolated CP43 complexes, which were analyzed assuming a single S-value [133, 134]. The lowest Huang-Rhys factor of a single dPSIIcc is $S = 0.03\pm0.0$ at 693.2±2.1 nm and the highest is $S = 0.8\pm0.1$ at 686.8±0.7 nm.

The values of the Huang-Rhys factors show no obvious correlation between coupling strength and wavelength position. From this result, we conclude that electrostatic, rather than exchange or dispersive interactions are the main contributors to the exciton-vibrational coupling in this system. This chapter is adapted from the paper in ref. [126].

THE JOURNAL OF PHYSICAL CHEMISTRY B

Article

pubs.acs.org/JPCB

Variation of Exciton-Vibrational Coupling in Photosystem II Core Complexes from *Thermosynechococcus elongatus* As Revealed by Single-Molecule Spectroscopy

Sepideh Skandary,[†] Martin Hussels,[†] Alexander Konrad,[†] Thomas Renger,[‡] Frank Müh,[‡] Martin Bommer,[§] Athina Zouni,[§] Alfred J. Meixner,[†] and Marc Brecht*[,†,∥]

[†]IPTC and Lisa+ Center, Universität Tübingen, Tübingen, Germany

[‡]Institut für Theoretische Physik, Johannes Kepler Universität, Linz, Austria

[§]Institut für Biologie, Humboldt Universität zu Berlin, Berlin, Germany

[∥]Zurich University of Applied Science Winterthur (ZHAW), Winterthur, Switzerland

Supporting Information

ABSTRACT: The spectral properties and dynamics of the fluorescence emission of photosystem II core complexes are investigated by single-molecule spectroscopy at 1.6 K. The emission spectra are dominated by sharp zero-phonon lines (ZPLs). The sharp ZPLs are the result of weak to intermediate exciton-vibrational coupling and slow spectral diffusion. For several data sets, it is possible to surpass the effect of spectral diffusion by applying a shifting algorithm. The increased signal-to-noise ratio enables us to determine the exciton-vibrational coupling strength (Huang–Rhys factor) with high precision. The Huang–Rhys factors vary between 0.03 and 0.8. The values of the Huang–Rhys factors show no obvious correlation between coupling strength and wavelength position. From this result, we conclude that electrostatic rather than exchange or dispersive interactions are the main contributors to the exciton-vibrational coupling in this system.

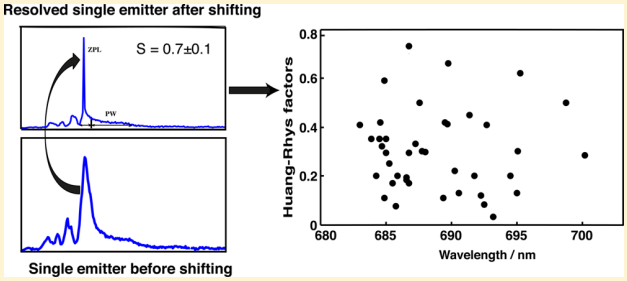

In photosynthetic light-harvesting complexes (also termed antenna proteins), an intricate interplay between different pigment molecules is responsible for light absorption and efficient excitation energy transfer (EET) to the reaction center (RC).[1,2] In oxygenic photosynthesis of cyanobacteria, green algae, and higher plants, the harvested energy is used to oxidize water and reduce plastoquinone in a membrane-embedded pigment–protein complex (PPC) called photosystem II (PSII).[3,4] The functional unit of PSII is a core complex (PSIIcc) that forms dimers (dPSIIcc), which in turn assemble into rows in cyanobacteria[5,6] or are part of a supercomplex with peripheral antennae in higher plants.[7,8] PSIIcc contains, besides the RC, two core antenna subunits referred to as CP43 and CP47 which are responsible for ultimately transferring the excitation energy to the RC, where the charge separation is initiated.[9−12] To understand EET in these systems, it is necessary to know the electronic energy levels of the involved, coupled chlorophyll (Chl) *a* pigments and the interactions of the electronic transitions with vibrational motions of the PPC.[13−15] Important information is obtained from the spectral properties of the fluorescence emitters of the antenna system.[16−18] The fluorescence spectrum of dPSIIcc exhibits a complicated temperature dependence in both plants[18,19] and cyanobacteria.[12,20] Both cases are characterized by a fluorescence maximum at 685 nm at higher temperatures (above 140 K) and the emergence of a second 695 nm fluorescence peak upon cooling down to 77 K. Further cooling reduces the intensity at 695 nm, so that mainly one peak at 685 nm is left at around 4 K. This complex behavior was explained[12] in terms of two distinct pools of Chls, F685 and F695, emitting at different wavelengths and both absorbing at lower wavelengths than the primary electron donor state in the RC. Therefore, these Chls are referred to as red-absorbing or red Chls. Whereas F695 carries the oscillator strength of one Chl, F685 has a larger oscillator strength due to a delocalized exciton state. At 4 K the fluorescence maximum is determined by the state with the higher oscillator strength, i.e., F685. Upon increasing the temperature, EET from F685 to the RC and subsequent quenching by electron transfer sets in and thereby diminishes the fluorescence intensity of this state. Since energy transfer from F695 is frozen out below 77 K, this state is still fully fluorescent and the fluorescence maximum shifts to the red between 4 and 77 K.[12] Note that isolated CP47 complexes do not show such a behavior, since no EET to the RC and subsequent quenching by electron transfer is possible. Instead,

Received: October 22, 2014
Revised: February 20, 2015
Published: February 24, 2015

DOI: 10.1021/jp510631x
J. Phys. Chem. B 2015, 119, 4203−4210

in isolated intact[21] CP47 complexes, the position of the fluorescence maximum was shown[22] to remain constant at 695 nm for $T \leq 75$ K and to move to shorter wavelengths at higher temperatures due to thermal population of higher exciton states.

Besides F685 and F695, a third emitter was identified in plant material, termed F689, that can be detected only in time-resolved fluorescence experiments below 77 K.[23] F685 was assigned to Chls in CP43,[24] whereas F695 was assigned to Chls in CP47.[24−26] Two tentative models assigned F689 to either CP43 or CP47 and left open the possibility that Chls of CP47 contribute to F685.[23] Similar assignments were made on the basis of theoretical studies aimed at the description of a variety of spectroscopic properties of dPSIIcc.[9,12] Reports using excitation-dependent fluorescence line narrowing (FLN)[17] and picosecond time-resolved fluorescence spectroscopy[23] at low temperatures showed inhomogeneous widths of the red chlorophyll bands, where different contributions showed strong overlap. The energy landscape of the CP43 protein was investigated with spectral hole-burning (SHB) and hole-recovery experiments in combination with thermocycling,[27] revealing distribution functions for the barrier heights separating different conformational substates of the protein. So far, these experiments were interpreted by assuming a single value for the Huang−Rhys factor S characterizing the strength of the exciton-vibrational coupling. In the present work, we want to investigate whether not only the electronic transition energy of a protein-bound pigment in PSIIcc but also its coupling to the protein vibrations can vary along the energy landscape of the protein. For Chl *a* in an organic glass and LH2 complexes of purple bacteria, such a variation was reported in combined hole burning, fluorescence line narrowing,[28] and in single molecule spectroscopy (SMS).[29]

SMS is an excellent technique to cope with inhomogeneous spectral widths and reveals subtle spectral details often obscured by averaging over heterogeneous ensembles.[30,31] At room temperature, spectral diffusion and photobleaching hamper the collection of detailed spectroscopic information for most single molecules.[32−35] Lowering the temperature reduces the impact of spectral diffusion,[35−37] and the emission profile of a single emitter composed of a sharp zero-phonon line (ZPL) and a so-called phonon wing (PW) becomes observable.[28,38−40] The ZPL belongs to pure electronic transitions. The PW on the low-energy side of the ZPL belongs to electronic transitions with excitations of vibrational quanta. This coupling is due to the interaction of the chromophore with its surrounding. The ZPL and PW can only be distinguished at low temperatures because of the temperature dependence of the homogeneous lineshape causing the PW to mask the zero-phonon contributions completely at temperatures above 100 K. The ratio between the intensity of the ZPL and PW depends on the strength of exciton-vibrational coupling expressed by the Huang−Rhys factor (S).[41−43] The dimensionless factor S is a measure for the linear exciton-vibrational coupling strength and characterizes the average number of vibrational quanta excited during a particular electronic transition.[44]

Even at low temperatures, the spectral properties of protein bound chromophores depend on time. The time dependence concerns the emission wavelength, intensity, exciton-vibrational coupling, and rate of spectral diffusion.[45,46] The most obvious effect visible in the spectra of single chromophores is spectral diffusion. The fluctuations of the site energy cause spectral jumps extending into the range of several nanometers.[45,46]

The ZPL and PW can be observed in time-dependent spectra series if the rate of spectral diffusion is smaller than the rate of data acquisition, whereas a complete broadening of the ZPLs results if the rate of spectral diffusion surpasses the rate of data acquisition.

In this study, we investigate the spectroscopic properties of dPSIIcc from *Thermosynechoccocus elongatus* at low temperature (1.6 K) at the single-complex level. All recorded fluorescence spectra series consist of sharp ZPLs that cover the whole emission range. We were able to overcome the effect of spectral diffusion for a selected number of lines using a shifting algorithm.[47,48] As a result, the resolved emission profiles of single emitters become visible and the Huang−Rhys factor S can be determined with high accuracy.

MATERIALS AND METHODS

Sample Preparation. Preparation and crystallization of dPSIIcc from *T. elongatus* are described elsewhere.[49] Extensive biochemical characterization of dPSIIcc are summarized in ref 50. For single-molecule spectroscopy redissolved crystals in buffer solution containing 100 mM PIPES (pH 7.0), 5 mM $CaCl_2$, 0.5 M betaine, and 0.03% β-DM showing high oxygen evolution activity were used.[49] The final dPSIIcc concentration was ∼3 pM. For single-molecule experiments less than 1 μL of the sample was sandwiched between two coverslips. Finally, the sample was transferred directly into the cryostat and rapidly plunged into liquid helium. Experiments were carried out using a home-built confocal microscope operating at 1.6 K as described recently.[51] A 665 nm CW diode laser set to 100 μW emission power was used to record spectra series with 100 spectra per data set.

Data Evaluation Process. Two algorithms have been used to evaluate the data sets. Both are implemented using the MATLAB software package. The first algorithm uses smoothing and filtering to detect spectral positions of ZPLs in spectra series and is described in ref 48. By applying it to all data sets a ZPL histogram has been achieved, which is discussed in the Results section.

The second algorithm is useful to overcome the broadening of spectra of single emitters, which are affected by spectral diffusion, for long accumulation times. It works on time-dependent spectra series where the position of the maximum intensity of an emitter is detected in a user-selected wavelength range. Then the single spectra are shifted in a circular manner that the intensity maxima are at the same position. Circular shifting means data points shifted out of the matrix boundaries are moved to the opposite end of the matrix. In the next step the shifted spectra are summed up, giving a spectrum of the single emitter with better signal-to-noise ratio. Finally, a linear baseline correction is applied. To achieve highly resolved single emitter profiles, the shifting wavelength range is selected around the ZPL and the PW, and single spectra showing low intensity or multiple positions of the single emitter are excluded.

To determine the Huang−Rhys factor the intensities of the ZPL, I_{ZPL}, and the PW, I_{PW}, are calculated by numerical integration and the Huang−Rhys factor, S, is obtained by

$$e^{-S} = \frac{I_{ZPL}}{I_{ZPL} + I_{PW}} \quad (1)$$

DOI: 10.1021/jp510631x
J. Phys. Chem. B 2015, 119, 4203−4210

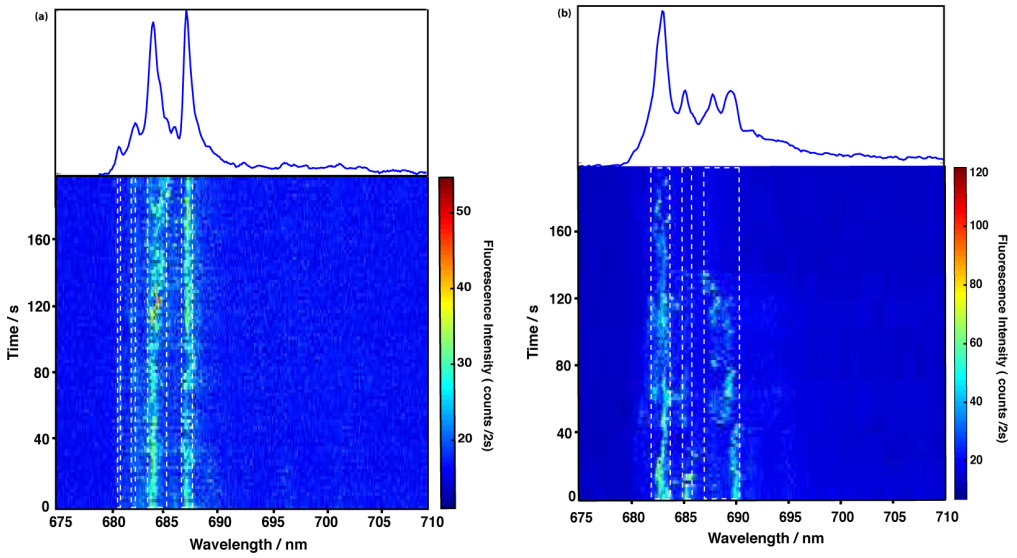

Figure 1. Fluorescence emission spectra of two individual dPSIIcc at low temperature (1.6 K). In both cases, 100 fluorescence emission spectra with an accumulation time of 2 s for each spectrum were recorded subsequently (λ_{exc} = 665 nm). The fluorescence intensity is color-coded (see color code to the right side of each graph). The confined spectral positions of the ZPLs are indicated by the white dashed lines. The average spectrum (on top) is obtained by summation of all spectra in one data set.

RESULTS

Individual dPSIIcc were detected by low temperature confocal microscopy.[20] Figure 1 shows two examples of the time-dependent fluorescence emission of single dPSIIcc. The data set shown in Figure 1a shows four ZPLs. Two sharp and relatively stable ZPLs at 684 and 687.5 nm can be found in the spectra series and the average spectrum, whereas the two weak ZPLs at 681 and 682.4 nm are hardly visible due to their low S/N ratio in time-dependent spectra series. In the data set shown in Figure 1b, one intense ZPL at 683 nm and two weaker ZPLs at 685.4 and 689.3 nm are observable. The first ZPL at 683 nm is relatively stable during the whole series, whereas the two other ZPLs at 685.4 and at 689.3 nm are distorted after 15 and 134 s, respectively. In the mean spectrum on top, the peak at 687.9 nm results from the ZPL which started at 689.3 nm.

ZPLs are clearly visible in all recorded spectra series in the wavelength range from 675 to 710 nm. They show dynamical variations of their spectral position and intensity, but their distribution as well as their time-dependent behavior varies from complex to complex. The variation of each ZPL position is confined to a certain spectral range as indicated by the white dashed lines in Figure 1. The width of this range was determined for clearly distinguishable ZPLs and is 2.5 ± 1.1 nm in the wavelength region from 680 to 705 nm.

The probability of finding a ZPL in a wavelength interval was evaluated for all measured spectra series. For this purpose, the spectral positions of the ZPLs were determined for all data sets by the first algorithm mentioned in the Materials and Methods section. Figure 2 shows the relative occurrence of ZPLs together with the average spectrum calculated for all data taken from single dPSIIcc during this study. The histogram shows the relative distribution of ZPL spectral positions as a function of wavelength between 675 and 710 nm. The ZPLs dominantly occurred in the range between 682 and 687 nm, which corresponds to the peak of the average spectrum with the maximum position at 684.7 nm, and their occurrence decreases at 689 to 701 nm. As it has been discussed in our previous report,[20] the amplitude of the fluorescence from the lowest

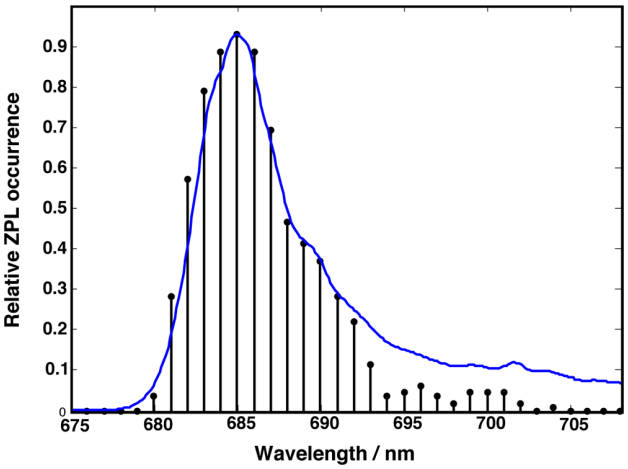

Figure 2. Comparison of the ZPL distribution (histogram) and the average emission spectrum for dPSIIcc. The average spectrum (solid line) represents the sum of all measured (142 data sets) emission spectra from single dPSIIcc at 1.6 K.

emitter F695 in PSIIcc is diminished in our SMS experiments, probably because of the accumulation of triplet states. At low temperatures, a significant part of the excitation is trapped on energetically low-lying antenna chlorophylls because uphill energy transfer to the reaction center is impossible. Because of the longer lifetime of the excited chlorophyll, the yield of fluorescence and triplet formation increases. Carotenoid triplets are formed subsequently by triplet−triplet transfer. The lifetime of Chl triplets decaying by triplet energy transfer to carotene is most likely in the submicrosecond domain.[52]

The determination of the Huang−Rhys factor requires the intensity of the ZPL, I_{ZPL}, and PW, I_{PW}. Determining the position and intensity of ZPLs is straightforward because the whole intensity of a ZPL is emitted within a small spectral range. However, the PWs are less intense and spread over a broader wavelength range than ZPLs. As a consequence,

DOI: 10.1021/jp510631x
J. Phys. Chem. B 2015, 119, 4203−4210

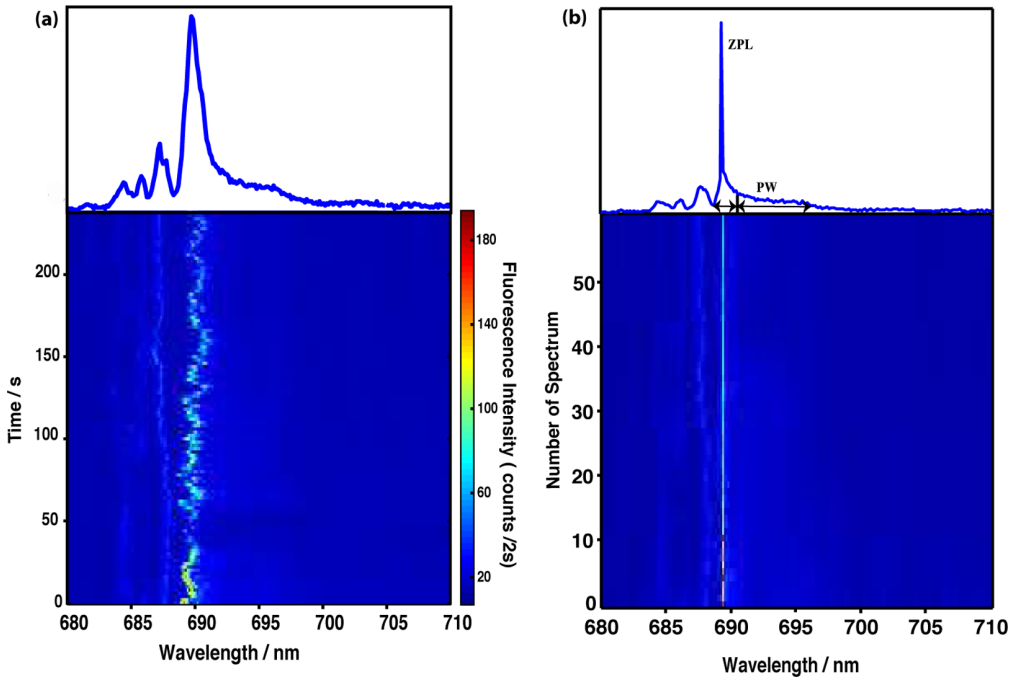

Figure 3. (a) Time-dependent fluorescence emission spectra of an individual dPSIIcc with 2 s time resolution. The average spectrum is given on top. (b) The same data set as (a) after applying the shifting procedure. The bar in the top separates the ZPL and the PW, and the double arrows indicate the spectral range of ZPL and PW. For further details, see the Supporting Information. For the depicted single-emitter profile, we calculated $S = 0.7 \pm 0.1$ with the mean position of ZPL at 689.8 ± 1.2 nm.

determination of PWs is more sensitive to interference with other emitters and background noise; therefore, it is difficult to determine their position and intensity because spectra with good signal-to-noise ratio are needed.

The average spectrum of time-dependent spectra series does not allow us to determine the Huang–Rhys factor because of spectral diffusion leading to multiple peaks and broadening of the spectra as can be seen in Figure 1. It is possible to resolve a ZPL and its accompanying PW if the emission is stable and the background signals can be separated. For this purpose, the position of ZPL is determined for all time-dependent spectra series (see Figure 3). Then all spectra are shifted along the wavelength axis and to one common mean position. After shifting, the background signals are subtracted by applying linear baseline correction.

Figure 3a shows one of the selected time-dependent spectra series with the average spectrum on top. Four ZPLs at 684.5, 685.9, 687.3, and 689.8 nm can be distinguished. However, the only suitable ZPL for applying the shifting algorithm is at 689.8 nm (mean position) because there is no overlap with the other emitters. The wavelength range from 688 to 698 nm was selected for the shifting procedure. Figure 3b shows the series after the shifting, together with the average spectrum (on top). It should be noted that due to shifting along wavelength, the original wavelength scale changed and the time scale converts to number of spectrum. The line at 689.8 nm in Figure 3a changed to a well-resolved line in Figure 3b showing ZPL and pronounced PW with obviously enhanced resolution and signal-to-noise ratio. The signal strength of the individual spectra is too low to resolve the shape of the PW correctly. Using the nicely resolved single ZPL and corresponding PW, we are able to determine the Huang–Rhys factor, *S*. Because of spectral interference of ZPLs and PWs, Huang–Rhys factors are calculated for several estimated borders between positions of ZPLs and PWs, and that is the reason for the relatively large error of the *S* values. For the depicted single-emitter profile, it is $S = 0.7 \pm 0.1$ with the mean position of ZPL at 689.8 ± 1.2 nm.

All data sets were scanned for ZPLs suitable to apply our shifting procedure. Overall, 41 ZPLs were found where *S* could be determined. Figure 4 shows a 2D-scatter plot (*S* versus wavelength) of all 41 ZPLs. The histograms in Figure 4 show the amount of resolved ZPLs according to their wavelength and Huang–Rhys factor values. The distribution of the contribution over the wavelength is in a reasonable agreement with ZPL occurrence in Figure 2. The ZPLs are found in the range of 682–700 nm; the *S* values vary between 0.03 and 0.8. Most of

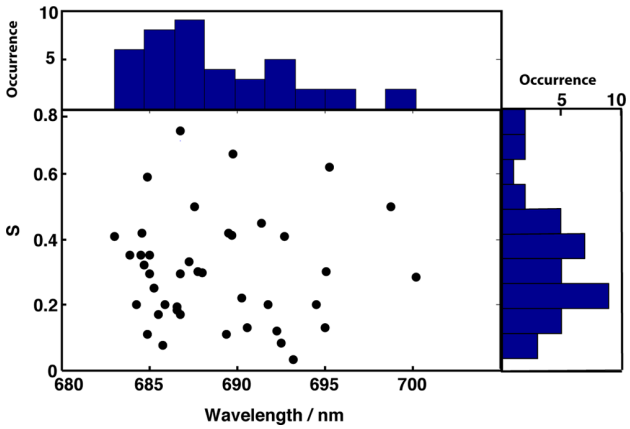

Figure 4. 2D-scatter plot of the wavelength-dependent distribution of the Huang–Rhys factor *S* for dPSIIcc. *S* was determined for 41 resolved emitters in 142 data sets of single dPSIIcc (for more details see text). For both dimensions, histograms are given additionally.

DOI: 10.1021/jp510631x
J. Phys. Chem. B 2015, 119, 4203–4210

the ZPLs occurred at 685 ± 1 nm, and their mean S value is 0.3, in agreement with hole-burning spectra on isolated CP43 complexes, which were analyzed assuming a single S-value.[27,53] Here, we have resolved the distribution of possible S-values of this state. We find a broad range of S-values for F685 as well as for the other emitting states, suggesting that the electron-vibrational coupling varies substantially along the multidimensional energy landscape of the protein. The lowest Huang–Rhys factor of a single dPSIIcc is $S = 0.03 \pm 0.01$ at 693.2 ± 2.1 nm, and the highest is $S = 0.8 \pm 0.1$ at 686.8 ± 0.7 nm (see Figure 4).

In contrast to earlier results obtained for the LH2 antenna of purple bacteria,[29] there is no obvious correlation between S and the ZPL emission wavelength except that the points are somewhat more crowded in the 685 nm region with $S < 0.4$ (Figure 4). One can find quite different values of S for the same ZPL position. For example, at 684.9 nm, we find $S = 0.11$ as well as $S = 0.59$. On the other hand, essentially the same value of S is found for ZPLs at different positions, e.g., $S = 0.35$ at 684.5 ± 1.2 and 683.9 ± 1.1 nm. In the range between 685 and 689 nm, the weakest exciton-vibrational coupling is $S = 0.07$ and the strongest $S = 0.8$. Nearly the same variation of exciton-vibrational coupling is found in the range between 690 and 700 nm with minimally $S = 0.03$ and maximally $S = 0.62$.

DISCUSSION

At 1.6 K the spectra are dominated by sharp ZPLs which are characteristic features of single molecules at low temperature. The ZPLs in the data sets of single dPSIIcc differ in their intensity and spectral positions (see Figure 1).

Multiple lines in different data sets can be the result of (i) spectral diffusion, (ii) static disorder, or (iii) different emitters.[20] (i) Most of the lines which are close to each other can be assigned to single emitters whose site energy changes due to dynamic variations as can be seen in Figure 1. Spectral diffusion is the main reason for variable shapes and positions of ZPLs observable in emission spectra of individual dPSIIcc. Mostly, spectral diffusion leads to time-dependent broadening of the emission (see Figure 1) and not to separated lines. (ii) Chlorophylls bound at the same site might have different transition energies. This includes the possibility that equivalent (symmetry-related) sites in the two dimer halves of dPSIIcc emit at different wavelengths. A Gaussian distribution is often used to describe the extent of static disorder within an ensemble with a fwhm of about 200 cm^{-1},[54] corresponding to about 10 nm wavelength range. (iii) Different low-energy traps corresponding to different Chls in dPSIIcc give rise to separated lines if the low-energy states are not connected to each other by efficient energy transfer leading rapidly to thermal equilibrium.

Stable ZPLs with small discrete jumps are observed (see Figure 1a) if the rate of spectral diffusion is in the range of the experimental accumulation time or slower (slow spectral diffusion). On the other hand, only broadened lines are visible if the rate of spectral diffusion is faster than the rate of data acquisition (fast spectral diffusion).[55]

Our shifting algorithm aims at a correction of the spectra for the effects of spectral diffusion to facilitate the determination of S. Clearly, the algorithm can only correct for the resolvable slow spectral diffusion, while the shifted spectra remain broadened by fast spectral diffusion. Nonetheless, by applying this procedure, we were able to determine the line shapes and Huang–Rhys factors for 41 individual emitters with high accuracy based on 142 recorded data sets.

Earlier analyses of bulk spectra suggest the presence of at least three different emitting entities, F685, F689, and F695,[9,12,23−26] corresponding to three different low-energy traps in dPSIIcc. This suggestion is supported by the present data; i.e., the ZPLs are distributed over a large wavelength range that can be divided roughly into three regions around 685, 689, and 695 nm, which might correspond to F685, F689, and F695, respectively. However, a clear-cut assignment of ZPLs to energy traps is not possible. An assignment would be facilitated by a correlation between ZPL position and S, but no such correlation is observed. There is merely a crowding of data points in the lower left corner of the scattering plot (Figure 4), suggesting that pigments contributing to F685 have preferentially a weak exciton-vibrational coupling (i.e., $S < 0.4$). This result is in agreement with hole-burning studies of isolated CP43 assigning $S \approx 0.3$ to the so-called A-state of CP43,[27,53] which likely corresponds (or at least contributes) to F685.[9]

The red-most state in dPSIIcc, i.e., F695, is assigned to the low-energy trap in CP47. This is proposed[9,10] to be due to Chl29 (in the nomenclature of Loll et al.[56]), but there are other assignments.[57] Hole-burning studies on isolated CP47 suggest this trap to have a relatively strong exciton-vibrational coupling with $S \approx 1.0$.[21] This is only partly in agreement with our results, since all our emitters, including those at low energies, where F695 is expected, have smaller S values. Hence, we have to conclude that we only see a nonrepresentative selection of ZPLs for the state F695 in our single-molecule experiments. As has been discussed in our previous publication,[20] the selection may occur due to the high excitation rate necessary for SMS. Triplet states could be accumulated at the low-energy state F695 of CP47, which, therefore, fluoresces less. It is expected that the Chl triplet states accumulating at F695 are quenched by nearby carotenoids to prevent photodamage that can occur if the triplet state of Chl is reacting with triplet oxygen to form the poisonous singlet oxygen. Of course, we cannot entirely exclude that such or other type of photodamage occurs. In this case, our interpretation of the data relies on the assumption that the photodamage stays local and, therefore, has no influence on the Huang–Rhys factors of the other low-energy sites, which is reasonable. It is an open question why the remaining emitters of F695 exhibit a weaker electron-vibrational coupling than the ensemble on average. It seems that the states with higher exciton-vibrational coupling can more easily undergo an intersystem crossing to the triplet state, probably because the excess energy can be better dissipated by the protein environment during the transition. Finally, we note that also the low-energy emitting states show a random variation of S values.

In contrast to the present data, positive correlations between the wavelength of the ZPL position and the Huang–Rhys factor were reported for the LH2 antenna of purple bacteria[29] and for Chl a in a glassy matrix of 1-propanol.[28] The question arises: Under which circumstances is there a correlation between the solvatochromic shift (i.e., the environment-induced shift of the ZPL position) of the transition energy of a pigment and the strength of the dynamic modulation of this transition energy by environmental vibrations (represented by S)? In the case of LH2, most likely the mixing between exciton states and interchromophore charge transfer (CT) states is responsible for the red-shift as well as for the enhanced electron-vibrational coupling. If the CT state is energetically

DOI: 10.1021/jp510631x
J. Phys. Chem. B 2015, 119, 4203−4210

above the exciton state, this mixing leads to a red-shift of the exciton state. The CT state borrows some oscillator strength from the exciton state, and the exciton state borrows some electron-vibrational coupling strength from the CT state.[58] Note that a CT state, due to its polar nature, exhibits a very strong electron-vibrational coupling.

In the case of Chl *a* in the organic glass, electrostatic as well as dispersive interactions are responsible for the electrochromic shift. Whereas the dispersive interaction, due to the higher polarizability of the excited state (with respect to the ground state) of the chromophore, leads to a red-shift of the transition energy, the electrostatic interaction can lead to both blue- and red-shifts.

As a general rule we expect a positive correlation between the red-shift and the Huang–Rhys factor, if a decrease in the distance between the chromophore and the environmental atoms (leading to an increase in the fluctuation of the transition energy) leads to a red-shift in the transition energy of the chromophore. In the case of the LH2 such a decrease in distance leads to an increase in wave function overlap and thereby to an increase in quantum-mechanic mixing between the exciton states and the CT state. In the case of Chl *a* in the organic glass, a decrease in distance leads to an increase in the dispersive interaction causing an electrochromic red-shift and/or an increase of the absolute magnitude of the electrostatic interaction, which may cause both a red- and blue-shift.

The latter aspect becomes important in proteins. As electrostatic calculations of static site energies and spectral densities of the dynamic pigment–protein coupling show, an electrochromic red-shift in general does not correlate with the Huang–Rhys factor, that is, the integral over the spectral density of the site energy fluctuations.[14,15] In principle, all scenarios are possible: anticorrelation, correlation, and no correlation. Since the electrostatic site energy shifts contain contributions of different signs, depending on the relative position of the charge density of the protein in the difference potential between excited and ground state of the chromophore, the different contributions may partially compensate each other in the static site energy. In contrast, if the charge density is varied in a correlated way (e.g., due to normal mode vibrations of the pigment–protein complex), one could well imagine that the different contributions add constructively in the dynamic modulation of the transition energy.

We, therefore, conclude that for the present system electrostatic interactions are responsible for the static and dynamic shifts of the transition energies of the low-energy exciton states.

The large scattering of the Huang–Rhys factor indicates that the respective Chls are exposed to a certain amount of variability in the interaction with their close surrounding. A measure to determine the flexibility of parts of a protein in the X-ray structure is given by the crystallographic *B*-factors. Figure 5 shows the *B*-factors of dPSIIcc. Chls 11, 48, and 49 show the largest *B*-factors in PSII (using the nomenclature of Loll et al.[56]). Among the Chls showing an increased *B*-factor is Chl29 of CP47. Chl29 seems to be responsible for the emission at 695 nm,[9,11,12,60] and Chl11 also is supposed to be red-shifted significantly.[9,12] Other studies assign Chl26 as the mostly red-shifted.[57] In the case of CP43, pigments with large red-shifts were proposed to be Chls 37, 43, and 45[9,12,61] or Chls 37 and 44.[62] There seems to be no correlation between these red-shifts and an increased *B*-factor. Irrespective of the preliminary character of these assignments, this seems to indicate that there

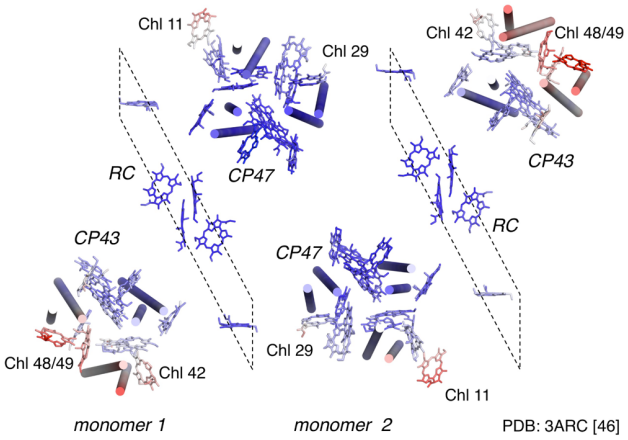

Figure 5. Distribution of the Debye–Waller factor (*B*-factor) for the Chl *a* in X-ray structure of dPSIIcc (PDB: 3ARC).[59] The averaged *B*-factors vary between 20 (colored deep blue) and 50 (deep red). Blue color indicates a small *B*-factor, and red indicates a high *B*-factor. Chl *a* molecules at the outer rim of dPSIIcc show an increased *B*-factor; one is Chl29 of CP47.

is no correlation between red-shift and Huang–Rhys factor, in agreement with our results.

Weak exciton-vibrational coupling strengths as observed here are common for photosynthetic antenna complexes.[63,64] Our SMS study gives uniquely detailed information on the exciton-vibrational coupling where it allows us to determine the Huang–Rhys factor accurately through the homogeneous broadened spectra, whereas SHB and FLN were so far interpreted by assuming a single *S*-value.[28,65,66]

It is encouraging to see that our average *S*-value for F685 ($S = 0.3$) agrees with the *S*-value inferred from SHB experiments on CP43 complexes,[27,53] where F685 is supposed to be located.[9,12] The underlying large variations of the individual *S*-values ($0.1 < S < 0.6$) for this state clearly show that the exciton-vibrational coupling of protein-bound pigments in PSII can vary substantially along the energy landscape of the protein. This result has implications also for the calculation of EET. So far, *S* was assumed to be constant, since no detailed information was available for PSII. In future calculations, it will be interesting to see how the energy transfer changes if a distribution of *S*-values is taken into account.

CONCLUSION

In summary, we have found that the electron-vibrational coupling of protein-bound pigments with low excitation energies in PSIIcc varies substantially. This conclusion can be drawn irrespectively of the accumulation of triplet states, which likely occurs under our experimental conditions and causes the mostly red-shifted emitters to be underrepresented. An implicit assumption in our analysis is that the presence of triplet states does not affect the variations of Huang–Rhys factors. Since these variations are not correlated with the emission wavelength, we conclude that electrostatic interactions are the main contributor to the electron-vibrational coupling in this system.

ASSOCIATED CONTENT

Supporting Information

Description of the algorithm to calculate *S* and the error in the evaluation of the *S*-factors are explained in detail. This material is available free of charge via the Internet at http://pubs.acs.org.

DOI: 10.1021/jp510631x
J. Phys. Chem. B 2015, 119, 4203–4210

AUTHOR INFORMATION

Corresponding Author

*Phone +49-7071-29-76239; Fax +49-7071-29-5490; e-mail marc.brecht@uni-tuebingen.de (M.B.).

Notes

The authors declare no competing financial interest.

ACKNOWLEDGMENTS

This work was supported by the Heisenberg-Program of the Deutsche Forschungsgemeinschaft DFG (BR 4102/1-1 and BR 4102/2-1), by the DFG within the framework of the cluster of excellence on unifying Concepts in catalysis (UniCat), project B1, coordinated by the TU Berlin, Sfb 1078, project A5 (A.Z.), HFSP RGP0063/2013, and by the Austrian Science Fund (FWF), project P24774-N27 (T.R.).

REFERENCES

(1) van Grondelle, R.; Novoderezhkin, V. I. Energy transfer in photosynthesis: experimental insights and quantitative models. *Phys. Chem. Chem. Phys.* **2006**, *8*, 793−807.

(2) Scholes, G. D.; Fleming, G. R.; Olaya-Castro, A.; van Grondelle, R. Lessons from nature about solar light harvesting. *Nat. Chem.* **2011**, *3*, 763−774.

(3) Müh, F.; Zouni, A. Light-induced water oxidation in photosystem II. *Front. Biosci.* **2011**, *16*, 3072−3132.

(4) Müh, F.; Zouni, A. Light-induced quinone reduction in photosystem II. *Biochim. Biophys. Acta* **2012**, *1817*, 44−65.

(5) Mörschel, E.; Schatz, G. H. Correlation of photosystem II complexes with exoplasmatic freeze-fracture particles of thylakoids of the cyanobacterium *Synechococcus-sp*. *Planta* **1987**, *172*, 145−154.

(6) Folea, I. M.; Zhang, P.; Aro, E.-M.; Boekema, E. J. Domain organization of photosystem II in membranes of the cyanobacterium *Synechocystis* PCC6803 investigated by electron microscopy. *FEBS Lett.* **2008**, *582*, 1749−1754.

(7) Dekker, J. P.; Boekema, E. J. Supramolecular organization of thylakoid membrane proteins in green plants. *Biochim. Biophys. Acta* **2005**, *1706*, 12−39.

(8) Caffarri, S.; Kouril, R.; Kereiche, S.; Boekema, E. J.; Croce, R. Functional architecture of higher plant photosystem II supercomplexes. *EMBO J.* **2009**, *28*, 3052−3063.

(9) Raszewski, G.; Renger, T. Light harvesting in photosystem II core complexes is limited by the transfer to the trap: can the core complex turn into a photoprotective mode? *J. Am. Chem. Soc.* **2008**, *130*, 4431−4446.

(10) Müh, F.; Renger, T.; Zouni, A. Crystal structure of cyanobacterial photosystem II at 3.0Å resolution: a closer look at the antenna system and the small membrane-intrinsic subunits. *Plant Physiol. Biochem.* **2008**, *46*, 238−264.

(11) Renger, T.; Schlodder, E. Optical properties, excitation energy and primary charge transfer in photosystem II: theory meets experiment. *J. Photochem. Photobiol., B* **2011**, *104*, 126−141.

(12) Shibata, Y.; Nishi, S.; Kawakami, K.; Shen, J. R.; Renger, T. Photosystem II does not possess a simple excitation energy funnel: time-resolved fluorescence spectroscopy meets theory. *J. Am. Chem. Soc.* **2013**, *135*, 6903−6914.

(13) Renger, T.; Marcus, R. A. On the relation of protein dynamics and exciton relaxation in pigment-protein complexes: an estimation of the spectral density and a theory for the calculation of optical spectra. *J. Chem. Phys.* **2002**, *116*, 9997−10019.

(14) Renger, T.; Klinger, A.; Steinecker, F.; Schmidt am Busch, M.; Numata, J.; Müh, F. Normal mode analysis of the spectral density of the Fenna-Matthews-Olson light-harvesting protein: how the protein dissipates the excess energy of excitons. *J. Phys. Chem. B* **2012**, *116*, 14565−14580.

(15) Renger, T.; Müh, F. Understanding photosynthetic light-harvesting: a bottom up theoretical approach. *Phys. Chem. Chem. Phys.* **2013**, *15*, 3348−3371.

(16) Groot, M. L.; Peterman, E. J. G.; van Stokkum, I. H. M.; Dekker, J. P.; van Grondelle, R. Triplet and fluorescing states of the CP47 antenna complex of photosystem II studied as a function of temperature. *Biophys. J.* **1995**, *68*, 281−290.

(17) Groot, M. L.; Frese, R. N.; de Weerd, F. L.; Bromek, K.; Pettersson, A.; Peterman, E. J. G.; van Stokkum, I. H. M.; van Grondelle, R.; Dekker, J. P. Spectroscopic properties of the CP43 core antenna protein of photosystem II. *Biophys. J.* **1999**, *77*, 3328−3340.

(18) Krausz, E.; Hughes, J. L.; Smith, P. J.; Pace, R. J.; Arsköld, S. P. Assignment of the low-temperature fluorescence in oxygen-evolving photosystem II. *Photosynth. Res.* **2005**, *84*, 193−199.

(19) Andrizhiyevskaya, E. G.; Chojnicka, A.; Bautista, J. A.; Diner, B. A.; van Grondelle, R.; Dekker, J. P. Origin of the F685 and F695 fluorescence in photosystem II. *Photosynth. Res.* **2005**, *84*, 173−180.

(20) Brecht, M.; Skandary, S.; Hellmich, J.; Glöckner, C.; Konrad, A.; Hussels, M.; Meixner, A.; Zouni, A.; Schlodder, E. Spectroscopic properties of photosystem II core complexes from *Thermosynechococcus elongatus* revealed by single-molecule experiments. *Biochim. Biophys. Acta* **2014**, *1837*, 773−781.

(21) Neupane, B.; Dang, N. C.; Acharya, K.; Reppert, M.; Zazubovich, V.; Picorel, R.; Seibert, M.; Jankowiak, R. Insight into the electronic structure of the CP47 antenna protein complex of photosystem II: hole burning and fluorescence study. *J. Am. Chem. Soc.* **2010**, *132*, 4214−4229.

(22) Acharya, K.; Neupane, B.; Reppert, M.; Feng, X.; Jankowiak, R. On the unusual temperature-dependent emission of the CP47 antenna protein complex of photosystem II. *J. Phys. Chem. Lett.* **2010**, *1*, 2310−2315.

(23) Komura, M.; Shibata, Y.; Itoh, S. A new fluorescence band F689 in photosystem II revealed by picosecond analysis at 4−77 K: function of two terminal energy sinks F689 and F695 in PSII. *Biochim. Biophys. Acta* **2006**, *1757*, 1657−1668.

(24) van Dorssen, R.; Breton, J.; Plijter, J.; Satoh, K.; van Gorkom, H.; Amesz, J. Spectroscopic properties of the reaction center and of the 47 kDa chlorophyll protein of photosystem II. *Biochim. Biophys. Acta* **1987**, *893*, 267−274.

(25) van Dorssen, R.; Plijter, J.; Dekker, J.; den Ouden, A.; Amesz, J.; Gorkom, H. Spectroscopic properties of chloroplast grana membranes and of the core of photosystem II. *Biochim. Biophys. Acta* **1987**, *890*, 134−143.

(26) Dekker, J. P.; Hassoldt, A.; Pettersson, A.; van Roon, H.; Groot, M. L.; van Grondelle, R. On the nature of the F695 and F685 emission of photosystem II. In *Photosynthesis: From Light to Biosphere*; Mathis, P., Ed.; Kluwer Academic Publishers: Dordrecht, The Netherlands, 1995; Vol. *1*, pp 53−56.

(27) Najafi, M.; Herascu, N.; Seibert, M.; Picorel, R.; Jankowiak, R.; Zazubovich, V. Spectral hole-burning, recovery and thermocycling in chlorophyll-protein complexes: distribution of barriers on the protein energy landscape. *J. Phys. Chem. B* **2012**, *116*, 11780−11790.

(28) Rätsep, M.; Pajusalu, M.; Freiberg, A. Wavelength-dependent electron-phonon coupling in impurity glasses. *Chem. Phys. Lett.* **2009**, *479*, 140−143.

(29) Kunz, R.; Timpmann, K.; Southall, J.; Cogdell, R. J.; Freiberg, A.; Köhler, J. Exciton self trapping in photosynthetic pigment-protein complexes studied by single-molecule spectroscopy. *J. Phys. Chem. B* **2012**, *116*, 11017−11023.

(30) van Oijen, A. M.; Ketelaars, M.; Köhler, J.; Aartsma, T. J.; Schmidt, J. Unraveling the electronic structure of individual photosynthetic pigment-protein complexes. *Science* **1999**, *285*, 400−402.

(31) Tamarat, P.; Maali, A.; Lounis, B.; Orrit, M. Ten years of single-molecule spectroscopy. *J. Phys. Chem. A* **2000**, *104*, 1−16.

(32) Lu, H. P.; Xie, X. S. Single-molecule spectral fluctuations at room temperature. *Nature* **1997**, *385*, 143−146.

(33) Rutkauskas, D.; Novoderezhkin, V. I.; Cogdell, R. J.; van Grondelle, R. Fluorescence spectroscopy of conformational changes of single LH2 complexes. *Biophys. J.* **2005**, *88*, 422−435.

(34) Schleifenbaum, F.; Blum, C.; Subramaniam, V.; Meixner, A. J. Single-molecule spectral dynamics at room temperature. *Mol. Phys.* **2009**, *107*, 1923−1942.

DOI: 10.1021/jp510631x
J. Phys. Chem. B 2015, 119, 4203−4210

(35) Berlin, Y.; Burin, A.; Friedrich, J.; Köhler, J. Low temperature spectroscopy of proteins. part II: experiments with single protein complexes. *Phys. Life Rev.* **2007**, *4*, 64−89.
(36) Shibata, Y.; Ishikawa, H.; Takahashi, S.; Morishima, I. Time-resolved hole-burning study on myoglobin: fluctuation of restricted water within distal pocket. *Biophys. J.* **2001**, *80*, 1013−1023.
(37) Hofmann, C.; Ketelaars, M.; Matsushita, M.; Michel, H.; Aartsma, T. J.; Köhler, J. Single-molecule study of the electronic couplings in a circular array of molecules: light-harvesting-2 complex from *Rhodospirillum molischianum*. *Phys. Rev. Lett.* **2003**, *90*, 013004.
(38) Huang, K.; Rhys, A. Theory of light absorption and non-radiative transitions in F-centres. *Proc. R. Soc. London, A* **1950**, *204*, 406−423.
(39) Pullerits, T.; Monshouwer, R.; van Mourik, F.; van Grondelle, R. Temperature-dependence of electron-vibronic spectra of photosynthetic systems-computer-simulations and comparison with experiment. *Chem. Phys.* **1995**, *194*, 395−407.
(40) Renge, I. Impurity spectroscopy in glasses and disordered crystals: inhomogeneous broadening and electron phonon coupling. *J. Lumin.* **2008**, *128*, 413−420.
(41) Rebane, K. K. *Impurity Spectra of Solids*; Plenum: New York, 1970.
(42) Personov, R. I. In *Spectroscopy and Excitation Dynamics of Condensed Molecular Systems*; Agranovich, V. M., Hochstrasser, R. M., Eds.; North Holland: Amsterdam, 1983; Chapter 10.
(43) Peterman, E. J. G.; Pullerits, T.; Grondelle, R.; Amerongen, H. Electron-phonon coupling and vibronic fine structure of light-harvesting complex II of green plants: temperature dependent absorption and high-resolution fluorescence spectroscopy. *J. Phys. Chem. B* **1997**, *101*, 4448−4457.
(44) Pieper, J.; Rätsep, M.; Irrgang, K. D.; Freiberg, A. Chromophore-chromophore and chromophore-protein interactions in monomeric light-harvesting complex II of green plants studied by spectral hole burning and fluorescence line narrowing. *J. Phys. Chem. B* **2009**, *113*, 10870−10880.
(45) Hofmann, C.; Aartsma, T. J.; Michel, H.; Köhler, J. Direct observation of tiers in the energy landscape of a chromoprotein: a single-molecule study. *Proc. Natl. Acad. Sci. U. S. A.* **2003**, *100*, 15534−15538.
(46) Brecht, M.; Hussels, M.; Schlodder, E.; Karapetyan, N. V. Red antenna states of photosystem I trimers from *Arthrospira platensis* revealed by single-molecule spectroscopy. *Biochim. Biophys. Acta* **2012**, *1817*, 445−452.
(47) Hofmann, C.; Michel, H.; van Heel, M.; Köhler, J. Multivariate analysis of single-molecule spectra: surpassing spectral diffusion. *Phys. Rev. Lett.* **2005**, *94*, 195501.
(48) Hussels, M.; Brecht, M. Effect of glycerol and PVA on the conformation of photosystem I. *Biochemistry* **2011**, *50*, 3628−3637.
(49) Kern, J.; Loll, B.; Luneberg, C.; DiFiore, D.; Biesiadka, J.; Irrgang, K. D.; Zouni, A. Purification, characterisation and crystallisation of photosystem II from *Thermosynechococcus elongatus* cultivated in a new type of photobioreactor. *Biochim. Biophys. Acta* **2005**, *1706*, 147−157.
(50) Zouni, A.; Kern, J.; Frank, J.; Hellweg, T.; Behlke, J.; Saenger, W.; Irrgang, K. Size determination of cyanobacterial and higher plant photosystem II by gel permeation chromatography, light scattering, and ultracentrifugation. *Biochemistry* **2005**, *44*, 4572−4581.
(51) Hussels, M.; Konrad, A.; Brecht, M. Confocal sample-scanning microscope for single-molecule spectroscopy and microscopy with fast sample exchange at cryogenic temperatures. *Rev. Sci. Instrum.* **2012**, *83*, 123706.
(52) Bittl, R.; Schlodder, E.; Geisenheimer, I.; Lubitz, W.; Cogdell, R. J. Transient EPR and absorption studies of carotenoid triplet formation in purple bacterial antenna complexes. *J. Phys. Chem. B* **2001**, *23*, 5525−5535.
(53) Herascu, N.; Najafi, M.; Amunts, A.; Pieper, J.; Irrgang, K.-D.; Picorel, R.; Seibert, M.; Zazubovich, V. Parameters of the protein energy landscapes of several light-harvesting complexes probed via spectra hole growth kinetics measurements. *J. Phys. Chem. B* **2011**, *115*, 2737−2747.
(54) Raszewski, G.; Diner, B. A.; Schlodder, E.; Renger, T. Spectroscopic properties of reaction center pigments in photosystem II core complexes: revision of the multimer model. *Biophys. J.* **2008**, *95*, 105−119.
(55) Brecht, M.; Studier, H.; Radics, V.; Nieder, J. B.; Bittl, R. Spectral diffusion induced by proton dynamics in pigment-protein complexes. *J. Am. Chem. Soc.* **2008**, *130*, 17487−17493.
(56) Loll, B.; Kern, J.; Saenger, W.; Zouni, A.; Biesiadka, J. Towards complete cofactor arrangement in the 3.0Å resolution structure of photosystem II. *Nature* **2005**, *438*, 1040−1044.
(57) Reppert, M.; Achary, K.; Neupane, B.; Jankowiak, R. Lowest electronic states of the CP47 antenna protein complex of photosystem II: simulation of optical spectra and revised structural assignments. *J. Phys. Chem. B* **2010**, *114*, 11884−11898.
(58) Renger, T. Theory of optical spectra involving charge transfer states: dynamic localization predicts a temperature dependent optical band shift. *Phys. Rev. Lett.* **2004**, *93*, 188101.
(59) Umena, Y.; Kawakami, K.; Shen, J. R.; Kamiya, N. Crystal structure of oxygen-evolving photosystem II at a resolution of 1.9Å. *Nature* **2011**, *473*, 55−60.
(60) de Weerd, F. L.; Palacios, M. A.; Andrizhiyevskaya, E. G.; Dekker, J. P.; van Grondelle, R. Identifying the lowest electronic states of the chlorophylls in the CP47 core antenna protein of photosystem II. *Biochemistry* **2002**, *41*, 15224−15233.
(61) Müh, F.; Madjet, M. E.; Renger, T. Structure-based simulation of linear optical spectra of the CP43 core antenna of photosystem II. *Photosynth. Res.* **2012**, *111*, 87−101.
(62) Reppert, M.; Zazubovich, V.; Dang, N. C.; Seibert, M.; Jankowiak, R. Low-energy chlorophyll states in the CP43 antenna protein complex: simulation of various optical spectra. II: simulation of optical spectra and revised structural assignments. *J. Phys. Chem. B* **2008**, *112*, 9934−9947.
(63) Reddy, N.; Lyle, P. A.; Small, G. J. Application of spectral hole burning spectroscopies to antenna and reaction center complexes. *Photosynth. Res.* **1992**, *31*, 167−194.
(64) Pieper, J.; Voigt, J.; Small, G. J. Chlorophyll *a* Franck-Condon factors and excitation energy transfer. *J. Am. Chem. Soc.* **1999**, *103*, 2319−2322.
(65) Pieper, J.; Voigt, J.; Renger, G.; Small, G. J. Analysis of phonon structure in line-narrowed optical spectra. *Chem. Phys. Lett.* **1999**, *310*, 296−302.
(66) Kikas, J. Effects of inhomogenety and site selective impurity-phonon coupling in solid solutions. *Chem. Phys. Lett.* **1987**, *57*, 511−513.

DOI: 10.1021/jp510631x
J. Phys. Chem. B 2015, 119, 4203−4210

Chapter 3: Role of Missing Carotenoid in Reducing the Fluorescence of Single Monomeric Photosystem II Core Complexes

The fluorescence of mPSIIcc from the cyanobacterium *T. elongatus*, originating from redissolved crystals, is investigated by using SMS at 1.6 K. The emission spectra of individual mPSIIcc are dominated by ZPLs, showing the existence of different emitters compatible with the F685, F689, and F695 bands. The intensity of F695 is reduced in single mPSIIcc as compared to single dPSIIcc. Crystal structures show that one of the β-Car cofactors located at the monomer-monomer interface in dPSIIcc is missing in mPSIIcc. This β-Car is in van-der-Waals distance to Chl17 in the CP47 subunit. We suggest that F695 is located at this Chl at the monomer-monomer interface. A loss of β-Car cofactors in mPSIIcc preparations will lead to an increased lifetime of the triplet state, which can explain the reduced singlet emission of F695 as observed in SMS. Here, the spectroscopic properties of single mPSIIcc and single dPSIIcc are compared and their differences are discussed. Combining this finding with chemical and crystallographic analyses of the samples, a proposal for the location of the F695 emitter in the structure of PSIIcc has been made.

This chapter is adapted from the manuscript, which is in preparation for submitting [135].

Journal Name

ARTICLE

Role of Missing Carotenoid in Reducing the Fluorescence of Single Monomeric Photosystem II Core Complexes

Received 00th January 20xx,
Accepted 00th January 20xx

DOI: 10.1039/x0xx00000x

www.rsc.org/

Sepideh Skandary [a], Frank Müh [b], Imran Ashraf [a], Mohamed Ibrahim [c], Michael Metzger [a], Athina Zouni [c], Alfred J. Meixner [a], and Marc Brecht. [a, d, e]

The fluorescence of monomeric photosystem II core complexes (mPSIIcc) of the cyanobacterium *Thermosynechococcus elongatus*, originating from redissolved crystals, is investigated by using single-molecule spectroscopy (SMS) at 1.6 K. The emission spectra of individual mPSIIcc are dominated by sharp zero-phonon lines, showing the existence of different emitters compatible with the F685, F689, and F695 bands reported formerly. The intensity of F695 is reduced in single mPSIIcc as compared to single PSIIcc-dimers (dPSIIcc). Crystal structures show that one of the β-carotene (β-Car) cofactors located at the monomer-monomer interface in dPSIIcc is missing in mPSIIcc. This β-Car in dPSIIcc is in van-der-Waals distance to chlorophyll (Chl) 17 in the CP47 subunit. We suggest that this Chl contributes to the F695 emitter. A loss of β-Car cofactors in mPSIIcc preparations will lead to an increased lifetime of the triplet state of Chl 17, which can explain the reduced singlet emission of F695 as observed in SMS.

1 Introduction

The photosystem II core complex (PSIIcc) is a light-driven water-plastoquinone-oxidoreductase, which is at the heart of oxygenic photosynthesis due to its ability to abstract electrons from water [1-4]. Several high-resolution crystal structures are available for dimeric PSIIcc (dPSIIcc) from the thermophilic cyanobacteria *Thermosynechococcus elongatus* (*T. elongatus*) [5-7] and *T. vulcanus* [8, 9]. In addition, Broser et al. [10] showed the first crystal structure of a highly active monomeric form of PSIIcc (mPSIIcc) from *T. elongatus*. This characterization together with a spectroscopic analysis revealed that in mPSIIcc 1.3 ± 0.2 β-carotene (β-Car) pigments per monomer are missing in mPSIIcc compared to dPSIIcc.

PSIIcc harbors the reaction center (RC), in which the light-induced electron transfer reactions take place [1] that result in water oxidation [3] and quinone reduction [2]. Besides, PSIIcc contains a core antenna system consisting of the subunits CP43 and CP47 (reviewed in ref. [11]) the purpose of which is to absorb light and funnel the excitation energy to the RC. Important information about this antenna system is obtained inter alia from fluorescence data. The fluorescence spectrum of dPSIIcc shows a complicated temperature dependence in both samples from cyanobacteria [12, 13] and higher plants, [14, 15] which was explained [12] by the existence of two distinct pools of chlorophylls (Chls), F685 and F695, that emit at different wavelengths and both absorb at lower energies than the primary donor state in the RC ("red Chls"). A third emitter was identified in plant material, termed F689, which can be detected only in time-resolved fluorescence experiments at temperatures below 77 K [16].

Several assignments of these emitters to CP43 and CP47 have been discussed in the literature [12, 15-23], but there is yet no consensus about the molecular identity of the emitting Chls. Reports employing excitation-dependent fluorescence line-narrowing [24] and picosecond time-resolved fluorescence spectroscopy [16] showed that the spectra of the various emitters are inhomogeneously broadened and strongly overlapping. The problem of ensemble averaging can be circumvented by SMS [25, 26]. However, at room temperature spectral diffusion and photo-bleaching obscure the observation of detailed spectroscopic information from most chromophores at the single-molecule level [27-31]. Lowering the temperature to less than 100 K reduces the impact of spectral diffusion [31, 32], and the emission profiles of single emitters become observable. The emission profile of a single chromophore is composed of a sharp zero-phonon line (ZPL) and a phonon-wing (PW) [33-38].

[a] *IPTC and LISA+ Center, University of Tübingen, Tübingen, Germany,*
[b] *Institute of Theoretical Physics, Johannes Kepler University Linz, Linz, Austria,*
[c] *Institute of Biology, Humboldt University of Berlin, Berlin, Germany,*
[d] *Reutlingen University, Process Analysis and Technology, Reutlingen, Germany*
[e] *E-mail: marc.brecht@reutlingen-university.de Phone: +49-7121-271-2065. Fax: +49-7121-270-2077*

[f] *Electronic Supplementary Information (ESI) available: S1: Brief description of the algorithm used to determine the wavelength position of the most intense fluorescence emission and its full width at half-maximum. S2: Molecular surface of mPSIIcc (Figure 5). S3: Description of the kinetic model and model calculations (Figure 6) as well as a derivation of the used equations; See file attached as ESI-mPSII.*

For the first time, the fluorescence of single dPSIIcc at 1.6 K was reported by our group [13, 39]. Here, we report the fluorescence of single mPSIIcc and figure out the differences to single dimers. Combining this finding with chemical and crystallographic analyses of the mPSIIcc and dPSIIcc crystals, we arrive at a proposal for the location of Chls in the structure of PSIIcc that could contribute to the F695 emission.

3 Experimental section

All samples investigated in this work originate from redissolved crystals of PSIIcc. Preparation and crystallization of mPSIIcc from *T. elongatus* is described by Broser et al. [10]. For SMS, redissolved crystals were diluted in buffer solution containing 100 mM PIPES (pH 7.0), 0.5 M betaine, 5 mM $CaCl_2$ and 0.03% β-DM [39, 40]. The dPSIIcc from *T. elongatus* have been isolated and purified as described in ref. [40]. The sample was diluted in buffer solution as explained in ref. [39, 13]. In further steps, for both samples, 30% glycerol (w/w) was added to their buffer solutions. The final PSIIcc concentration was approximately 3 pM. For single-molecule experiments, less than 1 µL of the sample was sandwiched between two coverslips. Finally, the sample was transferred directly into the pre-cooled cryostat, T = 4.2 K, and rapidly plunged into liquid helium. Temperatures below 4.2 K are generated by pumping the helium gas. Experiments were carried out using a home-built confocal microscope operating at 1.6 K as described in ref. [41].

2 Results and Discussion

The shape of the fluorescence spectra of individual mPSIIcc varies from complex to complex. Figure 1 shows two examples of time-dependent spectral sequences taken from two representative single mPSIIcc under the same experimental conditions. The time-averaged spectra are shown on top. Figure 1a shows that the dataset is dominated by four intense fluorescence lines at 684.5, 685.8, 689.2 and 698.2 nm, respectively. They are visible during the whole time of data acquisition. It is obvious that these emitters show quite different spectral diffusion behavior as a function of time. Figure 1b shows a dataset of another single mPSIIcc complex. The average spectrum shows one intense ZPL at 685.8 nm as well as two ZPLs with lower intensities at 684.1 and 691.0 nm.
The probability of finding a ZPL in a wavelength interval was evaluated for all measured spectra series. The spectral positions of ZPLs in each dataset are detected by an algorithm described earlier [39]. Based on this information the frequency of occurrence of ZPL positions can be determined. Figure 2a shows the relative occurrence of all ZPLs as histogram together with the average spectrum calculated for all datasets taken from individual mPSIIcc. Most ZPLs occurred in the range 684 - 687 nm, which corresponds to the maximum of the average

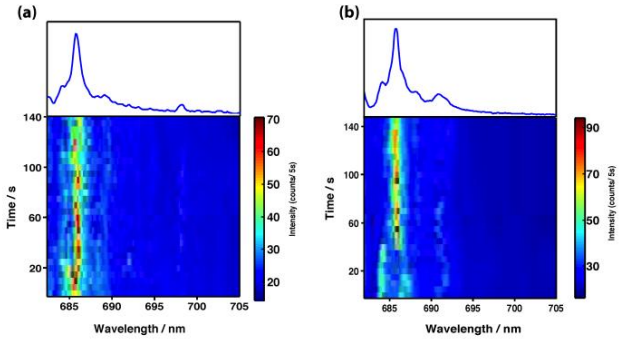

Figure 1: Sequence of fluorescence emission spectra of two single mPSIIcc (a and b). The fluorescence intensity is color-coded (see scale to the right of each graph). The average spectra are shown at the top. Integration time per spectrum is 5 s with an excitation wavelength of 665 nm at a temperature of 1.6 K.

spectrum at 685.6 nm. Comparing the ZPL occurrence of mPSIIcc with those of dPSIIcc (as reported in [39]) shows that the ZPLs of F695 have been diminished. Figure 2b shows the full width at half maximum (fwhm) versus the wavelength positions of the most intense contributions in the fluorescence spectrum of each single mPSIIcc determined by using the algorithm described in ref. [42] as algorithm I (see also S1). Around 90% of them are found within the wavelength range 686 ± 2 nm and have a fwhm less than 3 nm. From Figure 2a, it is obvious that ZPLs at > 690 nm are low in intensity and as a consequence, they do not contribute to the data points in Figure 2b.
In Figure 3 the average emission spectrum obtained from the summation of 46 datasets of single mPSIIcc (red curve) is shown together with the average spectrum of single dPSIIcc (blue curve). The maximum intensity of mPSIIcc and dPSIIcc is at 685.6 nm. The average spectrum of mPSIIcc shows a clear difference around 695 nm compared to the average spectrum of dPSIIcc, indicating that the emission due to F695 is weaker in monomers than in dimers.

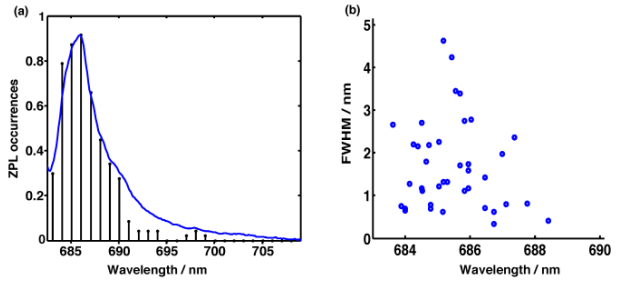

Figure 2: (a) ZPL occurrence (histogram) and average emission spectrum (solid line) of mPSIIcc. The latter represents the sum of all 46 datasets (measured at 1.6 K). (b) Scatter-plot of fwhm versus wavelength position obtained from the most intense peak in each spectrum of single mPSIIcc.

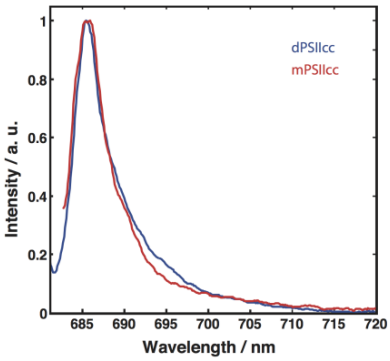

Figure 3: Comparison between the average of the whole single-molecule datasets of mPSIIcc (red) and dPSIIcc (blue) diluted in the same buffer. The excitation wavelength was 665 nm and the spectra were recorded at a temperature of 1.6 K.

This difference suggests that there is one specific red-shifted emitter with reduced fluorescence intensity, while emitters at higher energy show the same characteristics in mPSIIcc and in dPSIIcc. Therefore, we conclude that the fluorescence due to the emitter designated as F695 is more quenched in monomers than in dimers.

The samples have been prepared in the same way as those used in crystallographic studies of PSIIcc and thus are chemically and structurally well characterized. These studies showed that there is no major structural difference between monomeric and dimeric PSIIcc, and both are fully active in water oxidation [5, 10]. Regarding the pigment composition, mPSIIcc has the same Chl inventory as dPSIIcc, but 1.3 ± 0.2 β-Car are missing per monomer in redissolved crystals of mPSIIcc [10]. This result is confirmed by X-ray crystallography. In particular, the dPSIIcc samples studied recently were prepared in a way similar to those used by Loll et al. [5] and Guskov et al. [6] (PDB 3BZ1 and 3BZ2). The mPSIIcc samples are prepared in the same way as those used by Broser et al. [10] (PDB 3KZI).

The arrangement of Chls and β-Car in dPSIIcc according to PDB 3BZ1/2 is shown in Figure 4a. This arrangement of pigments is the same in mPSIIcc except for one missing β-Car, which is BCR 528 highlighted in blue in Figure 4a. The latter β-Car is found in a bridging position across the monomer-monomer interface. Therefore, it may detach due to its exposed location in the monomer. However, there are five β-Car at the monomer-monomer interface in dPSIIcc, so that four further β-Car are to a certain extent surface-exposed (i.e., exposed to the detergent phase) in mPSIIcc (Figure 5, Supporting Information S2). In the X-ray diffraction analysis of mPSIIcc at 3.6 Å resolution [10], the electron density for most carotenoids is not continuous, and their localization is mainly based on the electron density of the ionone rings and by analogy to the β-Car positions in the dPSIIcc-structure at 2.9 Å resolution. Thus, it cannot be excluded that there is an inhomogeneity in the crystal as regards the occupancy of the β-Car binding sites. This together with the exposed positions of the carotenoids at the monomer-monomer interface (Figure 5, S2) implies that actually more than one β-Car could be missing in a single mPSIIcc complex.

It is instructive to also consider the more recent crystal structures of dPSIIcc at higher resolution. These are the structure of *T. elongatus* at 2.44 Å resolution (PDB 4PJ0 [7]) and that of *T. vulcanus* at 1.9 Å resolution (refined PDB 3WU2 [8]). In both cases, dPSIIcc is prepared in a slightly different manner, which could affect the extraction of carotenoids from the complex. Indeed, in both of these structures, the carotenoid designated as BCR 115 by Guskov et al. [6] (see Figure 4a) is missing. This result demonstrates that carotenoids in PSIIcc are principally prone to a preparation-dependent loss due to their peripheral location. However, all other carotenoids are found in all dPSIIcc-structures regardless of the details of the biochemical procedures and can thus be expected to be more tightly bound to dPSIIcc despite being surface-exposed. Furthermore, the only missing carotenoid in the more recent dPSIIcc-structures, BCR 115, is not in van-der-Waals contact with any Chl (Figure 4a). Therefore, we are led to the conclusion that the spectroscopic differences between mPSIIcc and dPSIIcc observed in the present SMS data, which are interpreted as arising from changed Chl/ β-Car interactions (see below), are indeed most likely due to alterations of the monomer-monomer interface.

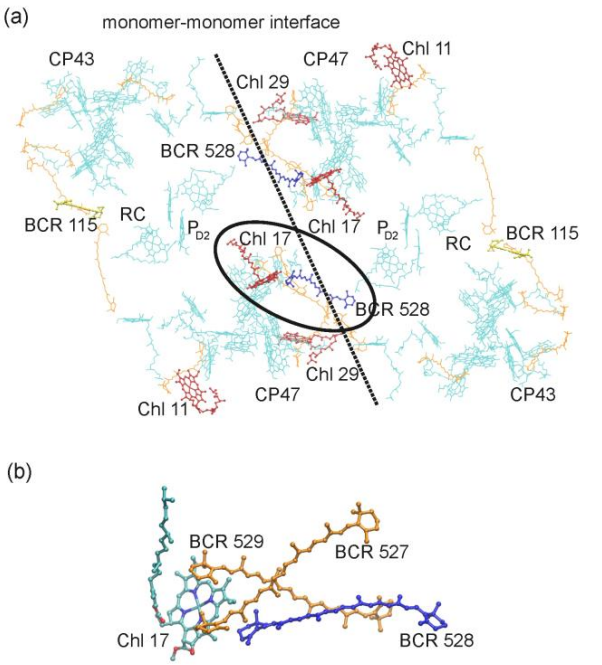

Figure 4: (a) Arrangement of Chl (cyan) and β-Car (BCR, orange) pigments in dPSIIcc (from PDB 3BZ1 and 3BZ2); the monomer-monomer interface (dashed line), Chls 11, 17, and 29 (red) highlighted. BCR 528 (blue) is missing in mPSIIcc (PDB 3KZI), while BCR 115 (yellow) is missing in more recent crystal structures of dPSIIcc (PDB 4PJ0 and 3WU2). The black ellipse indicates the pigments shown enlarged in Figure 4b. (b) A closer look at the interaction of Chl 17 in CP47 with the β-Car BCR 528 (blue) as well as BCR 527 and 529 (orange) located at the monomer-monomer interface. Figures made with VMD [43].

The accumulation of Chl triplet states (^{3}Chl) in CP47 and CP43 can be expected on those Chls, which have the lowest singlet transition energies and contribute mostly to the fluorescence.

In particular, F695, which has the lowest transition energy, will be subject to intersystem crossing and triplet accumulation. Under these conditions, the contribution of such a chromophore to the singlet emission as detected in SMS will be reduced (see [13] and below).

Triplet formation will also occur under native working conditions of the antenna system. To avoid the formation of harmful singlet oxygen, natural antenna systems employ carotenoids to quench ^{3}Chl by triplet-triplet energy transfer. This transfer requires overlapping wavefunctions between a Chl and a carotenoid and thus a close vicinity of the two pigments. As a consequence of such an interaction, the lifetime of ^{3}Chl will be decreased and the fluorescence intensity of the Chl in SMS increased. On the other hand, if a triplet quenching carotenoid in the vicinity of the Chl is lost, the lifetime of ^{3}Chl will be increased and the singlet emission will be diminished.

As a proof of principle that this mechanism works, we performed calculations on the basis of the simple kinetic model depicted in Figure 6a (Supporting Information S3). The three states in this model are the ground state of the system (S_0) as well as the first excited singlet state (S_1) and the first triplet state (T_1) of the emitter. k_{21} and k_{23} are the rate constants for fluorescence and intersystem crossing of the emitter, respectively (neglecting internal conversion as suggested in [44]). We take $1/k_{21}$ = 18 ns as the natural lifetime of the S_1 state of Chl *a* based on the considerations in ref. [45].

Because of the rather high triplet yield of Chl *a* (64% in ether solution [44]), we set $\gamma = k_{23}/k_{21} = 1.8$ resulting in an intersystem crossing rate of $(10\ \text{ns})^{-1}$. The triplet lifetime $\tau = 1/k_{31}$ is normally in the order of 1 ms, but can be expected to be reduced to the ns timescale due to interaction of the emitter with one or more carotenoids, i.e., it is determined by the rate k_{TT} of triplet-triplet energy transfer from Chl to β-Car. However, regeneration of the ground state of the single PSIIcc requires also decay of the β-Car triplet state, which is in the µs range. Thus, k_{31} is some unknown combination of k_{TT} and the inverse triplet lifetime of β-Car. The excitation rate k_{12} can be estimated on the basis of the laser intensity of 100 µW (corresponding to a photon flux of 6.6×10^{20} cm^{-2} s^{-1}) and an absorption cross section of PSIIcc of about 7×10^{-15} cm^2 at 665 nm to be in the order of 1 µs^{-1}. Since we do not know the exact value of k_{31}, we consider a hypothetical increase of τ from 0.5 to 1 µs due to the loss of one carotenoid in the vicinity of the emitter. The corresponding ratios $\kappa = k_{12}/k_{31} = \tau\ k_{12}$ are chosen to 1 and 2, respectively, to keep k_{12} constant. Under these conditions, the steady-state population of the S_1 state is reduced by 25% (Figure 6b, S3). This reduction is in the same order of magnitude as the reduction of fluorescence intensity at 695 nm in mPSIIcc compared to dPSIIcc (Figure 3). Therefore, an increase of the triplet lifetime of the 695 nm emitter can, in principle, explain the effect. At significantly lower excitation rates, the effect vanishes. For the particular values of κ chosen in the simulations shown in Figure 6c, there is no change in the singlet population at all. Hence, the effect is unlikely to be detectable in conventional fluorescence spectroscopy. We conclude that a change in the triplet lifetime of the emitter can have a measurable influence on the fluorescence intensity in SMS experiments because of the high excitation rate.

In PSIIcc, a number of Chls are close to β-Car pigments. Notably, there is one Chl (no. 17 in the numbering scheme of Loll et al. [5]; for an overview, see ref. [11]), which is located at the monomer-monomer interface and in van-der-Waals distance to three β-Car [11]. One of these is BCR 528, which is missing in monomer preparations (Figure 4). The other two β-Cars (BCR 527 and 529, Figure 4b) are also exposed in mPSIIcc and might be lost to a certain extent (Figure 5, S2). Therefore, it is reasonable to suggest that Chl 17 is the pigment that gives rise to the emission at 695 nm that is diminished in mPSIIcc.

This assignment is in agreement with proposals in the literature that F695 is associated with CP47, but it is in disagreement with assignments of particular Chls. Until recently, the most popular candidate for F695 was Chl 29 based on earlier mutagenesis work [46]. However, as discussed in ref. [23], it is actually impossible to draw conclusions about the molecular identity of F695 from these data. Recently, it was demonstrated that depletion of the subunit PsbH affects the F695 emitter [20]. Since PsbH forms a hydrogen bond to Chl 29 [11], these data were also interpreted as indicating Chl 29 to be a low-energy Chl. However, it is not clear whether such a hydrogen bond is sufficient to cause a strong redshift of the Q_y band of Chl *a*. Furthermore, PsbH is also in contact with Chl 11. Indeed, a very recent study of isolated CP47 from spinach employing circularly polarized luminescence (CPL) in combination with structure-based simulations of optical spectra provided evidence that Chl 11 is the lowest-energy Chl in these samples [23]. On the other hand, the present data suggest that a Chl located at the monomer-monomer interface contributes to the F695 emission. While Chl 11 is located at the periphery of dPSIIcc (Figure 4a), Chls 17 and 29 are candidates for emitters located at the monomer-monomer interface and being in contact with carotenoids that might be lost in mPSIIcc preparations (for Chl to β -Car distances, see [11]). Based on the above discussion of the carotenoids in mPSIIcc, we prefer Chl 17, but we cannot exclude Chl 29.

Taking the various data together, we propose that there are at least two low-energy Chls contributing to F695 in intact cyanobacterial PSIIcc, one being Chl 11 and the other Chl 17 or 29. It remains to be investigated, whether there are differences in the optical properties of these Chls between cyanobacterial and plant PSIIcc as well as between intact core complexes and isolated CP47. Further experiments on various samples are required, e.g., SMS and CPL, to clarify these issues.

Chl 17 is located in a suitable position close to the RC pigments. The center-to-center distance $R_{Mg\text{-}Mg}$ between Chl 17 of CP47 and P_{D2} of the RC is 29.8 Å based on PDB 3BZ1/2. However, in dPSIIcc, Chl 17 comes also close to its counterpart in the second monomer ($R_{Mg\text{-}Mg}$ = 36.9 Å) and close to P_{D2} in the RC of the second monomer ($R_{Mg\text{-}Mg}$ = 45.8 Å). If an energy sink of the core antenna system is located at Chl 17, the excitation energy will be guided to this point, from where it can be delivered to either RC in the dimer or to the antenna system of the other monomer. If a RC is closed (i.e., the

acceptor side reduced), the excitation energy can flow back from the RC to the antenna system via Chl 17 and can be delivered to the other RC. A redshifted Chl 17 might facilitate such an energy back-flow. In this way, the use of solar energy is made more efficient in the dimer. A similar mechanism might be at work in dPSIIcc superstructures that occur in the native thylakoid membrane of cyanobacteria [7]. Thus, from the viewpoint of structure-function relationships, it seems to make sense to associate an energy trap of the core antenna system of PSIIcc with the position of Chl 17 and, in order to quench triplet states preferentially formed at such a trap, place three β-Car pigments in its vicinity.

4 Conclusions

In summary, we conclude that the spectroscopic differences between the presented SMS datasets of mPSIIcc and dPSIIcc arise from changed Chl/ β-Car interactions most likely due to alterations of the monomer-monomer interface. A loss of β-Car cofactors in mPSIIcc preparations leads to an increased lifetime of the triplet state of Chl 17, which can explain the reduced singlet emission of F695 as observed in our SMS.

Acknowledgements

This work was supported by the Deutsche Forschungsgemeinschaft (DFG) within the framework of the cluster of excellence on unifying concepts in catalysis (UniCat), project B1, coordinated by the TU Berlin, Sfb 1078, project A5 (M. I., A.Z.), HFSP RGP0063/2013.

References

1 T. Cardona, A. Sedoud, N. Cox, A.W. Rutherford, *Biochim. Biophys. Acta,* 2012, **1817**, 26-43.
2 F. Müh, C. Glöckner, J. Hellmich, A. Zouni, *Biochim. Biophys. Acta,* 2012, **1817**, 44-65.
3 F. Müh, A. Zouni, *Front. Biosci.*, 2011, **17**, 3072-3132.
4 J. Yano, V. Yachandra, *Chem. Rev.,* 2014, **114**, 4175-4205.
5 B. Loll, J. Kern, W. Saenger, A. Zouni, J. Biesiadka, *Nature*, 2005, **438**, 1040-1044.
6 A. Guskov, J. Kern, A. Gabdulkhakov, M. Broser, A. Zouni, W. Saenger, *Nat. Struct. Mol. Biol.,* 2009, **16**, 334-342.
7 J. Hellmich, M. Bommer, A. Burkhardt, M. Ibrahim, J. Kern, A. Meents, F. Müh, H. Dobbek, A. Zouni, *Structure*, 2014, **22**, 1607-1615.
8 Y. Umena, K. Kawakami, J. R. Shen, N. Kamiya, *Nature*, 2011, **473**, 55-60.
9 F. H. M. Koua, Y. Umena, K. Kawakami, J.R. Shen, *Proc. Natl. Acad. Sci. U.S.A.,* 2013, **110**, 3889-3894.
10 M. Broser, A. Gabdulkhakov, J. Kern, A. Guskov, F. Müh, W. Saenger, A. Zouni, *J. Biol. Chem.,* 2010, **285**, 26255-26262.
11 F. Müh, T. Renger, A. Zouni*, Plant Physiol. Biochem.,* 2008, **46**, 238-264.
12 Y. Shibata, S. Nishi, K. Kawakami, J. R. Shen, T. Renger, *J. Am. Chem. Soc.,* 2013, **135**, 6903-6914.
13 M. Brecht, S. Skandary, J. Hellmich, C. Glöckner, A. Konrad, M. Hussels, A.J. Meixner, A. Zouni, E. Schlodder, *Biochim. Biophys. Acta*, 2014, **1837**, 773-781.
14 E. Krausz, J.L. Hughes, P.J. Smith, R.J. Pace, S.P. Årsköld, *Photosynth. Res.,* 2005, **84**, 193-199.
15 E.G. Andrizhiyevskaya, A. Chojnicka, J.A. Bautista, B.A. Diner, R. van Grondelle, J.P. Dekker, *Photosynth. Res.,* 2005, **84**, 173-180.
16 M. Komura, Y. Shibata, S. Itoh, *Biochim. Biophys. Acta*, 2006, **1757**, 1657-1668.
17 G. Raszewski, T. Renger, *J. Am. Chem. Soc.,* 2008, **130**, 4431-4446.
18 F. Müh, M. Plöckinger, H. Ortmayer, M. Schmidt am Busch, D. Lindorfer, J. Adolphs, T. Renger, *J. Photochem. Photobiol. B: Biol.,* 2015, **152**, 286-300.
19 M. Reppert, V. Zazubovich, N. C. Dang, M. Seibert, R. Jankowiak, *J. Phys. Chem. B*, 2008, **112**, 9934-9947;
20 S. E. D'Haene, R. Sobotka, L. Bučinská, J. P. Dekker, J. D. Komenda, *Biochim. Biophys. Acta,* 2015, **1847**, 1327-1334.
21 M. Reppert, K. Acharya, B. Neupane, R. Jankowiak, *J. Phys. Chem. B*, 2010, **114**, 11884-11898.
22 B. Neupane, N. C. Dang, K. Acharya, M. Reppert, V. Zazubovich, R. Picorel, M. Seibert, R. Jankowiak, *J. Am. Chem. Soc.*, 2010, **132**, 4214-4229.
23 J. Hall, T. Renger, F. Müh, R. Picorel, E. Krausz, *Biochim. Biophys. Acta*, 2016, **1857**, 1580-1593.
24 M.L. Groot, R.N. Frese, F.L. de Weerd, K. Bromek, A. Pettersson, E.J.G. Peterman, I.H.M. van Stokkum, R. van Grondelle, J. P. Dekker, *Biophys. J.,* 1999, **77**, 3328-3340.
25 A.M. van Oijen, M. Ketelaars, J. Köhler, T.J. Aartsma, J. Schmidt, *Science*, 1999, **285**, 400-402.
26 P. Tamarat, A. Maali, B. Lounis, M. Orrit, *J. Phys. Chem. A*, 2000, **104**, 1-16.
27 H.P. Lu, X.S. Xie, *Nature*, 1997, **385**, 143-146.
28 D. Rutkauskas, V. Novoderezhkin, R.J. Cogdell, R. van Grondelle, *Biophys. J.,* 2005, **88**, 422-435.
29 F. Stracke, C. Blum, S. Becker, K. Müllen, A.J. Meixner*, J. Chem. Phys.* 2004, **300**, 153-164.
30 F. Schleifenbaum, C. Blum, V. Subramaniam, A.J. Meixner, *Mol. Phys.,* 2009, **107**, 1923-1942.
31 Y. Berlin, A. Burin, J. Friedrich, J. Köhler, *Phys. Life Rev.,* 2007, **4**, 64-89.
32 C. Hofmann, M. Ketelaars, M. Matsushita, H. Michel, T.J. Aartsma, J. Köhler, *Phys. Rev. Lett*., 2003, **90**, 13004.
33 K. Huang, A. Rhys, *Proc. Roy. Soc. Lond. A*, 1950, **204**, 406-423.
34 T. Pullerits, R. Monshouwer, F. van Mourik, R. van Grondelle, *Chem. Phys*., 1995, **194**, 395-407.
35 I. Renge, *J. Lumin*, 2008, **128**, 413-420.
36 M. Rätsep, M. Pajusalu, A. Freiberg, *Chem. Phys. Lett.,* 2009, **479**, 140-143.
37 C. Hofmann, T.J. Aartsma, H. Michel, J. Köhler, *Proc. Natl. Acad. Sci. U.S.A.*, 2003, 100, 15534-15538.
38 M. Brecht, M. Hussels, E. Schlodder, N.V. Karapetyan, *Biochim. Biophys. Acta* , 2012, **1817**, 445-452.
39 S. Skandary, M. Hussels, A. Konrad, T. Renger, F. Müh, M. Bommer, A. Zouni, A.J. Meixner, M. Brecht, *J. Phys. Chem. B*, 2015, **119**, 4203-4210.
40 J. Kern, B. Loll,C. Lüneberg, D. DiFiore, J. Biesiadka, K. D. Irrgang, A. Zouni, *Biophys. Acta*, 2005, **1706**, 147–157.
41 M. Hussels, A. Konrad, M. Brecht, *Rev. Sci. Instrum*. 2012, **83**, 123706.
42 Hussels, M.; Brecht, M. *Biochemistry*, 2011, **50**, 3628-3637.
43 W. Humphrey, A. Dalke, K. Schulten, *J. Mol. Graphics*, 1996, **14**, 33-38.
44 P. G. Bowers, G. Porter, *Proc. Roy. Soc. Lond. A*, 1967, **296**, 435-441.
45 T. Renger, M.E. Madjet, F. Müh, I. Trostmann, F.J. Schmitt, C. Theiss, H. Paulsen, H.J. Eichler, A. Knorr, G. Renger, *J. Phys. Chem. B*, 2009, **113**, 9948-9957.
46 G. Shen and W. F.J. Vermaas, *Biochemistry*, 1994, **33**, 7379-7388.

Chapter 4: Polarization Dependent Single-Molecule Spectroscopy of Photosystem I

The fluorescence of single PSI-M from *T. elongatus* is shown for the first time by SMS at low temperature, 1.6 K, and they are compared to the results of SMS PSI-T. The fluorescence of individual PSI is dominated by both thr ZPL and a broad intensity distributions at low temperature. These contributions differ in their number, intensity and wavelength positions for single PSI complexes.

The average emission spectrum is obtained for the summation of all 70 datasets of single PSI-M (see Figure 3 in ref. [77]), showed the maximum intensity is located at 726.6±0.5 nm, which is close to the values reported for single PSI-T from *T. elongatus* (with the same preparations). The corresponding FWHM for single PSI-M is 29.6±0.4 nm, whereas for single PSI-T, FWHM is slightly wider (31.8±0.5 nm) [132]. Additionally, in the average spectrum of single PSI-M some contributions are missing in intervals between 730 nm to 760 nm as compared to the average spectrum of PSI-T.

Polarization dependent single-molecule spectroscopy provides detailed insight into the fluorescence dynamics of the red Chls and their interactions with other chromophores were mainly happened by EET. Comparing the spectral dynamics between trimeric and monomeric single PSI complexes, the single PSI-M complexes show less spectral diversity of their fluorescence than single PSI-T. In the presence of these differences, the analysis of the polarization dependent datasets from single PSI-M is more feasible than for PSI-T. This chapter is adapted from the paper in ref. [127].

Polarization Dependent Single-Molecule Spectroscopy of Photosystem I

S. Skandary, [a] A. Konrad, [a] M. Hussels, [a] A. J. Meixner, [a] M. Brecht [a,b]

[a]University of Tübingen, IPTC and Lisa+ Center, Tübingen, Germany,
[b]Zurich University of Applied Science Winterthur (ZHAW), Winterthur, Switzerland

ABSTRACT

Single-molecule spectroscopy (SMS) at low temperature was used to study the spectral properties, heterogeneities and spectral dynamics of the chlorophyll *a* (Chl *a*) molecules responsible for the fluorescence emission of photosystem I (PS I). The fluorescence spectra of single PS I complexes are dominated by several red-shifted Chl *a* molecules categorized into red pools called C708 and C719. By polarization dependent measurements we demonstrate spectrally separate emissions corresponding to C708 and C719 in single PS I monomers and trimers. Moreover, we compared the results of SMS polarization dependent between monomeric and trimeric PS I complexes and give an estimation for the orientation between these red pools. As a consequence, we get new insight into the energy transfer towards and between the red Chl *a* molecules in PS I complexes.

Keywords: photosynthesis, single–molecule spectroscopy, polarization, exciton energy transfer

1. INTRODUCTION

Photosystem I (PS I) is one of two trans-membrane pigment-protein complexes essential for oxygenic photosynthesis. PS I is located in the thylakoid membranes of cyanobacteria, algae and plants and mediates light-induced electron transfer from plastocyanin or cytochrome C_6 on the lumenal side to Ferredoxin on the stromal side.[1] The first step of the photosynthetic reaction is the absorption of a photon by the antenna system of PS I followed by subsequent energy transfer to the reaction center. At this point, the captured excitation energy is used to induce a trans-membrane charge separation starting at the chlorophyll (Chl) pair P700, which has its main absorption is at 700 nm.[1,2]

The PS I complex from cyanobacteria differs from higher plants and algae in organization and content of polypeptides, however, there is a well-resolved structural model for the cyanobacterium *Thermosynechococcus elongatus* (*Th. elongatus*) from X-ray crystallography.[3–5] According to X-ray analysis of the trimeric PS I core complex from the cyanobacterium (*Th. elongatus*), the structure exhibits 12 protein subunits and 127 cofactors performing light harvesting and electron transfer. These cofactors include 96 Chls, 22 carotenoids (Car), two phylloquinones, three ironsulfur (4Fe-4S) clusters, and four lipids for each PS I monomer.[3,4,6]

In green plants, algae and cyanobacteria, Chl *a* molecules show absorbance at wavelengths larger than the primary donor P700.[7,8] These red-shifted Chl *a* molecules are often called the long-wavelength (also red or low-energy) Chls (LWC).[9] If the excitation energy is localized at these LWCs, a direct excitation of P700 to P700* is impossible and the energy is trapped. For this case, additional activation energy, e.g., thermal energy provided by the phonon bath, is necessary to oxidize P700 and start the charge separation process.[10–13] The red Chls have crucial impacts on the kinetics of energy transfer and trapping. However, up to now, it is under debate whether the energy transfer within the antenna system proceeds along well-defined pathways or utilizes variable routes.[14–16] Thus, it is necessary to obtain more details about spectral properties of these Chl *a* molecules using the advantages of various spectroscopic methods.

The PS I from cyanobacteria can be isolated in monomeric and trimeric forms.[17,18] The trimer is proposed to be the native form, at least under certain physiological conditions.[19] The trimeric PS I from *Th. elongatus* is the most stable PS I complex of which also the most resolved three-dimensional (3D) structure has been determined.[3]

Further author information: (Send correspondence to Dr. Marc Brecht)
Brecht M.: E-mail:marc.brecht@uni-tuebingen.de, Telephone: +49-7071-29-76239

Nanoimaging and Nanospectroscopy III, edited by Prabhat Verma, Alexander Egner, Proc. of SPIE
Vol. 9554, 95541H · © 2015 SPIE · CCC code: 0277-786X/15/$18 · doi: 10.1117/12.2207523

The occurrence of LWC in the core antenna, that absorb even further into the red, is unique to cyanobacteria. The spectral characteristics and the number of red Chl *a* molecules are species dependent. PS I trimers (PS I-T) contain usually more red Chls than PS I monomers (PS I-M).[20] The arrangement of red Chls is shown in Fig. 1 for both PS I-T and PS I-M. The trimeric and monomeric species, absorb light at room temperature and show a probability of >95 % of inducing charge separation.[21] This indicates that energy exchange between monomers is negligible and a single monomer can be used to describe the optical properties of PS I.[22]

The absorption spectra of PS I from *Th. elongatus* reveal two red pools[23–26] with the main absorption bands at 708 and 719 nm denoted commonly as C708 and C719, respectively. The distinction of two pools remains tentative due to a large spectral overlap of the respective bands.[23] Additionally, a red subpool (C715) was found by the analysis of nonphotochemical hole burning (NPHB) spectra.[27] The trimeric and monomeric PS I from *Th. elongatus* exhibit the same number of LWCs for C708, but for monomers, they are lower in C719.[8] The absorption spectra of the trimeric complexes at 5 K indicate a more ordered structure compared with monomers. But the monomeric complexes showed less absorption around 720 nm.[8] In addition, the quantum yield of charge separation in monomers is higher than in trimers at 4 K, which can be explained by the lower number of LWCs in C719.[8]

The quantum efficiency of photochemistry is virtually not affected by the LWCs at room temperature. While, at cryogenic temperature, the fluorescence of the long-wavelength pigments increases considerably, suggesting that a significant part of excitation energy is no longer able to reach P700.[8] Thus, at lower temperatures, the red Chls act as traps for the excitation energy leading to the consequence that quantum efficiency of the charge separation decreases while the fluorescence intensity increases.[8,28]

The unstructured shape of the ensemble fluorescence spectra limits one to obtain detailed information about the spectral characteristics of the red pools.[25] Therefore, the site selective spectroscopic techniques like single-molecule spectroscopy (SMS)[29,30] are effective methods to reveal subtle spectral details often obscured by averaging over heterogeneous ensembles and inhomogeneously broadened spectral bands.[29,31] Additionally, lowering the temperature reduces the impact of spectral diffusion[32–34] which is one of the main limitations of single-molecule experiments at room temperature.[34–40]

The assignment of red antenna states in single PS I-T from *Th. elongatus* was reported earlier *et al.*[41] In this study, we show the fluorescence spectra of single PS I-T and PS I-M both from *Th. elongatus* at 1.6 K. Additionally, the polarization dependent measurements allow us to determine the spectral distributions of LWCs in single PS I complexes which can not be detected without polarization measurements. The polarization dependent measurements reveal spectrally separated fluorescence bands at low temperature with distinguishable polarization. Moreover, we compare the results of polarization dependent SMS between monomeric and trimeric PS I complexes and estimate the orientation between the red pools.

2. MATERIALS AND METHODS

Experimental Methods

PS I-T and PS I-M from *Th. elongatus* have been isolated as described in Ref.[6,20] The purified PS I (for both trimer and monomer experiments) were diluted in buffer solution (pH 7.5) containing 20 mM Tricine, 25 mM $MgCl_2$, and 0.4 mM % β-DM detergent to reach Chl *a* concentration of 20 μM. This amount of detergent is adequate for the critical solubilization of PS I concentration of 0.5 μM to avoid PS I aggregation.[42] In further steps, the PSI-containing (buffer) solution was diluted (with the same buffer conditions) to a final PS I concentration of $\sim$3 pM. About 1 μl of this suspension was placed between two glass cover slips. Finally, the sample was transferred directly into the cryostat and rapidly plunged into liquid helium. Experiments were carried out using a home-built confocal microscope operating at 1.6 K as described in Ref.[41,43]

For PS I-T measurements, the excitation power measured directly behind the beam-scanning module was 100 μW, and the excitation wavelength was 680 nm, while a broadband fiber laser with 40 MHz repetition rate (SuperK Extreme 40 MHz VIS, NKT photonics) combined with an AOTF set to 675 nm was used for excitation of PS I-Ms. The excitation intensity of the laser was 10 μW. For the polarization measurements, a combination of a $\lambda/2$-waveplate (10RP52-2, Newport) on a motorized rotator (PRM1/MZ8, Thorlabs) and a polarizing beamdisplacer (BD27, Thorlabs) is placed into the optical path in front of the spectrograph. The polarizing

beamdisplacer splits the light into two beams with perpendicular polarizations, which can be acquired simultaneously by the CCD-camera. In combination with the rotating $\lambda/2$-waveplate it is possible to measure spectrally resolved the fluorescence intensity as a function of rotator angle.[43] For PS I-T measurements a constantly rotating Glan-Thompson polarizer combined with a $\lambda/4$ waveplate were placed in front of the spectrograph.

Data evaluation process

Discrete Fourier transformation (DFT) has been used to determine the phase between different contributions of polarization dependent fluorescence emission, recorded as a function of waveplate rotation angle. Rotating the $\lambda/2$ waveplate two fluorescence spectra series can be recorded depending on the rotation angle of the waveplate with respect to the initial orientation. Both spectra series contain the same information and differ only in phase. The $\lambda/2$ waveplate rotates the polarization of the incident light by the double of the angle between the polarization plane and towards the crystal axis. Together with the symmetry of polarization this leads to a modulation period of 90° rotation angle of the waveplate. In addition, with the known frequency of the rotator this gives the expected modulation frequency of the spectra along the angle axis. This method allows us to determine for each polarization dependent data set the angle between the projected transitions dipole moments (TDMs) in the detection plane. For more details, please see supporting information in Ref.[44]

3. RESULTS AND DISCUSSION

3.1 Results

The spectral properties of the fluorescence data sets of individual PS I-T and PS I-M complexes recorded at low temperature (1.6 K) are analyzed. The number and spectral positions of emitters responsible for the fluorescence of single PS I complexes are obtained from the analysis of their polarization data sets. In Figs. 2 and 3 two fluorescence data sets of single PS I-T and PS I-M complexes are shown.

Fig. 2 shows time dependent and polarization dependent data sets of single PS I-T complexes. Fig. 2a shows the time dependent data set of single PS I-T and the respective average spectrum on top. This data set is characterized mainly by sharp lines called zero phonon lines (ZPLs) and broad intensity distributions. Three ZPLs are at 711, 713.3 and 714.8 nm, respectively and one broad emission with mean peak position at 723.9 nm. The ZPLs remain restricted to distinct spectral positions. The first ZPL at 711 nm stays stable up to 74 s and performs several spectral jumps up to the end of data set. The two other ZPLs are rather stable in the whole data set. Fig. 2b shows the spectra of the same complex with distinguished polarization. The rotation of polarizer shows the modulations between emitters with nonparallel TDMs. Four contributions are visible with separated spectral positions in polarization dependent data set and they are marked in Fig. 2b. However, due to the existence of different lines, determination of their mutual angles in single PS I-T is not straightforward.

Fig. 3 shows time dependent and polarization dependent data sets of single PS I-M complexes. Fig. 3a shows the time dependent data set of single PS I-M and the respective average spectrum on top. This data set is characterized mainly by a broad emission around 728.4 nm. Fig. 3b shows the polarization dependent data set of the same complex. The accumulation time in polarization dependent spectra of single PS I-M complex was increased to 10 s in order to enhance the S/N ratio, due to the lower signal intensity compared to single PS I-T data sets. Two pronounced contributions with the mean spectral positions at 713 and 730 nm can be distinguished. These two contributions are visible at separated spectral positions. In this representation, it can be seen more clearly that the intensity of each emitter is shifted by almost 45 degree of waveplate rotation angle. When the contribution with peak position at 713 nm is intense, the other at 730 nm is weak. This behavior is consistent for the whole spectra series of this data set. Using the algorithm explained in Material and Method section, an almost perpendicular alignment between the projected TDMs of the respective contributions can be estimated.

As described above, the phase between both contributions of single PS I-M fluorescence spectra were determined for each data set using data evaluation process explained in Material and Method section. Those data sets with tilted and distorted spectral shapes were not used for analysis. We applied our evaluation method on 49 data sets and were able to determine a statistically significant distribution of angles between two contributions

denoted as β. During our evaluation we assign the contribution at lower wavelength to C708 and that at higher wavelength to C709. In Fig. 4 the resulting distribution of β between the fluorescence of C708 and C719 is given. The maximum is between 80 and 90 degree and the histogram shows a decay profile for decreasing angles from 90 to 10 degrees.[44] The scatter plot in Fig. 5 shows the fluorescence intensity ratio of C708/C719 versus angle β for all data sets. In this evaluation, the intensity ratio of C708/C719 yields no correlation to the determined angle of β.

3.2 Discussion

The fluorescence of individual PS I are dominated by ZPLs and broad intensity distributions at low temperatures. These contributions differ in their number, intensity and wavelength positions for single PS I complexes. Multiple lines in single PS I data sets can be the result of different emitters, spectral diffusion, and static disorder.[45,46] The spectral diffusion is the main broadening mechanism within the time scale of the actual accumulation time[38,47,48] in single PS I complexes.

The X-ray structure of PS I in Fig. 1 shows the arrangement of red Chls. The absorption spectrum revealed that each monomer of PS I complex has the same number of red Chls for C708 and a lower number red Chls (2 instead of 4) for C719;[8,20] this deviation was explained by some strongly coupled aggregates contributing to C719 present in PS I-T as a result of the trimerization, which are missing in PS I-M.[6,20] Therefore, the fluorescence of monomers is expected to show the same intensity at the spectral position of C708 and a decreased fluorescence at the position of C719 compared to trimers. Moreover, in single-molecule experiments P700 is mostly in its oxidized state due to the high excitation rates necessary for the experiments.[20,41] Accordingly, the fluorescence of single PS I-M is affected by the oxidized state of P700. It has been shown that the emission of LWCs from C715 around 734 nm is most probably quenched by the oxidized P700[20] and as a consequence, the fluorescence of single PS I-M in this wavelength range is decreased. Therefore, the fluorescence of single PS I-M is expected to be originated by C708 and C719.

Polarization dependent single-molecule spectroscopy provides detailed insight into the fluorescence dynamics of the red Chls and their interactions with other chromophores mainly mediated by excitation energy transfer (EET). Comparing the spectral dynamics between trimeric and monomeric single PS I complexes, the single PS I-M complexes show less spectral diversity of their fluorescence than single PS I-T (Figs. 2, 3). Furthermore, EET between monomers found in PS I-T is not possible in PS I-M. In the presence of these differences, the analysis of the polarization dependent data sets from single PS I-M is more feasible than for PS I-T.

The analysis of the polarization measurements allows us to clearly distinguish overlapping emission bands. There are two spectrally separated contributions in single PS I-M polarization dependent data set (Fig. 3b), whereas time dependent data set (Fig. 3a) shows only one broad emission band over the whole wavelength range. Hence, using our polarization measurements we are able to separate contributions even if they show remarkable spectral overlap.

The evaluation of the angles between the projected TDMs corresponding to the red pools in PS I-M shows a maximum between 80 and 90 degree (Fig. 4). Therefore, an almost perpendicular orientation of the TDMs corresponding to C708 and C719 can be assumed, wherby this statement can be deduced by Monte Carlo simulations shown in Ref.[44] However, there is lack of correlation between the angles and the intensity ratio (e.g. C708/C719), which can be explained by the randomly oriented PS I complex system in space.

This insight allows us to discuss the possible energy transfer pathways responsible for exciting C708 and C719. The EET between chromophors is usually described by the frame work of FRET originally developed by Förster.[49] To describe an antenna pigment as a part of the energy transfer chain, it is shown that the EET depends on the distance and orientations of TDMs of molecule by using the dipole-dipole approximation:[14,50,51]

$$V_{12} = \frac{\overrightarrow{\mu_1}.\overrightarrow{\mu_2}}{r^3} - 3\frac{(\overrightarrow{\mu_1}.\overrightarrow{r})(\overrightarrow{\mu_2}.\overrightarrow{r})}{r^5}. \quad (1)$$

Here, V_{12} is the coupling potential between two dipoles, $\overrightarrow{\mu_1}$ and $\overrightarrow{\mu_2}$ representing the TDMs of the red pools, $\overrightarrow{r}$ is the vector connecting the centers of the dipoles and r is their separation in space. Using orientation factor κ which is defined by $\kappa = \hat{u}\ .\ \hat{v}$ - 3 $(\hat{u}\ .\ \hat{R})$ $(\hat{v}\ .\ \hat{R})$, with $\hat{u}$ and $\hat{v}$ being unit vector of TDMs and $\hat{R}$ unit vector of line

joining their centers.[14] According to this, if the TDMs of two dipoles are oriented almost perpendicular to each other, their κ tend toward zero ($\kappa_{12} \simeq 0$) if their connection vector also has a perpendicular orientation to the center of TDMs. For such a weak coupling, each dipole can be considered as a separate emitter. Apparently, our polarization dependent fluorescence data sets show two spectrally separated emitters with almost perpendicular orientations at the wavelengths assigned to C708 and C719. Thus, we can conclude that there is no direct energy transfer pathway between these two pools within PS I-M complexes. Both, C708 and C719, have to get fed from different energetically higher lying antenna states by two different pathways. From this, we can conclude that the energy transferred from higher lying energy states to the red Chls at low temperature are not trapped only by one final lowest energy state.

3.3 Acknowledgments

We appreciate Dr. Eberhard Schlodder for the PSI samples and helpful discussions. This work was supported by Heisenberg-Program of the Deutsche Forschungsgemeinschaft DFG (BR 4102/1-1 and BR 4102/2-1) and Financial support from the German Research Council (DFG) for ME1600/13-1.

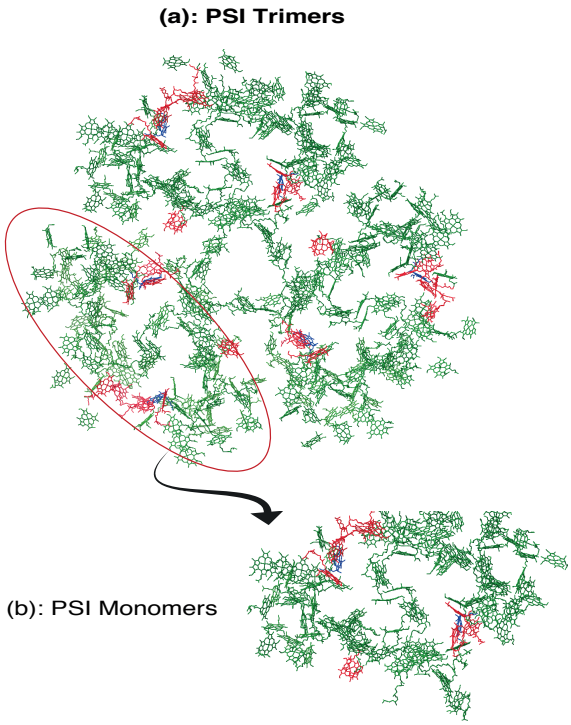

Figure 1. Arrangement of the Chls in PS I. Red colors are red Chl *a* (a): PS I-T and (b): PS I-M. The figure is produced from Protein Data Bank file 1JB0. pdb.[3]

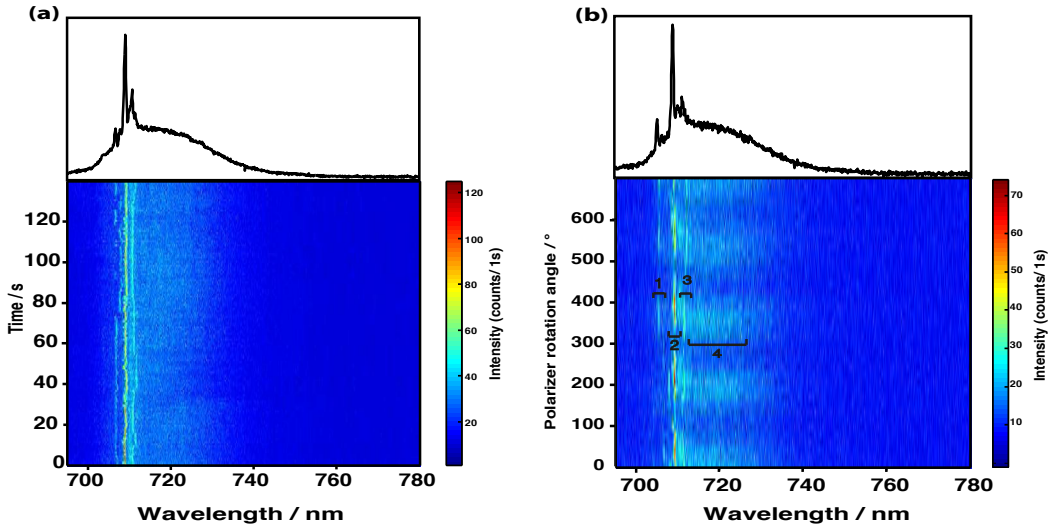

Figure 2. (a): The time dependent data set of single PS I-T with the average spectrum on top. (b): Polarization dependent fluorescence spectra of a single PS I-T with the average spectrum on top. The acquisition time was 1 s for each spectrum. The individual spectra were recorded in steps of 10 degree. Excitation wavelength 680 nm; temperature 1.6 K.

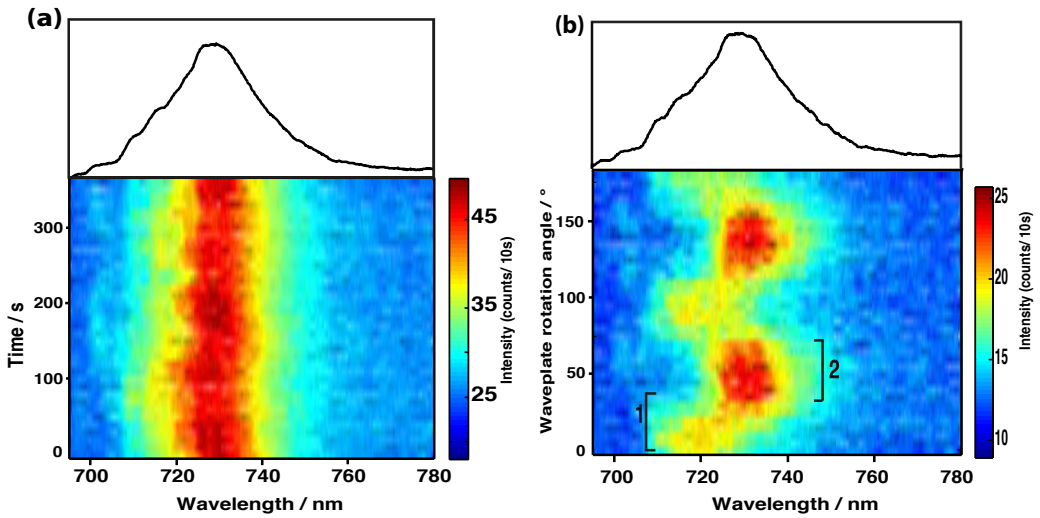

Figure 3. (a): The time dependent data set of PS I-M and with the average spectrum on top. (b): Polarization dependent fluorescence spectra of a single PS I-M with the average spectrum on top. The acquisition time was 10 s for each spectrum. The individual spectra were recorded in steps of 5 degree. Excitation wavelength 675 nm; temperature 1.6 K.

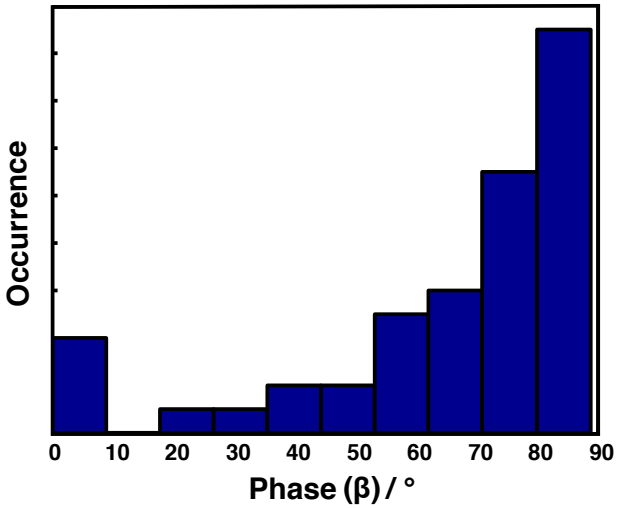

Figure 4. The distribution of angles (β) between the contributions of C708 and C719 in the fluorescence spectra of single PS I-M from *Th. elongatus*. The analysis was carried out on 49 polarization dependent data sets as described in the text.

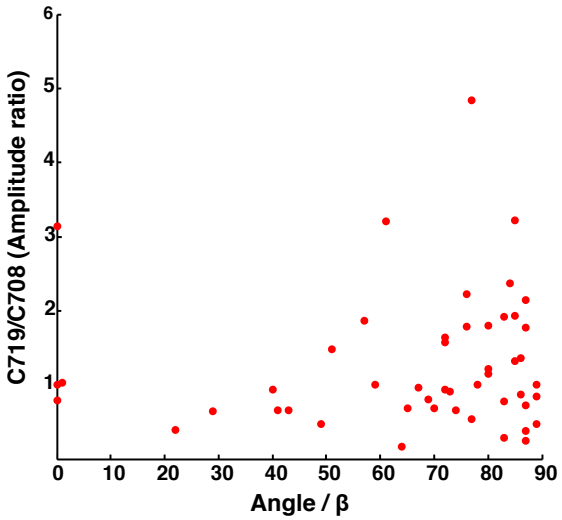

Figure 5. The fluorescence intensity ratio of the contributions C719/C708 versus angle (β) in the fluorescence spectra of single PSI-M.

REFERENCES

1. K. Brettel, "Electron transfer and arrangement of the redox cofactors in photosystem I," *Biochim. Biophys. Acta* **1318**, pp. 322–373, 1997.
2. K. Brettel and W. Leibl, "Electron transfer in photosystem I," *Biochim. Biophys. Acta* **1507**, pp. 100–114, 2001.
3. P. Jordan, P. Fromme, H. T. Witt, O. Klukas, W. Saenger, and N. Krauss, "Three-dimensional structure of cyanobacterial photosystem I at 2.5 å resolution," *Nature* **411**(6840), pp. 909–917, 2001.
4. P. Fromme, P. Jordan, and N. Krauss, "Structure of photosystem I," *Biochim. Biophys. Acta* **1507**(1-3), pp. 5–31, 2001.
5. A. Ben-Shem, F. Frolow, and N. Nelson, "Crystal structure of plant photosystem I," *Nature* **426**(6967), pp. 630–635, 2003.
6. E. El-Mohsnawy, M. J. Kopczak, E. Schlodder, M. Nowaczyk, H. E. Meyer, B. Warscheid, N. V. Karapetyan, and M. Rogner, "Structure and function of intact photosystem I monomers from the cyanobacterium *Thermosynechococcus Elongatus*," *Biochemistry.* **49**, 2010.
7. B. Gobets, M. Ericsson, L. Palsson, V. Shubin, N. Karapetyan, R. van Grondelle, and J. Dekker, "Site selected polarized fluorescence spectroscopy of photosystem I particles isolated from the cyanobacteria *spirulina platensis*," *Prog. Biophys. Mol. Biol.* **65**, pp. 221–221, 1996.
8. L. O. Palsson, C. Flemming, B. Gobets, R. van Grondelle, J. P. Dekker, and E. Schlodder, "Energy transfer and charge separation in photosystem I: P700 oxidation upon selective excitation of the long-wavelength antenna chlorophylls of *synechococcus elongatus*," *Biophys. J.* **74**, pp. 2611–2622, 1998.
9. B. Gobets and R. van Grondelle, "Energy transfer and trapping in photosystem I," *Biochim. Biophys. Acta* **1507**, pp. 80–99, 2001.
10. M. K. Sener, D. Y. Lu, T. Ritz, S. Park, P. Fromme, and K. Schulten, "Robustness and optimality of light harvesting in cyanobacterial photosystem I," *J. Phys. Chem. B* **106**(32), pp. 7948–7960, 2002.
11. A. Rivadossi, G. Zucchelli, F. M. Garlaschi, and R. C. Jennings, "The importance of psi chlorophyll red forms in light-harvesting by leaves," *Photosyn. Res.* **60**, pp. 209–215, 1999.
12. B. Gobets, I. H. M. van Stokkum, F. van Mourik, J. P. Dekker, and R. van Grondelle, "Excitation wavelength dependence of the fluorescence kinetics in photosystem I particles from *synechocystis* PCC 6803 and *synechococcus elongatus*," *Biophys. J.* **85**, pp. 3883–3898, Dec. 2003.
13. B. Bruggemann, K. Sznee, V. I. Novoderezhkin, R. van Grondelle, and V. May, "From structure to dynamics: Modeling exciton dynamics in the photosynthetic antenna PSI," *J. Phys. Chem. B* **108**, pp. 13536–13546, 2004.
14. M. Byrdin, P. Jordan, N. Krauss, P. Fromme, D. Stehlik, and E. Schlodder, "Light harvesting in photosystem I: Modeling based on the 2.5-Å structure of photosystem I from *Synechococcus Elongatus*," *Biophys. J.* **83**, pp. 433–457, 2002.
15. M. Brecht, "Spectroscopic characterization of photosystem I at the single-molecule level," *Mol. Phys.* **107**, pp. 1955–1974, 2009.
16. A. Konrad, A. Trost, S. Skandary, M. Hussels, A. Meixner, and N. Karapetyan, "Manipulating the excitation transfer in photosystem I by a fabry- perot metal resonator with optical sub-wavelength dimensions," *Phys. Chem. Chem. Phys.* **16**, pp. 6175–6181, 2014.
17. E. Boekema, J. Dekker, M. van Heel, M. Rögner, W. Saenger, I. Witt, and H. Witt, "Evidence for a trimeric organization of the photosystem I complex from the thermophilic cyanobacterium *synechococcus sp*," *FEBS Lett.* **217**, pp. 283– 286, 1987.
18. M. U. Rögner, Mühlenhoff, E. J. Boekema, and H. T. Witt, "Mono-,di- and trimeric PS I reaction center complexes isolated from the thermophilic Cyanobacterium *synechococcus sp.* size, shape and activity," *Biochim. Biophys. Acta* **1015**, pp. 415–424, 1990.
19. J. Kruip, D. Bald, E. Boekema, and M. Rögner, "Evidence for the existence of trimeric and monomeric photosystem I complexes in thylakoid membranes from cyanobacteria," *Photosynth. Res.* **40**, pp. 279 – 286, 1994.

20. E. Schlodder, M. Hussels, M. Cetin, N. V. Karapetyan, and M. Brecht, "Fluorescence of the various red antenna states in photosystem I complexes from cyanobacteria is affected differently by the redox state of P700.," *Biochim. Biophys. Acta* **1807**, pp. 1423–31, 2011.
21. S. Turconi, J. Kruip, G. Schweitzer, M. Rögner, and A. R. Holzwarth, "A comparative fluorescence kinetics study of photosystem I monomers and trimers from *synechocystis* PCC 6803.," *Photosynth. Res.* **49**, pp. 263–268, 1996.
22. D. Abramavicius and S. Mukamel, "Exciton delocalization and transport in photosystem I of cyanobacteria *Synechococcus Elongates*: Simulation study of coherent two-dimensional optical signals," *J. phys. chem. B.* **113**, pp. 6097–6108, 2009.
23. L. O. Palsson, J. P. Dekker, E. Schlodder, R. Monshouwer, and R. van Grondelle, "Polarized site-selective fluorescence spectroscopy of the long-wavelength emitting chlorophylls in isolated photosystem I particles of *synechococcus elongatus*," *Photosyn. Res.* **48**, pp. 239–246, 1996.
24. M. Byrdin, I. Rimke, E. Schlodder, D. Stehlik, and T. A. Roelofs, "Decay kinetics and quantum yields of fluorescence in photosystem I from *synechococcus elongatus* with P700 in the reduced and oxidized state: Are the kinetics of excited state decay trap-limited or transfer-limited?," *Biophys. J.* **79**, pp. 992–1007, 2000.
25. B. Gobets, H. van Amerongen, R. Monshouwer, J. Kruip, M. Rögner, R. van Grondelle, and J. P. Dekker, "Polarized site-selected fluorescence spectroscopy of isolated photosystem I particles," *Biochim. Biophys. Acta* **1188**, pp. 75–85, 1994.
26. R. N. Frese, M. A. Palacios, A. Azzizi, I. H. M. van Stokkum, J. Kruip, M. Rogner, N. V. Karapetyan, E. Schlodder, R. van Grondelle, and J. P. Dekker, "Electric field effects on red chlorophylls, beta-carotenes and P700 in cyanobacterial photosystem I complexes," *Biochim. Biophys. Acta* **1554**, pp. 180–191, 2002.
27. V. Zazubovich, S. Matsuzaki, T. W. Johnson, J. M. Hayes, P. R. Chitnis, and G. J. Small, "Red antenna states of photosystem I from cyanobacterium *synechococcus elongatus*: a spectral hole burning study," *Chem. Phys.* **275**, pp. 47–59, 2002.
28. E. Schlodder, M. Cetin, M. Byrdin, I. V. Terekhova, and N. V. Karapetyan, "$P700^+$- and $^3P700$- induced quenching of the fluorescence at 760 nm in trimeric photosystem I complexes from the cyanobacterium *arthrospira platensis*," *Biochim. Biophys. Acta* **1706**, pp. 53–67, 2005.
29. P. Tamarat, A. Maali, B. Lounis, and M. Orrit, "Ten years of single-molecule spectroscopy," *J. Phys. Chem. A.* **104**, pp. 1–16, 2000.
30. T. Vosgröne and A. J. Meixner, "Surface and resonance enhanced micro raman spectroscopy of xanthene dyes: From the ensemble to single molecules," *Chem. Phys. Chem* **6**, pp. 154–163, 2005.
31. A. M. van Oijen, M. Ketelaars, J. Köhler, T. J. Aartsma, and J. Schmidt, "Unraveling the electronic structure of individual photosynthetic pigment-protein complexes," *Science* **285**, pp. 400–402, 1999.
32. Y. Shibata, H. Ishikawa, S. Takahashi, and I. Morishima, "Time-resolved hole-burning study on myoglobin: Fluctuation of restricted water within distal pocket," *Biophys. J.* **80**, pp. 1013–1023, Feb. 2001.
33. C. Hofmann, M. Ketelaars, M. Matsushita, H. Michel, T. J. Aartsma, and J. Köhler, "Single-molecule study of the electronic couplings in a circular array of molecules: Light-harvesting-2 complex from *Rhodospirillum Molischianum*," *Phys. Rev. Lett.* **90**, p. 013004, 2003.
34. Y. Berlin, A. Burin, J. Friedrich, and J. Köhler, "Low temperature spectroscopy of proteins. part II: Experiments with single protein complexes," *Phys. Life Rev.* **4**, pp. 64–89, 2007.
35. H. P. Lu and X. S. Xie, "Single-molecule spectral fluctuations at room temperature," *Nature* **385**, pp. 143–146, 1997.
36. F. Stracke, C. Blum, S. Becker, K. Muellen, and A. Meixner, "Intrinsic conformer jumps observed by single molecule spectroscopy in real time," *Chem. Phys. Lett.* **325**, pp. 196–202, 2000.
37. C. Blum, F. Stracke, S. Becker, K. Muellen, and A. Meixner, "Discrimination and interpretation of spectral phenomena by room-temperature single-molecule spectroscopy," *J. Phys. Chem. A* **105**, pp. 6983–6990, 2001.
38. H. Piwonski, C. Stupperich, A. Hartschuh, J. Sepiol, A. Meixner, and J. Waluk, "Imaging of tautomerism in a single molecule," *J. Am. Chem. Soc.* **127**, pp. 5302–5303, 2005.

39. D. Rutkauskas, V. I. Novoderezhkin, R. J. Cogdell, and R. van Grondelle, "Fluorescence spectroscopy of conformational changes of single LH2 complexes," *Biophys. J.* **88**, pp. 422–435, 2005.
40. F. Schleifenbaum, C. Blum, V. Subramaniam, and A. J. Meixner, "Single-molecule spectral dynamics at room temperature," *Mol. Phys.* **107**, pp. 1923–1942, 2009.
41. M. Brecht, H. Studier, A. F. Elli, F. Jelezko, and R. Bittl, "Assignment of red antenna states in photosystem I from *Thermosynechoccocus Elongatus* by single-molecule spectroscopy," *Biochemistry* **46**, pp. 799–806, 2007.
42. F. Müh and A. Zouni, "Extinction coefficients and critical solubilisation concentrations of photosystems I and II from *Thermosynechococcus Elongatus*," *Biochim. Biophys. Acta* **1708**, pp. 219–228, 2005.
43. M. Hussels, A. Konrad, and M. Brecht, "Confocal sample-scanning microscope for single-molecule spectroscopy and microscopy with fast sample exchange at cryogenic temperatures," *Rev. Sci. Instrum.* **83**, p. 123706, 2012.
44. S. Skandary, A. Konrad, M. Hussels, A. Meixner, and M. Brecht, "Orientations between red antenna states of photosystem I monomers from *thermosynechococcus elongatus* revealed by single-molecule spectroscopy," *Submitted* , 2015.
45. M. Brecht, S. Skandary, J. Hellmich, C. Glöckner, A. Konrad, M. Hussels, A. Meixner, A. Zouni, and E. Schlodder, "Spectroscopic properties of photosystem II core complexes from *Thermosynechococcus elongatus* revealed by single-molecule experiments," *Biochim. Biophys. Acta* **1837**, pp. 773–781, 2014.
46. S. Skandary, M. Hussels, A. Konrad, T. Renger, F. Müh, M. Bommer, A. Zouni, A. Meixner, and M. Brecht, "Variation of exciton-vibrational coupling in photosystem II core complexes from *thermosynechococcus elongatus* as revealed by single-molecule experiments," *J. Chem. Phys. B.* **119**, pp. 4203–4210, 2015.
47. M. Brecht, H. Studier, V. Radics, J. B. Nieder, and R. Bittl, "Spectral diffusion induced by proton dynamics in pigment–protein complexes," *J. Am. Chem. Soc.* **130**, pp. 17487 – 17493, 2008.
48. M. Brecht, V. Radics, J. B. Nieder, and R. Bittl, "Protein dynamics-induced variation of excitation energy transfer pathways," *Proc. Nat. Acad. Sci. USA* **106**, pp. 11857–11861, 2009.
49. T. Förster, "Energiewanderung und Fluoreszenz," *Naturwissenschaften* **33**(6), pp. 166–175, 1946.
50. T. Renger, V. May, and O. Kühn, "Ultrafast excitation energy transfer dynamics in photosynthesis pigment–protein complexes," *Phys. Rep.* **343**, pp. 137–254, 2001.
51. D. Abramavicius, B. Palmieri, D. Voronine, F. Sanda, and S. Mukamel, "Coherent multidimensional optical spectroscopy of excitons in molecular aggregates; quasiparticle versus supermolecule perspectives," *Chem. Rev.* **109**, pp. 2350–2408, 2009.

Chapter 5: Orientations Between Red Antenna States of Photosystem I Monomers from *Thermosynechococcus elongatus* Revealed by Single-Molecule Spectroscopy

Numerous studies [20, 22, 30], revealed that Chl *a* molecules have a crucial impact on the kinetics of energy transfer and trapping. Up to now, it is under discussion whether the energy transfer within this antenna system proceeds along well-defined pathways or utilizes variable routes [78, 97, 136]. For this purpose, it is necessary to obtain more details about spectral distributions of these Chl *a* molecules using the advantages of various spectroscopic methods. Finding out detailed information about the LWCs of PSI-M responsible for the emissions of red contributions, polarization dependent experiments on single PSI-M were performed, which allow to draw conclusions on the relative orientation of the respective red Chls.
The polarization dependent measurements reveal two spectrally separated fluorescence bands of single PSI-M complexes at low temperature with distinguishable polarization. The analysis of these datasets indicates that the orientation between the emitters corresponding to these two contributions depends on the mutual orientations between the TDMs of the respective emitters. Moreover, the experimental and simulation results are compared. This comparison enables one to estimate the real angle between the TDMs of the respective emitters of C708 and C719. Finally, several candidates for red coupled Chl dimers based on the X-ray structure of PSI are discussed. [33]. This chapter is adapted from the paper in ref. [77].

THE JOURNAL OF PHYSICAL CHEMISTRY B

Article

pubs.acs.org/JPCB

Orientations between Red Antenna States of Photosystem I Monomers from *Thermosynechococcus elongatus* Revealed by Single-Molecule Spectroscopy

Sepideh Skandary,[†] Alexander Konrad,[†] Martin Hussels,[†] Alfred J. Meixner,[†] and Marc Brecht*[,†,‡]

[†]IPTC and Lisa+ Center, University of Tübingen, D-72076 Tübingen, Germany

[‡]Zurich University of Applied Science (ZHAW), CH-8401 Winterthur, Switzerland

Supporting Information

ABSTRACT: Single-molecule spectroscopy at low temperature was used to study the spectral properties, heterogeneities, and spectral dynamics of the chlorophyll *a* (Chl *a*) molecules responsible for the fluorescence emission of photosystem I monomers (PS I-M) from the cyanobacterium *Thermosynechococcus elongatus*. The fluorescence spectra of single PS I-M are dominated by several red-shifted chlorophyll *a* molecules named C708 and C719. The emission spectra show broad spectral distributions and several zero-phonon lines (ZPLs). Compared with the spectra of the single PS I trimers, some contributions are missing due to the lower number of C719 Chl's in monomers. Polarization-dependent measurements show an almost perpendicular orientation between the emitters corresponding to C708 and C719. These contributions can be assigned to chlorophyll dimers B18B19, B31B32, and B32B33.

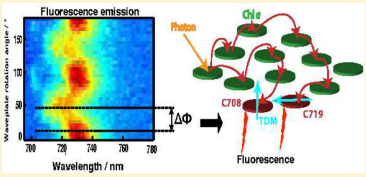

INTRODUCTION

Photosystem I (PS I) is one of two transmembrane pigment–protein complexes essential for oxygenic photosynthesis. It is located in the thylakoid membranes of cyanobacteria, algae, and plants and mediates light-induced electron transfer from plastocyanin or cytochrome C_6 on the lumenal side to ferredoxin on the stromal side.[1] The first step of the photosynthetic reaction is the absorption of a photon by the antenna system of PS I, followed by subsequent energy transfer to the reaction center. At this point, the captured excitation energy is used to induce a transmembrane charge separation starting at the chlorophyll (Chl) pair P700, which has its main absorption at 700 nm.[1,2]

The absorption spectra of PS I from green plants, algae, and cyanobacteria show the existence of Chl *a* molecules absorbing at lower energy with respect to the usual Q_y absorption at 664 nm for Chl *a* in 80% acetone,[3,4] and in particular at wavelengths larger than that of the primary donor P700.[5,6] These red-shifted Chl *a* molecules are often called the long-wavelength (also red or low-energy) Chl's (LWCs).[7] If the excitation energy is localized at these LWCs, a direct excitation of P700 is not possible any more, and the energy is trapped. Additional activation energy, e.g., thermal energy provided by the phonon bath, is necessary to oxidize P700 and start the charge separation process.[8−11] (For a detailed discussion of the properties of the red-Chl *a*, we refer the reader to ref 12.)

Detailed analysis of the absorption spectra of *Thermosynechococcus elongatus* yields the separation of the red emitting Chl's into two pools.[13−16] Their main absorption bands are at 708 and 719 nm, denoted commonly as C708 and C719, respectively. The distinction of two pools remains tentative due to a large spectral overlap of the respective bands.[13] Additionally, a red subpool (C715) was found by analysis of non-photochemical hole-burning spectra.[17] Estimations for the number of Chl *a* molecules involved in the red pool in *Th. elongatus* are based on the integrated absorbance at wavelengths longer than 700 nm. Zazubovich et al.[17] determined 7 Chl *a*'s belonging to the red pool (under the assumption that 96 Chl *a* molecules are in one PS I monomer), while Palsson et al.[13,18] estimated 9−11 Chl *a* molecules (assuming 110 Chl *a* molecules). Normalized to same number of Chl *a*'s, both estimations are in reasonable agreement.[19] Numerous studies[6,7,14] revealed that these Chl's have a crucial impact on the kinetics of energy transfer and trapping. Until now, it has been under discussion whether the energy transfer within this antenna system proceeds along well-defined pathways or utilizes variable routes.[20−22] For this purpose, it is necessary to obtain more details about the spectral distributions of these Chl *a* molecules using the advantages of various spectroscopic methods.

PS I from cyanobacteria can be isolated in monomeric and trimeric forms.[23,24] The trimer is proposed to be the native form, at least under certain physiological conditions.[25] Both the trimeric and monomeric species absorb light at room temperature and show a probability of >95% of inducing charge separation.[26] Energy exchange between monomers seems to be negligible, and as a consequence single monomer can be used to describe the optical properties of PS I. [27]

Special Issue: Wolfgang Lubitz Festschrift

Received: May 10, 2015
Revised: July 8, 2015

DOI: 10.1021/acs.jpcb.5b04483
J. Phys. Chem. B XXXX, XXX, XXX−XXX

At room temperature, the quantum efficiency of photochemistry is virtually not affected by the LWCs. However, recent studies using far-red excitation provided a deeper insight into the efficiency of charge separation by LWCs in PS I. [12] The thermal energy of the surrounding enables efficient uphill energy transfer via bulk Chl's to P700. At cryogenic temperatures, however, the fluorescence of the long-wavelength pigments increases considerably, suggesting that a significant part of the excitation energy is no longer able to reach P700. [6] Thus, at lower temperatures, the red Chl's act as traps for the excitation energy, which means the quantum efficiency of the charge separation decreases while the fluorescence intensity increases.[6,28]

The numbers of LWCs for trimeric and monomeric PS I from *Th. elongatus* are equal in C708, but they are lower in C719 for monomers.[6] The absorption spectra of the trimeric complexes at 5 K indicate a more ordered structure compared with monomers. The most remarkable difference can be observed around 720 nm, where the monomeric complexes show less absorption. In addition, the quantum yield of charge separation in monomers is higher than that in trimers at 4 K, which can be explained by the lower number of LWCs in C719.[6]

Due to the unstructured shape of the ensemble fluorescence spectra, it is difficult to obtain detailed information about the spectral characteristics of the red pools.[15] Therefore, site-selective spectroscopic techniques like spectral hole burning, fluorescence line narrowing,[29] and single-molecule spectroscopy (SMS)[30,31] are effective methods. SMS is an excellent technique to cope with inhomogeneous broadening and reveals subtle spectral details often obscured by averaging over heterogeneous ensembles.[30,32]

At room temperature, spectral diffusion and photobleaching hamper the collection of detailed spectroscopic information for most single molecules.[33−39] Lowering the temperature reduces the impact of spectral diffusion,[39−41] and the emission profile of a single emitter composed of a sharp zero-phonon line (ZPL) and so-called phonon wing (PW), which consist of vibrational sidebands, becomes observable.[42−45] The PW on the low-energy side of the ZPL is caused by the interaction of the chromophore with its surroundings, leading to the excitation of phonons (lattice vibrational modes).[46]

The first single-molecule spectra of PS I at cryogenic temperature were recorded by Jelezko et al.[47] Furthermore, assignment of red antenna states in single PS I-T from *Th. elongatus* was reported by Brecht et al.[19] In this study, we show the fluorescence of single PS I-M from *Th. elongatus* at 1.6 K for the first time. To obtain detailed information about the LWCs of PS I-M responsible for the emissions of these contributions, we performed polarization-dependent experiments on single PS I-M, allowing us to draw conclusions about the relative orientation of the respective red Chl's. The polarization-dependent measurements reveal two spectrally separated fluorescence bands at low temperature with distinguishable polarization. Analysis of our data sets indicates that the orientation between the emitters corresponding to these two contributions depends on the mutual orientation of the transition dipole moments (TDMs) of the respective emitters. Moreover, we compare our experimental results with simulations based on the projected polarization of a randomly oriented pairs of emitting dipoles with fixed angles. This comparison enables us to estimate the real angle between the TDMs of the respective emitters of C708 and C719. Finally, we discuss several candidates for red-coupled Chl dimers based on the X-ray structure of PS I. [48]

MATERIALS AND METHODS

Sample Preparation. PS I-Ms from *Th. elongatus* have been isolated as described in refs 49 and 50. The purified PS I-Ms were diluted in buffer solution (pH 7.5) containing 20 mM Tricine, 25 mM $MgCl_2$, and 0.4 mM β-DM detergent to reach a Chl *a* concentration of 20 μM. This amount of detergent is adequate for the critical solubilization of a PS I-M concentration of 0.5 μM to avoid PS I aggregation.[51] In further steps, the PSI-containing (buffer) solution was diluted (with the same buffer conditions) to a PS I-M concentration of ∼3 pM. About 1 μL of this suspension was placed between two glass coverslips. Finally, the sample was transferred directly into the cryostat and rapidly plunged into liquid helium. Experiments were carried out using a home-built confocal microscope operating at 1.6 K, as described in ref 52.

A broadband fiber laser with 40 MHz repetition rate (SuperK Extreme 40 MHz VIS, NKT Photonics) combined with an acousto-optic tunable filter set to 675 nm was used for excitation. The excitation intensity of the laser was 10 μW, measured before entering the cryostat. The highest resolution of the spectrometer (Shamrock 500 spectrograph with 400 lines/mm gratings in combination with Andor Newton back-illuminated deep-depleted CCD) is ∼0.05 nm. In a sequence of spectra, the usual exposure time for each spectrum was 2 s. For polarization measurements, a combination of a $\lambda/2$ waveplate (10RP52-2, Newport) on a motorized rotator (PRM1/MZ8, Thorlabs) and a polarizing beam displacer (BD27, Thorlabs) can be moved into the optical path in front of the spectrograph. The polarizing beam displacer splits the light into two beams with perpendicular polarizations, which can be acquired individually by the CCD camera. In combination with the rotating $\lambda/2$ waveplate, it is possible to measure spectrally resolved the fluorescence intensity as a function of rotator angle.[52]

Data Evaluation Process. For determining the phase between different contributions in fluorescence emission, an analysis based on discrete Fourier transformation was applied on two-dimensional fluorescence spectra, which are recorded as a function of waveplate rotation angle. Using our setup described above, the s- and p-polarized components of the emission are acquired simultaneously. Rotating the $\lambda/2$ waveplate, two fluorescence spectra series can be recorded, depending on the rotation angle of the waveplate with respect to the initial orientation. Both spectra series contain same information and differ only in phase. The $\lambda/2$ waveplate rotates the polarization of the incident light by double the angle between the polarization plane and toward the crystal axis. Together with the symmetry of polarization, this leads to a modulation period of 90° rotation angle of the waveplate. In addition, with the known frequency of the rotator this gives the expected modulation frequency of the spectra along the angle axis. For more information, see Supporting Information S1.

Determination of the Phase Difference between Two Arbitrarily Distributed Vectors. For a pair of emitting dipoles, representing the contributions of the polarization-dependent fluorescence data sets, their TDMs are denoted as $\vec{\mu}_1$ and $\vec{\mu}_2$, enclosing the angle α. In our case, $\vec{\mu}_1$ corresponds to the TDM of the emitter C708 and $\vec{\mu}_2$ corresponds to the TDM of the emitter C719, whereby the angle α is assumed to be constant for all single PS I-M complexes. However, the

DOI: 10.1021/acs.jpcb.5b04483
J. Phys. Chem. B XXXX, XXX, XXX−XXX

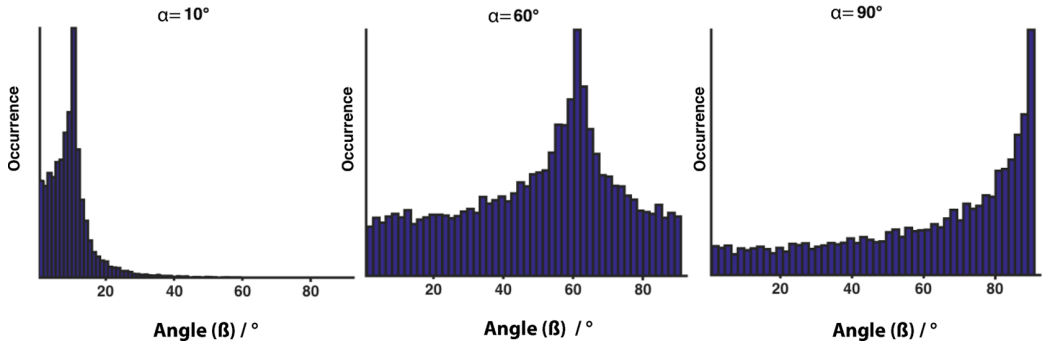

Figure 1. Angular distribution for the projection of a randomly rotated pair of vectors with fixed angles α = 10°, 60°, and 90°. The maximum of the phase difference distributions stays with the fixed angle.

orientation of each observed single PS I-M complex and also the pair of vectors corresponding to the respective emitters are arbitrarily distributed in space. By our measurement technique, we are not able to observe the three-dimensional polarization vectors but only their two-dimensional projections onto the plane of the camera, denoted as $\vec{\nu}_1$ and $\vec{\nu}_2$, which enclose the angle β. However, determining a large distribution of angles β from different polarization-dependent data sets of the single PS I-M complexes, enables us to draw conclusions on the value of α. Therefore, a simple simulation is used to illustrate the distribution of the projected angles for the randomly oriented vector-pair depending only on the angle α. Therefore, two vectors $\vec{\mu}_1$ and $\vec{\mu}_2$ with angle α are randomly rotated using Euler rotation theorem and then projected into the detection plane in order to get the projected angle β. For more details, see Supporting Information S2. Repeating this procedure for a large number of random rotations, yields a broad distribution for a given α, exhibiting its maximum occurrence around the value of α. In Figure 1, the distribution of the observable angles β is shown exemplarily for α = 10°, 60°, and 90°. It can be seen that each histogram exhibits its maximum around the given angle α. Respecting the experimental restriction, we are not able to detect fluorescence of emitters, $\vec{\mu}_1^*$ or $\vec{\mu}_2^*$, oriented perpendicular to the detection plane. We excluded the respective angles β from the distribution of one of the randomly oriented vectors related 10° or less to the optical axis because they cannot be detected due to the limitation of the objective numerical aperture. Thus, by experimentally determining a statistically significant number of angles β, each representing the evaluated phase of a polarization-dependent data sets, we are able to determine α.

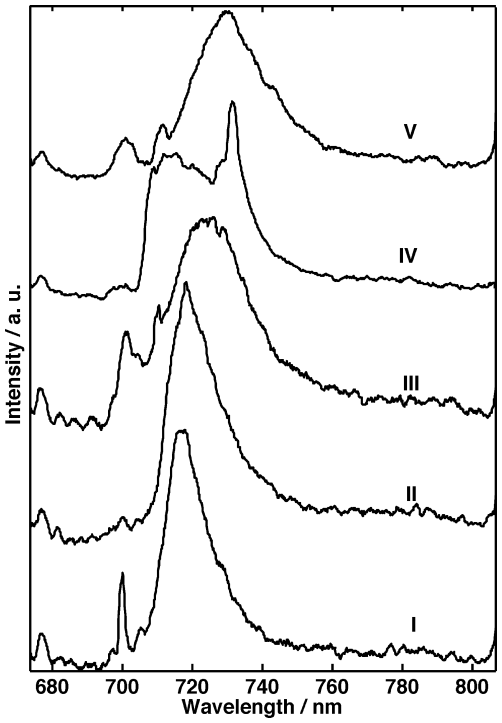

Figure 2. Single-molecule fluorescence spectra of PS I-M from *Th. elongatus*. Spectra were recorded on different individual complexes at 1.6 K. For better comparability, all spectra are scaled to a similar magnitude. The accumulation time was 72 s. Excitation wavelength was 675 nm.

RESULTS

The spectral properties of the fluorescence spectra series of 70 individual PS I-M were analyzed at low temperature (1.6 K). A selection of five fluorescence spectra (denoted *I*–*V*) of different single PS I-M is shown in Figure 2. The complete acquisition time for each data set was 72 s. For better comparability, all spectra were scaled to a similar magnitude. The emission spectra of single PS I-M are characterized by sharp ZPLs and a broad intensity distribution covering the whole emission range from 700 to 780 nm.

Despite of all differences between the dynamics of the emitters in time-dependent data sets of single PS I-M, the fluorescence range covered by the ZPLs is restricted to a defined spectral range within nanometer scale. However, the ZPLs are not prominently distributed in all spectra series but they are visible in few data sets, whereby their spectral distribution as well as their time-dependent behavior varies from complex to complex. For more detailed information, please see Supporting Information S3 and S4.

Figure 3 shows the average emission spectrum obtained for the summation of all 70 data sets of single PS I-M (red curve). The maximum intensity is located at 726.6 ± 0.5 nm, which is close to the values reported for single PS I-T from *Th. elongatus* in buffer solution (blue curve, taken from ref 53). The corresponding fwhm for single PS I-M is 29.6 ± 0.4 nm, whereas for single PS I-T, fwhm is slightly wider (31.8 ± 0.5 nm).[53] Additionally, in the average spectrum of single PS I-M (see Figure 3) some contributions are missing in intervals between 730 and 760 nm compared to the average spectrum of trimers (see Discussion).

DOI: 10.1021/acs.jpcb.5b04483
J. Phys. Chem. B XXXX, XXX, XXX−XXX

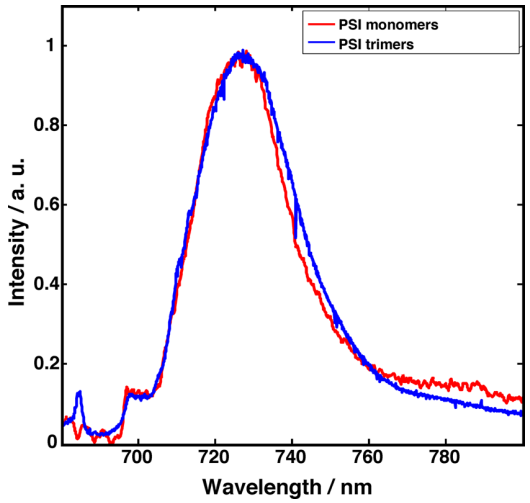

Figure 3. Average spectra obtained from the summation of 70 PS I-M (red curve) and 137 PS I-T (blue curve) data sets in buffer solution. The average spectrum of PS I-T is taken from ref 53. Both data sets are scaled to a similar amplitude for a better comparison.

The number and spectral positions of emitters responsible for the fluorescence of single PS I-M are obtained from the analysis of their polarization. Figures 4 and 5 show two fluorescence data sets of a single PS I-M as a function of the rotation angle of the waveplate in front of the spectrograph. This angle is defined with respect to an arbitrary laboratory axis and is uncorrelated to the polarization of the excitation light. In both data sets, the dependence of the emission spectra on the waveplate orientation is shown for s- and p-polarization. However, the accumulation time was increased to 10 s to enhance the S/N ratio, because the intensity of signal was attenuated in the presence of the wave plate and the polarizing beam displacer. Figure 4a shows the time-dependent data sets of single PS I-M and the respective average spectrum on top. A broad emission band can be seen in the time-dependent spectra series and in the average spectrum. Figure 4b shows the spectra of a single PS I-M complex with distinguished s- and p-polarization data sets. Here, two contributions are visible with separated spectral positions. When the contribution with peak position at 715.9 nm is intense (e.g., s-polarization data set) the other at 729.2 nm is weak. This behavior is consistent for the whole spectra series of this data set. Therefore, an almost perpendicular alignment between the projected polarization vectors of the respective contributions can be estimated. Figure 4c shows the integrated emission intensity for both contributions as a function of rotation angle over the spectral range between 706.7 and 749.3 nm. In this representation, it can be seen more clearly that the intensity of each emitter is shifted by almost 45° by the angle of the waveplate. Due to that phase shift, an almost perpendicular orientation of the projected polarization vectors can be assigned.

Figure 5a shows another time-dependent data set and the average spectrum on top. Figure 5b shows a weak contribution with spectral peak positions at 715.2 nm and an intense contribution at 730.4 nm in data sets with s- and p-polarization. The contributions show a certain overlap in time-dependent spectra series. In contrast to the data set in Figure 4b, both contributions show nearly no phase shift (see Figure 5c). Thus, a parallel alignment of the projected polarization vectors can be assumed. This difference between these two data sets can be explained simply by the different orientations of observed single PS I-M complexes. As described above, the phase between both contributions of single PS I-M were determined for each data

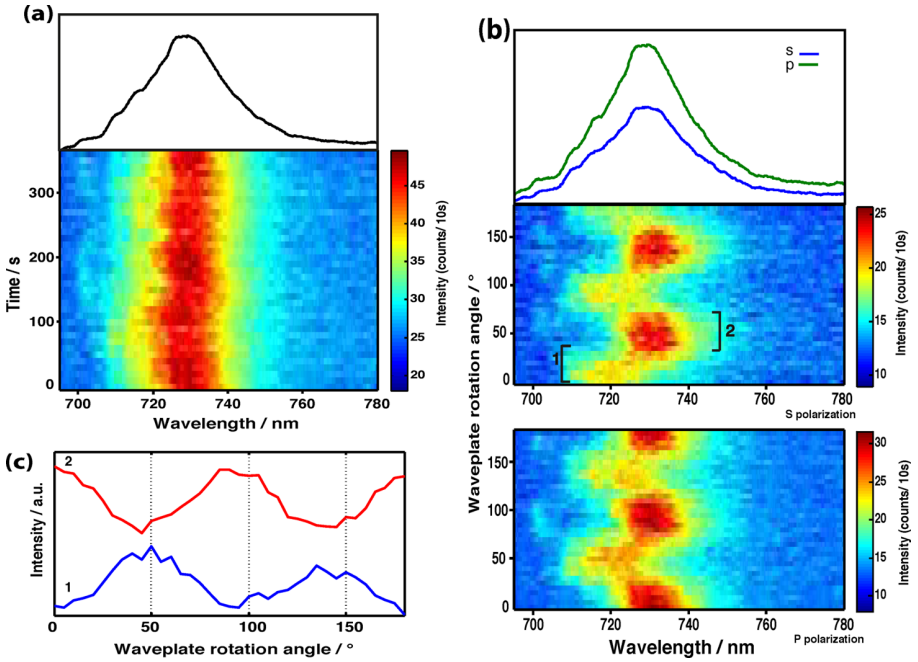

Figure 4. (a) Time-dependent data sets and the average on the top. Excitation wavelength 675 nm; temperature 1.6 K. (b) Sequence of fluorescence spectra of a single PS I-M as a function of the rotation of the waveplate in front of the spectrograph is shown. Two contributions are numbered at their spectral positions. This data set contains 37 spectra, and the acquisition time was 10 s for each spectrum. The individual spectra were recorded in steps of 5°. The waveplate rotation angle is shown on the right side. (c) Integrated fluorescence intensity versus angle of two corresponding contributions of the single PS I-M is shown. The angle between two contributions has been estimated around 90°.

DOI: 10.1021/acs.jpcb.5b04483
J. Phys. Chem. B XXXX, XXX, XXX−XXX

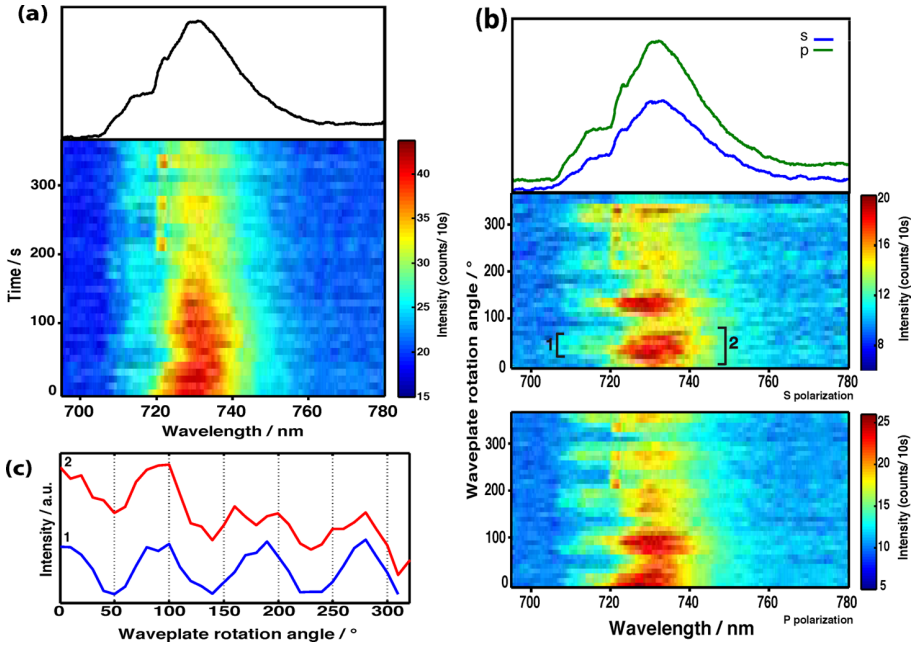

Figure 5. (a) Time-dependent data sets and the average on the top. Excitation wavelength 675 nm; temperature 1.6 K. (b) Sequence of fluorescence spectra of a single PS I-M as a function of the rotation of the waveplate in front of the spectrograph is shown. Two contributions are numbered at their spectral positions. This data set contains 37 spectra, and the acquisition time was 10 s for each spectrum. The individual spectra were recorded in steps of 10°. The waveplate rotation angle is shown on the right side. (c) Integrated fluorescence intensity versus angle of two corresponding contributions of the single PS I-M is shown. The angle between two contributions has been estimated around 0°.

set using data evaluation process explained in the Materials and Methods section (also see Supporting Information S1). Only data sets with tilted and distorted spectral shapes were not used for analysis. Therefore, by applying our evaluation method described above on 49 data sets, statistically significant distribution of angles β could be determined. In Figure 6,

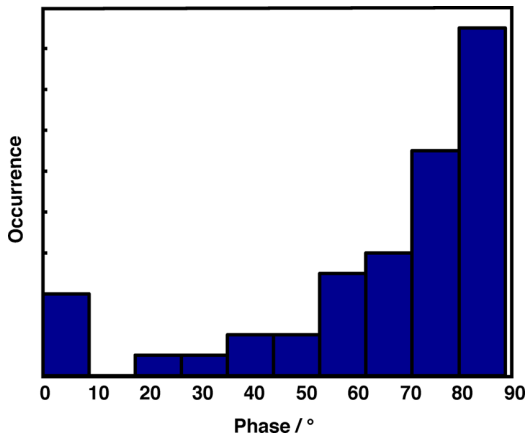

Figure 6. Distribution of angles between two contributions of single PS I-M from *Th. elongatus* for 49 fluorescence polarization-dependent data sets.

this distribution is shown and has its maximum between 80 and 90°. The histogram shows a decay profile for decreasing angles from 90 to 10°, as expected from simulations. Comparing the experimentally determined distribution (Figure 6) with the simulated histograms (Figure 1), we approximate α be within the range between 80 and 90°.

The analysis of the polarization measurements allows us to clearly distinguish overlapping emission bands in the fluorescence. In Figure 7, the distributions of the spectral

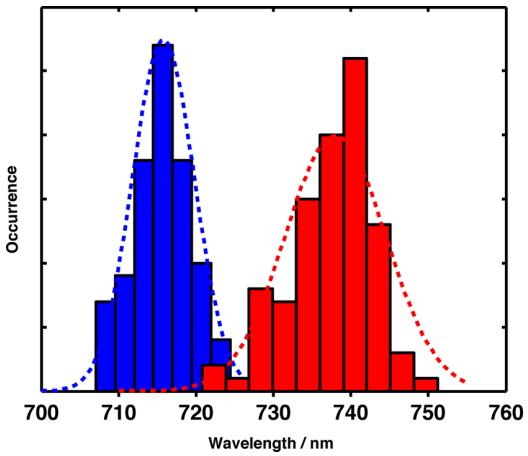

Figure 7. Histogram plots obtained from the statistical analysis of the fluorescence polarization spectra of single PSI-M. Blue histograms show the spectral distributions of C708 contributions. Red histograms show the spectral distributions of C719 contributions. Dotted lines are Gaussian fitted curves for each contribution.

peak positions of the short (blue bars) and the long (red bars) wavelength contributions of all data sets of single PS I-M are shown. The spectral distribution of each contribution has been assigned regardless whether the intense contribution is a ZPL or broad emission. Figure 7 clearly demonstrates two spectrally separated contributions in single PS I-M data sets whereas spectra without polarization-dependent analysis show only one broad emission band over the whole wavelength range.

DOI: 10.1021/acs.jpcb.5b04483
J. Phys. Chem. B XXXX, XXX, XXX−XXX

Table 1. Angles (deg) between the TDMs of the Candidates for the Red-Emitting Chl's in PS I-M from *Th. elongatus*[a]

Coupled Chl *a*	B22B34	B31B32	B32B33	A24A35	A38A39	A33A34	A26A27	B24B25	A16A17	B37B38	A16A25	A31A32	A32B7
B18B19	**90**	**86**	**80**	78	50	66	44	45	22	52	50	61	53
B22B34		61	70	12	**80**	65	**86**	**81**	69	**87**	74	45	73
B31B32			11	73	58	69	63	60	**88**	60	58	34	34
B32B33				47	31	48	39	36	**80**	32	48	37	28
A24A35					**88**	59	**85**	**90**	58	**85**	65	54	**81**
A38A39						39	8	5	50	8	27	43	7
A33A34							35	39	50	31	16	72	45
A26A27								5	42	8	21	41	15
B24B25									49	9	26	36	10
A16A17										30	37	74	56
B37B38											20	42	14
A16A25												62	34
A31A32													28

[a]Those angles larger than 80° matching our experimentally acquired result are highlighted in bold.

DISCUSSION

The fluorescence spectra of the individual PS I-M are dominated by ZPLs and broad intensity distributions (Figure 2) at low temperatures. These contributions differ in number, intensity, and wavelength positions for each single PS I-M. In our data sets, the fluorescence spectra of single PS I-M can be separated into two wavelength regions: the region <710 nm where almost stable ZPLs are detected and the region >710 nm, where broad intensity distributions are dominating the spectra (see Supporting Information S3 and S4). Spectral diffusion is the main broadening mechanism within the time scale of the actual accumulation time (2 s).[36,54,55] The broadening mechanism is comparable for C708 and C719, the difference is the value of the electron−phonon coupling. Based on the initial shape of the single emitter, the spectral diffusion process yields a faster broadening for emitters with high Huang−Rhys factors (C719) than for those with lower Huang−Rhys factors (C708). The average spectrum of all single-complex PS I-M data sets (Figure 3) is in good agreement with the results reported for ensemble spectra of PS I-M by Schlodder et al. with oxidized P700.[50] Comparing our spectra with this reference is most reasonable, because due to the high flux of light, which is necessary to perform SMS, P700 is held out in its oxidized state.[19,50] As shown by Figure 3, the fluorescence of monomers and trimers show comparably intensities between 705 and 730 nm, while the intensity of the monomer spectrum is decreased between 730 and 760 nm. This can be explained by the different number of Chl's. The PS I-M and PS I-T complexes have the same number of red Chl's for C708, whereas PS I-M complex contains lower number of C719 Chl's;[6,50] in trimers some strongly coupled aggregates contributing to C719 are present as a result of the trimerization.[49,50]

Single-molecule spectroscopy combined with the polarization measurement provides a detailed insight into the fluorescence dynamics of the red Chl's and their interaction with other chromophores mainly mediated by excitation energy transfer (EET). Single PS I-M complexes show less spectral diversity of their fluorescence compared with PS I-T. Therefore, the analysis of the polarization-dependent data sets from single PS I-M is more feasible than for PS I-T. Using our polarization measurements we are able to separate two contributions of single monomer fluorescence into blue and red wavelength bands showing almost no spectral overlap. The blue wavelength band of single PS I-M at <720 nm is assigned to C708,[47,56,57] whereas the red wavelength band at >720 nm is most probably related to the emission of C719.[19,21] The evaluation of the angles between the projected polarization vectors corresponding to these contributions show a maximum between 80 and 90° (Figure 6). By the comparison of this distribution with simulated histograms, we are able to estimate an almost perpendicular three-dimensional orientation of the TDMs corresponding to C708 and C719.

This insight allows us to discuss the possible energy transfer pathways responsible for exciting C708 and C719. The EET between chromophors is usually described by the framework of FRET originally developed by Förster.[58] To describe an antenna pigment as a part of the energy transfer chain, it is shown that the EET depends on the distance and orientations of TDMs of the molecules by using the dipole−dipole approximation:[20,59,60]

$$V_{12} = \frac{\overrightarrow{\mu_1}\cdot\overrightarrow{\mu_2}}{r^3} - 3\frac{(\overrightarrow{\mu_1}\cdot\vec{r})(\overrightarrow{\mu_2}\cdot\vec{r})}{r^5} \quad (1)$$

Here, V_{12} is the coupling potential between two dipoles, $\vec{\mu}_1$ and $\vec{\mu}_2$ representing the TDMs of the red pools, $\vec{r}$ is the vector connecting the centers of the dipoles, and r is their separation in space. Orientation factor κ is defined by $\kappa = \hat{u}\cdot\hat{v} - 3(\hat{u}\cdot\hat{R})(\hat{v}\cdot\hat{R})$, with $\hat{u}$ and $\hat{v}$ being unit vectors of TDMs and $\hat{R}$ the unit vector of the line joining their centers.[20] According to this, if the TDMs of two dipoles are oriented almost perpendicular to each other, their κ tends toward zero ($V_{12} \simeq 0$) if their connection vector also has a perpendicular orientation to the center of TDMs. For such a weak coupling, each dipole can be considered as a separate emitter. For parallel orientation the coupling potential is maximized, which can lead to strong coupling between two Chl's behaving together as one emitter. Apparently, our polarization-dependent fluorescence data sets show two spectrally separated and mutually perpendicular arranged emitters at the wavelengths assigned to C708 and C719.

To obtain more detailed information about the emission from the coupled LWCs assigned to C708 and C719 in PS I-M complex, we calculated the orientations between coupled red Chl candidates in PS I complexes from *Th. elongatus* discussed in the literature.[8,20,48,50,61] The orientations of their respective TDMs were calculated using the spatial information on the Chl's provided by the X-ray structure of PS I from *Th. elongatus* (1JB0;[48] see Supporting Information S5). Table 1 shows the

DOI: 10.1021/acs.jpcb.5b04483
J. Phys. Chem. B XXXX, XXX, XXX−XXX

results of these calculations whereas the candidate-pairs enclosing angles larger than 80 degree are highlighted. The suggested dimer candidates in Table 1 were taken from Byrdin et al.[20] Among the Chl's showing almost perpendicular orientation, those pairs assigned to the same Chl pool, e.g., C708 or C719, can be ruled out as potential candidates, because in our polarization-dependent data sets, we did not observe two perpendicular contributions both at the wavelengths assigned to C708 or C719. Therefore, the dimer pairs B18B19−B22B34, B22B34−A38A39, and B22B34−B37B38 should be ruled out due to their assignment to C708,[8,50,61] If there is a second emitter in the blue wavelength region we should have observed two components for the blue wavelength range. The results from reduced-minus-oxidized spectra showed that the emission from C715 is probably quenched by oxidized P700 (see Figure 4 in ref 50). Thus, the dimers assigned to C715 (A26A27, A24A35, and B24B25)[8,50] cannot be candidates for the red wavelength range.

Under these assumptions, dimers B18B19 and A16A17, assigned to C708,[50] and B31B32 and B32B33, assigned to C719,[50] with matching mutual orientations remain. However, A16A17 cannot be considered as a strongly coupled dimer, and its TDM of the low-energy exciton state is not parallel-oriented to the membrane plane;[20] therefore, A16A17−B31B32 and A16A17−B32B33 are not suitable candidates. So, the remaining candidates are B18B19−B31B32 (C708−C719) and B18B19−B32B33 (C708−C719), exhibiting strong excitonic coupling energy and a parallel orientation of their low-energy excitonic state to the membrane plane.[20,50,61] Moreover, calculating the orientation factor κ for the candidates B18B19−B31B32 (κ = 0.32) and B18B19−B32B33 (κ = 0.55) yields very low, almost negligible coupling potential. Thus, we can conclude that there is no direct energy transfer pathway between these two pools within PS I-M complexes. Both C708 and C719 have to be fed from different, energetically higher lying antenna states by two different pathways (see Figure 8). From this, we can conclude that the energy transferred from higher lying energy states to the red Chl's at low temperature is not trapped only by one final lowest energy state.[21] Their fluorescence is expected in the blue and red wavelength regions, respectively. Consequently, we can conclude that these pairs might be the most promising candidates responsible for the fluorescence of PS I-M.

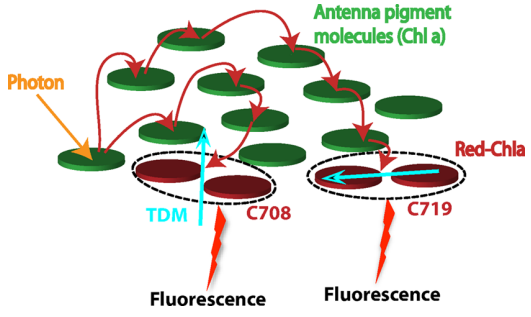

Figure 8. Schematic representation of the EET in PS I-M. The number of participating Chl *a* molecules was reduced to the minimal number sufficient for the qualitative description. Red Chl's coupled as dimers schematically show two main emitters of PS I-M, with perpendicular TDMs assigned to C708 and C719. It illustrates a direct feeding of the red pools C708 and C719 by energetically higher lying antenna states where each one emits separately due to their perpendicular TDMs.

CONCLUSION

The fluorescence of a single PS I-M from *Th. elongatus* shows the same contributions for C708 as the fluorescence of a single PS I-T; differences in the contributions are attributed to C719, mostly due to the lower number of C719 Chl's in monomers. The polarization-dependent data set of a single PS I-M complex demonstrates two spectrally separate emissions, corresponding to C708 and C719. We estimate almost perpendicular orientation between these two contributions and conclude that they are not connected with each other via energy-transfer pathways. Finally, these contributions can be assigned to Chl dimers B18B19, B31B32, and B32B33.

ASSOCIATED CONTENT

Supporting Information

The Supporting Information is available free of charge on the ACS Publications website at DOI: 10.1021/acs.jpcb.5b04483.

S1, procedure for determining the angle between dierent components in polarization-dependent data sets; S2, description of a pair of emitting dipoles with arbitrary distributions; S3, statistical analysis of kinetic information; S4, spectral positions of ZPLs; and S5, illustration of the TDM vector of a Chl *a* molecule and the coupling vectors (PDF)

AUTHOR INFORMATION

Corresponding Author

*Phone: +49-7071-29-76239. Fax: +49-7071-29-5490. E-mail: marc.brecht@uni-tuebingen.de.

Notes

The authors declare no competing financial interest.

ACKNOWLEDGMENTS

We thank Dr. Eberhard Schlodder for the PSI samples and helpful discussions. This work was supported by Heisenberg-Program of the Deutsche Forschungsgemeinschaft (DFG BR 4102/1-1 and BR 4102/2-1), along with financial support from the German Research Council (DFG ME1600/13-1).

REFERENCES

(1) Brettel, K. Electron Transfer and Arrangement of the Redox Cofactors in Photosystem I. *Biochim. Biophys. Acta, Bioenerg.* **1997**, *1318*, 322−373.

(2) Brettel, K.; Leibl, W. Electron Transfer in Photosystem I. *Biochim. Biophys. Acta, Bioenerg.* **2001**, *1507*, 100−114.

(3) Schlodder, E. Introduction to Optical Methods in Photosynthesis. *Photosynth. Res.* **2009**, *101*, 93−104.

(4) Porra, R.; Thompson, W.; Kriedemann, P. Determination of Accurate Extinction Coefficients and Simultaneous-Equations for Assaying Chlorophyll-a and Chlorophyll-b Extracted with 4 Different Solvents-Verification of the Concentration of Chlorophyll Standards by Atomic-Absorption Spectroscopy. *Biochim. Biophys. Acta, Bioenerg.* **1989**, *975*, 384−394.

(5) Gobets, B.; Ericsson, M.; Palsson, L.; Shubin, V.; Karapetyan, N.; van Grondelle, R.; Dekker, J. Site Selected Polarized Fluorescence Spectroscopy of Photosystem I Particles Isolated from the Cyanobacteria *Spirulina Platensis*. *Prog. Biophys. Mol. Biol.* **1996**, *65*, 156.

(6) Palsson, L. O.; Flemming, C.; Gobets, B.; van Grondelle, R.; Dekker, J. P.; Schlodder, E. Energy Transfer and Charge Separation in Photosystem I: P700 Oxidation Upon Selective Excitation of the Long-Wavelength Antenna Chlorophylls of *Synechococcus Elongatus*. *Biophys. J.* **1998**, *74*, 2611−2622.

DOI: 10.1021/acs.jpcb.5b04483
J. Phys. Chem. B XXXX, XXX, XXX−XXX

(7) Gobets, B.; van Grondelle, R. Energy Transfer and Trapping in Photosystem I. *Biochim. Biophys. Acta, Bioenerg.* **2001**, *1507*, 80−99.
(8) Sener, M. K.; Lu, D. Y.; Ritz, T.; Park, S.; Fromme, P.; Schulten, K. Robustness and Optimality of Light Harvesting in Cyanobacterial Photosystem I. *J. Phys. Chem. B* **2002**, *106*, 7948−7960.
(9) Rivadossi, A.; Zucchelli, G.; Garlaschi, F. M.; Jennings, R. C. The Importance of PSI Chlorophyll Red Forms in Light-Harvesting by Leaves. *Photosynth. Res.* **1999**, *60*, 209−215.
(10) Gobets, B.; van Stokkum, I. H. M.; van Mourik, F.; Dekker, J. P.; van Grondelle, R. Excitation Wavelength Dependence of the Fluorescence Kinetics in Photosystem I Particles from *Synechocystis* PCC 6803 and *Synechococcus Elongatus*. *Biophys. J.* **2003**, *85*, 3883−3898.
(11) Bruggemann, B.; Sznee, K.; Novoderezhkin, V. I.; van Grondelle, R.; May, V. From Structure to Dynamics: Modeling Exciton Dynamics in the Photosynthetic Antenna PSI. *J. Phys. Chem. B* **2004**, *108*, 13536−13546.
(12) Schlodder, E.; Lendzian, F.; Meyer, J.; Cetin, M.; Brecht, M.; Renger, T.; Karapetyan, N. V. Long-wavelength limit of photochemical energy conversion in photosystem I. *J. Am. Chem. Soc.* **2014**, *136*, 3904−3918.
(13) Palsson, L. O.; Dekker, J. P.; Schlodder, E.; Monshouwer, R.; van Grondelle, R. Polarized Site-Selective Fluorescence Spectroscopy of the Long-Wavelength Emitting Chlorophylls in Isolated Photosystem I Particles of *Synechococcus Elongatus*. *Photosynth. Res.* **1996**, *48*, 239−246.
(14) Byrdin, M.; Rimke, I.; Schlodder, E.; Stehlik, D.; Roelofs, T. A. Decay Kinetics and Quantum Yields of Fluorescence in Photosystem I from *Synechococcus Elongatus* with P700 in the Reduced and Oxidized State: Are the Kinetics of Excited State Decay Trap-Limited or Transfer-Limited? *Biophys. J.* **2000**, *79*, 992−1007.
(15) Gobets, B.; van Amerongen, H.; Monshouwer, R.; Kruip, J.; Rögner, M.; van Grondelle, R.; Dekker, J. P. Polarized Site-Selected Fluorescence Spectroscopy of Isolated Photosystem I Particles. *Biochim. Biophys. Acta, Bioenerg.* **1994**, *1188*, 75−85.
(16) Frese, R. N.; Palacios, M. A.; Azzizi, A.; van Stokkum, I. H. M.; Kruip, J.; Rogner, M.; Karapetyan, N. V.; Schlodder, E.; van Grondelle, R.; Dekker, J. P. Electric Field Effects on Red Chlorophylls, Beta-Carotenes and P700 in Cyanobacterial Photosystem I Complexes. *Biochim. Biophys. Acta, Bioenerg.* **2002**, *1554*, 180−191.
(17) Zazubovich, V.; Matsuzaki, S.; Johnson, T. W.; Hayes, J. M.; Chitnis, P. R.; Small, G. J. Red Antenna States of Photosystem I from Cyanobacterium *Synechococcus Elongatus*: a Spectral Hole Burning Study. *Chem. Phys.* **2002**, *275*, 47−59.
(18) Palsson, L. O.; Gobets, B.; Fleming, C.; Ericsson, L. M.; van Grondelle, R.; Schlodder, E.; Dekker, J. P. Long-Wavelength Antenna Pigments in Photosystem I. *Prog. Biophys. Mol. Biol.* **1996**, *65*, 217−217.
(19) Brecht, M.; Studier, H.; Elli, A. F.; Jelezko, F.; Bittl, R. Assignment of Red Antenna States in Photosystem I from *Thermosynechoccocus Elongatus* by Single-Molecule Spectroscopy. *Biochemistry* **2007**, *46*, 799−806.
(20) Byrdin, M.; Jordan, P.; Krauss, N.; Fromme, P.; Stehlik, D.; Schlodder, E. Light Harvesting in Photosystem I: Modeling Based on the 2.5-Å Structure of Photosystem I from *Synechococcus Elongatus*. *Biophys. J.* **2002**, *83*, 433−457.
(21) Brecht, M. Spectroscopic Characterization of Photosystem I at the Single-Molecule Level. *Mol. Phys.* **2009**, *107*, 1955−1974.
(22) Konrad, A.; Trost, A.; Skandary, S.; Hussels, M.; Meixner, A.; Karapetyan, N.; Brecht, M. Manipulating the Excitation Transfer in Photosystem I by a Fabry-Perot Metal Resonator with Optical Sub-Wavelength Dimensions. *Phys. Chem. Chem. Phys.* **2014**, *16*, 6175−6181.
(23) Boekema, E.; Dekker, J.; van Heel, M.; Rögner, M.; Saenger, W.; Witt, I.; Witt, H. Evidence for a Trimeric Organization of the Photosystem I Complex from the Thermophilic Cyanobacterium *Synechococcus SP*. *FEBS Lett.* **1987**, *217*, 283−286.
(24) Rögner, M. U.; Mühlenhoff, X.; Boekema, E. J.; Witt, H. T. Mono-, Di- and Trimeric PSI Reaction Center Complexes Isolated from the Thermophilic Cyanobacterium *Synechococcus SP*. Size, Shape and Activity. *Biochim. Biophys. Acta, Bioenerg.* **1990**, *1015*, 415−424.
(25) Kruip, J.; Bald, D.; Boekema, E.; Rögner, M. Evidence for the Existence of Trimeric and Monomeric Photosystem I Complexes in Thylakoid Membranes from Cyanobacteria. *Photosynth. Res.* **1994**, *40*, 279−286.
(26) Turconi, S.; Kruip, J.; Schweitzer, G.; Rögner, M.; Holzwarth, A. R. A Comparative Fluorescence Kinetics Study of Photosystem I Monomers and Trimers from *Synechocystis* PCC 6803. *Photosynth. Res.* **1996**, *49*, 263−268.
(27) Abramavicius, D.; Mukamel, S. Exciton Delocalization and Transport in Photosystem I of Cyanobacteria *Synechococcus Elongates*: Simulation Study of Coherent Two-Dimensional Optical Signals. *J. Phys. Chem. B* **2009**, *113*, 6097−6108.
(28) Schlodder, E.; Cetin, M.; Byrdin, M.; Terekhova, I. V.; Karapetyan, N. V. $P700^{+}$- and $^{3}P700$- Induced Quenching of the Fluorescence at 760 nm in Trimeric Photosystem I Complexes from the Cyanobacterium *Arthrospira Platensis*. *Biochim. Biophys. Acta, Bioenerg.* **2005**, *1706*, 53−67.
(29) Purchase, R.; Bonsma, S.; Jezowski, S.; Gallus, J.; Konz, F.; Volker, S. The Power of Line-Narrowing Techniques: Applications to Photosynthetic Chromoprotein Complexes and Autofluorescent Proteins. *Opt. Spectrosc.* **2005**, *98*, 699−711.
(30) Tamarat, P.; Maali, A.; Lounis, B.; Orrit, M. Ten Years of Single-Molecule Spectroscopy. *J. Phys. Chem. A* **2000**, *104*, 1−16.
(31) Vosgröne, T.; Meixner, A. J. Surface and Resonance Enhanced Micro Raman Spectroscopy of Xanthene Dyes: From the Ensemble to Single Molecules. *ChemPhysChem* **2005**, *6*, 154−163.
(32) van Oijen, A. M.; Ketelaars, M.; Köhler, J.; Aartsma, T. J.; Schmidt, J. Unraveling the Electronic Structure of Individual Photosynthetic Pigment-Protein Complexes. *Science* **1999**, *285*, 400−402.
(33) Lu, H. P.; Xie, X. S. Single-Molecule Spectral Fluctuations at Room Temperature. *Nature* **1997**, *385*, 143−146.
(34) Stracke, F.; Blum, C.; Becker, S.; Muellen, K.; Meixner, A. Intrinsic Conformer Jumps Observed by Single Molecule Spectroscopy in Real Time. *Chem. Phys. Lett.* **2000**, *325*, 196−202.
(35) Blum, C.; Stracke, F.; Becker, S.; Muellen, K.; Meixner, A. Discrimination and Interpretation of Spectral Phenomena by Room-Temperature Single-Molecule Spectroscopy. *J. Phys. Chem. A* **2001**, *105*, 6983−6990.
(36) Piwonski, H.; Stupperich, C.; Hartschuh, A.; Sepiol, J.; Meixner, A.; Waluk, J. Imaging of Tautomerism in a Single Molecule. *J. Am. Chem. Soc.* **2005**, *127*, 5302−5303.
(37) Rutkauskas, D.; Novoderezhkin, V. I.; Cogdell, R. J.; van Grondelle, R. Fluorescence Spectroscopy of Conformational Changes of Single LH2 Complexes. *Biophys. J.* **2005**, *88*, 422−435.
(38) Schleifenbaum, F.; Blum, C.; Subramaniam, V.; Meixner, A. J. Single-Molecule Spectral Dynamics at Room Temperature. *Mol. Phys.* **2009**, *107*, 1923−1942.
(39) Berlin, Y.; Burin, A.; Friedrich, J.; Köhler, J. Low Temperature Spectroscopy of Proteins. Part II: Experiments with Single Protein Complexes. *Phys. Life Rev.* **2007**, *4*, 64−89.
(40) Shibata, Y.; Ishikawa, H.; Takahashi, S.; Morishima, I. Time-Resolved Hole-Burning Study on Myoglobin: Fluctuation of Restricted Water within Distal Pocket. *Biophys. J.* **2001**, *80*, 1013−1023.
(41) Hofmann, C.; Ketelaars, M.; Matsushita, M.; Michel, H.; Aartsma, T. J.; Köhler, J. Single-Molecule Study of the Electronic Couplings in a Circular Array of Molecules: Light-Harvesting-2 Complex from *Rhodospirillum Molischianum*. *Phys. Rev. Lett.* **2003**, *90*, 013004.
(42) Huang, K.; Rhys, A. Theory of Light Absorption and Non-Radiative Transitions in F-Centres. *Proc. R. Soc. London, Ser. A* **1950**, *204*, 406−423.
(43) Pullerits, T.; Monshouwer, R.; van Mourik, F.; van Grondelle, R. Temperature-Dependence of Electron-Vibronic Spectra of Photosynthetic Systems-Computer-Simulations and Comparison with Experiment. *Chem. Phys.* **1995**, *194*, 395−407.

DOI: 10.1021/acs.jpcb.5b04483
J. Phys. Chem. B XXXX, XXX, XXX−XXX

(44) Renge, I. Impurity Spectroscopy in Glasses and Disordered Crystals: Inhomogeneous Broadening and Electron Phonon Coupling. *J. Lumin.* **2008**, *128*, 413−420.
(45) Rätsep, M.; Pajusalu, M.; Freiberg, A. Wavelength-Dependent Electron-Phonon Coupling in Impurity Glasses. *Chem. Phys. Lett.* **2009**, *479*, 140−143.
(46) Jankowiak, R.; Reppert, M.; Zazubovich, V.; Pieper, J.; Reinot, T. Site Selective and Single Complex Laser-Based Spectroscopies: A Window on Excited State Electronic Structure, Excitation Energy Transfer, and Electron-Phonon Coupling of Selected Photosynthetic Complexes. *Chem. Rev.* **2011**, *111*, 4546−4598.
(47) Jelezko, F.; Tietz, C.; Gerken, U.; Wrachtrup, J.; Bittl, R. Single-Molecule Spectroscopy on Photosystem I Pigment-Protein Complexes. *J. Phys. Chem. B* **2000**, *104*, 8093−8096.
(48) Jordan, P.; Fromme, P.; Witt, H. T.; Klukas, O.; Saenger, W.; Krauss, N. Three-Dimensional Structure of Cyanobacterial Photosystem I at 2.5 Å Resolution. *Nature* **2001**, *411*, 909−917.
(49) El-Mohsnawy, E.; Kopczak, M. J.; Schlodder, E.; Nowaczyk, M.; Meyer, H. E.; Warscheid, B.; Karapetyan, N. V.; Rogner, M. Structure and Function of Intact Photosystem I Monomers from the Cyanobacterium *Thermosynechococcus Elongatus*. *Biochemistry* **2010**, *49*, 4740−4751.
(50) Schlodder, E.; Hussels, M.; Cetin, M.; Karapetyan, N. V.; Brecht, M. Fluorescence of the Various Red Antenna States in Photosystem I Complexes from Cyanobacteria is Affected Differently by the Redox State of P700. *Biochim. Biophys. Acta, Bioenerg.* **2011**, *1807*, 1423−31.
(51) Müh, F.; Zouni, A. Extinction Coefficients and Critical Solubilisation Concentrations of Photosystems I and II from *Thermosynechococcus Elongatus*. *Biochim. Biophys. Acta, Bioenerg.* **2005**, *1708*, 219−228.
(52) Hussels, M.; Konrad, A.; Brecht, M. Confocal Sample-Scanning Microscope for Single-Molecule Spectroscopy and Microscopy with Fast Sample Exchange at Cryogenic Temperatures. *Rev. Sci. Instrum.* **2012**, *83*, 123706.
(53) Hussels, M.; Brecht, M. Effect of Glycerol and PVA on the Conformation of Photosystem I. *Biochemistry* **2011**, *50*, 3628−3637.
(54) Brecht, M.; Studier, H.; Radics, V.; Nieder, J. B.; Bittl, R. Spectral Diffusion Induced by Proton Dynamics in Pigment-Protein Complexes. *J. Am. Chem. Soc.* **2008**, *130*, 17487−17493.
(55) Brecht, M.; Radics, V.; Nieder, J. B.; Bittl, R. Protein Dynamics-Induced Variation of Excitation Energy Transfer Pathways. *Proc. Natl. Acad. Sci. U. S. A.* **2009**, *106*, 11857−11861.
(56) Hayes, J. M.; Matsuzaki, S.; Ratsep, M.; Small, G. J. Red Chlorophyll a Antenna States of Photosystem I of the Cyanobacterium *Synechocystis SP* PCC6803. *J. Phys. Chem. B* **2000**, *104*, 5625−5633.
(57) Rätsep, M.; Johnson, T. W.; Chitnis, P. R.; Small, G. J. The Red-Absorbing Chlorophyll a Antenna States of Photosystem I: A Hole-Burning Study of *Synechocystis SP* PCC 6803 and its Mutants. *J. Phys. Chem. B* **2000**, *104*, 836−847.
(58) Förster, T. Energiewanderung und Fluoreszenz. *Naturwissenschaften* **1946**, *33*, 166−175.
(59) Renger, T.; May, V.; Kühn, O. Ultrafast Excitation Energy Transfer Dynamics in Photosynthesis Pigment-Protein Complexes. *Phys. Rep.* **2001**, *343*, 137−254.
(60) Abramavicius, D.; Palmieri, B.; Voronine, D.; Sanda, F.; Mukamel, S. Coherent Multidimensional Optical Spectroscopy of Excitons in Molecular Aggregates; Quasiparticle versus Supermolecule Perspectives. *Chem. Rev.* **2009**, *109*, 2350−2408.
(61) Karapetyan, N. V.; Schlodder, E.; van Grondelle, R.; Dekker, J. P. The Long Wavelength Chlorophylls in Photosystem I. In *Photosystem I: The Light-Driven Plastocyanin:Ferredoxin Oxidoreductase*; Golbeck, J. H., Ed.; Advances in Photosynthesis and Respiration *24*; Springer: Berlin, 2006; pp 177−192.

DOI: 10.1021/acs.jpcb.5b04483
J. Phys. Chem. B XXXX, XXX, XXX−XXX

Chapter 6: Effects of Irregular Bimetallic Nanostructures on the Optical Properties of Photosystem I from *Thermosynechococcus elongatus*

The fluorescence of PSI trimers from *T. elongatus* in proximity to bimetallic plasmonic nanostructures have been explored by SMS at 1.6 K. PSI serves as a model for biological multichromophore-coupled systems with high potential for biotechnological applications. Plasmonic nanostructures were fabricated by thermal annealing of thin metallic films as Au/Au and Au/Ag with different size, shape and inter-structure spacing. They were used to investigate the influence of plasmonic interaction on optical properties of PSI. The size of the nanostructures is not the same but varying between 6–47 nm in diameter for Au/Au sample and between 6–36 nm for Ag/Au sample. The fluorescence of PSI has been enhanced due to the coupling with plasmonic nanostructures. The profile of PSI-Au/Au is similar to PSI-Ag/Au, however, the intensity enhancement is different. An enormous increase in the mean intensity of PSI-Au/Au and PSI-Ag/Au samples is evident. Enhancement factors up to 22.9 and 5.1 are observed for individual PSI complexes coupled to Au/Au and Ag/Au samples, respectively. Additionally, a wavelength dependence of fluorescence enhancement is observed, which can be explained by the multichromophoric composition of PSI. This chapter is adapted from the paper in ref. [137].

Photonics **2015**, *2*, 838-854; doi:10.3390/photonics2030838

OPEN ACCESS

photonics

ISSN 2304-6732

www.mdpi.com/journal/photonics

Article

Effects of Irregular Bimetallic Nanostructures on the Optical Properties of Photosystem I from *Thermosynechococcus elongatus*

Imran Ashraf [1], Sepideh Skandary [1], Mohammad Y. Khaywah [2,3], Michael Metzger [1], Alfred J. Meixner [1], Pierre M. Adam [2] and Marc Brecht [1,4,*]

[1] IPTC and Lisa+ Center, University of Tübingen, Auf der Morgenstelle 18, 72076 Tübingen, Germany; E-Mails: imran.ashraf@iptc.uni-tuebingen.de (I.A.); sepideh.skandary@uni-tuebingen.de (S.S.); michael.metzger@uni-tuebingen.de (M.M.); alfred.meixner@uni-tuebingen.de (A.J.M.)

[2] Laboratory of Nanotechnology, Instrumentation and Optics, University of Technology of Troyes, 12 Rue Marie Curie, CS 42060, 10004 Troyes Cedex, France; E-Mails: mohammad_yehia.khaywah@utt.fr (M.Y.K.); pierre_michel.adam@utt.fr (P.M.A.)

[3] Laboratory of Materials, Catalysis, Environment and Analytical Methods, Lebanese University, Campus Rafic Hariri, Hadath-Beirut, Lebanon

[4] Zurich University of Applied Science Winterthur (ZHAW), Technikumstrasse 13, 8401 Winterthur, Switzerland

* Author to whom correspondence should be addressed; E-Mail: marc.brecht@uni-tuebingen.de; Tel.: +49-7071-29-76239; Fax: +49-7071-29-5490.

Received: 29 June 2015 / Accepted: 19 July 2015 / Published: 23 July 2015

Abstract: The fluorescence of photosystem I (PSI) trimers in proximity to bimetallic plasmonic nanostructures have been explored by single-molecule spectroscopy (SMS) at cryogenic temperature (1.6 K). PSI serves as a model for biological multichromophore-coupled systems with high potential for biotechnological applications. Plasmonic nanostructures are fabricated by thermal annealing of thin metallic films. The fluorescence of PSI has been intensified due to the coupling with plasmonic nanostructures. Enhancement factors up to 22.9 and 5.1 are observed for individual PSI complexes coupled to Au/Au and Ag/Au samples, respectively. Additionally, a wavelength dependence of fluorescence enhancement is observed, which can be explained by the multichromophoric composition of PSI.

Keywords: plasmonic; bimetallic nanostructures; thermal annealing; photosystem I; single-molecule spectroscopy; fluorescence emission enhancement

1. Introduction

The effects of metallic surfaces and nanostructures on the optical properties (fluorescence quenching or enhancement) of molecules nearby were discussed already in the late 1960s and 1970s [1–3]. The fluorescence enhancement and photostability of those molecules due to plasmonic nanostructures in their vicinity influenced many research areas. Based on altered spontaneous emission rates, various devices, e.g., surface plasmon-enhanced LEDs [4], plasmon-enhanced optical sensors [5,6], single-photon sources for quantum cryptography [7] and photonic crystal lasers [8,9], have been revealed. In 2002, Geddes *et al.* considered the outcome of the near-field of metallic nanoparticles on the brightness and photostability of chromophores for the first time and introduced the term metal-enhanced fluorescence (MEF) [10]. Details of the real mechanism of MEF are still part of the discussion today. However, changes in the local field stimulated by metallic nanostructures and modifications in radiative decay rates are two acknowledged procedures for the fluorescence enhancement [8,11,12]. The fluorescence of fluorophores can be controlled by controlling the distance between fluorophore and plasmonic active particles, their relative orientation, size, shape and the surrounding medium [11]. The interaction of plasmonic nanostructures with fluorophores increases their radiative decay rates and quantum yield. The increased decay rates yield an increase of the photostability of fluorophores, as the fluorophores spend less time in an excited state before returning back to the ground state [13]. The ability to increase the brightness of the fluorophore with adjacent plasmonic nanostructures simplifies the detection of the fluorophores at the single-molecule level, which otherwise is difficult due to low signal intensities.

The prior studies of our group showed the influence of plasmonic interactions on the fluorescence intensity of photosystem I (PSI) using the silver island films (SIFs), gold nanoparticles (AuNP) and ordered monometallic nanostructures, called Fischer patterns. An increase in fluorescence up to 37-fold accompanied by a shift in peak position of fluorescence have been reported [14–16]. Recently, an enhancement in fluorescence up to 200-fold for PSI coupled to SIFs at room temperature have also been reported by Czechowski *et al.* [17]. In this article, however, we have explored the effects of coupling PSI with disordered and arbitrary-shaped bimetallic nanostructures. The nanostructure samples are fabricated on commercial glass coverslips by thermal annealing of thin metallic films. The choice of this fabrication technique is made because it is a relatively simple and low cost way of fabrication. In addition, this technique is able to produce large-scale substrates, and optical properties of the nanostructures can be tuned easily [18,19]. The fluorescence of PSI deposited on bimetallic nanostructures is investigated using a home-built confocal microscopy setup operating at a cryogenic temperature (1.6 K).

PSI isolated from *Thermosynechococcus elongatus* (*Th. elongatus*) is used for the investigation, because it is one of the most sophisticated and efficient multi-subunit trans-membrane complexes, responsible for harvesting solar energy to support light-induced charge separations. PSI absorbs over a broad spectral range of the solar radiation reaching the Earth's surface. Irrespective of the wavelength,

approximately each absorbed photon by PSI is used to induce electron translocation, which turns over to a quantum yield for charge separation of almost unity [20]. Such remarkable quantum yield makes PSI a promising candidate for photoelectronic and photochemical devices [21–24]. The X-ray structure analysis of PSI from *Th. elongatus* resolved at 2.5 Å [25] revealed that trimeric PSI have a clover leaf structure of 22 nm in diameter [26]. The monomeric form of PSI from *Th. elongatus* is comprised of $\sim$ 96 chlorophyll (Chl) molecules responsible for light harvesting, excitation energy transfer and charge separation [25,27]. The electron transport chain positioned in the center of monomeric PSI consists of a dimer of Chl molecules named P700, A_0, A_1 and iron-sulfur clusters (F_X, F_A and F_B) [26,27]. P700, the reaction center (RC), is the primary electron donor [26]. After absorption of light by the antenna system, the excitation energy is transferred to P700, where a light-induced charge separation takes place [27,28]. The light harvesting antennas in PSI contain the coupled Chls as dimers and trimers, which absorb at a wavelength higher than 700 nm. Some of them are located near the electron transfer chain. Because of their lower site energies than P700, these pigments are also called red Chls or long wavelength Chls (LWCs) [26,28–30]. Although the actual functions of these LWCs are still under discussion, the key roles may lie in increasing the spectral width of light absorption and funneling the excitation energy to the center of the complex [26]. At room temperature, the energy absorbed by LWCs is transferred to P700 through the uphill energy transfer mechanism. At low temperatures, the transfer of energy to P700 is blocked, and the absorbed energy is trapped by LWCs, which is then partially released in the form of fluorescence [28].

Single-molecule spectroscopy (SMS) is used to study the fluorescence of the LWCs in the presence of plasmonic nanostructures. The important aspect of SMS is to unravel information hidden in ensemble spectra by avoiding ensemble averaging effects [31]. At a cryogenic temperature, conformational fluctuations in proteins and their environment are reduced. Therefore, the photo and frequency stability of protein-bound chromophores at lower temperatures increase, and spectroscopic studies with high spectral sensitivity become possible [32]. Therefore, probing single PSI complexes coupled to plasmonic nanostructures, using SMS below the liquid helium (He) temperature, provides a chance for comprehensive investigation. Based on this detailed investigation, the impacts of the plasmonic nanostructures on the optical properties of PSI are discussed.

2. Experimental Section

Bimetallic nanostructures were fabricated on thin commercial glass coverslips of 20 mm $\times$ 20 mm by using the thermal annealing technique. Prior to metal evaporation, the glass substrates were washed with a mixture of detergent (Decon 90) and double-distilled water with a volume ratio of 1:9 in a water bath at 50 °C for 20 min. In order to ensure that all of the detergent residues had been removed, the washing process was repeated twice with double-distilled water in the ultrasonic cleaner, and afterwards, the substrates were dried by using a N_2 stream. The thin layer of metal (2 nm) was deposited by using a vacuum evaporator under a high vacuum of pressure 1.0 $\times$ 10^{-6} Torr. For fabrication of the Au/Au sample (*i.e.*, Au-T-Au-T-Au), three successive evaporations of thin gold films were conducted, where each two evaporations were separated by thermal annealing (T). Evaporating the same quantity of gold in three successive evaporations separated by thermal annealing provides denser nanoparticles with a

smaller inter-particle distance. Similarly, for fabrication of Ag/Au sample (*i.e.*, Ag-T-Au), at first 2-nm thin film of silver was deposited followed by thermal annealing and deposition of thin film of gold. Figure 1a shows a schematic diagram of both of the samples. Every thermal annealing operation was performed for 20 s by using hot plate at 250 °C.

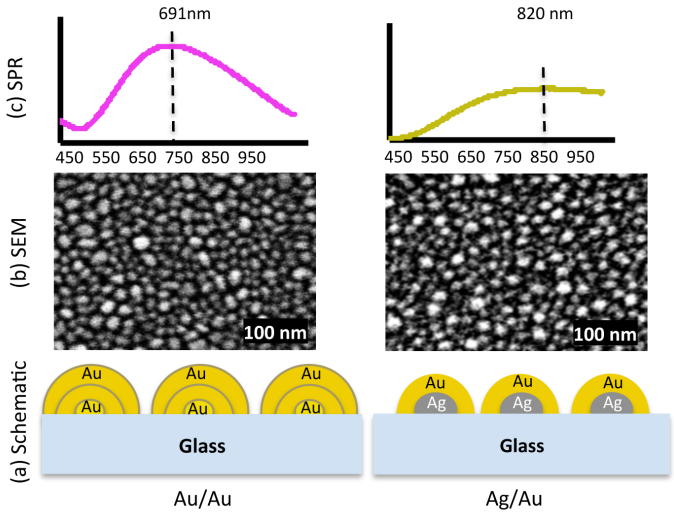

Figure 1. (**a**) Exaggerated schematic diagram of two nanostructured substrates, Au/Au and Ag/Au. (**b**) The SEM images show that the nanostructures are different in shape, size and inter-structure spacing. In the Au/Au sample, the smallest size is ≈ 6 nm and the largest ≈ 47 nm, and for Ag/Au sample, the smallest size is ≈ 6 nm and the largest ≈ 36 nm. (**c**) SPR spectra of the respective samples. The extinction peaks for samples Au/Au and Ag/Au are at 691 nm and 820 nm, respectively.

Trimeric PSI from *Th. elongatus* used in this study has been isolated as described in [33]. The purified PSI trimers were diluted in buffer solution to achieve a low concentration (∼ 3 pM), which is necessary for SMS. The detailed procedure for the preparation of the buffer is explained in [14]. To form a hybrid, less than 1 μL of this highly diluted solution was sandwiched between metallic nanostructures and bare glass coverslips and transferred to a pre-cooled (4.2 K) cryostat. SMS is performed by using a home-built confocal microscope setup operating at cryogenic temperature ∼1.6 K [34]. A *cw* diode laser at a wavelength of 665 nm was used as an excitation source for fluorescence measurements. In total, 100 spectra were collected for one dataset from one isolated coupled complex by using the excitation power of 100 μW.

3. Results

Irregular bimetallic nanostructures fabricated by thermal annealing of thin metallic films, having different size, shape and inter-structure spacing were used to investigate the influence of plasmonic interaction on optical properties of PSI [18]. The schematic diagram shown in Figure 1a is a simplified representation of the composition of two different nanostructures used in our experiments. The fabrication conditions, *i.e.* pressure, annealing temperature, annealing timing and film thickness *etc.*,

were kept same for all samples. The nanostructures are disorganised with arbitrary shape. Some of the them are round shape while others are more elongated. Figure 1b shows the scanning electron microscope (SEM) images of the respective nanostructures. The size of the nanostructures is not same but varying between 6–47 nm in diameter for Au/Au sample and between 6–36 nm for Ag/Au sample. The average diameter of the nanostructures for Au/Au is $\approx$ 19 nm with standard deviation of 6.1 nm (for particle size distribution see supplementary information), while for Ag/Au sample the average diameter is $\approx$ 18 nm with standard deviation of 6.4 nm. Figure 1c shows the surface plasmon resonance (SPR) spectra of these samples. The extinction peaks of Au/Au and Ag/Au samples are at 691 nm and 820 nm, respectively. The extinction spectrum of Au/Au sample is intense and well shaped with defined peak, whereas the extinction spectrum of Ag/Au is broad with low intensity. The differences in extinction spectra of two samples are because of their different metal compositions, size, shape and inter-structure spacing [18].

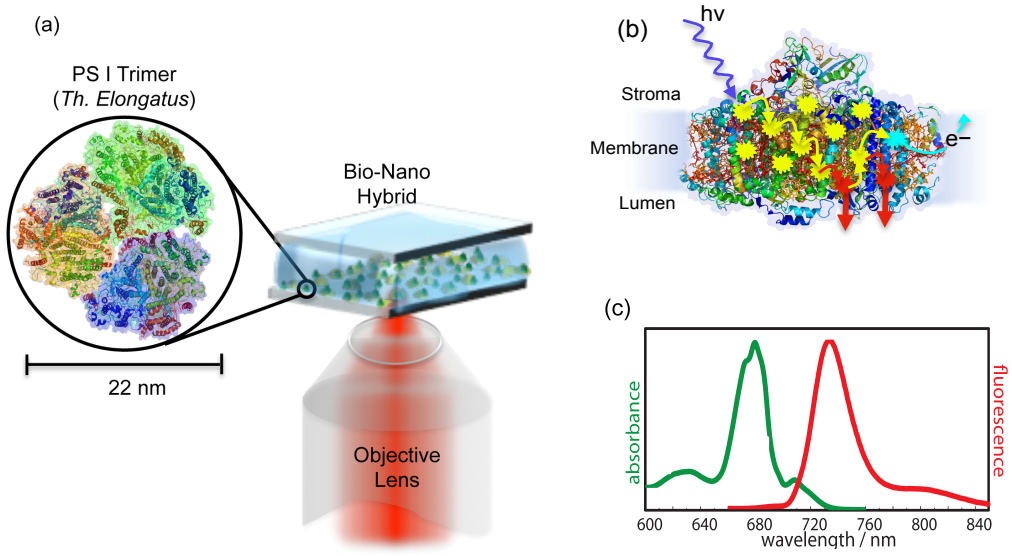

Figure 2. (**a**) Schematic illustration of experimental arrangement. A buffer solution containing isolated and purified photosystem I (PSI) trimers from *Th. elongatus* is sandwiched between metallic nanostructures and a bare glass coverslip. The green dots represent PSI trimers, while random yellow dots are metallic nanostructures. The inset shows the trimeric PSI from *Th. elongatus* (protein data bank (PDB) entry: 1JB0). The same objective is used for the excitation and collection of back reflected light. (**b**) The side view of PSI in monomeric form with exaggerated details about the excitation energy transfer (EET) pathways. At ambient temperatures, the captured excitation energy is transferred along the transfer chain (shown by yellow arrows) to the reaction center (RC) (represented by cyan explosion symbol), where light-induced charge separation takes place. However, at low temperatures, the energy transfer to the RC is blocked, so instead of charge separation, the captured energy is partially released in the form of fluorescence from red Chls (represented by red arrows). Around 96 Chls per monomer participate in the energy transfer process. (**c**) Absorption and emission spectra of ensemble PSI from *Th. elongatus* at a low temperature (77 K) in the oxidized state, adopted from [28].

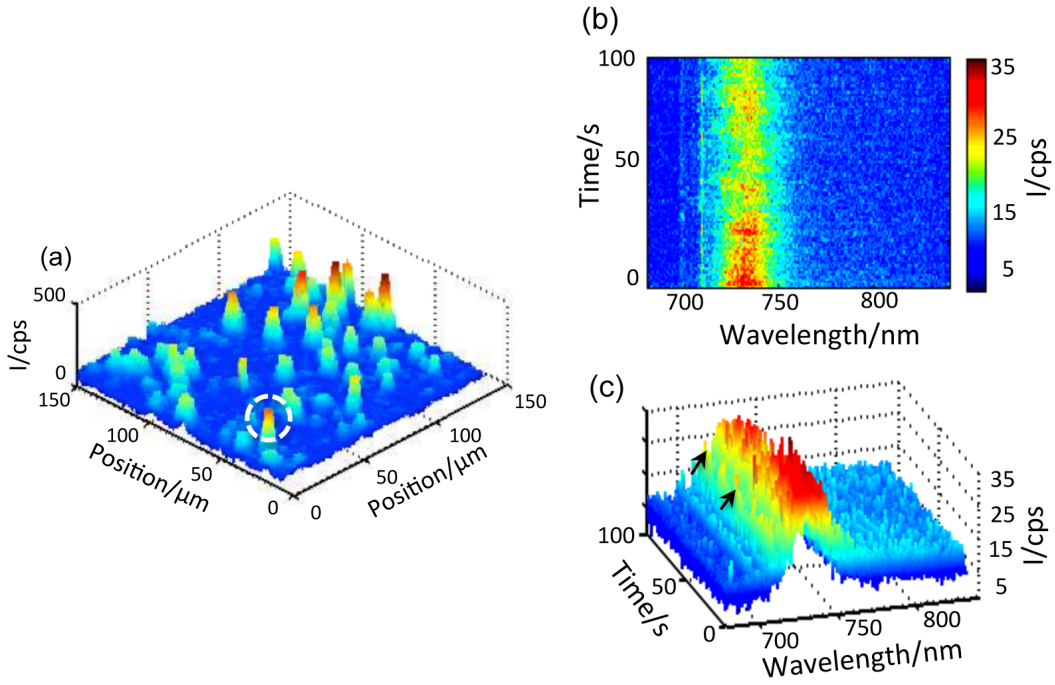

Figure 3. (**a**) Confocal fluorescence 3D scan of PSI-Au/Au. The bright spots, which are visible in almost the entire image range, are from individual PSI-Au/Au pairs. The white circle highlights the exemplary individual pair from which the sequence of spectra are collected. (**b**) The time-dependent dataset consists of 100 fluorescence spectra taken from the highlighted single PSI-Au/Au pair with an integration time of 1 s per spectra. (**c**) The 3D view of the sequence of 100 spectra.

These bimetallic nanostructures were coupled to PSI to form the bio-nano hybrids. To achieve the coupling of PSI with nanostructures, a solution of PSI trimers from *Th. elongatus* was deposited on top of metallic nanostructures, which were then covered with bare glass coverslips, as shown in Figure 2a. These samples were named PSI-Au/Au and PSI-Ag/Au. An additional sample was prepared as a reference by sandwiching single PSI complexes between two bare glass coverslips and was named PSI-glass. To ensure the observation of individual coupled pairs in the entire width of the excitation beam's focus, a very low concentration of PSI trimers ($\sim$ 3 pM) in the solution was used. The samples were prepared outside of the cryostat and subsequently were inserted quickly onto the scanning desk in the cooled cryostat (4.2 K) by using our fast sample transfer mechanism introduced in [34]. The samples were scanned in the *xy* direction over a specific range. Figure 3a shows one of the confocal fluorescence 3D scan images taken from the PSI-Au/Au sample. The bright spots that are visible in almost the entire image range are from individual coupled PSI complexes. The deviation of the spots from a circular shape can be attributed to the low image quality of the microscope objective used at low temperature. From each of these coupled PSI complexes, a spectra series consisting of 100 spectra was recorded continuously with an acquisition time of 1 s per spectrum. Figure 3b shows one example of the time-dependent dataset taken from the highlighted exemplary individual coupled pair of the PSI-Au/Au sample. In Figure 3c, the 3D view of time-dependent dataset is shown. Notably, intense zero phonon

lines (ZPLs) marked with black arrows around 710 nm and a broad emission in the region around 729 nm dominate the whole dataset. The peak position of each individual spectrum can be seen as jumping in a certain wavelength range. Furthermore, photoblinking accompanied with a decay in intensity is obvious from the dataset over time. These spectral features, *i.e.*, the appearance of zero phonon lines and jumps in the peak position of each spectrum, clearly indicate the fluorescence of a single molecule.

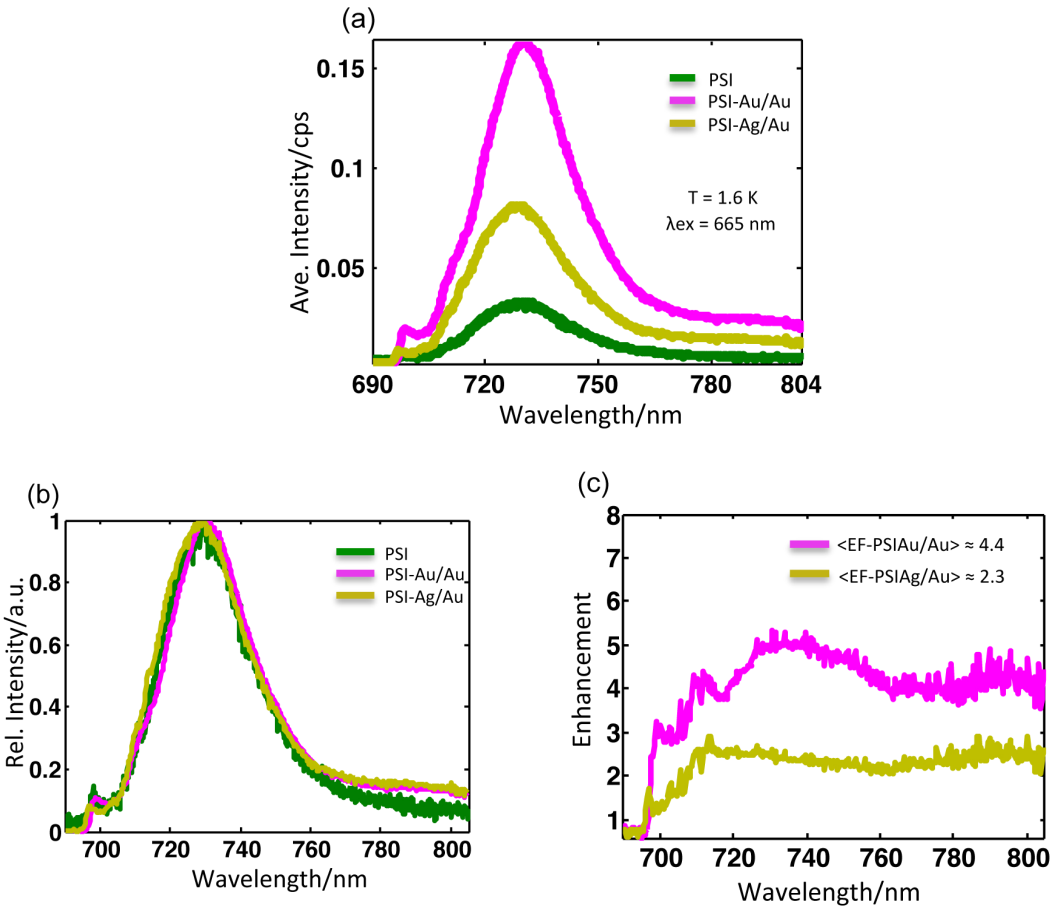

Figure 4. (**a**) Average fluorescence spectra of all samples after baseline correction at T = 1.6 K upon excitation at 665 nm. The accumulation time for PSI-glass was 2 s, while for PSI-Au/Au and PSI-Ag/Au, it was 1 s. (**b**) The normalized average spectra were scaled to the same maximum value after baseline correction. No pronounced broadening in the linewidth of any sample was found. (**c**) Wavelength-dependent enhancement spectra obtained after dividing the average spectra of PSI-Au/Au and PSI-Ag/Au by the average spectrum of PSI-glass. More enhancement was observed around main peak region (730 nm) and in the far red region ($>$ 780 nm).

Figure 4a shows the corresponding mean intensity spectra of all of the datasets from samples PSI-glass (green), PSI-Au/Au (magenta) and PSI-Ag/Au (yellow). The emission profiles of these samples with normalized intensity are shown in Figure 4b. The profile of PSI-Au/Au is similar to PSI-Ag/Au; however, the intensity enhancement is different. An enormous increase in the mean intensity

of PSI-Au/Au and PSI-Ag/Au samples is evident. The full width at half maximum (FWHM) of the average spectra for PSI-glass, PSI-Au/Au and PSI-Ag/Au is 27.6, 27.3 and 28.3 nm, respectively.

Table 1 shows the comparison of different values for the different samples. The change in FWHM due to metallic nanostructures in the neighborhood is quite small. A slight increase in FWHM for the PSI-Ag/Au sample as compared to PSI-glass, while a minor decrease for PSI-Au/Au are spotted. The spectral position of emission maxima for PSI-glass was found at 730.4 nm, whereas for PSI-Au/Au with a slight red shift at 731.3 nm and for PSI-Ag/Au with a slight blue shift at 729.7 nm. Compared to the profile of PSI-glass, an additional broad shoulder in the emission profile of PSI-Au/Au and PSI-Ag/Au in the far red region between 780–850 nm is detected. Analogous to the main peaks, the additional shoulder of the PSI-Au/Au sample was also more intense compared to the PSI-Ag/Au sample.

Table 1. Comparison of enhancement factors, linewidths and standard deviations of enhancement factors observed for uncoupled and coupled PSI complexes.

Sample	PSI-glass	PSI-Au/Au	PSI-Ag/Au
Emission Maximum (nm)	730.4	731.3	729.7
FWHM (nm)	27.6	27.3	28.3
Average Enhancement	-	4.4	2.3
Max. Enhancement	-	22.9	5.1
Standard Deviation	0.3	3.9	0.8

The wavelength-dependent enhancement in intensities of PSI-Au/Au and PSI-Ag/Au samples are plotted at 690–805 nm after dividing by the average spectra of PSI-glass. The resulting wavelength-dependent enhancement spectra are shown in Figure 4c. For the PSI-Au/Au sample, a continuous fluorescence enhancement with three intensified domains, *i.e.*, one broad one in the region at 720–760 nm and two relatively narrow domains, *i.e.* at 706–716 nm and at 780–805 nm, was recorded. A similar trend of continuous enhancement was seen for the PSI-Ag/Au sample, but intensity enhancement was comparatively decreased as compared to the PSI-Au/Au sample. Furthermore, there was only one prominent domain at 780–805 nm with a comparatively high intensity. It is worth noting that, because of the dependence of the selected procedure on the elimination of background contributions, the risk of error in a spectral region with low intensity becomes higher compared to the high intensity spectral region.

All nanostructures lead to an emission enhancement of coupled PSI complexes. For calculating enhancement factors, the intensity counts from individual datasets of PSI-Au/Au and PSI-Ag/Au samples were integrated after baseline correction and compared with average intensity counts of PSI-glass. The distribution of the relative intensities from individual complexes of PSI-Au/Au and PSI-Ag/Au with respect to PSI-glass are displayed in Figure 5. The relative intensity of individual datasets of PSI-Au/Au and PSI-Ag/Au samples with respect to the mean intensity of PSI-glass is referred to as the enhancement factor. The intensity histogram of PSI-glass (green) shows almost a Gaussian shape, while the histograms of the enhancement factors for PSI-Au/Au and PSI-Ag/Au initially increase steeply to a maximum value and decay approximately exponentially afterwards. The insets are the SEM micrographs of metallic nanostructures with information about their respective fabrication methods, surface coverage and the size of the nanostructures. For PSI-Au/Au, the average increase in fluorescence intensity is 4.4 $\pm$ 3.9-fold,

while for PSI-Ag/Au, it increases by 2.3 ± 0.8-fold. However, for individual datasets, the maximum enhancement factors for PSI-Au/Au and PSI-Ag/Au samples are 22.9 and 5.1, respectively. The average enhancement factors for both PSI-Au/Au and PSI-Ag/Au samples are higher than those previously reported for hybrid of PSI with ordered gold Fischer patterns (PSI-AuΔ) [14].

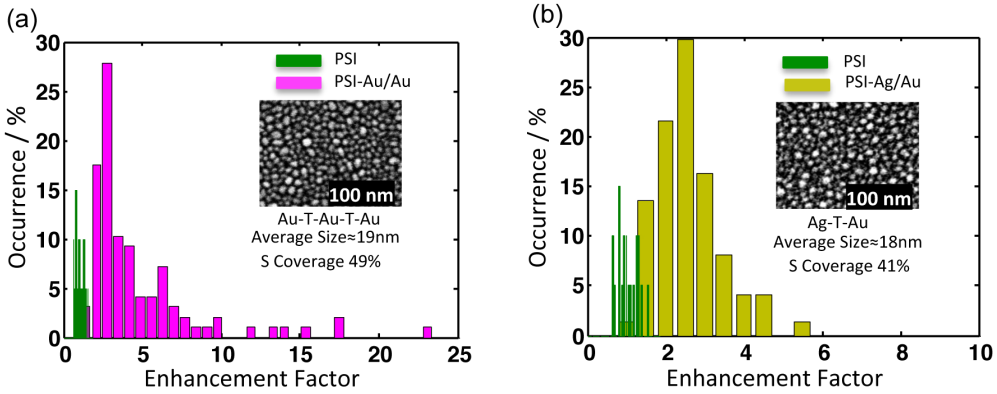

Figure 5. Comparison of the integrated fluorescence intensities of (**a**) PSI-Au/Au (magenta) and (**b**) PSI-Ag/Au (yellow) with PSI-glass in green. The insets are the SEM images of the respective nanostructures. The counts of individual datasets were integrated after baseline correction. The average enhancement factors for PSI-Au/Au and PSI-Ag/Au are 4.4 ± 3.9 and 2.3 ± 0.8, respectively. The *x*-axis defines the enhancement factor, whereas the *y*-axis shows the relative percentage of occurrence of the datasets with respective enhancement factors.

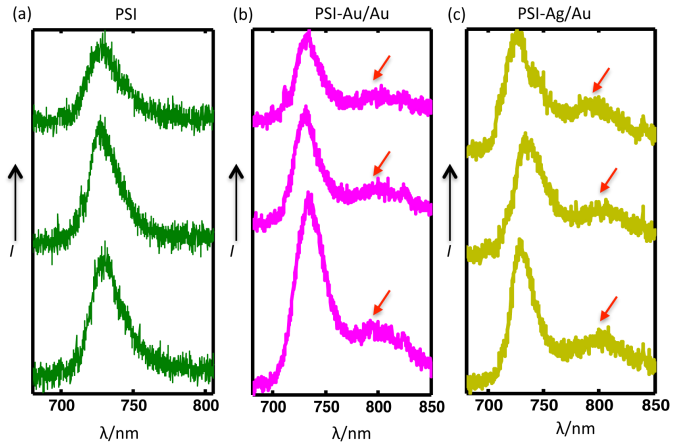

Figure 6. Comparison of three individual datasets from three single complexes of each (**a**) PSI-glass (**b**) PSI-Au/Au and (**c**) PSI-Ag/Au. The red arrows point to the broad enhanced shoulders appearing in the far red region (from 780–850 nm) for almost all coupled complexes of PSI-Au/Au and PSI-Ag/Au samples. The accumulation time for each PSI was 2 s, while for PSI-Au/Au and PSI-Ag/Au, it was 1 s.

The comparison of the spectra from three individual complexes of each, PSI-glass, PSI-Au/Au and PSI-Ag/Au, are shown in Figure 6. Clear, distinctive and broad enhanced shoulders, which appeared for both of the PSI-Au/Au and PSI-Ag/Au samples in the wavelength range 780–850 nm, are elaborated. The red arrows point out these broad shoulders, which were consistent in all datasets of PSI-Au/Au and PSI-Ag/Au with varying intensity; while such shoulders have not been detected for PSI-glass.

4. Discussion

The fluorescence enhancement of bio-molecules due to metal nanostructures or nanoparticles in close vicinity has been reported before [14–16,35,36]. The aforementioned results have shown an increased fluorescence of PSI trimers induced by the plasmonic nanostructures Au/Au and Ag/Au, fabricated by the thermal annealing process. Recent studies have revealed that the spectral overlap between absorption spectra of the fluorophore and extinction spectra from metallic nanoparticles [37–39], their mutual distance [40], relative orientation [41] and peak position of SPR of metallic nanoparticles [37,42] play critical roles in changing the fluorescence of the fluorophores. Therefore, the nanostructures having different SPR peak positions and covering a broad range of wavelengths were fabricated. The SPR peak positions of the nanostructures are tuned by adjusting the fabrication conditions, e.g., metallic film thickness, annealing temperature, time for annealing, *etc.* [18]. The background signals of these nanostructures are negligibly small as compared to the background signals of spherical AuNPs or SIFs [14,16]. Therefore, the data evaluations for PSI-Au/Au and PSI-Ag/Au samples are easier compared to PSI-AuNPs and PSI-SIFs [15]. Any analysis to separate the signals emanating from PSI or from nanostructures is not necessary.

Both of the plasmonic nanostructures used for the investigation yield an enhancement in the fluorescence of PSI. Although the enhancements of fluorescence intensity of PSI-Au/Au and PSI-Ag/Au are lower compared to PSI-AuNPs and PSI-SIFs [15], the low auto-luminescence of these structures makes them the preferred tool for spectroscopy [16]. On average, the integral fluorescence intensity of PSI-Au/Au increases by a factor of 4.4 $\pm$ 3.9 compared to PSI-glass. For the PSI-Ag/Au sample, the corresponding value is 2.3 $\pm$ 0.8, as can be seen in Figure 4. However, it is worthwhile to note that for the individual complex of PSI-Au/Au, we even observed an increase in intensity of fluorescence up to 22.9-fold and for the PSI-Ag/Au sample up to 5.1-fold (Figure 5). The average enhancement factor due to Au/Au nanostructures is almost two-times bigger than the ordered gold triangles (AuΔ); however, due to the Ag/Au nanostructures, the enhancement factor is comparable to the results reported for ordered AuΔ [14,16]. The difference in enhancement factors of PSI-Au/Au and PSI-Ag/Au is mainly attributed to the difference of the spectral overlap between the absorption of PSI and the extinction spectra of Au/Au and Ag/Au nanostructures [39]. The effect of plasmonic nanostructures on changing the fluorescence (*i.e.*, quenching or enhancing) of fluorophore strongly depends on the spectral overlap of plasmon resonance, the absorption spectrum of the fluorophore and excitation wavelength [37,39,43]. The fluorescence responses of proteins have shown that the enhanced fluorescence was observed for the excitation in the spectral zone of metallic nanostructures [39]. Furthermore, for dyes, the brightest fluorescence is reported, where the emission peak of dyes is slightly red shifted to the localized surface plasmon resonance (LSPR)

peak of nanoparticles [37,42]. For the PSI-Au/Au sample, the excitation of PSI is within the spectral zone of the Au/Au sample's plasmon resonance, and also the extinction spectrum is more intensive and narrow, with the SPR peak position blue shifted to the emission peak of PSI. Therefore, the maximum enhancement of fluorescence complies with the reported results of Beyer *et al.* [39]. On the other hand, the amount of overlap between extinction spectra of Ag/Au and absorption of PSI is less than the overlap between extinction spectra of Au/Au and absorption of PSI, and the peak position of the SPR is red shifted to the emission peak position of PSI trimer from $Th.\ elongatus$, causing less enhancement of the fluorescence.

The histograms in Figure 5 show that the distributions of the intensity values for individual complexes of PSI-Au/Au and PSI-Ag/Au samples are more heterogeneously distributed than PSI-glass. The standard deviations of intensity distributions for PSI-glass, PSI-Au/Au and PSI-Ag/Au samples are presented in Table 1. The high standard deviation of enhancement factors of PSI-Au/Au and PSI-Ag/Au samples can be because of: (i) heterogeneity in the size of the metallic nanostructures [44]; (ii) the distance dependence of the interaction between plasmonic nanostructures and fluorophores [40]; and (iii) different emission/excitation dipole orientations. The size of individual metallic nanostructures used in our experiments is not homogenous, but it varies between 6–47 nm for the Au/Au substrate and between 6–36 nm for the Ag/Au substrate, as can be seen by the SEM images in Figure 1 (the size distribution of the nanostructures is given in [19]). Simulations and theoretical studies have shown that with the increase of the size of the particles, the electric field gets more intense and also extends further out from the particle [45]. Depending on the strength of the field, the fluorescence enhancement varies. Applying the same analogy, broad variation in the size of nanostructures produces a broad distribution of the near-field of nanostructures. As a result, the high standard deviations of the fluorescence enhancement factors are observed for Au/Au and Ag/Au samples (Figure 5). Distance-dependent enhancement and quenching of the fluorescence of fluorophores was observed by Anger *et al.* [40]. They calculated a distance-dependent enhancement curve for a fluorophore coupled to AuNP and found that the fluorescence is quenched for distances shorter than approximately 2 nm and reaches the maximum value at a 5-nm distance. At a distance higher than 5 nm, the fluorescence of the coupled fluorophore decayed exponentially, leading to vanishing enhancement around 80 nm, suggesting the absence of any coupling between the nanoparticle and the fluorophore. PSI used for the investigation in this study is a protein complex of a diameter of around 22 nm with a clover-shaped structure composed of around 288 Chl molecules in its trimeric form [26]. After hybridization with metallic nanostructures, the distance dependence of fluorescence plays its part. As some of the emitter Chls are in the distance range for maximum enhancement, while others are in the range for quenching of fluorescence, so the ultimate enhancement factors will be different for different coupled complexes, resulting in the broad distribution of the enhancement factor.

The influence of the plasmonic interactions on the functionality of photosynthetic proteins was studied by Govorov *et al.* [22] and Krassen *et al.* [46]. They established that PSI complexes maintain their charge-transfer and light harvesting capability close to nanoparticles. Based on the literature, the modifications in the structure of PSI complexes due to nanostructures in the proximity seems improbable [15,23,46–49]. Analogous to the observations of single-chromophore systems and two-chromophore FRET-coupled systems [35,44,50], the PSI coupled to the plasmonic nanostructures

Chapter 7: Manipulating the Excitation Transfer in Photosystem I Using a Fabry–Perot Metal Resonator with Optical Subwavelength Dimensions

The controlled and modified fluorescence and energy transfer properties of PSI were shown by using a newly developed approach to produce optical subwavelength microcavities for cryogenic temperature issues [136]. The reason to choose *Arthrospira platensis* was because it has a broad and structured fluorescence emission at 710 and 760 nm. By changing the distance between mirrors, the electromagnetic field mode structure around PSI is varied affecting the emission and energy transfer properties, which allows one to selectively enhance signals of resonant emitters and suppress off-resonant emission.

By comparing the experimental data with simulations, we showed how excitation transfer within PSI is affected by the microcavity. The ability to control the energy transfer within such efficient energy converters as photosynthetic proteins can establish the opportunity for enhancing the efficiencies of bio-solar applications. The defined control of the resonance conditions by microcavities makes them a preferable tool to study the effects of additional electromagnetic modes on the energy transfer in any coupled multi-chromophore system. The resonator geometry excludes the direct contact of the proteins with any surface. Possible quenching or denaturation of the complexes close to metal surfaces are still insuperable obstacles for studies with proteins and nanostructures, which can be avoided by resonators. This chapter is adapted from the paper in ref. [136].

PCCP

PAPER

View Article Online
View Journal | View Issue

Cite this: *Phys. Chem. Chem. Phys.*, 2014, **16**, 6175

Manipulating the excitation transfer in Photosystem I using a Fabry–Perot metal resonator with optical subwavelength dimensions†

Alexander Konrad,[a] Anna-Lisa Trost,[a] Sepideh Skandary,[a] Martin Hussels,[a] Alfred J. Meixner,[a] Navasard V. Karapetyan[b] and Marc Brecht*[ac]

Received 9th December 2013,
Accepted 5th February 2014

DOI: 10.1039/c3cp55195d

www.rsc.org/pccp

We demonstrate controlled modification of the fluorescence and energy transfer properties of Photosystem I (PSI) – one of the most important light harvesting systems – by using a newly developed approach to produce optical subwavelength microcavities for cryogenic temperature issues. The experiments were carried out on PSI from the cyanobacterium *Arthrospira platensis* as it shows a broad and structured fluorescence emission. By changing the distance between the cavity forming mirrors, the electromagnetic field mode structure around PSI is varied affecting the emission and energy transfer properties, which allows us to selectively enhance signals of resonant emitters and suppress off-resonant emission. By comparing the experimental data with simulations, we are able to show how excitation transfer within PSI is affected by the microcavity. The ability to control the energy transfer within such efficient energy converters as photosynthetic proteins can establish the opportunity for enhancing the efficiencies of bio-solar applications. The defined control of the resonance conditions by microcavities makes them a preferable tool to study the effects of additional electromagnetic modes on the energy transfer in any coupled multi-chromophore system. The resonator geometry excludes the direct contact of the proteins with any surface. Possible quenching or denaturation of the complexes close to metal surfaces is still an insuperable obstacle for studies with proteins and nanostructures, which can be avoided by resonators.

1 Introduction

Optical microcavities are efficient tools to tailor the fluorescence of embedded emitters to a narrow spectral range.[1] Placing an emitter within a confined geometry of a resonator modifies its emission properties,[2] in particular, the spectral, spatial and temporal distributions. According to Fermi's golden rule, the spontaneous emission lifetime of a dipole emitter depends on both the transition dipole moment and the density of modes of the electromagnetic field.[3] Inside cavities, the density of modes coupling to the dipole emitter is changed with respect to free space and hence the emission rate of the emitter. This effect – first described by Purcell[2] – can be used to enhance and shape the fluorescence emission down to the single particle/molecule level.[4–7] One type of such cavities is realized by Fabry–Perot like microresonators, which are emerging devices for manipulating optical properties of fluorophores.[6] In the last few years, experimental studies on cavity-controlled photo-luminescence have been carried out on model systems such as single quantum dots,[8] molecules,[4] atoms,[9] nitrogen-vacancy centers in diamonds[10] and simple energy transfer systems.[11,12] In this article, we demonstrate first optical experiments of a prominent and complex energy transfer coupled protein system confined in an optical resonator at cryogenic temperatures (1.6 K). We selectively tune the fluorescence of emitting pools in Photosystem I (PSI) by a subwavelength microcavity and describe the consequent modifications in the exciton transfer dynamics.

PSI is one of the key proteins of the photosynthetic apparatus and a promising candidate for bio-solar applications.[13–15] Especially, interactions with electric fields created by plasmonic nanostructures have attracted a lot of attention during the last few years.[13,14,16–22] The attractiveness of PSI relies partially on its simple function, which is capturing and converting solar energy into electric energy. For this purpose around 100 chlorophyll

[a] *Institut für Physikalische und Theoretische Chemie, Universität Tübingen, Auf der Morgenstelle 18, 72076 Tübingen, Germany. E-mail: marc.brecht@uni-tuebingen.de; Fax: +49-7071-29-5490; Tel: +49-7071-29-76239*
[b] *A.N. Bakh Institute of Biochemistry, Russian Academy of Sciences, Leninsky Prospect, 33, 119071 Moscow, Russia*
[c] *Zürcher Hochschule für Angewandte Wissenschaften, Institut für Angewandte Mathematik und Physik, Technikumstrasse 13, 8401 Winterthur, Switzerland*

† Electronic supplementary information (ESI) available. See DOI: 10.1039/c3cp55195d

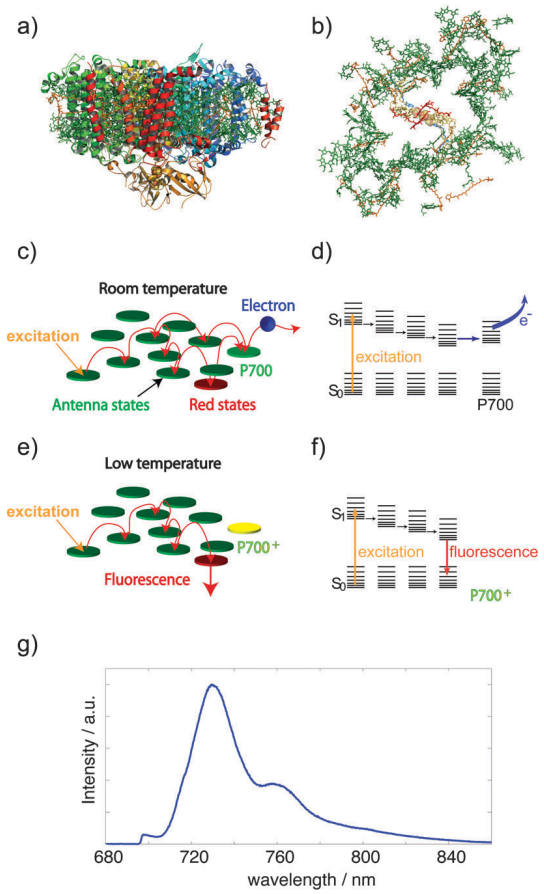

Fig. 1 Photosystem I from oxygenic photosynthesis. (a) Side view of PSI from cyanobacteria (protein data bank (PDB) entry: 1JB0).[24] (b) Top view of PSI without the protein backbone. In each monomer about 100 chlorophyll molecules (green) absorb excitation energy and transfer it to a chlorophyll dimer (red) in the reaction center[23] which absorbs at 700 nm (P700). (c and d) Illustration of excitation-energy transfer pathways at ambient temperatures and an energy-level scheme. Upon excitation of P700 a charge-separated state across the membrane is formed.[23] Interestingly, red chlorophyll states (red) with lower excitation energies than P700 are also involved in energy transfer. (e and f) At low temperatures the transfer from the red chlorophylls towards P700 is partially blocked, as a consequence these chlorophylls become fluorescent. (g) The low temperature fluorescence emission of PSI trimers (blue) is composed of several contributions having different wavelength positions, width and intensity (for further details, see ref. 25 and 26).

molecules per monomer are involved in efficient light-harvesting and excitation energy transfer leading to light induced charge separation in the reaction center and a subsequent transfer of an electron (Fig. 1a–d).[23] An intriguing feature of the PSI core antenna of cyanobacteria is the presence of several chlorophyll (Chl) molecules absorbing at lower energy than the reaction center at 700 nm (P700). These Chls have a pronounced effect on the excitation energy transfer within the whole antenna system (Fig. 1c–f).[27] These red-shifted Chls are often referred to as "red-most" Chls or long-wavelength Chls (for details see ref. 25 and 28). At low temperatures, these long-wavelength Chls act as traps for excitons, partially releasing this excitation energy as fluorescence (Fig. 1e–f).[23] The fluorescence emission of PSI is a composition of several spectroscopically discernible contributions from different long-wavelength Chls.[25] The high quality of the protein preparations, the large absorption cross section, the red-shifted emission and its prominence makes PSI a perfect system to analyze the influence of external fields on the optical properties and excitation energy transfer dynamics of coupled multi-chromophoric systems.[16–18,22,29]

The modifications of the excitation energy transfer in PSI embedded in a subwavelength microcavity result in altered fluorescence spectra which are observed using a confocal microscope. Revealing these altered exciton transfer dynamics is achieved by comparing the experimental spectra with simulated spectra of uncoupled chromophores. The resonance wavelength and with that the cavity length can be measured and modified by scanning the position of the focal spot (confocal volume) over the microcavity as shown in Fig. 2. This approach enables the collection of transmission and fluorescence spectra of PSI complexes exposed to different electromagnetic field mode structures. Production and application of the microresonators at cryogenic temperatures are described in the ESI.† Altering transfer efficiencies in transfer coupled systems embedded in resonators by modifying their optical properties has already been shown by Andrew *et al.*[12] or Schleifenbaum *et al.*[11] who used model systems at room temperature. It has been shown for such coupled systems that microcavities enable the enhancement and characterization of luminescence bands which are suppressed in free space. Addressing individual fluorescent pools in PSI is hampered by large lifetime variations,[30,31] overlapping of spectral bands,

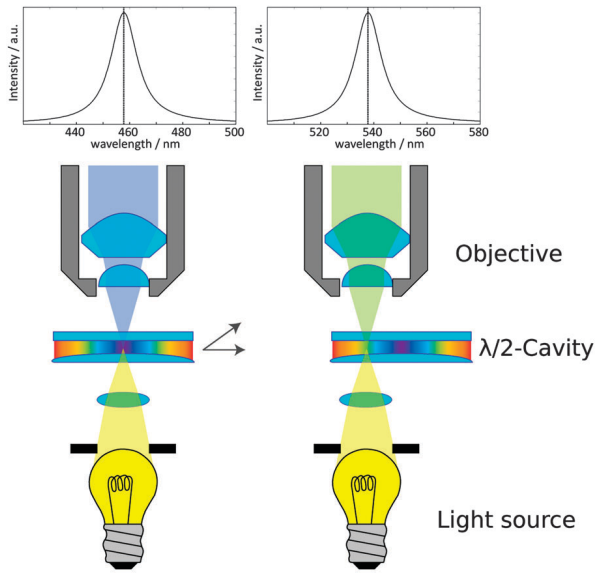

Fig. 2 Simplified scheme showing the scanning of the focal spot over a $\lambda/2$ microcavity. The curved shape of one of the mirrors results in a continuous change of the resonance conditions as indicated by the rainbow colors inside the cavity. The cavity is illuminated by a white light source to determine the cavity properties at the focal spot; only the components fulfilling the resonance conditions pass the cavity. This light is collected by an objective yielding the transmission spectrum (on top). The resonance wavelength of the resonator is changed simply, by changing the position of the focal spot in relation to the cavity (right). For detailed information concerning the setup and manufacturing of the cavities, see also the ESI.†

potentially hidden quenched pools and spectral diffusion even at cryogenic temperatures. In this article we report on the selective control of the energy transfer in a complex and one of the most important protein systems in nature for the first time. We can also confirm previously reported[22,25,32] approaches addressing fluorescent Chl pools by measurements and the used model for interpretation. With our new approach for low temperature Fabry–Perot resonators any biological sample can be prepared and frozen in standard solutions like water–glycerol-mixtures. Contrary to experiments with nanostructures, we can also exclude any chemical interaction of the proteins at metal surfaces due to a large cavity mode volume and a glass spacing layer on the silver mirrors. Conformational changes or denaturation induced by nearby metal surfaces is a severe problem for observing native protein states. The defined control of light-harvesting and energy-transfer coupled system is one prerequisite for developing or improving bio-solar devices.

2 Results and discussion

In the first order of interference of the cavity ($\lambda/2$ region), several positions with different resonance conditions were selected as illustrated in Fig. 2. At these positions, the white light transmission spectrum of the cavity and the fluorescence emission of PSI were recorded one after the other. For each position, the cavity length was determined from the white light transmission spectrum (as shown in the ESI†). The $\lambda/2$ region contains only one matching order of resonator modes in the wavelength range of the absorption and emission of PSI. This gives the opportunity to control the mode density with high precision over a large spectral range. The excited photosystems in the resonator are forced to enhanced decoherence resulting in changed lifetimes and restricted energy distribution.

Several fluorescence spectral series with tuned resonance frequencies of the resonator covering the whole wavelength range of the fluorescence emission of PSI were collected. Fig. 3a shows four emission spectra (blue curves) out of one series together with the corresponding Lorentzian fits of the white light transmission spectra (black curves). For comparison, the spectrum on top shows the free space emission spectrum of PSI trimers from *A. platensis* (blue curve). The same spectrum is also displayed in Fig. 3b described by a multiple Gaussian fit (see also Table 1). The four measured spectra at selected resonance wavelengths differ extremely from the free-space spectrum but also from each other. Mostly emission around the white light transmission maximum is enhanced and emission on the long wavelength side inhibited. On the short wavelength

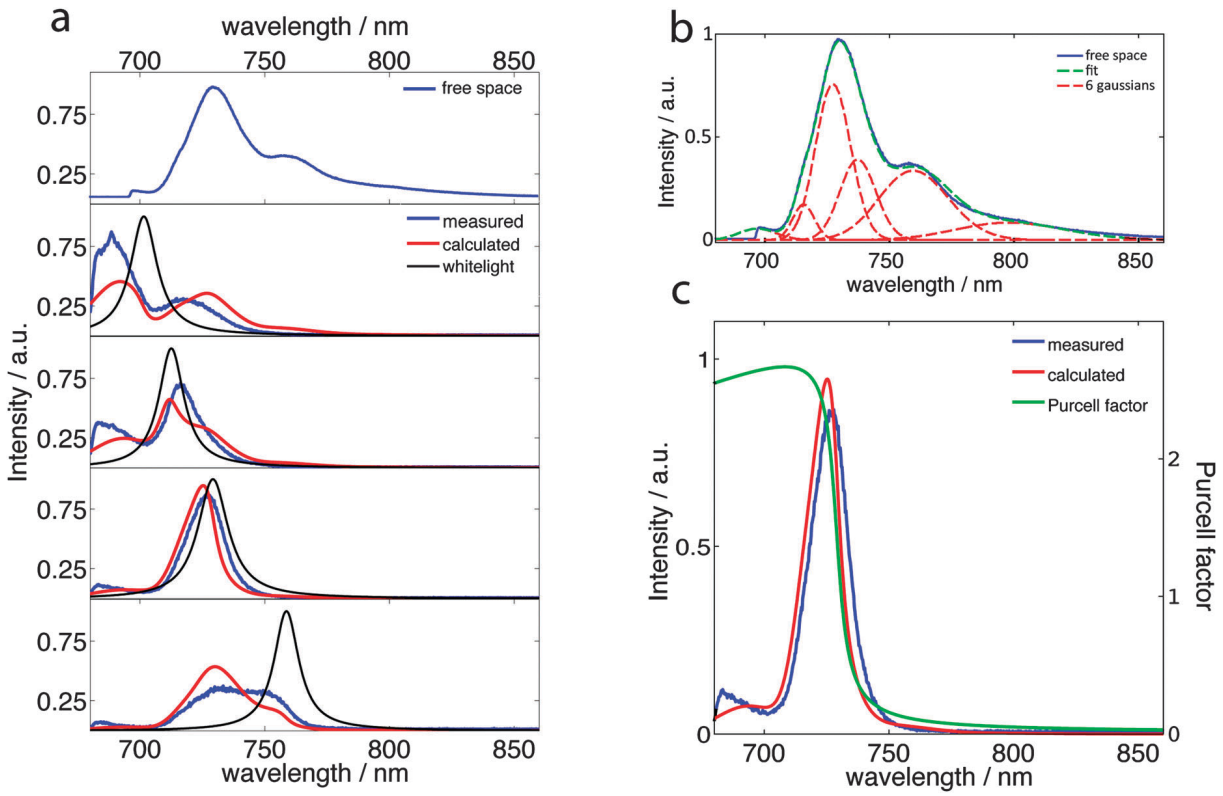

Fig. 3 (a) Four measured (blue curves) and calculated (red curves) fluorescence spectra of PSI placed inside the microresonator at different cavity lengths. The white light transmission (black curves) shows their resonance wavelengths at 702, 712, 730, and 759 nm. On top, the free-space fluorescence spectrum of PSI trimers from *A. platensis* is given (the drop down of the intensity at <695 nm is due to the longpass filter used). (b) The free space spectrum of PSI from *A. platensis* (blue curve) together with a fit (green dotted curve) based on six individual Gaussian functions (red dotted curves), the details are given in the text and in Table 1. (c) One selected set of measured (blue curves) and calculated spectrum (red curves) in combination with the Purcell factor (green curve) as given in ref. 33 and the ESI.†

Table 1 Comparison of parameters resulting from a fit of the free-space emission spectrum of PSI trimers from *A. platensis* with wavelength positions of fluorescent pools reported in the literature

Gaussian	Wavelength/nm	Width/nm	Pool
1	697	21	F699[32]
2	715	12	F714[26]
3	727	20	F726[25,26]
4	737	20	F731[25]
5	759	39	F760[26]
6	798	62	—

side angular distribution modes are still able to couple with emitters to enhance their radiative rate, visible in Fig. 3c by the shown Purcell factor distribution.[33] We claim that the influences on PSI resulting in the shown spectra are on the one hand determined by the spectral shaping of the Purcell factor and on the other hand by altered transfer dynamics, depending on changed population/depopulation rates.

To highlight the pure contribution caused by modifications within the transfer dynamics we simulated the emission spectrum of PSI inside the cavity without assuming any coupling between the emitting pools and compared these simulations with the experiment. The method for simulating the cavity influenced spectra is based on ref. 7. The main concept is grounded on the assumption that the spectral band and its overall intensity are proportional to the fluorescence quantum yield and the population probability of its corresponding emitter. In a cavity, the radiative rate is altered leading to a changed intensity of the band. Also the shape of the spectral band is changed due to the spectral shape of the cavity mode distribution. Therefore, the characteristic spectral distribution of the Purcell factor enables enhancing or suppressing and addressing of single emitting bands inside a composite spectrum. For this purpose the single spectral bands of the free-space PSI spectrum are characterized by Gaussian fits (see Fig. 3b). Five Gaussian contributions, centered at 697, 715, 727, 737 and 760 nm, are used with wavelength positions and widths in agreement with the recently reported positions of the red-emitting states, for details, see ref. 25, 26 and 32. A sixth contribution at 798 nm is not reported for PSI in the literature up to now, but the contribution is necessary to reconstruct the emission profile properly. The spectral position and the width of all six contributions together with the assigned red Chls are summarized in Table 1.

Each Gaussian is overlapped with the corresponding Purcell factor distribution for each corresponding resonance wavelengths. The spectral distribution of the Purcell factors was calculated by using ref. 33. Finally the six single shaped Gaussians were summed up again and scaled to same integral intensity as the corresponding measured spectrum to make their comparison feasible. A more detailed description is given in the ESI.†

Fig. 3a and c show experimental (blue) and simulated spectra (red) at various resonance wavelengths. Each experimental spectrum differs from its corresponding simulation with various degrees within various spectral regions, indicating the additional effect of disturbed transfer pathways inside PSI. Fig. 4a and b show the complete fluorescence spectral series of experimental (a) and calculated (b) spectra for resonance wavelengths between 697 and 850 nm (white circles). Comparing (a) and (b) it can be seen that the simulations of the uncoupled system differ slightly for specific wavelength ranges from the experiment. To highlight these specific differences between coupled and uncoupled systems the simulated series was subtracted from the experimental series, whose result is shown in Fig. 4c. This series now shows the fluorescence enhancement/inhibition (violet/red), depending on wavelengths and cavity lengths, of the coupled system compared to the uncoupled system. Red colors show less fluorescence to the simulation, meaning a lowered population of these emitting pools, while violet and blue show more fluorescence, meaning an increased population of these emitting pools. Positive values

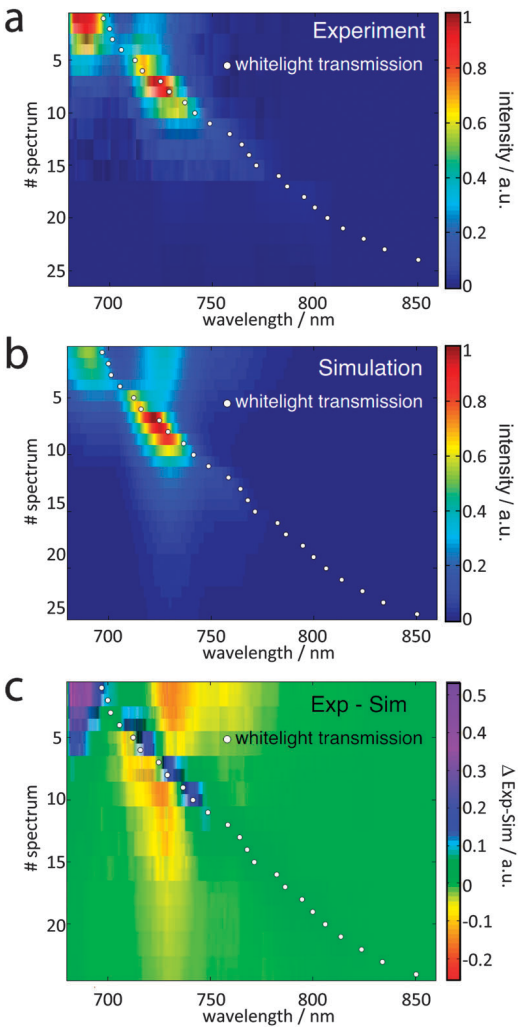

Fig. 4 (a) Contour plot of a fluorescence spectral series of experimental data taken from a scan of the resonance wavelength of the resonator over the emission profile of PSI from *A. platensis*. The resonance wavelength of the resonator is given by white dots; it varies between 697 nm and 850 nm. (b) Contour plot of a fluorescence spectral series of the calculated spectra based on the conditions given in (a) and without respect to coupling between the emitters. (c) Contour plot showing the difference between the plots given in (a) and (b) revealing the cavity induced modifications in the energy transfer dynamics. Violet means more emission, red less emission of the coupled to the uncoupled system.

can be observed for the first five spectra in the region at ~690 nm and for spectra with number 3–10 close to their resonance wavelengths. Negative values are observed for almost all spectra in the wavelength range close to the emission maximum of PSI.

The specific effects of alterations of the process rates in PSI can be seen in Fig. 4 and are schematically visualized in Fig. 5. Spectra with resonances <720 nm show increased intensity at wavelengths around 690 nm. This enhanced fluorescence indicates a deactivation of states, which show virtually no fluorescence emission in the absence of the resonator. This can be explained by an increased residence time of excitons at these emitters and therefore an inhibited transfer to chromophores with lower energies. Also the off-resonant (longer wavelengths than transmission maximum) emitters are inhibited in their radiative deactivation leading to increased saturation than to free space. The spectra with resonances >750 nm show lowered intensity for all emitting pools, mostly for Chls emitting at around 730 nm. This can be explained by the enhanced deactivation of all fluorescent Chls because of the flattened flank of the Purcell factor to short wavelengths. Therefore a lowered excitonic population probability of these emitters induced by the resonator compared with the simulations can be assumed.

The most striking effects are found in the wavelength areas of the pools F699, F726 and F731 (see Table 1). In Fig. 5 this behavior is sketched for three different mirror spacings. On the left the modified spectra are shown (red) with the corresponding transmission spectra (gray) below the free-space spectrum on top. On the right the arrangement of the Chl, the emitting pools (see Table 1) and their deactivation rates are sketched by red arrows.

The specific arrangement and coupling of the chromophores in PSI is optimized for efficient excitation transfer to the reaction center.[34] The energy transfer efficiency between chromophores depends on the spectral overlap, distance, and orientation,[34,35] the individual relaxation properties and saturation effects of long-living states. This means, each Chl within the transfer chain features a characteristic time and probability of accepting, containing and transferring an exciton. By changing one or more Chl relaxation rates within PSI all other relaxation properties are influenced. Such cavity enhanced transfer efficiency changes have been shown already for two simple systems under ambient conditions: a two-chromophore model system[12] and the fluorescent protein DsRed.[6,11]

As a consequence, the field in the microresonator can change the specific and controllable exciton distribution within PSI by involving additional chromophores in excitation energy transfer[19,22,29] or by changing the evolution inside the energy transfer pathways by enhanced/inhibited population/depopulation of excited states. Fig. 4 also supports the assignment of the fluorescent pools according to Table 1. Obvious deviations between experiment and simulation are only found in wavelength regions corresponding to reported Chl pools.

Comparable effects on the fluorescence emission of different photosynthetic complexes were recently observed in the vicinity of plasmonic nanostructures.[20,22,29] Such effects on optical

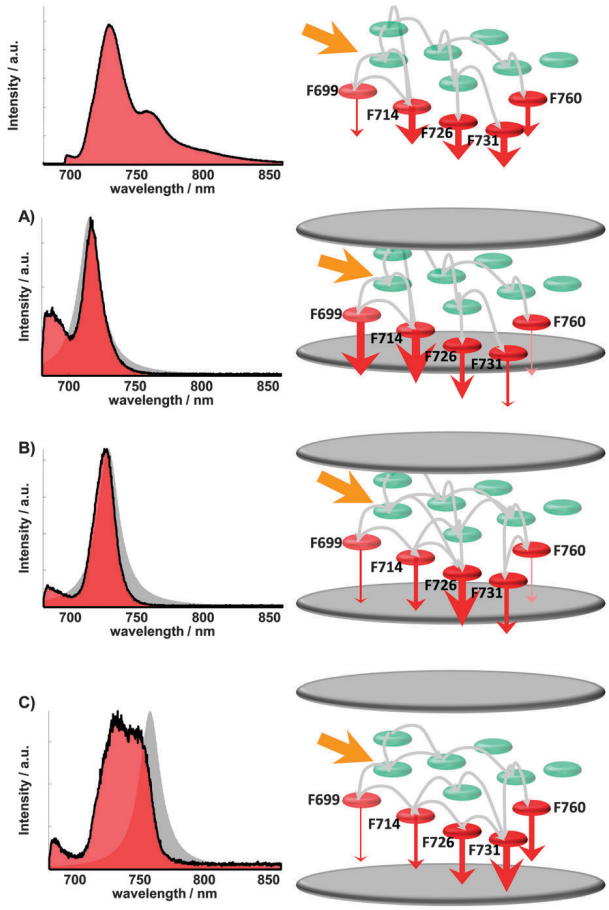

Fig. 5 Visualization of altered excitation energy transfer pathways in Photosystem I (exaggerated and simplified). From (A) to (C) the cavity length increases, noticeable by the spectral position of the white light transmission (grey area). The set of radiative transition rates and the population of the red states are modified by the additional mode density depending on mirror spacing. Changing the radiative rate (to free space) as a depopulation channel of a certain luminescent chlorophyll containing pool also alters the population dynamics of its corresponding transferring and receiving pools. The observed spectrum is a superposition of every single pool emission (see Table 1), depending on its population amount, the wavelength dependent resonator emission pattern and the radiative rate enhancement/inhibition. The altered spectrum enables therefore statements on the relative population probability of every luminescent pool. The altered occupations, indicated by Fig. 4, are visualized exemplarily on the right side by the thickness of the red arrows illustrating the emission intensity, together with the corresponding spectra (left, red area).

properties of chromophores are induced by the optical near-field of the nanostructures.[36,37] The interaction between pigments and the electric near-field of plasmonic nanostructures shows a strong distance- and orientation-dependence.[36,37] A fluorophore coupled to an Au nanosphere of 100 nm diameter shows within 13 nm a change from quenching to maximum enhancement,[36] this value is even smaller than the diameter of a PSI trimer (~20 nm). As a consequence, the effect of a plasmonic near field on the different Chls in one single protein complex can vary between quenching and maximal enhancement.[20,22,29] If one aims to control the optical properties of a protein complex by plasmonic nanostructures a precise positioning in the sub-nanometer regime is required and in

addition, the relative orientations must be controlled. As a consequence, studies to investigate the interaction of the electromagnetic fields produced by plasmonic nanostructures are hindered by these constraints. Optical microcavities, however, exhibit several advantages. The field distribution within a Fabry–Perot resonator is well defined by the distance between the mirrors and it changes only slightly over the dimension of a single protein ($\lambda/2$ *vs.* 20 nm for PSI); therefore the mode structure of the electric field at the position of the proteins can be determined directly from the transmission spectrum. This approach simplifies theoretical modeling of the decoherence induced by the mode structure and provides further insights into coherent or incoherent parts of the transfer. Another advantage compared to metallic nanostructures lies in the possibility to exclude chemical interactions with the protein complexes. The protein structure can be altered or even denaturized upon direct contact with metal surfaces.[38,39] Thus, in experiments with proteins close to metal surfaces or structures one can never be sure to gather information on native states. The volume of the microcavity is comparably large and a spacing layer of SiO_2 covering the silver surfaces prevents interactions completely. Therefore, chemical interactions by the field enhancing geometry on luminescent proteins can be excluded in the reported experiments. In principle, all pigment–proteins can be investigated by the resonator production and sample transfer[40] method presented here.

3 Experimental section

A schematic along with a detailed description of the manufacturing process of low temperature cavities and the confocal microscope used for efficient excitation and detection of the emission of PSI in the microresonator are given in the ESI.†

In short, the microcavity consists of two silver mirrors one being planar and one being slightly curved such that the gap between the mirrors slowly increases with increasing distance from the center, shown in Fig. 2. The cavity mirrors were fabricated by coating quartz substrates with several layers. The first layer is made of 1 nm chromium, followed by a silver layer (60 nm bottom and 30 nm top mirror), a 1 nm gold layer that is finally covered by a 30 nm SiO_2 layer, which acts as a spacer between the proteins and the silver surface. Their reflectivity was determined by transmission spectroscopy to be 0.95 (bottom) and 0.90 (top) @ 700 nm.

On one of the coated glass substrates less than 1 μL of the PSI containing sample solution was placed and then covered by a second coated glass substrate. This sandwich was transferred to the sample holder designed for our low temperature setup (for details see ref. 40). The sample holder is fixed on a stage for squeezing the mirrors together yielding a Fabry–Perot resonator showing concentric Newton rings in transmission indicating variable mirror distances and resonance conditions. The whole squeezer (including the sample holder and the sample) is then transferred into a Dewar flask filled with liquid nitrogen. The frozen sample solution acts as a glue holding the squeezed mirrors in position. A home-built sample transfer system[40] enables us to transfer the squeezed resonator into the cold cryostat (4.2 K) without temperature increase during handling and transfer. After mounting the sample inside the cryostat, the temperature is lowered to 1.6 K.

The wavelength of the cavity mode perpendicular to the mirror surfaces was determined from the white light transmission spectrum (see Fig. S2 and S4 in the ESI†). The design of our low temperature microresonator results in a quality factor of ~60 (fwhm ~ 15 nm in the transmission spectrum at 1.6 K), which is several times smaller than the full width at half maximum of the emission spectrum of PSI trimers from *A. platensis*. All fluorescence measurements were done with cw-excitation at 665 nm.

4 Conclusion

In conclusion, our experiments show an altered fluorescence emission of PSI in an optical microresonator with subwavelength dimensions. Comparing the experimental data with simulations assuming uncoupled emitters provides the intensity changes caused by altered energy transfer pathways. Particularly chlorophyll molecules with site-energies close to that of the reaction center undergo much stronger deactivation through fluorescence emission as the uncoupled model, indicating an increased presence probability of excitons. We suppose that altered responses can generally be expected for multichromophore coupled systems in any resonate optical structure. The mode density can be changed by microcavities in a defined manner in a very simple way. Any structural distortion or denaturation of the proteins by the metallic surfaces in our experiments can be ruled out. Therefore, optical microresonators are superior to plasmonic nanostructures for studying the influence of optical fields on any kind of luminescent particles.

Acknowledgements

Financial support from the German Research Council (DFG) for ME1600/13-1 and Heisenberg-Programm (BR 4102/1-1 and BR 4102/2-1), the Russian Academy of Sciences, program MCB and RFBR (Grant 14-04-00148a, to N.V.K.) is gratefully acknowledged.

References

1 K. J. Vahala, *Nature*, 2003, **424**, 839–846.
2 E. M. Purcell, *Phys. Rev.*, 1946, **69**, 681.
3 E. Fermi, *Rev. Mod. Phys.*, 1932, **4**, 88–132.
4 M. Steiner, F. Schleifenbaum, C. Stupperich, A. V. Failla, A. Hartschuh and A. J. Meixner, *J. Lumin.*, 2006, **119**, 167–172.
5 M. Steiner, A. V. Failla, A. Hartschuh, F. Schleifenbaum, C. Stupperich and A. J. Meixner, *New J. Phys.*, 2008, **10**, 123017.
6 S. Bar, A. Chizhik, R. Gutbrod, F. Schleifenbaum, A. Chizhik and A. J. Meixner, *Anal. Bioanal. Chem.*, 2010, **396**, 3–14.
7 A. I. Chizhik, A. M. Chizhik, A. M. Kern, T. Schmidt, K. Potrick, F. Huisken and A. J. Meixner, *Phys. Rev. Lett.*, 2012, **109**, 223902.

8 D. Englund, D. Fattal, E. Waks, G. Solomon, B. Zhang, T. Nakaoka, Y. Arakawa, Y. Yamamoto and J. Vuckovic, *Phys. Rev. Lett.*, 2005, **95**, 013904.
9 T. Aoki, B. Dayan, E. Wilcut, W. P. Bowen, A. S. Parkins, T. J. Kippenberg, K. J. Vahala and H. J. Kimble, *Nature*, 2006, **443**, 671–674.
10 S. Schietinger, T. Schroder and O. Benson, *Nano Lett.*, 2008, **8**, 3911–3915.
11 F. Schleifenbaum, K. Elgass, M. Steiner, J. Enderlein, S. Peter and A. Meixner, *Proc. SPIE*, 2009, **7185**, 718504.
12 P. Andrew and W. L. Barnes, *Science*, 2000, **290**, 785–788.
13 R. A. Grimme, C. E. Lubner, D. A. Bryant and J. H. Golbeck, *J. Am. Chem. Soc.*, 2008, **130**, 6308–6309.
14 C. E. Lubner, R. Grimme, D. A. Bryant and J. H. Golbeck, *Biochemistry*, 2010, **49**, 404–414.
15 A. Mershin, K. Matsumoto, L. Kaiser, D. Yu, M. Vaughn, M. K. Nazeeruddin, B. D. Bruce, M. Graetzel and S. Zhang, *Sci. Rep.*, 2012, **2**, 234.
16 L. Frolov, Y. Rosenwaks, C. Carmeli and I. Carmeli, *Adv. Mater.*, 2005, **17**, 2434–2437.
17 A. O. Govorov and I. Carmeli, *Nano Lett.*, 2007, **7**, 620–625.
18 I. Carmeli, I. Lieberman, L. Kraversky, Z. Fan, A. O. Govorov, G. Markovich and S. Richter, *Nano Lett.*, 2010, **10**, 2069–2074.
19 J. B. Nieder, PhD thesis, Freie Universitaet Berlin, Germany, 2011.
20 S. R. Beyer, S. Ullrich, S. Kudera, A. T. Gardiner, R. J. Cogdell and J. Koehler, *Nano Lett.*, 2011, **11**, 4897–4901.
21 H. Toporik, I. Carmeli, I. Volotsenko, M. Molotskii, Y. Rosenwaks, C. Carmeli and N. Nelson, *Adv. Mater.*, 2012, **24**, 2988–2991.
22 M. Brecht, M. Hussels, J. B. Nieder, H. Fang and C. Elsässer, *Chem. Phys.*, 2012, **406**, 15–20.
23 B. Gobets and R. van Grondelle, *Biochim. Biophys. Acta*, 2001, **1507**, 80–99.
24 P. Fromme, P. Jordan and N. Krauss, *Biochim. Biophys. Acta, Bioenerg.*, 2001, **1507**, 5–31.
25 E. Schlodder, M. Hussels, M. Cetin, N. V. Karapetyan and M. Brecht, *Biochim. Biophys. Acta*, 2011, **1807**, 1423–1431.
26 M. Brecht, M. Hussels, E. Schlodder and N. V. Karapetyan, *Biochim. Biophys. Acta, Bioenerg.*, 2012, **1817**, 445–452.
27 A. N. Melkozernov, *Photosynth. Res.*, 2001, **70**, 129–153.
28 N. V. Karapetyan, E. Schlodder, R. van Grondelle and J. P. Dekker, *Photosystem I: The Light-Driven Plastocyanin: Ferredoxin Oxidoreductase*, Advances in Photosynthesis and Respiration, Springer, 2006, vol. 24.
29 J. B. Nieder, R. Bittl and M. Brecht, *Angew. Chem., Int. Ed.*, 2010, **49**, 10217–10220.
30 B. Gobets, I. H. M. van Stokkum, M. Rogner, J. Kruip, E. Schlodder, N. V. Karapetyan, J. P. Dekker and R. van Grondelle, *Biophys. J.*, 2001, **81**, 407–424.
31 B. Gobets, I. H. M. van Stokkum, F. van Mourik, J. P. Dekker and R. van Grondelle, *Biophys. J.*, 2003, **85**, 3883–3898.
32 M. Brecht, V. Radics, J. B. Nieder, H. Studier and R. Bittl, *Biochemistry*, 2008, **47**, 5536–5543.
33 G. Bjork, *IEEE J. Quantum Electron.*, 1994, **30**, 2314–2318.
34 M. Byrdin, P. Jordan, N. Krauss, P. Fromme, D. Stehlik and E. Schlodder, *Biophys. J.*, 2002, **83**, 433–457.
35 M. Yang, A. Damjanovic, H. M. Vaswani and G. R. Fleming, *Biophys. J.*, 2003, **85**, 140–158.
36 P. Anger, P. Bharadwaj and L. Novotny, *Phys. Rev. Lett.*, 2006, **96**, 113002.
37 A. M. Kern, A. J. Meixner and O. J. F. Martin, *ACS Nano*, 2012, **6**, 9828–9836.
38 L. Shang, Y. Z. Wang, J. G. Jiang and S. J. Dong, *Langmuir*, 2007, **23**, 2714–2721.
39 S. Chah, M. R. Hammond and R. N. Zare, *Chem. Biol.*, 2005, **12**, 323–328.
40 M. Hussels, A. Konrad and M. Brecht, *Rev. Sci. Instrum.*, 2012, **83**, 123706.

Chapter 8: Resolution Enhancement For Low-Temperature Scanning Microscopy By Cryostat Immersion Imaging

In this chapter, a simple method to enhance the resolution of an image using the confocal microscope under cryogenic conditions is shown. Using a MO with high numerical aperture (NA) and an immersion fluid with low freezing temperature, one is able to reach an NA > 1 at cryogenic temperature. The MO and the sample were both placed inside the inner chamber of the cryostat to reduce distortions induced by temperature gradients. The simplicity of the whole procedure makes a remarkable step towards the development of cryo-super-resolution microscopy. This chapter is adapted from the paper in ref. [138].

Resolution Enhancement For Low-Temperature Scanning Microscopy By Cryostat Immersion Imaging

Michael Metzger[1], Alexander Konrad[1], Sepideh Skandary[1], Imran Ashraf[1], Alfred J. Meixner[1] and Marc Brecht[1,2,*]

[1] *Institute of Physical and Theoretical Chemistry, University of Tuebingen, Germany*

[2] *Zurich University of Applied Science, Institute of Applied Mathematics and Physics, Winterthur, Switzerland*

[*] *marc.brecht@uni-tuebingen.de*

Abstract: Here we report a simple way to enhance the resolution of a confocal scanning microscope under cryogenic conditions. Using a microscope objective (MO) with high numerical aperture (NA) and an immersion fluid with low freezing temperature we were able to reach an NA $>$ 1 at a temperature around 160 K. The MO and the sample were both placed inside the inner chamber of the cryostat to reduce distortions induced by temperature gradients. The image quality of our commercial available MO was further enhanced by scanning the sample (desk scanning) and not the exciting laser beam (beam scanning). The simplicity of the whole procedure marks a remarkable step towards the development of cryo super-resolution microscopy and correlative light and electron cryo microscopy (cryoCLEM).

OCIS codes: (000.0000) General.

References and links

1. M. Minsky, "Memoir on inventing the confocal scanning microscope," *Scanning*, vol. 10, pp. 128–138, July 1988.
2. G. Lin, M. K. Chawla, K. Olson, C. A. Barnes, J. F. Guzowski, C. Bjornsson, W. Shain, and B. Roysam, "A multi-model approach to simultaneous segmentation and classification of heterogeneous populations of cell nuclei in 3d confocal microscope images," *Cytometry Part A*, vol. 71A, pp. 724–736, Sept. 2007.

3. E. Abbe, “Beitrge zur theorie des mikroskops und der mikroskopischen wahrnehmung,” vol. 9, no. 1, pp. 413–418–, 1873.
4. M. Bates, B. Huang, G. T. Dempsey, and X. W. Zhuang, “Multicolor super-resolution imaging with photo-switchable fluorescent probes,” *Science*, vol. 317, pp. 1749–1753, Sept. 2007.
5. E. Betzig, G. H. Patterson, R. Sougrat, O. W. Lindwasser, S. Olenych, J. S. Bonifacino, M. W. Davidson, J. Lippincott-Schwartz, and H. F. Hess, “Imaging intracellular fluorescent proteins at nanometer resolution,” *Science*, vol. 313, pp. 1642–1645, Sept. 2006.
6. M. Friedenberger, M. Bode, A. Krusche, and W. Schubert, “Fluorescence detection of protein clusters in individual cells and tissue sections by using toponome imaging system: sample preparation and measuring procedures,” *Nature Protocols*, vol. 2, no. 9, pp. 2285–2294, 2007.
7. S. W. Hell, M. Dyba, and S. Jakobs, “Concepts for nanoscale resolution in fluorescence microscopy,” *Current Opinion In Neurobiology*, vol. 14, pp. 599–609, Oct. 2004.
8. S. Manley, J. M. Gillette, G. H. Patterson, H. Shroff, H. F. Hess, E. Betzig, and J. Lippincott-Schwartz, “High-density mapping of single-molecule trajectories with photoactivated localization microscopy,” *Nature Methods*, vol. 5, pp. 155–157, Feb. 2008.
9. M. J. Rust, M. Bates, and X. W. Zhuang, “Sub-diffraction-limit imaging by stochastic optical reconstruction microscopy (storm),” *Nature Methods*, vol. 3, pp. 793–795, Oct. 2006.
10. M. Sackrow, C. Stanciu, M. A. Lieb, and A. J. Meixner, “Imaging nanometre-sized hot spots on smooth au films with high-resolution tip-enhanced luminescence and raman near-field optical microscopy,” *Chemphyschem*, vol. 9, pp. 316–320, Feb. 2008.
11. C. Stanciu, M. Sackrow, and A. J. Meixner, “High na particle- and tip-enhanced nanoscale raman spectroscopy with a parabolic-mirror microscope,” *Journal of Microscopy-oxford*, vol. 229, pp. 247–253, Feb. 2008.
12. R. Zondervan, F. Kulzer, M. A. Kol’chenko, and M. Orrit, “Photobleaching of rhodamine 6g in poly(vinyl alcohol) at the ensemble and single-molecule levels,” *Journal of Physical Chemistry A*, vol. 108, pp. 1657–1665, Mar. 2004.
13. W. E. Moerner and M. Orrit, “Illuminating single molecules in condensed matter,” *Science*, vol. 283, pp. 1670–+, Mar. 1999.
14. R. Kaufmann, C. Hagen, and K. Grunewald, “Fluorescence cryo-microscopy: current challenges and prospects.,” *Current opinion in chemical biology*, vol. 20, pp. 86–91, June 2014.
15. R. Kaufmann, P. Schellenberger, E. Seiradake, I. M. Dobbie, E. Y. Jones, I. Davis, C. Hagen, and K. Grunewald, “Super-resolution microscopy using standard fluorescent proteins in intact cells under cryo-conditions,” *Nano Letters*, vol. 14, pp. 4171–4175, July 2014.
16. S. Weisenburger, B. Jing, A. Renn, and V. Sandoghdar, “Cryogenic localization of single molecules with angstrom precision,” vol. 8815, pp. 88150D–88150D–9, 2013.
17. S. Weisenburger, B. Jing, D. Hanni, L. Reymond, B. Schuler, A. Renn, and V. Sandoghdar, “Cryogenic colocalization microscopy for nanometer-distance measurements,” *Chemphyschem*, vol. 15, pp. 763–770, Mar. 2014.
18. Y. Shibata, W. Katoh, T. Chiba, K. Namie, N. Ohnishi, J. Minagawa, H. Nakanishi, T. Noguchi, and H. Fukumura, “Development of a novel cryogenic microscope with numerical aperture of 0.9 and its application to photosynthesis research,” *Biochimica Et Biophysica Acta-bioenergetics*, vol. 1837, pp. 880–887, June 2014.
19. M. Yoshita, T. Sasaki, M. Baba, and H. Akiyama, “Application of solid immersion lens to high-spatial resolution photoluminescence imaging of gaas quantum wells at low temperatures,” *Applied Physics Letters*, vol. 73, pp. 635–637, Aug. 1999.

20. M. Vollmer, H. Giessen, W. Stolz, W. W. Ruhle, L. Ghislain, and V. Elings, "Ultrafast nonlinear subwavelength solid immersion spectroscopy at t = 8 k," *Applied Physics Letters*, vol. 74, pp. 1791–1793, Mar. 1999.
21. W. X. Li, S. C. Stein, I. Gregor, and J. Enderlein, "Ultra-stable and versatile widefield cryo-fluorescence microscope for single-molecule localization with sub-nanometer accuracy," *Optics Express*, vol. 23, pp. 3770–3783, Feb. 2015.
22. C. L. Schwartz, V. I. Sarbash, F. I. Ataullakhanov, J. R. Mcintosh, and D. Nicastro, "Cryo-fluorescence microscopy facilitates correlations between light and cryo-electron microscopy and reduces the rate of photobleaching," *Journal of Microscopy*, vol. 227, pp. 98–109, Aug. 2007.
23. A. Rigort, E. Villa, F. J. B. Bauerlein, B. D. Engel, and J. M. Plitzko, "Integrative approaches for cellular cryo-electron tomography: Correlative imaging and focused ion beam micromachining," 2012.
24. L. F. van Driel, J. A. Valentijn, K. M. Valentijn, R. I. Koning, and A. J. Koster, "Tools for correlative cryo-fluorescence microscopy and cryo-electron tomography applied to whole mitochondria in human endothelial cells," *European Journal of Cell Biology*, vol. 88, pp. 669–684, Nov. 2009.
25. A. Briegel, S. Y. Chen, A. J. Koster, J. M. Plitzko, C. L. Schwartz, and G. J. Jensen, "Correlated light and electron cryo-microscopy," 2010.
26. M. Schorb and J. A. G. Briggs, "Correlated cryo-fluorescence and cryo-electron microscopy with high spatial precision and improved sensitivity," *Ultramicroscopy*, vol. 143, pp. 24–32, Aug. 2014.
27. M. A. Le Gros, G. McDermott, M. Uchida, C. G. Knoechel, and C. A. Larabell, "High-aperture cryogenic light microscopy," *Journal of Microscopy-oxford*, vol. 235, pp. 1–8, July 2009.
28. E. A. Smith, B. P. Cinquin, M. Do, G. McDermott, M. A. Le Gros, and C. A. Larabell, "Correlative cryogenic tomography of cells using light and soft x-rays," *Ultramicroscopy*, vol. 143, pp. 33–40, Aug. 2014.
29. M. Hussels, A. Konrad, and M. Brecht, "Confocal sample-scanning microscope for single-molecule spectroscopy and microscopy with fast sample exchange at cryogenic temperatures," *Review of Scientific Instruments*, vol. 83, p. 123706, Dec. 2012.
30. T. L. Jennings, S. G. Becker-Catania, R. C. Triulzi, G. L. Tao, B. Scott, K. E. Sapsford, S. Spindel, E. Oh, V. Jain, J. B. Delehanty, D. E. Prasuhn, K. Boeneman, W. R. Algar, and I. L. Medintz, "Reactive semiconductor nanocrystals for chemoselective biolabeling and multiplexed analysis," *Acs Nano*, vol. 5, pp. 5579–5593, July 2011.
31. W. W. Yu, L. H. Qu, W. Z. Guo, and X. G. Peng, "Experimental determination of the extinction coefficient of cdte, cdse, and cds nanocrystals," *Chemistry of Materials*, vol. 15, pp. 2854–2860, July 2003.
32. H. M. Brecht, M., "Vorrichtung und verfahren zum transferieren eines probenhalters von einer transportvorrichtung zu einer scanvorrichtung," 2012.
33. C. M. Sparrow, "On Spectroscopic Resolving Power," *Astrophys. J.* , vol. 44, p. 76, Sept. 1916.
34. Q. Wu, G. D. Feke, R. D. Grober, and L. P. Ghislain, "Realization of numerical aperture 2.0 using a gallium phosphide solid immersion lens," *Applied Physics Letters*, vol. 75, pp. 4064–4066, Dec. 1999.
35. J. P. Zinter and M. J. Levene, "Maximizing fluorescence collection efficiency in multiphoton microscopy," *Optics Express*, vol. 19, pp. 15348–15362, Aug. 2011.
36. S. Hell, S. W., G. Reiner, C. Cremer, and E. H. K. Stelzer, "Aberrations in confocal fluorescence microscopy induced by mismatches in refractive-index," *Journal of Microscopy*, vol. 169, pp. 391–405, Mar. 1993.
37. V. Hirschfeld and C. G. Hubner, "A sensitive and versatile laser scanning confocal optical microscope for single-molecule fluorescence at 77 k," *Review of Scientific Instruments*, vol. 81, p. 113705, Nov. 2010.
38. F. Grazioso, B. R. Patton, and J. M. Smith, "A high stability beam-scanning confocal optical microscope for low

temperature operation," *Review of Scientific Instruments*, vol. 81, p. 093705, Sept. 2010.

39. A. Konrad, F. Wackenhut, M. Hussels, A. J. Meixner, and M. Brecht, "Temperature dependent luminescence and dephasing of gold nanorods," *Journal of Physical Chemistry C*, vol. 117, pp. 21476–21482, Oct. 2013.
40. J. Dubochet, "The physics of rapid cooling and its implications for cryoimmobilization of cells," 2007.
41. C. van Rijnsoever, V. Oorschot, and J. Klumperman, "Correlative light-electron microscopy (clem) combining live-cell imaging and immunolabeling of ultrathin cryosections," *Nature Methods*, vol. 5, pp. 973–980, Nov. 2008.

1. Introduction

Light microscopy is an often used technique especially for investigating biological samples and for getting a deeper understanding of chemical and physical processes. Confocal microscopy developed by Marvin Minsky in 1957 [1] was a remarkable step that increased the imaging resolution for gaining spatial information on luminescent samples. The principle of confocal microscopy bases on seperating out-of-focus light by e.g. implementing a pinhole increasing the image contrast and enabling to gather 3D structures of different specimen such as biological cells [2]. Therefore, a high numerical aperture (NA) microscope objective (MO) with corrected aberrations is required for high quality images with a high axial and lateral resolution. The NA describes the acceptance cone of an objective (see equation 1),

$$NA = n \cdot \sin(\alpha), \tag{1}$$

where n is the refractive index of the medium between lens and the sample and α is the half-angle of the cone of light that can enter or exit the lens. According to equation 1 the NA of an air objective ($n_{air} = 1$) can never be larger than unity. In order to increase the NA and thus the resolution of a microscope an additional immersion fluid, such as water or immersion oil is used. The principle of immersion requires on the possibility to fill the volume between MO and sample by a transparent liquid with a high refractive index. Using immersion liquids also increases the collection efficiency of the MO by reducing refraction and reflection at the interfaces between MO and sample. Nevertheless, the lateral resolution of light microscopes is typically restricted by the diffraction limit given by [3].

$$d = \frac{\lambda}{2 \cdot NA}, \tag{2}$$

where λ is the wavelength of light and d is the resolvable feature size. Since several years, the diffraction limit hampering high resolution microscopy of nanoscopic particles or structures

(size below 200 nm) was overcome by various super-resolution techniques at ambient conditions [4, 5, 6, 7, 8, 9, 10, 11]. However, many chromophores or auto-fluorescent proteins are hardly observable at room temperature especially at the single molecule level due to their low signal intensities, various quenching effects and fast photo-bleaching [12]. Further problems related to biological samples are drifts and degradation during measurements. One common solution for all these problems can be achieved by reducing the temperature. This leads to a decrease of photobleaching effects and to an enhanced fluorescence signal up to two orders of magnitude allowing one to relinquish the usage of additional fluorophores working as labels [13]. Furthermore, effects of many biological samples like drifting and degradation are also eliminated. However, confocal cryogenic microscopy is challenging due to technical and mechanical requirements of the low temperatures environment. Beam scanning and wide field imaging, as common techniques under cryogenic temperatures cannot reach a high resolution and image quality because the MOs still usable at low temperatures are insufficiently corrected for aberrations. A further hurdle - if one aims to implement high-resolution techniques at low temperatures - is the low longterm stability of the whole setup. These instabilities are caused by temperature gradients at the interface between the room and the low temperatures segments of the setup [14]. Nevertheless, several approaches to increase the resolution of microscopes at cryogenic temperatures could be achieved. Kaufmann *et al.* [15] utilize the effect of photoswitching [16, 17] of fluorescent marker proteins by using a 0.75 NA MO for super-resolution fluorescence cryogenic-microscopy. Shibata *et al.* developed a microscope with NA of 0.9, where the MO is mounted inside of the cryogenic vacuum space [18]. One method exceeding an NA of unity, was achieved by using solid immersion lenses [19] exhibiting an NA of 1.23 [20] with the disadvantage of a very small field of view. A versatile widefield cryo-fluorescence microscope for single-molecule localization with good thermal and mechanical stability was recently developed by Li *et al.* [21], featuring however an NA of only 0.7. A further often used technique combines low temperatures flourescence microscopy with other imaging techniques like electron microscopy. One example bases on the application of long working distance MOs with NA of 0.7 [22] or 0.75 [23, 24] and is able to combine cryogenic fluorescence microscopy with cryo-electron microscopy [25]. Another setup developed by Schorb *et al.* applies a short working distance MO with an NA of 0.95 in combination with electron microscopy [26]. However, until today none of these techniques were able to provide a resolution and image quality compared to conventional microscopes at ambient conditions. The decisive factor under cryogenic conditions is that the simple application of immersion fluids to provide NAs above

unity is exceedingly problematic due to their high freezing temperatures. Additionally, most high-performance MOs are losing their high imaging properties and getting easily damaged by thermal stress [27]. One promising brightfield imaging approach to increase the resolution under cryogenic temperatures by immersing the microscope was reported by Le Gros *et al.* [27, 28]. They use liquid propane or iso-pentane as immersion fluids and an MO placed outside the sample area, cooled with a copper cooling strip by liquid nitrogen. Summarizing, all these techniques may reach a resolution comparable to microscopes at ambient conditions but at the cost of scan range, image quality or mechanical stability.

In this study, we present a microscope setup, which allows us to immerse an MO together with the sample both positioned inside the sample chamber of a ^{4}He-bath-cryostat. Thus, we are able to record confocal luminescence images with an effective NA larger than unity and scan ranges only limited by the travel range of the piezo steppers (travel range is limited to 15 $\times$ 15 mm). Additionally, combining our scanning stage construction [29] with a sample transfer system allows us to load frozen or vitrified samples into the cold cryostat and remove them after the measurements without heating the samples to ensure a stable cold chain. We demonstrate the capability of our approach by confocally imaged quantum dots (QD) at 160 K with 1-propanol immersed MO and could appoint the effective NA to be around 1.08.

2. Experimental setup

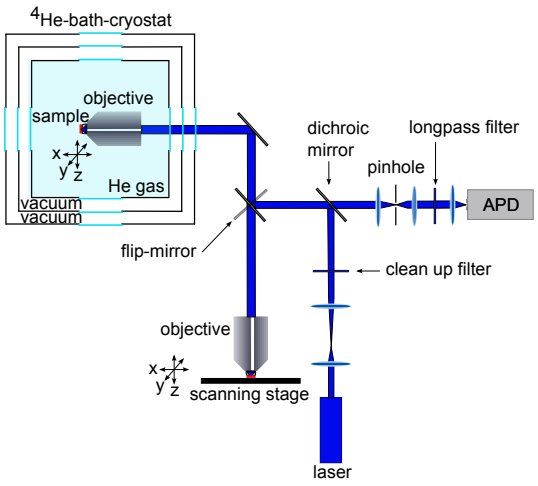

Fig. 1. Sketch of the low and room temperature setup for confocal imaging

According to the manufacturer, the QDs (ebioscience) have the following properties: Amine-Functionalized eFluor(R) 650NC nanocrystal with size about 8.7 nm in diameter showing an

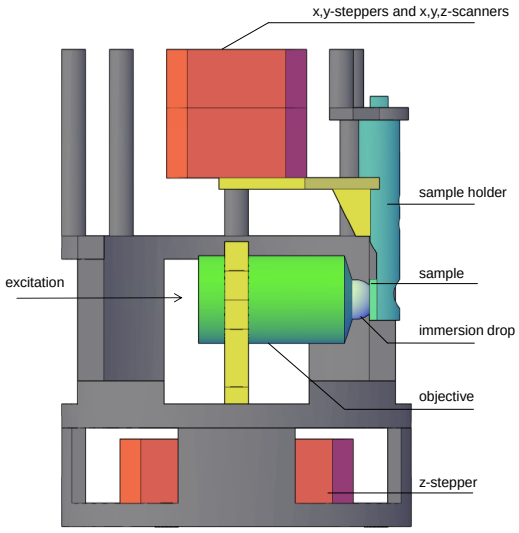

Fig. 2. Sketch of the probehead system for low temperature microscopy adapted from [29]. With a special sample transfer system, consisting of x, y, z, steppers (red), it is possible to transfer frozen (also vitrified) samples into the precooled cryostat.

emission at 650 nm [30]. They exhibit a relativly high absorption cross section, a large luminescence quantum yield, an emission maximum around 650 nm without any sidebands and a high photostability [31]. A droplet (1 μl) of QDs solution diluted in H_2O/glycerol with concentration 1 $pmol/l$ to guaranty single particle microscopy was deposited between two 4×4 mm^2 (thickness 200 μm) glass coverslips cleaned with chromosulfuric acid. For the room temperature experiments, we used two 22×22 mm^2 coverslips and immersion oil (Zeiss Immersol 518 F). For the low temperature experiments, we used 1-propanol as immersion fluid due to its physical properties, like viscosity, melting point (147 K) and transparency. The measurements were performed on a home-built confocal microscope consisting of a room and low temperature branch shown in Figure 1. An enlarged section of the sample transfer system and the inserted sample head implemented in the cryostat are shown in Figure 2. Scanning the sample with nanometer precision was achieved at ambient condition by a feed-back controlled three axis scanning table (Physik Instrumente P-517.3CL, $100 \times 100 \times 20$ μm) and at low temperatures by a multiaxis scanning stage (attocube steppers twice ANPx320 for x- and y-, ANPz101eXT for z-axis, scanners ANSxy100lr for x- and z-, ANSz100lr for y-axis) within a ^{4}He-bath-cryostat (Janis, SVT-200). The voltage dependent expansion of the scanners and their linearity were calibrated for the measuring temperature of 160 K by scanning a copper lattice grid (2000 lines/inch). The temperature dependent expansion deviation of the piezo scanners could be determined by the

calibration measurements allowing us to calculate the spatial expansion of the scanners very accuratly. For the immersion measurements at room and low temperature we used an MO with high NA (Microthek, 100 $\times$, $NA_{company} = 1.25$), for the experiments at low temperature without immersion an air MO (Microthek, 60 $\times$, $NA_{company} = 0.85$). From now on the NA given by the manufacturer will be abbreviated with $NA_{company}$, the theoretical NA by using different immersion liquids with NA_{theo} and the experimental determined NA with NA_{exp}. The temperature of 160 K in He atmosphere controlled by a cernox sensor (CX-1030-SD-HT 0.3L) is reached by cooling the cryostat with liquid nitrogen. Temperature variations during the measurements can be neglected due to the temperature control within the sample chamber by a cernox sensor close to the sample [29]. The reliability of the microscope and the temperature control could be demonstrated in a recent study by us [39]. A 488 nm *cw* laser diode (OBIS 488-20 LS) with a linear polarized Gaussian beam, which is coupled into the MO by a dichroic mirror (AHF, F48-487) was used for excitation of the QD. Their luminescence collected by the very same MO passes the dichroic mirror, a 30 μm pinhole and a longpass filter (AHF F76-490) and is finally detected by an avalanche photodiode (APD, Laser Components, COUNT-100C). For more details, the setup was described recently by Hussels *et al.* [29].

3. Results

Our home-built microscope [29, 32] equipped with an MO with high NA, allows us to mount, scan and record confocal luminescence images of different samples such as single QDs. Therefore, we apply a droplet of immersion liquid on the sample coverslip within three steps (Figure 3). First we precool our sample holder with mounted sample between two coverslips in a liquid nitrogen bath (Figure 3a, b). After that a few droplets of the immersion fluid 1-propanol were frozen directly on the coverslips (Figure 3c, d).

Our rapid sample transfer mechanism allows us to transfer the frozen sample with attached frozen immersion droplet on top into the precooled (140 K) cryostat [29]. After the mounting procedure, the sample holder was moved in front of the MO to achieve contact between the frozen immersion droplet and the MO. Then the sample chamber was heated slowly over the melting point (147 K) of 1-propanol to 160 K. Finally, we reduced the distance between sample and MO in order to bring the sample in the focus of the MO as shown in Figure 2. Figure 4 shows confocal scanning images of luminescent QDs both at a temperature of 160 K with (right) and without immersion (left). The image on the left side was recorded with a commonly used air MO ($NA_{company} = 0.85$). On the right side, a segment of an image of the same QD sample

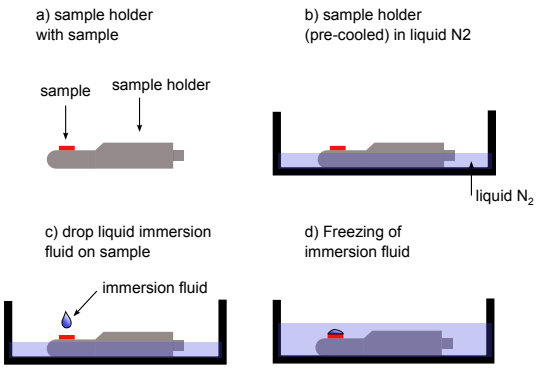

Fig. 3. Preparation of immersed sample. a) Prepared sample on sample holder b) precooled (liquid nitrogen) sample holder with prepared sample c) droping of 1-propanol droplets directly on the glass coverslips d) freezing of 1-propanol

measured with a high numerical MO ($NA_{company} = 1.25$) immersed with 1-propanol is shown. Both images show symmetrical spots representing single QDs. However, the spot diameters become visibly smaller with higher theoretical NA (with immersion). Thus, no distortions, drifts or other instabilities even with the immersed MO for the respective temperature disturb the measurements.

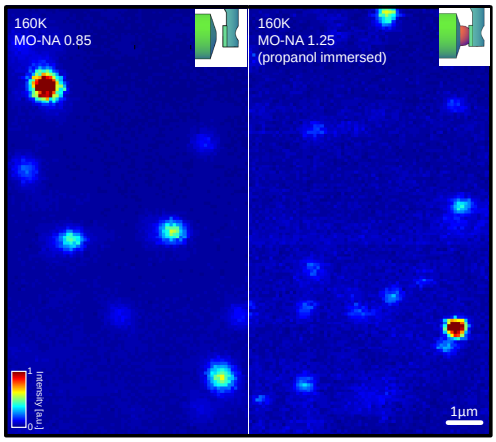

Fig. 4. Comparison of QD images at 160 K between an air MO with $NA_{company} = 0.85$ (left) and 1-propanol immersed MO (right).

To quantify the resolution and effective NA of the respective MO reached by our experiments we determine the point spread function (PSF) of several imaged QDs. As a reference measurement and to affirm the optical properties of the $NA_{company} = 1.25$ MO, we recorded several confocal images with the same MO at 300 K immersed with standard immersion oil. Evaluating the imaged QDs for these three measurement conditions (160 K with 1-propanol

immersion, without immersion and 300 K with oil immersion) allow us to determine the full width of half maximum (FWHM) of the PSF for each single spot as a measure for the resolution. In Figure 5 three spots are shown exemplarily for each condition, representing a single QD (A1, B1, C1) together with the cross section (A2, B2, C2) indicated by a white line in A1, B1, C1. According to Sparrows criterion [33, 34]:

$$FWHM = \frac{0.51 \cdot \lambda}{NA} = \frac{0.51 \cdot \lambda}{n \cdot \sin(\alpha)}, \tag{3}$$

where λ is the emission wavelength of the QD, n is the refractive index of the immersion liquid and α is the half-angle of the maximum cone of light that can enter or exit the lens, we are able to obtain the effective NA. Figure 5 A1 shows the spatially resolved QD luminescence at 160 K recorded with an air MO. The corresponding cross section (Figure 5 A2) showing the luminescence intensity as function of the x-axis scanner position in μm (blue line) was fitted by a Gaussian (red line) in order to determine the FWHM of the lateral PSF. Figure 5 B1 shows one spot out of an image recorded with the 1-propanol immersed $NA_{company} = 1.25$ MO of the same QD sample. Figure 5 C1, C2 show an image and corresponding cross-section measured with the same MO at 300 K immersed with standard immersion fluid (Zeiss Immersol^{T}M 518 F). If we compare these three cross sections it stands out that they are all symmetric and scale reciprocally with the theoretical effective NA as expected.

Table 1 summarizes everything about the three different measuring conditions. The bolded centre right column shows the results of our 1-propanol immersed measurements with a mean NA_{exp} of 1.08 determined by evaluating several PSFs for both, x and y directed cross sections.

Table 1. Comparison of our experimental results with an air objective, an oil immersed objective and the same objective immersed with 1-propanol.

	air objective	**immersion objective**	immersion objective
Immersion Liquid	–	**1-propanol**	immersion oil
Refractive Index	1.0	**1.385**	1.518
Temperatur [K]	160	**160**	300
NA_{exp}	0.82 $\pm$0.01	**1.08 $\pm$0.04**	1.15 $\pm$0.02
$NA_{company,theoretical}$	0.85	**1.15**	1.25

4. Discussion

The reported experiments represent the first fluorescence images under cryogenic conditions with a resolution, image quality and scan range comparable to images at standard ambient conditions. Our experimental results for single QDs show symmetrically shaped spots for each

Appendix A

Supporting information contains description of the algorithm to calculate S factor in ref. [126].

Variation of Exciton-Vibrational Coupling in Photosystem II Core Complexes from *Thermosynechococcus elongatus* as Revealed by Single-Molecule Spectroscopy

Sepideh Skandary,[1] Martin Hussels,[1] Alexander Konrad,[1] Thomas Renger,[2] Frank Müh,[2] Martin Bommer,[3] Athina Zouni,[3] Alfred Meixner,[1] and Marc Brecht[1,4]

[1]Universität Tübingen, IPTC and Lisa+ Center, Tübingen, Germany, [2]Johannes Kepler Universität, Institut für Theoretische Physik, Linz, Austria, [3]Humboldt Universität zu Berlin, Institut für Biologie, Berlin, Germany, and [4]Zurich University of Applied Science Winterthur (ZHAW), Winterthur, Switzerland

Description of the algorithm to calculate S:

The algorithm used to calculate the S factor is implemented in MATLAB and based on basic functions of MATLAB. It consist of several steps:

In the first step, the wavelength range covering the selected emitter in a spectra series is set by the user like it is shown in figure 1.

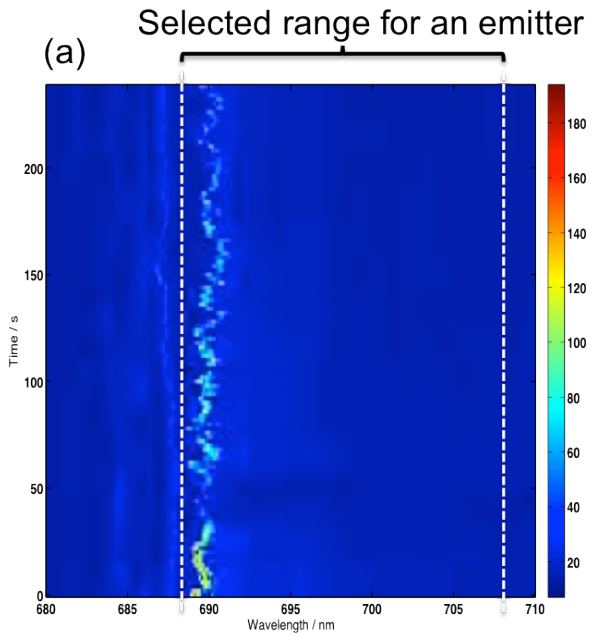

Figure (1): Single emitter suitable for shifting.

In the second step, each spectrum of the spectra series is shifted in a circular manner so that the maxima within the selected range are at the same position. As a result of this shifting, the absolute wavelength axis is no longer valid and therefore, it changed to a relative wavelength axis as shown in figure 2.

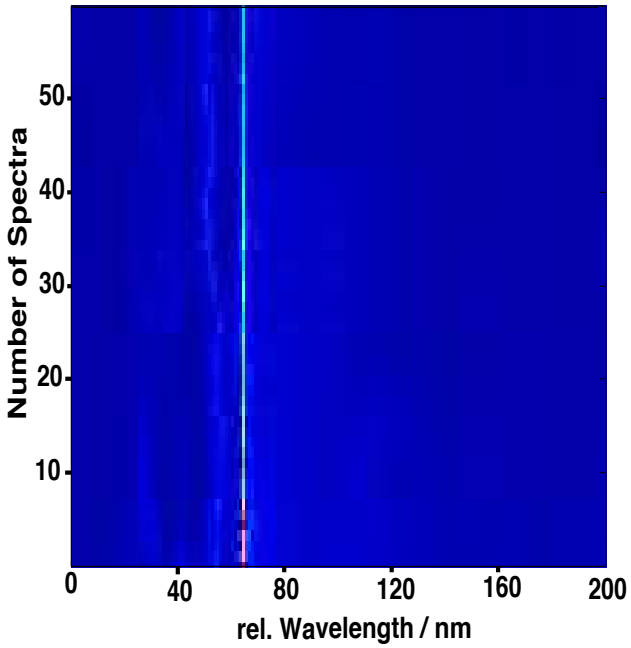

Figure (2): Resolved single emitter after shifting.

As one can see in figure 2, the shifting algorithm reduces the effects of spectral diffusion drastically.

In the third step, the mean spectrum of the shifted spectra series is calculated showing a nicely resolved ZPL and the PW (see figure 3).

In the fourth step, the user selects the ranges of the ZPL (12:24) and the PW (24:72) as shown in figure 3. This information is then used for the baseline correction by subtracting the lowest value within the ranges from the spectra. After the baseline correction the intensity within each range is summed up to gain the complete intensity for the ZPL and the PW.

In the fifth and last step S is calculated using the formula:

$$e^{-S} = \frac{I_{ZPL}}{I_{ZPL} + I_{PW}}$$

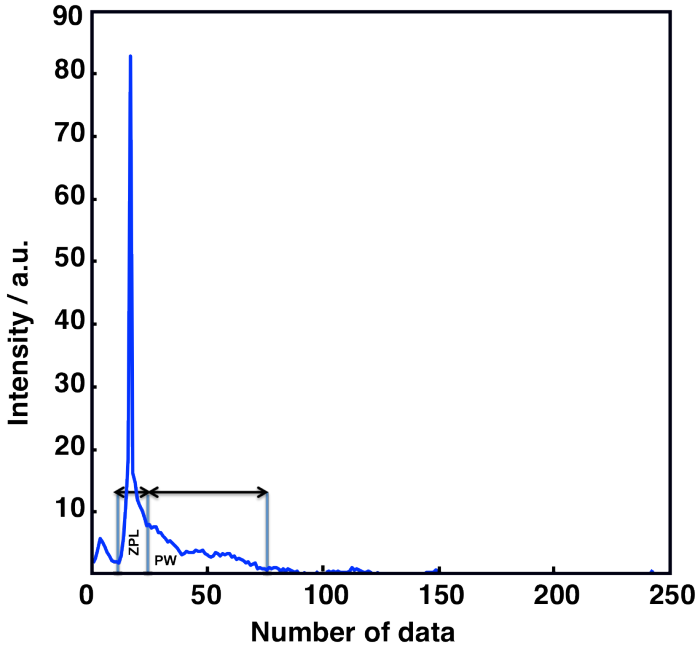

Figure (3): Resolved single emitter; the boundaries for I_{ZPL} and I_{PW} are shown. Both values are determined after baseline correction.

What is the error in the evaluation of the S-factors?

The determination of border where the ZPL ends and PW starts is not straightforward due to remaining contributions of spectral diffusion that was not eliminated by our shifting algorithm. We calculated several times I_{ZPL} and I_{PW} with different borders between PW and ZPL to estimate the error. Due to low intensity of the PW the position of the baseline has a strong influence on the determination of S. Therefore, we performed several baseline corrections and calculated S. From these values, we then determined the error of S by calculating the standard deviation.

Appendix B

Supporting information contains more details related to the results and discussion in ref. [135].

Supporting Information

Role of Missing Carotenoid in Reducing the Fluorescence of Single Monomeric Photosystem II Core Complexes

Sepideh Skandary [†], *Frank Müh* [‡], *Imran Ashraf* [†], *Mohamed Ibrahim* [♯], *Michael Metzger* [†], *Athina Zouni* [♯], *Alfred J. Meixner* [†], *and Marc Brecht* [*,†,§]

[†] IPTC and LISA[+] Center, University of Tübingen, Tübingen, Germany, [‡] Institute of Theoretical Physics, Johannes Kepler University Linz, Linz, Austria, [♯] Institute of Biology, Humboldt University of Berlin, Berlin, Germany, and [§] Reutlingen University, Process Analysis and Technology, Reutlingen, Germany

[*] E-mail: marc.brecht@reutlingen-university.de

[*] Phone: +49-7121-271-2065. Fax: +49-7121-271-2077

S1

This algorithm is used to determine the wavelength position of the most intense fluorescence emission and its full width at half-maximum (fwhm). In each data set, a constant offset due to the CCD camera is subtracted, and the wavelength position of the most intense contribution is determined. Starting from the maximum position, the width is determined where the intensity reaches half of the maximum value. The results are shown as 2D scattering plot in Figure 2a in the main text.

S2

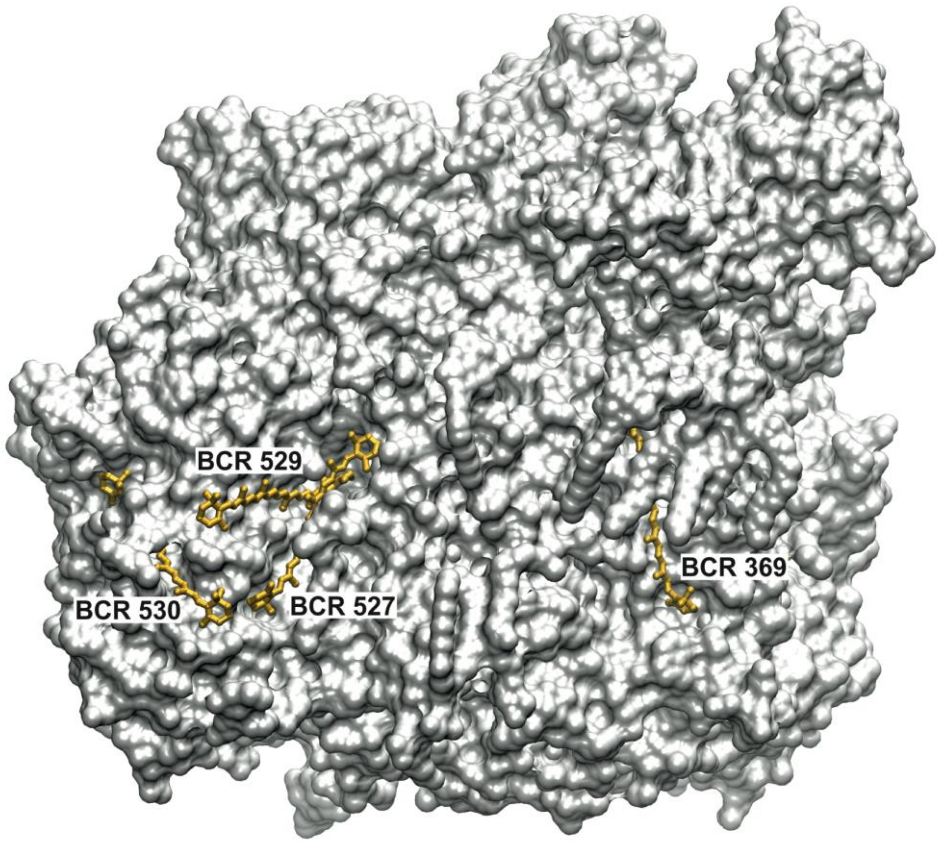

Figure 5: Molecular surface of mPSIIcc (PDB 3KZI). The view is on the dimerization surface [1], which is in contact with the second monomer in dPSIIcc and thus part of the monomer-monomer interface. The β-Car pigments (yellow) located at this interface are surface-exposed in mPSIIcc (i.e., exposed to the detergent phase) and despite being located in binding niches may detach from the complex. Figure made with VMD [2].

S3

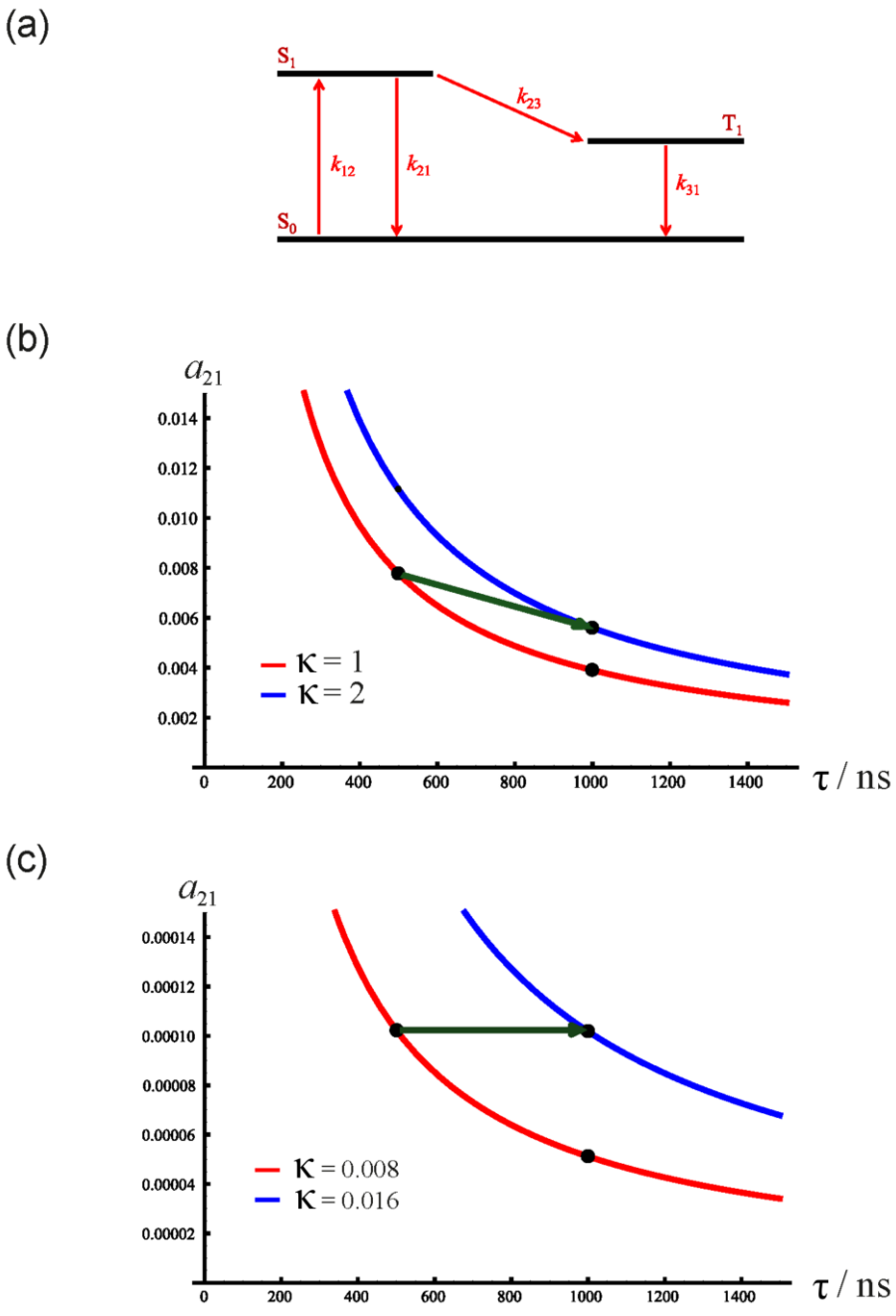

Figure 6: (a) Energy level diagram illustrating the kinetic model. k_{12}: excitation rate; k_{21}: fluorescence rate; k_{23}: intersystem crossing rate; $k_{31} = 1/\tau$: inverse triplet lifetime. (b) Steady-state population of the singlet state S_1 of the emitter (a_{21}) as a function of the triplet lifetime τ for two different values of the ratio $\kappa = k_{12}/k_{31} = \tau\, k_{12}$ ($\gamma := k_{23}/k_{21} = 1.8$, $1/k_{21} = 18$ ns). Both rates are in the same order of magnitude (i.e., κ is close to 1). The green arrow indicates the change in a_{21}, when τ is doubled from 500 to 1000 ns while keeping k_{12} constant (i.e., κ has to be doubled as well). (c) Same as in Figure 6b, but with a significantly lower excitation rate (i.e., significantly smaller κ for the same triplet lifetimes).

Kinetic model

To find the populations of the three states S_0 (singlet ground state), S_1 (first singlet excited state of the emitter) and T_1 (lowest triplet state of the emitter), we have to solve the set of differential equations related to the kinetic scheme depicted in Figure 6a. With the abbreviations

$$u_1 \equiv [S_0] \;\; ; \quad u_2 \equiv [S_1] \;\; ; \quad u_3 \equiv [T_1] \;\; ; \quad \mathbf{u} = \begin{pmatrix} u_1 \\ u_2 \\ u_3 \end{pmatrix} \tag{1}$$

we have to solve $\dot{\mathbf{u}} = \mathbf{A}\mathbf{u}$ with

$$\mathbf{A} = \begin{pmatrix} -k_{12} & k_{21} & k_{31} \\ k_{12} & -(k_{21}+k_{23}) & 0 \\ 0 & k_{23} & -k_{31} \end{pmatrix} \tag{2}$$

Determination of the roots from the condition

$$|\mathbf{A} - \lambda \mathbf{I}| = 0 \tag{3}$$

yields $\lambda_1 = 0$ and

$$\lambda_{2,3} = \frac{1}{2}\left(-p \pm \sqrt{p^2 - 4q}\right) \tag{4}$$

with

$$\begin{aligned} p &= k_{12} + k_{21} + k_{23} + k_{31} = -\lambda_2 - \lambda_3 \\ q &= k_{21}k_{31} + k_{23}k_{31} + k_{12}k_{23} + k_{12}k_{31} = \lambda_2\lambda_3 \end{aligned} \tag{5}$$

With the reasonable assumption $k_{21} > k_{31}$, it follows that $p^2 - 4q > 0$, so that all roots are real and we have:

$$u_i(t) = \sum_{k=1}^{3} a_{ik} e^{\lambda_k t} \qquad (i = 1,2,3) \tag{6}$$

Insertion of (6) into the system of differential equations yields for each k

$$\begin{aligned} a_{2k} &= a_{3k}\frac{(\lambda_k + k_{31})}{k_{23}} \\ a_{1k} &= a_{2k}\frac{(\lambda_k + k_{21} + k_{23})}{k_{12}} \end{aligned} \tag{7}$$

We assume that the system is in the S_0 state at $t = 0$. Then $u_1(0) = 1$, $u_2(0) = u_3(0) = 0$, and it follows from (6) that

$$\begin{aligned} a_{11} + a_{12} + a_{13} &= 1 \\ a_{21} + a_{22} + a_{23} &= 0 \\ a_{31} + a_{32} + a_{33} &= 0 \end{aligned} \tag{8}$$

Inserting (7) into (8) and taking into account that $\lambda_1 = 0$, yields three equations for the three quantities a_{3k} (k = 1,2,3), from which it follows that

$$\begin{aligned} a_{31} &= -a_{32} - a_{33} \\ a_{32} &= -a_{33}\frac{\lambda_3}{\lambda_2} \\ a_{33} &= \frac{k_{12}k_{23}}{\lambda_3^2 - \lambda_2\lambda_3} = \frac{k_{12}k_{23}}{\lambda_3^2 - q} \end{aligned} \tag{9}$$

In the following, we use units of ns^{-1} for the rates and assume $\gamma := k_{23}/k_{21} = 1.8$ (corresponding to a triplet yield of 64% for Chl *a* in ether solution and neglecting internal conversion [3]) as well as $1/k_{21} = 18$ ns [4]. Furthermore, we introduce the ratio $\kappa := k_{12}/k_{31}$ and the triplet lifetime $\tau = 1/k_{31}$. We then have:

$$\begin{aligned} p &= \frac{1+\kappa}{\tau} + \frac{1+\gamma}{18} \\ q &= \frac{1}{\tau}\left(\frac{1}{18} + \frac{1+\kappa}{10} + \frac{\kappa}{\tau}\right) \\ a_{2k} &= a_{3k}\,10\left(\lambda_k + \frac{1}{\tau}\right) \\ a_{1k} &= a_{2k}\frac{\tau}{\kappa}\left(\lambda_k + \frac{14}{90}\right) \\ a_{33} &= \frac{\kappa}{10\,\tau\,(\lambda_3^2 - q)} \end{aligned} \tag{10}$$

Of particular interest is the steady-state population (i.e., for $t \to \infty$) of S_1, which is given by

$$a_{21} = \frac{\kappa}{\tau^2\,(\lambda_3^2 - q)}\left(\frac{\lambda_3}{\lambda_2} - 1\right) \tag{11}$$

References

[1] M. Broser, A. Gabdulkhakov, J. Kern, A. Guskov, F. Müh, W. Saenger, A. Zouni, Crystal Structure of Monomeric Photosystem II from *Thermosynechococcus elongatus* at 3.6 Å Resolution, *J. Biol. Chem*., **2010**, 285, 26255-26262.

[2] W. Humphrey, A. Dalke, K. Schulten, VMD: Visual Molecular Dynamics. *J. Mol. Graphics* **1996**, 14, 33-38.

[3] P. G. Bowers, G. Porter, Quantum Yields of Triplet Formation in Solutions of Chlorophyll, *Proc. Roy. Soc. Lond. A*, **1967**, 296, 435-441.

[4] T. Renger, M.E. Madjet, F. Müh, I. Trostmann, F.-J. Schmitt, C. Theiss, H. Paulsen, H.J. Eichler, A. Knorr, G. Renger, Thermally Activated Superradiance and Intersystem Crossing in the Water-Soluble Chlorophyll Binding Protein, *J. Phys. Chem. B*, **2009**, 113, 9948-9957.

Appendix C

Supporting information contains more details related to the description of the algorithms, results and discussion in ref. [77].

Orientations Between Red Antenna States of Photosystem I Monomers from *Thermosynechococcus Elongatus* Revealed by Single-Molecule Spectroscopy

Sepideh Skandary,[†] Alexander Konrad,[†] Martin Hussels,[†] Alfred J. Meixner,[†] and Marc Brecht[*,†,‡]

University of Tübingen, IPTC and Lisa+ Center, Tübingen, Germany, and Zurich University of Applied Science Winterthur (ZHAW), Winterthur, Switzerland

E-mail: marc.brecht@uni-tuebingen.de

Phone: +49-7071-29-76239. Fax: +49-7071-29-5490

S1

The procedure for determining the angle between different components in polarization dependent data sets is based on discrete Fourier transformation (DFT). Figure 1 shows the workflow to determine the angle between two components clearly differing in polarization. Figure 1a shows the 2D data set of fluorescence spectra in dependence of the angle of the $\lambda/2$-waveplate. For analysis, DFT is applied on this data set along the angular (also time)

[*]To whom correspondence should be addressed
[†]University of Tübingen, IPTC and Lisa+ Center, Tübingen, Germany
[‡]Zurich University of Applied Science Winterthur (ZHAW), Winterthur, Switzerland

axis. In the second step, those Fourier components are selected corresponding to the expected modulation frequency caused by rotation of the $\lambda/2$-waveplate. Figure 1b and c show the amplitude and the phase of these components. In Figure 1b, two ranges of high amplitude can be identified and correlated to ranges of stable phase which is indicated by two dashed squares in Figure 1c. Then, using the phase plot (Figure 1c) their phase difference is calculated to 3.065 rad (nearly π). Due to the two-fold rotational symmetry of the polarization this gives two times the angular difference. Therefore, the angular difference of the polarization is then divided by two, which gives 1.532 rad (88 degree) for this example.

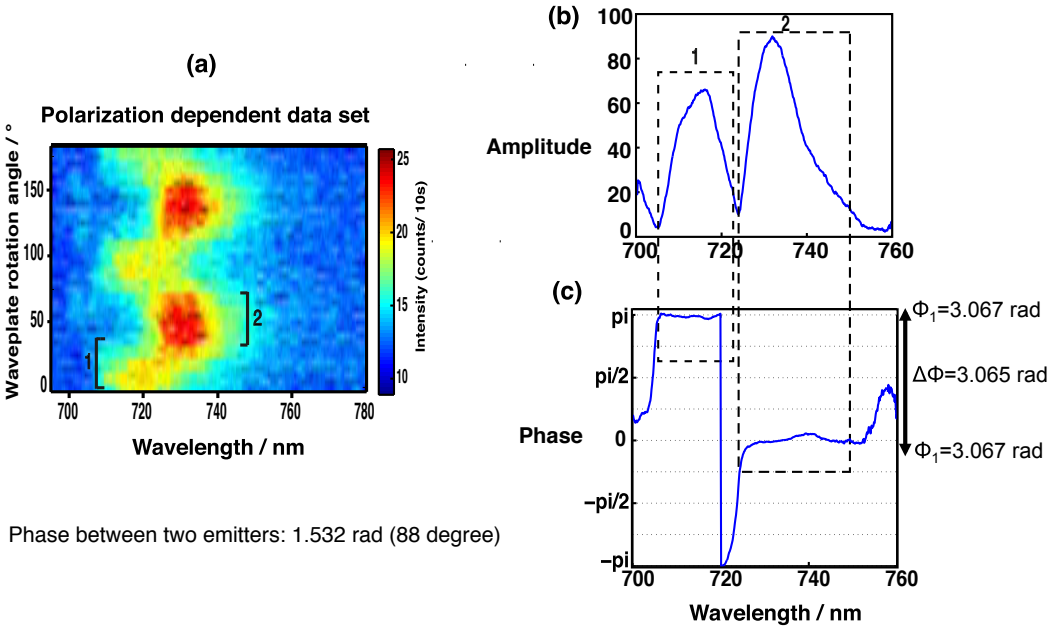

Figure 1: (a): Polarization dependent data sets with the angle nearly 90 degree between two emitters (1) and (2). (b): The amplitude modulation calculated by DFT. (c) The phase modulation calculated by DFT.

S2

For a pair of emitting dipoles with arbitary distributions, $\overrightarrow{\mu_1}$ and $\overrightarrow{\mu_2}$ are representing their TDMs responsible for fluorescence in polarization dependent data sets. The vectors $\overrightarrow{\mu_1}$ and $\overrightarrow{\mu_2}$ with angle α are shown in Figure 2 by green arrows. With respect to the arbitrary

orientation of each observed single monomer, this pair of vectors is rotated by a random angle around a random axis (calculated by the Euler rotation theorem). The new vectors, $\overrightarrow{\mu_1^*}$ and $\overrightarrow{\mu_2^*}$, shown in Figure 2 by blue arrows, represent now the emitters C708-C719 for a certain single PS I-M complex. The experimentally determined vectors $\overrightarrow{v_1}$ and $\overrightarrow{v_2}$, shown in Figure 2 by red arrows, enclosing the angle β can now be easily given by the projection onto the xy-plane, which is defined as the plane of the camera (detection plane).

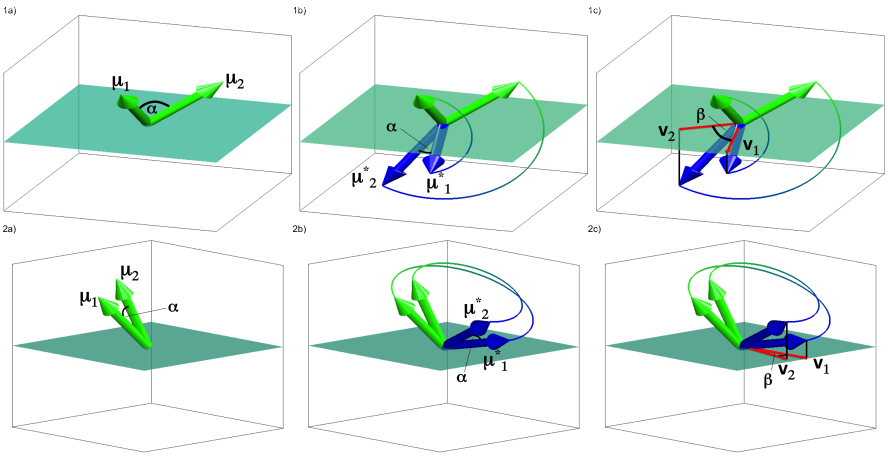

Figure 2: The TDMs of two emitters (green), the rotated vector pair (blue) and the projected vectors (red) which we detect during our polarization dependent measurements; (a): α= 60°, (b): α= 20°.

S3

To demonstrate all kinetic information of various recorded spectra of individual PS I-M data sets, a further statistical approach has been used. An algorithm (described as algorithm I in Ref.[1]) was used to determine the wavelength position of the most intense contributions in the fluorescence spectra of each individual PS I complex together with its full width at half maximum (FWHM). These parameters are determined regardless whether the intense contribution is a ZPL or a broad distribution. The result of this analysis applied on the whole data sets of single PS I-M is shown as a 2D scatter plot in Figure 3. The contributions are

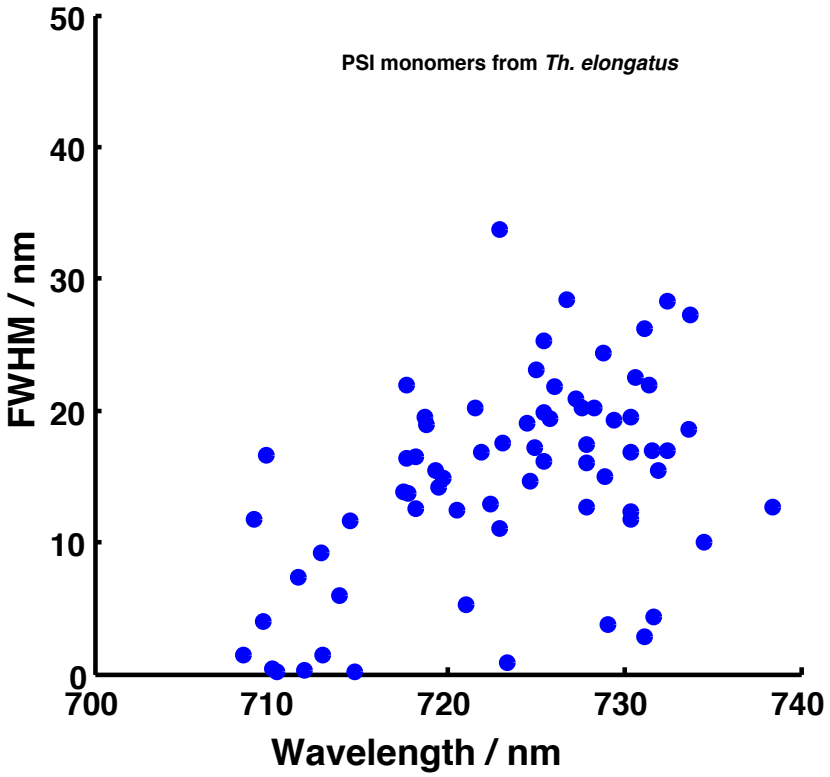

Figure 3: 2D-scatter plot obtained from the evaluation of the emission spectra of single PS I-M. Each dot represents the FWHM and wavelength position of the highest intensity peak in the spectra of individual PSI complexes.

scattered over a wide wavelength and line width range. 73% are found within a wavelength range from 717 to 735 nm and FWHM changed from 10 to 34 nm. 23% of the contributions are found within the wavelength range from 708 to 735 nm and FWHM less than 10 nm.

S4

The spectral positions of ZPLs were determined for all 70 individual data sets of monomers. Figure 4 shows the relative distributions of the spectral positions of ZPLs by counting their wavelength positions, their dynamics and occurrence along with the average spectrum of the whole data sets. For this purpose, the spectral positions of ZPLs for all single PS I-M data

sets were determined by using an algorithm explained in Ref.[1] Figure 4 shows the relative occurrence of ZPLs together with the average spectrum of the whole data sets taken from single PS I-M. The histogram shows the relative occurrence of ZPL spectral positions as a

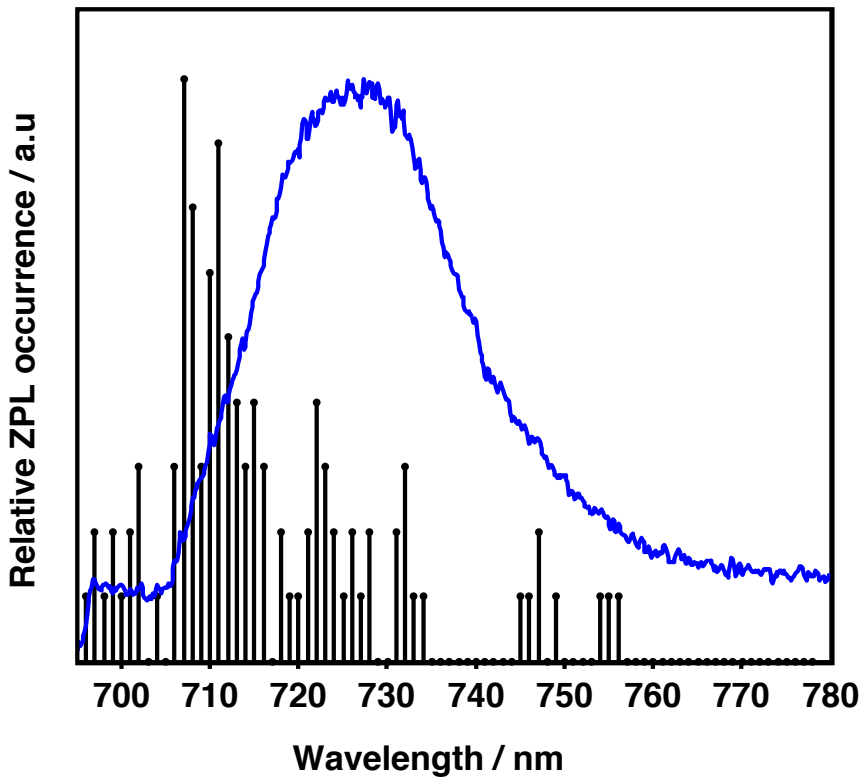

Figure 4: The ZPL distributions (histogram) and the average emission spectrum for PS I-M. The average spectrum (solid line) represents the summation of all data sets from single PS I-M at low temperature, 1.6 K. The data were scaled to similar amplitude.

function of wavelength between 695 nm to 780 nm. The ZPLs dominantly occurred in the range between 695 to 757 nm. The high relative occurrence of ZPLs are distributed in the spectral range <720 nm; The maximum are found at 707±1 nm. The peak of the average spectrum is at 726.6±0.1 nm (FWHM= 29.6±0.4 nm). The relative occurrence of ZPLs at 746 nm to 757 nm is very small. Based on their low integral intensity, these contributions are almost invisible in the average spectrum.

The major proportion of ZPLs of single PS I-M from *Th. elongatus* occurred around 710 nm

assigned to C708. Observed changes in the shape of ZPL distributions can be due to the environment of the involved chromophore assemblies.[1–4] The rate of conformational changes increases for chromophores of C715/C719 compared to C708, because less ZPLs are observed in the range >720 nm. For more detailed discussion, please see Ref.[4]

S5

For each Chl *a* molecule the TDM vectors were determined by the spatial information of the nitrogen atoms N_B and N_D given by the 1JB0. PDB-file as illustrated by Figure 5. For strong coupled Chls the determination of the resulting TDM is illustrated by Figure 6 and is based on the approximations made by Byrdin et al.[5]

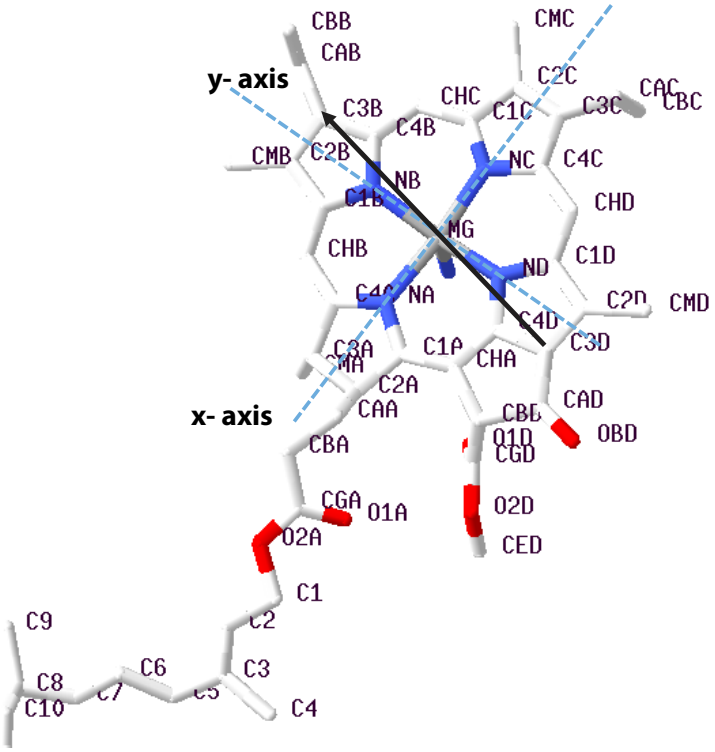

Figure 5: The black vector shows the TDM vector of each Chl *a* molecule.; from 1JB0. PDB; Jordan *et al.*[6]

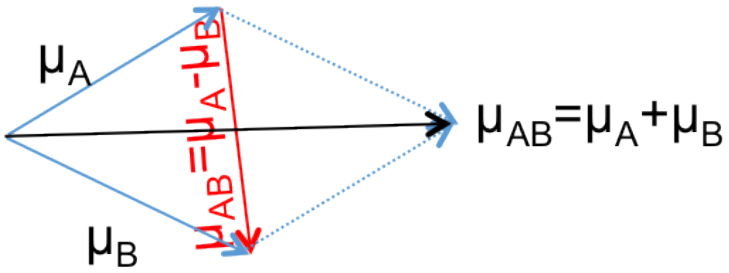

Figure 6: The coupling vectors.

Transition dipoles of coupled Chls e.g. B18B19 in table 1 in manuscript are calculated based on the approximation in table (3) of Byrdin et al.[5] (J $<$ 0 of sum bands (Σ) are energetically lower except for dimers: A16A17, A31A32 and A32B7, difference bands (Δ) are energetically lower.

References

(1) Hussels, M.; Brecht, M. Effect of Glycerol and PVA on the Conformation of Photosystem I. *Biochemistry* **2011**, *50*, 3628–3637.

(2) Brecht, M.; Hussels, M.; Schlodder, E.; Karapetyan, N. V. Red Antenna States of Photosystem I Trimers from *Arthrospira Platensis* Revealed by Single-Molecule Spectroscopy. *Biochim. Biophys. Acta* **2012**, *1817*, 445–452.

(3) Brecht, M.; Studier, H.; Elli, A. F.; Jelezko, F.; Bittl, R. Assignment of Red Antenna States in Photosystem I from *Thermosynechoccocus Elongatus* by Single-Molecule Spectroscopy. *Biochemistry* **2007**, *46*, 799–806.

(4) Brecht, M.; Studier, H.; Radics, V.; Nieder, J. B.; Bittl, R. Spectral Diffusion Induced by Proton Dynamics in Pigment–Protein Complexes. *J. Am. Chem. Soc.* **2008**, *130*, 17487 – 17493.

(5) Byrdin, M.; Jordan, P.; Krauss, N.; Fromme, P.; Stehlik, D.; Schlodder, E. Light Harvesting in Photosystem I: Modeling Based on the 2.5-Å Structure of Photosystem I from *Synechococcus Elongatus*. *Biophys. J.* **2002**, *83*, 433–457.

(6) Jordan, P.; Fromme, P.; Witt, H. T.; Klukas, O.; Saenger, W.; Krauss, N. Three-Dimensional Structure of Cyanobacterial Photosystem I at 2.5 Å Resolution. *Nature* **2001**, *411*, 909–917.

Acknowledgments

This doctoral thesis wouldn't be finalized without the helps and supports of many people. It is my pleasure to appreciate all of them here.

Hereby, I would like to express my sincere gratitude to my supervisor PD. Dr. Marc Brecht for the continuous support of my Ph.D study and related research, for his patience, motivation, thoughtful guidance and discussions about the research, and his warm encouragement when I had difficulties during this study.

My sincere thanks also go to Prof. Dr. Alfred J. Meixner, who provided me an opportunity to join his team, and who gave me access to the laboratory and research facilities. Without his precious supports, it would not be possible to conduct this research.

I would like to appreciate Dr. Eberhard Schlodder and Dr. Martin Hussels, for their generous insightful scientific discussions, guides and comments and encouragements. Also, I would like to thank Imran Ashraf, Dr. Alexander Konrad, Dr. Rigina Jäger and Dr. Xiao Wang for their scientific supports, stimulating discussions and troubleshooting in lab. I would like to thank all other colleagues from AG Brecht, AK Meixner and AG Scheele for the friendships as well as good advices and collaborations.

This thesis was done in collaboration with other research groups. I would like to acknowledge PD. Dr. Athina Zouni and her team at the Hombuldt University in Berlin for preparation of PSII sample. Many thanks to Dr. Frank Müh and Prof. Dr. Thomas Renger for all of theoretical contributions to this work and their valuable suggestions. I would like to thank Dr. Wolfgang Langer and MS. Bettina Kepler, both helped me during my studying and their administrative supports are always appreciated.

Last but not the least, I would like to thank my family for their supports of my PhD study. Special thanks go to my husband for his love and encouragement.

References

[1] R., H. de Vriend, H. de Groot, Artificial photosynthesis : for the conversion of sunlight to fuel, Leiden University, 2015.

[2] L. Hammarström, Artificial photosynthesis and solar fuels, Acc. Chem. Res. 42 (2009) 1859–1860.

[3] M. Ham, J. Choi, A. Boghossian, E. Jeng, R. Graff, D. Heller, A. Chang, A. Mattis, T. Bayburt, Y. Grinkova, A. Zeiger, K. Van Vliet, E. Hobbie, S. Sligar, C. A. Wraight, M. S. Strano, Photoelectrochemical complexes for solar energy conversion that chemically and autonomously regenerate, Nat. Chem. 2 (2010) 929.

[4] D. Hayes, G. B. Grif n, G. S. Engel, Engineering coherence among excited states in synthetic heterodimer systems, Science 340 (2013) 1431.

[5] H. Krassen, A. Schwarze, B. Friedrich, K. Ataka, O. Lenz, J. Heberle, Photosynthetic Hydrogen Production by a Hybrid Complex of Photosystem I and [NiFe]-Hydrogenase, Acs Nano 3 (12) (2009) 4055–4061.

[6] I. J. Iwuchukwu, M. Vaughn, N. Myers, H. ONeill, P. Frymier, B. D. Bruce, Self-organized photosynthetic nanoparticle for cell-free hydrogen production, Nat. Nanotechnol. 5 (2010) 73.

[7] A. Mershin, K. Matsumoto, L. Kaiser, D. Y. Yu, M. Vaughn, M. K. Nazeeruddin, B. D. Bruce, M. Graetzel, S. G. Zhang, Self-assembled photosystem-I biophotovoltaics on nanostructured TiO_2 *and* $ZnO, Sci.Rep.2(2012)234$.

[8] T. Hauch, Artificial photosynthesis: Looking to nature for alternative energy, DUJS.

[9] P. Tamarat, A. Maali, B. Lounis, M. Orrit, Ten years of single-molecule spectroscopy, J. Phys. Chem. A. 104 (2000) 1–16.

[10] W. E. Moerner, D. P. Fromm, Methods of single-molecule fluorescence spectroscopy and microscopy, Rev. Sci. Instrum. 74 (2003) 3597–3619.

[11] F. Müh, A. Zouni, Light-induced water oxidation in photosystem II, Front. Biosci. 16 (2011) 3072–3132.

[12] F. Müh, A. Zouni, Light-induced quinone reduction in photosystem II, Biochim. Biophys. Acta 1817 (2012) 44–65.

[13] K. Brettel, Electron transfer and arrangement of the redox cofactors in photosystem I, Biochim. Biophys. Acta 1318 (1997) 322–373.

[14] R. van Grondelle, V. I. Novoderezhkin, Energy transfer in photosynthesis: experimental insights and quantitative models, Phys. Chem. Chem. Phys. 8 (2006) 793–807.

[15] G. D. Scholes, G. R. Fleming, A. Olaya-Castro, R. van Grondelle, Lessons from nature about solar light harvesting, Nature Chem. 3 (2011) 763–774.

[16] K. Brettel, W. Leibl, Electron transfer in photosystem I, Biochim. Biophys. Acta 1507 (2001) 100–114.

[17] E. Schlodder, Introduction to optical methods in photosynthesis, Photosyn. Res. 101 (2009) 93–104. doi:10.1007/s11120-009-9446-y.

[18] R. Porra, W. Thompson, P. Kriedemann, Determination of accurate extinction coefficients and simultaneous-equations for assaying chlorophyll-a and chlorophyll-b extracted with 4 different solvents-verification of the concentration of chlorophyll standards by atomic-absorption spectroscopy, Biochim. Biophys. Acta 975 (1989) 384–394.

[19] N. V. Karapetyan, E. Schlodder, R. van Grondelle, J. P. Dekker, The Long Wavelength Chlorophylls in Photosystem I, Vol. 24, in Photosystem I: The Light–Driven Plastocyanin: Ferredoxin Oxidoreductase (Golbeck, J. H.,ed.), Springer, 2006.

[20] B. Gobets, R. van Grondelle, Energy transfer and trapping in photosystem I, Biochim. Biophys. Acta 1507 (2001) 80–99.

[21] M. Brecht, M. Hussels, E. Schlodder, N. V. Karapetyan, Red antenna states of photosystem I trimers from *arthrospira platensis* revealed by single-molecule spectroscopy, Biochim. Biophys. Acta 1817 (2012) 445–452.

[22] L. O. Palsson, C. Flemming, B. Gobets, R. van Grondelle, J. P. Dekker, E. Schlodder, Energy transfer and charge separation in photosystem I: P700 oxidation upon selective excitation of the long-wavelength antenna chlorophylls of *synechococcus elongatus*, Biophys. J. 74 (1998) 2611–2622.

[23] E. Schlodder, M. Cetin, M. Byrdin, I. V. Terekhova, N. V. Karapetyan, $P700^+$- and $^3P700$- induced quenching of the fluorescence at 760 nm in trimeric photosystem I complexes from the cyanobacterium *arthrospira platensis*, Biochim. Biophys. Acta 1706 (2005) 53–67.

[24] E. Boekema, J. Dekker, M. van Heel, M. Rögner, W. Saenger, I. Witt, H. Witt, Evidence for a trimeric organization of the photosystem I complex from the thermophilic cyanobacterium *synechococcus sp*, FEBS Lett. 217 (1987) 283– 286.

[25] M. U. Rögner, Mühlenhoff, E. J. Boekema, H. T. Witt, Mono-,di- and trimeric PS I reaction center complexes isolated from the thermophilic Cyanobacterium *synechococcus sp.* size, shape and activity, Biochim. Biophys. Acta 1015 (1990) 415–424.

[26] J. Kruip, D. Bald, E. Boekema, M. Rögner, Evidence for the existence of trimeric and monomeric photosystem I complexes in thylakoid membranes from cyanobacteria, Photosynth. Res. 40 (1994) 279 – 286.

[27] S. Turconi, J. Kruip, G. Schweitzer, M. Rögner, A. R. Holzwarth, A comparative fluorescence kinetics study of photosystem I monomers and trimers from *synechocystis* PCC 6803., Photosynth. Res. 49 (1996) 263–268.

[28] D. Abramavicius, S. Mukamel, Exciton delocalization and transport in photosystem I of cyanobacteria *Synechococcus Elongates*: Simulation study of coherent two-dimensional optical signals, J. phys. chem. B. 113 (2009) 6097–6108.

[29] L. O. Palsson, J. P. Dekker, E. Schlodder, R. Monshouwer, R. van Grondelle, Polarized site-selective fluorescence spectroscopy of the long-wavelength emitting chlorophylls in isolated photosystem I particles of *synechococcus elongatus*, Photosyn. Res. 48 (1996) 239–246.

[30] M. Byrdin, I. Rimke, E. Schlodder, D. Stehlik, T. A. Roelofs, Decay kinetics and quantum yields of fluorescence in photosystem I from *synechococcus elongatus* with P700 in the reduced and oxidized state: Are the kinetics of excited state decay trap-limited or transfer-limited?, Biophys. J. 79 (2000) 992–1007.

[31] B. Gobets, H. van Amerongen, R. Monshouwer, J. Kruip, M. Rögner, R. van Grondelle, J. P. Dekker, Polarized site-selected fluorescence spectroscopy of isolated photosystem I particles, Biochim. Biophys. Acta 1188 (1994) 75–85.

[32] R. N. Frese, M. A. Palacios, A. Azzizi, I. H. M. van Stokkum, J. Kruip, M. Rogner, N. V. Karapetyan, E. Schlodder, R. van Grondelle, J. P. Dekker, Electric field effects on red chlorophylls, beta-carotenes and P700 in cyanobacterial photosystem I complexes, Biochim. Biophys. Acta 1554 (2002) 180–191.

[33] P. Jordan, P. Fromme, H. T. Witt, O. Klukas, W. Saenger, N. Krauss, Three-dimensional structure of cyanobacterial photosystem I at 2.5 Å resolution, Nature 411 (2001) 909–917.

[34] Y. Umena, K. Kawakami, J. Shen, N. Kamiya, Crystal structure of oxygen-evolving photosystem ii at a resolution of 1.9Å, Nature 473 (2011) 50–60.

[35] T. Cardona, A. Sedoud, N. Cox, R. A. W., Charge separation in photosystem II: a comparative and evolutionary overview, Biochim. Biophys. Acta 1817 (2012) 26–43.

[36] J. Yano, V. Yachandra, Mn_4ca cluster in photosynthesis: Where and how water is oxidized to dioxygen, Chem. Rev. 114 (2014) 4175–4205.

[37] M. Broser, A. Gabdulkhakov, J. Kern, A. Guskov, F. Müh, W. Saenger, A. Zouni, Crystal structure of monomeric photosystem II from *thermosynechococcus elongatus* at 3.6å resolution, J. Biol. Chem. 285 (2010) 26255–26262.

[38] B. Loll, J. Kern, W. Saenger, A. Zouni, J. Biesiadka, Towards complete cofactor arrangement in the 3.0 Å resolution structure of photosystem II, Nature 438 (2005) 1040–1044.

[39] C. A. Tracewell, G. Brudvig, Multiple redox-active chlorophylls in the secondary electron-transfer pathways of oxygen-evolving photosystem II, Biochemistry 47 (2008) 11559–11572.

[40] E. Krausz, J. L. Hughes, P. J. Smith, R. J. Pace, S. P. Arsköld, Assignment of the low-temperature fluorescence in oxygen-evolving photosystem II, Photosynth. Res. 84 (2005) 193–199.

[41] E. G. Andrizhiyevskaya, A. Chojnicka, J. A. Bautista, B. A. Diner, R. van Grondelle, J. P. Dekker, Origin of the F685 and F695 fluorescence in photosystem II, Photosynth. Res. 84 (2005) 173–180.

[42] M. Brecht, S. Skandary, J. Hellmich, C. Glöckner, A. Konrad, M. Hussels, A. Meixner, A. Zouni, E. Schlodder, Spectroscopic properties of photosystem II core complexes from *Thermosynechococcus elongatus* revealed by single-molecule experiments, Biochim. Biophys. Acta 1837 (2014) 773–781.

[43] Y. Shibata, S. Nishi, K. Kawakami, J. R. Shen, T. Renger, Photosystem II does not possess a simple excitation energy funnel: Time-resolved fluorescence spectroscopy meets theory, J. Am. Chem. Soc. 135 (2013) 6903 – 6914.

[44] M. Komura, Y. Shibata, S. Itoh, A new fluorescence band F689 in photosystem II revealed by picosecond analysis at 4-77 K: Function of two terminal energy sinks F689 and F695 in PSII, Biochim. Biophys. Acta 1757 (2006) 1657–1668.

[45] R. J. van Dorssen, J. Breton, J. J. Plijter, K. Satoh, H. van Gorkom, J. Amesz, Spectroscopic properties of the reaction center and of the 47 kDa chlorophyll protein of photosystem II, Biochim. Biophys. Acta 893 (1987) 267–274.

[46] R. J. van Dorssen, J. J. Plijter, J. P. Dekker, A. den Ouden, J. Amesz, H. J. Gorkom, Spectroscopic properties of chloroplast grana membranes and of the core of photosystem II, Biochim. Biophys. Acta 890 (1987) 134–143.

[47] J. P. Dekker, A. Hassoldt, A. Pettersson, H. van Roon, M. L. Groot, R. van Grondelle, On the nature of the F695 and F685 emission of photosystem II in: P. Mathis (Ed.),

photosynthesis: from light to biosphere, Kluwer Academic Publishers, Dordrecht, The Netherlands, 1 (1995) 53–56.

[48] A. M. van Oijen, M. Ketelaars, J. Köhler, T. J. Aartsma, J. Schmidt, Unraveling the electronic structure of individual photosynthetic pigment-protein complexes, Science 285 (1999) 400–402.

[49] H. P. Lu, X. S. Xie, Single-molecule spectral fluctuations at room temperature, Nature 385 (1997) 143–146.

[50] D. Rutkauskas, V. I. Novoderezhkin, R. J. Cogdell, R. van Grondelle, Fluorescence spectroscopy of conformational changes of single LH2 complexes, Biophys. J. 88 (2005) 422–435.

[51] F. Schleifenbaum, C. Blum, V. Subramaniam, A. J. Meixner, Single–molecule spectral dynamics at room temperature, Mol. Phys. 107 (2009) 1923–1942.

[52] Y. Berlin, A. Burin, J. Friedrich, J. Köhler, Low temperature spectroscopy of proteins. part II: Experiments with single protein complexes, Phys. Life Rev. 4 (2007) 64–89.

[53] Y. Shibata, H. Ishikawa, S. Takahashi, I. Morishima, Time-resolved hole-burning study on myoglobin: Fluctuation of restricted water within distal pocket, Biophys. J. 80 (2001) 1013–1023.

[54] C. Hofmann, M. Ketelaars, M. Matsushita, H. Michel, T. J. Aartsma, J. Köhler, Single-molecule study of the electronic couplings in a circular array of molecules: Light-harvesting-2 complex from *Rhodospirillum Molischianum*, Phys. Rev. Lett. 90 (2003) 013004.

[55] K. Huang, A. Rhys, Theory of light absorption and non-radiative transitions in f-centres, Proc. Roy. Soc. Lond. A, 204 (1950) 406–423.

[56] T. Pullerits, R. Monshouwer, F. van Mourik, R. van Grondelle, Temperature-dependence of electron-vibronic spectra of photosynthetic systems-computer-simulations and comparison with experiment, Chem. Phys. 194 (1995) 395–407.

[57] I. Renge, Impurity spectroscopy in glasses and disordered crystals: Inhomogeneous broadening and electron phonon coupling, J. Lumin. 128 (2008) 413–420.

[58] M. Rätsep, M. Pajusalu, A. Freiberg, Wavelength-dependent electron-phonon coupling in impurity glasses, Chem. Phys. Lett. 479 (2009) 140–143.

[59] K. K. Rebane, Impurity spectra of solids, Plenum, New York, 1970.

[60] R. I. Personov, In 'Spectroscopy and excitation dynamics of condensed molecular systems', Agranovich, V. M., and Hochstrasser, R. M., Eds.; North Holland: Amsterdam, Chapter 10, 1983.

[61] E. J. G. Peterman, T. Pullerits, R. Grondelle, H. Amerongen, Electron-phonon coupling and vibronic fine structure of light-harvesting complex II of green plants: temperature dependent absorption and high-resolution fluorescence spectroscopy, J. Phys. Chem. B 101 (1997) 4448–4457.

[62] J. Pieper, M. Rätsep, K. D. Irrgang, A. Freiberg, Chromophore-chromophore and chromophore-protein interactions in monomeric light-harvesting complex II of green plants studied by spectral hole burning and fluorescence line narrowing, J. Phys. Chem. B 113 (2009) 10870–10880.

[63] T. Renger, V. May, O. Kühn, Ultrafast excitation energy transfer dynamics in photosynthesis pigment–protein complexes, Phys. Rep. 343 (2001) 137–254.

[64] L. Hanson, Molecular orbital theory of monomer pigments, in: H. Scheer (Ed.), CRC Press, Baton Rouge, 1991.

[65] M. Gouterman, Spectra of porphyrins, J. Mol. Spectrosc. 6 (1961) 138–163.

[66] P. Atkins, Physical Chemistry, Oxford University Press, 1978.

[67] R. van Grondelle, J. P. Dekker, T. Gillbro, V. Sundstrom, Energy-transfer and trapping in photosynthesis, Biochimica et Biophysica Acta - Bioenergetics 1187 (1994) 1–65.

[68] T. Förster, Zwischenmolekulare Energiewanderung Und Fluoreszenz, Annalen Der Physik 2 (1948) 55–75.

[69] D. L. Dexter, A theory of sensitized luminescence in solids, The Journal of Chemical Physics 21 (5) (1953) 836–850. doi:10.1063/1.1699044.
URL http://link.aip.org/link/?JCP/21/836/1

[70] T. Ansbacher, H. Srivastava, T. Stein, R. Baer, m. Merkxc, A. Shurkiz, Calculation of transition dipole moment in fluorescent proteins—towards efficient energy transfer, Phys. Chem. Chem. Phys. 14 (2012) 4109–4117.

[71] R. van Grondelle, Excitation-energy transfer, trapping and annihilation in photosynthetic systems, Biochim. Biophy. Acta 811 (1985) 147–195.

[72] N. J. Fraser, H. Hashimoto, R. J. Cogdell, Carotenoids and bacterial photosynthesis: The story so far ..., Photosynthesis Research 70 (2001) 249–256.

[73] T. J. Aartsma, J. Matysik, Biophysical Techniques in Photosynthesis II, Vol. 26, Springer, 2008.

[74] W. Parson, V. Nagarajan, Light-Harvesting Antennas in Photosynthesis, Vol. 13, Kluwer Academic Publichers Dodrecht/Boston/London, 2003.

[75] M. K. Sener, D. Y. Lu, T. Ritz, S. Park, P. Fromme, K. Schulten, Robustness and optimality of light harvesting in cyanobacterial photosystem I, J. Phys. Chem. B 106 (2002) 7948–7960.

[76] A. Damjanovic, T. Ritz, K. Schulten, Energy transfer between carotenoids and bacteriochlorophylls in light-harvesting complex II of purple bacteria, Phys. Rev. E 59 (1999) 3293.

[77] S. Skandary, A. Konrad, M. Hussels, A. Meixner, M. Brecht, Orientations between red antenna states of photosystem I monomers from *thermosynechococcus elongatus* revealed by single-molecule spectroscopy, J Phys Chem B. 119 (2015) 13888–1389.

[78] M. Byrdin, P. Jordan, N. Krauss, P. Fromme, D. Stehlik, E. Schlodder, Light harvesting in photosystem I: Modeling based on the 2.5-Å structure of photosystem I from *Synechococcus Elongatus*, Biophys. J. 83 (2002) 433–457.

[79] E. Schlodder, M. Hussels, M. Cetin, N. V. Karapetyan, M. Brecht, Fluorescence of the various red antenna states in photosystem I complexes from cyanobacteria is affected differently by the redox state of P700., Biochim. Biophys. Acta 1807 (2011) 1423–31.

[80] F. Schleifenbaum, C. Blum, M. Brecht, A. Meixner, Single-molecule spectroscopy, Handbook of spectroscopy: Second, Enlarged Edition, 2014.

[81] W. P. Ambrose, W. E. Moerner, Fluorescence spectroscopy and spectral diffusion of single impurity molecules in a crystal, Nature 349 (1991) 225–227.

[82] M. A. Bopp, Y. W. Jia, L. Q. Li, R. J. Cogdell, R. M. Hochstrasser, Fluorescence and photobleaching dynamics of single light-harvesting complexes, Proceedings of The National Academy of Sciences of The United States of America 94 (1997) 10630–10635.

[83] M. Orrit, J. Bernard, R. I. Personov, High-resolution spectroscopy of organic-molecules in solids - from fluorescence line narrowing and hole-burning to single-molecule spectroscopy, Journal of Physical Chemistry 97 (1993) 10256–10268.

[84] R. Jankowiak, J. M. Hayes, G. J. Small, Spectral hole-burning spectroscopy in amorphous molecular-solids and proteins, Chem. Rev. 93 (1993) 1471–1502.

[85] B. Kozankiewicz, M. Orrit, Single-molecule photophysics, from cryogenic to ambient conditions, Chem. Soc. Rev. 43 (2014) 1029.

[86] E. Hooley, X. T. Hao, Single molecule spectroscopy, The University of Melbourne home page: Ultrafast and Microspectroscopy Laboratories, The University of Melborn, Australia.

[87] R. Bittl, E. Schlodder, I. Geisenheimer, W. Lubitz, R. J. Cogdell, Transient EPR and absorption studies of carotenoid triplet formation in purple bacterial antenna complexes., J. Phys. Chem. B 23 (2001) 5525–5535.

[88] J. Pieper, J. Voigt, G. Renger, G. J. Small, Analysis of phonon structure in line-narrowed optical spectra, Chem. Phys. Lett. 310 (1999) 296–302.

[89] H. Frauenfelder, S. G. Sliar, P. G. Wolynes, The Energy Landscapes and Motions of Proteins, Science 254 (1991) 1598–1603.

[90] M. Hussels, M. Brecht, Evidence for direct binding of glycerol to photosystem I, FEBS Lett. 585 (2011) 2445–2449.

[91] H. Lesch, J. Schlichter, J. Friedrich, J. M. Vanderkooi, Molecular probes: What is the range of their interaction with the environment?, Biophys. J. 86 (2004) 467–472.

[92] R. G. Smock, L. M. Gierasch, Sending Signals Dynamically, Science 324 (2009) 198–203.

[93] C. Hofmann, T. J. Aartsma, H. Michel, J. Köhler, Direct observation of tiers in the energy landscape of a chromoprotein: a single-molecule study, Proc. Nat. Acad. Sci. U.S.A. 100 (2003) 15534–15538.

[94] D. Rutkauskas, J. Olsen, A. Gall, R. J. Cogdell, C. N. Hunter, R. van Grondelle, Comparative study of spectral flexibilities of bacterial light-harvesting complexes: Structural implications, Biophysical Journal 90 (2006) 2463–2474.

[95] V. I. Goldanskii, Chemical-reactions at very low-temperatures, Annual Review of Physical Chemistry 27 (1976) 85–126.

[96] M. Brecht, H. Studier, V. Radics, J. B. Nieder, R. Bittl, Spectral diffusion induced by proton dynamics in pigment–protein complexes, J. Am. Chem. Soc. 130 (2008) 17487 – 17493.

[97] M. Brecht, Spectroscopic characterization of photosystem I at the single-molecule level, Mol. Phys. 107 (2009) 1955–1974.

[98] M. Brecht, V. Radics, J. B. Nieder, R. Bittl, Protein dynamics-induced variation of excitation energy transfer pathways, Proc. Nat. Acad. Sci. USA 106 (2009) 11857–11861.

[99] Molecular Mechanism of Photosynthesis, in: R.E. Blankenship (Ed.), Blackwell Science, Oxford,, 2002.

[100] P. Fromme, P. Jordan, N. Krauss, Structure of photosystem I, Biochim. Biophys. Acta 1507 (2001) 5–31.

[101] A. Ben-Shem, F. Frolow, N. Nelson, Crystal structure of plant photosystem I, Nature 426 (2003) 630–635.

[102] E. El-Mohsnawy, M. J. Kopczak, E. Schlodder, M. Nowaczyk, H. E. Meyer, B. Warscheid, N. V. Karapetyan, M. Rogner, Structure and function of intact photosystem I monomers from the cyanobacterium *Thermosynechococcus Elongatus*, Biochemistry. 49 (2010) 4740–4751.

[103] B. Gobets, M. Ericsson, L. Palsson, V. Shubin, N. Karapetyan, R. van Grondelle, J. Dekker, Site selected polarized fluorescence spectroscopy of photosystem I particles isolated from the cyanobacteria *spirulina platensis*, Prog. Biophys. Mol. Biol. 65 (1996) 221–221.

[104] A. Rivadossi, G. Zucchelli, F. M. Garlaschi, R. C. Jennings, The importance of psi chlorophyll red forms in light-harvesting by leaves, Photosyn. Res. 60 (1999) 209–215.

[105] B. Gobets, I. H. M. van Stokkum, F. van Mourik, J. P. Dekker, R. van Grondelle, Excitation wavelength dependence of the fluorescence kinetics in photosystem I particles from *synechocystis* PCC 6803 and *synechococcus elongatus*, Biophys. J. 85 (2003) 3883–3898.

[106] B. Bruggemann, K. Sznee, V. I. Novoderezhkin, R. van Grondelle, V. May, From structure to dynamics: Modeling exciton dynamics in the photosynthetic antenna PSI, J. Phys. Chem. B 108 (2004) 13536–13546.

[107] E. Schlodder, F. Lendzian, J. Meyer, M. Cetin, M. Brecht, T. Renger, N. V. Karapetyan, Long-wavelength limit of photochemical energy conversion in photosystem I, J. Am. Chem. Soc. 136 (2014) 3904–3918.

[108] V. Zazubovich, S. Matsuzaki, T. W. Johnson, J. M. Hayes, P. R. Chitnis, G. J. Small, Red antenna states of photosystem I from cyanobacterium *synechococcus elongatus*: a spectral hole burning study, Chem. Phys. 275 (2002) 47–59.

[109] L. O. Palsson, B. Gobets, C. Fleming, L. M. Ericsson, R. van Grondelle, E. Schlodder,

J. P. Dekker, Long-wavelength antenna pigments in photosystem I, Prog. In Biophys. and Mol. Bio. 65 (1996) 217–217.

[110] M. Brecht, H. Studier, A. F. Elli, F. Jelezko, R. Bittl, Assignment of red antenna states in photosystem I from *Thermosynechoccocus elongatus* by single-molecule spectroscopy, Biochemistry 46 (2007) 799–806.

[111] E. Mörschel, G. H. Schatz, Correlation of photosystem II complexes with exoplasmatic freeze-fracture particles of thylakoids of the cyanobacterium *Synechococcus-sp*, Planta 172 (1987) 145–154.

[112] I. M. Folea, P. Zhang, E.-M. Aro, E. J. Boekema, Domain organization of photosystem II in membranes of the cyanobacterium *Synechocystis* PCC6803 investigated by electron microscopy, FEBS Lett. 582 (2008) 1749–1754.

[113] J. P. Dekker, E. J. Boekema, Supramolecular organization of thylakoid membrane proteins in green plants, Biochim. Biophys. Acta 1706 (2005) 12–39.

[114] S. Caffarri, R. Kouril, S. Kereiche, E. J. Boekema, R. Croce, Functional architecture of higher plant photosystem II supercomplexes, EMBO J. 28 (2009) 3052–3063.

[115] G. Raszewski, T. Renger, Light harvesting in photosystem II core complexes is limited by the transfer to the trap: Can the core complex turn into a photoprotective mode?, J. Am. Chem. Soc. 130 (2008) 4431–4446.

[116] F. Müh, T. Renger, A. Zouni, Crystal structure of cyanobacterial photosystem II at 3.0 Å resolution: a closer look at the antenna system and the small membrane-intrinsic subunits, Plant Physiol. Biochem. 46 (2008) 238–264.

[117] T. Renger, E. Schlodder, Optical properties, excitation energy and primary charge transfer in photosystem II: Theory meets experiment, J. Photochem. Photobiol. B 104 (2011) 126–141.

[118] E. J. G. Peterman, H. van Amerongen, R. van Grondelle, J. P. Dekker, The nature of the excited state of the reaction center of photosystem ii of green plants: A high-resolution

fluorescence spectroscopy study, Proceedings of the National Academy of Sciences of the United States of America 95 (1998) 6128–6133.

[119] M. L. Groot, E. J. G. Peterman, I. H. M. van Stokkum, J. P. Dekker, R. van Grondelle, Triplet and fluorescing states of the CP47 antenna complex of photosystem II studied as a function of temperature, Biophys. J. 68 (1995) 281–290.

[120] M. L. Groot, R. N. Frese, F. L. de Weerd, K. Bromek, A. Pettersson, E. J. G. Peterman, I. H. M. van Stokkum, R. van Grondelle, J. P. Dekker, Spectroscopic properties of the CP43 core antenna protein of photosystem II, Biophys. J. 77 (1999) 3328–3340.

[121] B. Neupane, N. C. Dang, K. Acharya, M. Reppert, V. Zazubovich, R. Picorel, M. Seibert, R. Jankowiak, Insight into the electronic structure of the CP47 antenna protein complex of photosystem II: hole burning and fluorescence study, J. Am. Chem. Soc. 132 (2010) 4214–4229.

[122] K. Acharya, B. Neupane, M. Reppert, X. Feng, R. Jankowiak, On the unusual temperature-dependent emission of the CP47 antenna protein complex of photosystem II, J. Phys. Chem. Lett. 1 (2010) 2310–2315.

[123] M. Minsky, Memoir on inventing the confocal scanning microscope, Scanning 10 (1988) 128–138.

[124] J. B. Pawley, Handbook of Biological Confocal Microscopy, Plenum Press, New York, 1989.

[125] M. Hussels, A. Konrad, M. Brecht, Confocal sample-scanning microscope for single-molecule spectroscopy and microscopy with fast sample exchange at cryogenic temperatures, Rev. Sci. Instrum. 83 (2012) 123706.

[126] S. Skandary, M. Hussels, A. Konrad, T. Renger, F. Müh, M. Bommer, A. Zouni, A. Meixner, M. Brecht, Variation of exciton-vibrational coupling in photosystem II core complexes from *thermosynechococcus elongatus* as revealed by single-molecule experiments, J. Chem. Phys. B. 119 (2015) 4203–4210.

[127] S. Skandary, A. Konrad, M. Hussels, A. Meixner, M. Brecht, Polarization-dependent single-molecule spectroscopy on photosystem I, Proc. SPIE 9554, doi:10.1117/12.2207523.

[128] A. Zouni, J. Kern, J. Frank, T. Hellweg, J. Behlke, W. Saenger, K. Irrgang, Size determination of cyanobacterial and higher plant photosystem II by gel permeation chromatography, light scattering, and ultracentrifugation, Biochemistry 44 (2005) 4572–4581.

[129] J. Kern, B. Loll, C. Lüneberg, D. DiFiore, J. Biesiadka, K. D. Irrgang, A. Zouni, Purification, characterisation and crystallisation of photosystem II from *Thermosynechococcus elongatus* cultivated in a new type of photobioreactor, Biochim. Biophys. Acta 1706 (2005) 147–157.

[130] F. Müh, A. Zouni, Extinction coefficients and critical solubilisation concentrations of photosystems I and II from *Thermosynechococcus Elongatus*, Biochim. Biophys. Acta 1708 (2005) 219–228.

[131] C. Hofmann, H. Michel, M. van Heel, J. Köhler, Multivariate analysis of single-molecule spectra: surpassing spectral diffusion, Phys. Rev. Lett. 94 (2005) 195501.

[132] M. Hussels, M. Brecht, Effect of glycerol and PVA on the conformation of photosystem I, Biochemistry 50 (2011) 3628–3637.

[133] N. Herascu, M. Najafi, A. Amunts, J. Pieper, K.-D. Irrgang, R. Picorel, M. Seibert, V. Zazubovich, Parameters of the protein energy landscapes of several light-harvesting complexes probed via spectra hole growth kinetics measurements, J. Phys. Chem. B 115 (2011) 2737–2747.

[134] M. Najafi, N. Herascu, M. Seibert, R. Picorel, R. Jankowiak, V. Zazubovich, Spectral hole-burning, recovery and thermocycling in chlorophyll-protein complexes: distribution of barriers on the protein energy landscape, J. Phys. Chem. B 116 (2012) 11780–11790.

[135] S. Skandary, F. MḦ, I. Ashraf, M. Metzger, A. Zouni, A. Meixner, M. Brecht, Single-molecule spectroscopy of monomeric photosystem II from *thermosynechococcus elongatus*, in prepration.

[136] A. Konrad, A. Trost, S. Skandary, M. Hussels, A. Meixner, N. Karapetyan, Manipulating the excitation transfer in photosystem I by a fabry- perot metal resonator with optical sub-wavelength dimensions, Phys. Chem. Chem. Phys. 16 (2014) 6175–6181.

[137] I. Ashraf, S. Skandary, M. Khaywah, M. Metzger, A. Meixner, P. Adam, M. Brecht, Effects of irregular bimetallic nanostructures on the optical properties of photosystem I from *thermosynechococcus elongatus*, Photonics 2 (2015) 838–854.

[138] M. Metzger, A. Konrad, S. Skandary, I. Ashraf, A. Meixner, M. Brecht, Resolution enhancement for low-temperature scanning microscopy by cryostat immersion imaging, Opt. Express 24 (2016) 13023–13032.